U-Pb Geochronological Constraints on the Tectonic and Thermal Evolution of Paleoproterozoic Crust in the Grand Canyon, Arizona

by

David Paul Hawkins

B.A., Biology
Clark University
1983

M.S., Geology
The George Washington University
1991

Submitted to the Department of Earth, Atmospheric and Planetary Sciences
in Partial Fulfillment of the Requirements for the Degree of

Doctor of Philosophy

at the
Massachusetts Institute of Technology

July 1996
[September 1996]

Signature of Author.....
Department of Earth, Atmospheric and Planetary Sciences
July 30, 1996

Certified by.....
Samuel A. Bowring
Thesis Supervisor

Accepted by.....
Thomas H. Jordan
Department Head

U-Pb Geochronological Constraints on the Tectonic and Thermal Evolution of Paleoproterozoic Crust in the Grand Canyon, Arizona

by

David Paul Hawkins

Submitted to the Department of Earth, Atmospheric and Planetary Sciences on July 30, 1996 in Partial Fulfillment of the Requirements for the Degree of Doctor of Philosophy

ABSTRACT

The Upper Granite Gorge of the Grand Canyon exposes mid-crustal levels of an extensive Paleoproterozoic orogenic system that was assembled, accreted and incorporated into the North American craton between 1.8 and 1.6 Ga. This study combines field observations, petrography, igneous and metamorphic petrology and U-Pb geochronology of zircon, monazite, xenotime and sphene to evaluate in detail the significance of the measured U-Pb dates and to use those dates to construct a tectonic and thermal evolution for Paleoproterozoic middle crust in this part of the orogen.

U-Pb dates are interpreted using field observations, petrography, back-scattered electron imaging, micro-sampling of previously imaged crystals of monazite and xenotime and models for Pb diffusion. This approach reveals that: 1) some samples contain minerals with simple U-Pb systematics; 2) in some samples primary monazite and xenotime crystals are partially replaced by secondary monazite that probably formed during subsolidus fluid-mineral interaction; 3) reverse discordance in U-Pb monazite analyses fro the Grand Canyon appears to be caused by processes involving exchange of elemental Pb indicating that both the U-Pb dates and the Pb-Pb dates are unreliable; and 4) metamorphic sphene from several samples preserve cooling dates from which closure temperatures and integrated cooling rates are calculated.

The Upper Gorge exposes 1750 to 1732 Ma metavolcanic and metasedimentary rocks intruded by 1741 to 1713 Ma mafic to intermediate plutons. These arc-related rocks, which locally developed on older (1840 Ma) basement, were deformed, metamorphosed and intruded by peraluminous granite dikes and sills during the Yavapai orogeny between 1710 and 1680 Ma. Steeply-dipping shear zones divide the transect into crustal blocks that preserve contrasting peak metamorphic conditions (upper greenschist to lower granulite facies) and cooling histories. In several blocks, the rocks cooled relatively rapidly for about 10 m.y. after the peak of metamorphism and then cooled more slowly (<5°C/m.y.) for at least 15 m.y. In contrast, a crustal block in the middle of the transect preserves evidence for growth of metamorphic zircon, monazite, xenotime and sphene between 1665 Ma and 1560 Ma. The contrasting thermal histories of the blocks suggests that displacement along some of the block-bounding shear zones post-dated the Yavapai orogeny by at least 150 m.y.

Thesis Advisor: Samuel A. Bowring
Associate Professor of Geology and Geochemistry

ACKNOWLEDGMENTS

As I sit down to acknowledge all the folks who have contributed to this thesis I am overcome by emotion. It is amazing to me how many 'simple twists of fate' have brought me to this moment. For example, as an uninspired undergraduate, lacking direction, I chose to take Physical and Historical Geology to avoid subjecting myself to organic chemistry. I reasoned that I wouldn't have to work as hard and I could see more Grateful Dead concerts during the fall and spring semesters/tours. Little did I know that 14 years later I'd be sitting here writing the acknowledgments to a doctoral dissertation in Geology. Of course, I wouldn't be here if Richard Tollo hadn't been the professor that taught the geology courses at Clark University and hadn't happened to come across my application for graduate school several years later at George Washington University. Eventually, I finished a Masters degree under Dick's guidance. Dick Tollo also introduced me to the work of a 'young, energetic field-oriented geochronologist' named Sam Bowring (who happened to be a student in a class that Dick TA'ed years earlier at the University of New Hampshire) and therefore defined the path that led to this moment. Dick's influences on my career are profound and I thank him for giving me the opportunity.

After GWU I moved to Washington University in St. Louis to start a PhD program and after a short time I decided to work with that 'young, energetic field-oriented geochronologist' (funny how that description of Sam is so completely incomplete). During my second year at Wash U, Sam was courted by MIT. I will never forget the excitement in the lab during Sam's lengthy deliberation: Clark Isachsen and I were always coming up with ways to convince Sam to move to Boston. I will always remember how much I wanted Sam to go MIT despite the difficulties it might cause me at Wash U. In the end, Sam decided to move to MIT and, much to my surprise and delight, he suggested that I apply to MIT so that we could continue our work in the southwestern United States. Sam's faith in me at that point in my life far-exceeded the faith I had in myself. The decision to move to MIT was one of the most difficult decisions my wife, Mary, and I had made up to that point. I was not sure that I was up to the challenge and my fear of mathematics was at an all-time high. In no small way, Sam's faith in me carried me through those difficult times.

When I arrived at MIT, I was happy to find that the G&G faculty were approachable, affable and extremely supportive. It was a real confidence-booster to be treated more like a colleague than a graduate student. The relationship between the graduate students and the faculty is, in my view, one of the many strengths of the MIT program. I thank Kip Hodges for his advice and camaraderie, and for being an excellent communicator and teacher. I thank Tim Grove for his enthusiasm, for guiding me through my second generals project, and especially for the trip to Newfoundland (one the highlights of my doctoral program—there's really nothing quite like walking on the Earth's mantle!). I would also like to thank John Southard for giving me numerous teaching opportunities, both as a teaching assistant and as a lecturer for the Boston Bay Group. Finally I'd like to thank John Grotzinger and Clark Burchfiel for their advice and good humor in the hallways of the department and in the field.

The early days at MIT were indeed difficult. I don't think I would have gotten through without the support, advice, camaraderie and help of my fellow graduate

students. Dave Applegate, Meg Coleman, Dave Dinter, Glenn Gaetani, Nancy Harris, Martha House, Audrey Huerta, Allison MacFarlane, Dave McCormick, CJ Northrup, Shane Pelechaty, Alberto Saal, Bev Saylor, Cathy Summa, Dawn Sumner, Tom Wagner (and others whom I may have forgotten) taught me a great deal during the first few semesters. During the post-generals phase of my MIT career, I had the great pleasure of interacting with Anke Friedrich, Mark Schmitz, and Jim Van Orman. All of my colleagues, knowingly and unknowingly, helped me navigate the emotional roller coaster ride of graduate school. Much love, many thanks and best wishes to all.

Nancy Dallaire and Pat Walsh provided much needed logistical assistance and an occasional shot in the arm. Thanks and best wishes to you both. Thanks also to Bill Olszewski for teaching me some of the finer points of isotope geochemistry. I also want to thank Meg Thompson from Wellesley College for her encouragement over the last couple of years. And, of course, I thank Dick Latvala whose picks reinvigorated my spirit during the last two months of writing.

I had the great fortune of working in a spectacular field area. Rafting down the Colorado River in the Grand Canyon was the thrill-of-a-lifetime. The trips were organized, implemented and paid for by Karl Karlstrom and Brad Ilg at the University of New Mexico and Mike Williams at the University of Massachusetts, Amherst. My deepest thanks to Karl, Brad and Mike for making it all happen and for our countless discussions on the thermal evolution of continental lithosphere. I'd also like to thank the various boatmen, cooks and field assistants that came on the trips, especially Kelly Smith whose skill at his craft and philosophy of life will always be an inspiration.

Working in the Mass Spectrometry lab at MIT was a rewarding experience heightened by the advice, guidance and assistance of Sam's students and post-doctoral fellows: Kevin Chamberlain, Drew Coleman, Jesse Dann, Todd Housh, and Clark Isachsen. In addition to teaching me the ropes, Kevin, Jesse, Clark and Drew helped me learn to deal with the daily trials and tribulations of working in the lab. My interaction with Clark was especially rewarding, and his patience and understanding during emotionally challenging times saved me on more than one occasion. Much love and thanks, Clark. Drew also deserves special thanks: Drew was there for me during the best and worst of times and through it all he never refused to help out or to do 'just one more favor'. Much love and thanks, Drew — I wish you all the best at BU. Speaking of favors, Kathy Davidek's generosity probably takes the cake. Kathy was always willing to lend a hand—her kindness, consideration and companionship in the lab are greatly appreciated. Much love and many thanks, Kathy. Knowing that the lab is in your hands makes leaving less difficult.

Of course, Sam is the true spirit of the lab. I am at a loss to find the words to acknowledge and thank Sam for all he has done for me. What can you say about someone who brought me to MIT despite my mediocre academic record, built-up my confidence from ground-zero, gave me free-reign of the lab, placed a tremendous amount of responsibility on my shoulders, and showed me, through his actions, a desire to see me not just succeed, but to excel? Sam is one of those rare individuals who recognizes hidden potential in people and finds ways to transform that potential into accomplishments. The fact that I am sitting here today writing these acknowledgments is testimony to Sam's ability as an advisor. If I am successful in my professional career, it is because of Sam's persistence, caring and nurturing. Thanks Sam. Thanks for everything.

Finally I'd like to thank my family. My parents have always given me the freedom to make my own mistakes. Even when I went down the wrong path, they never ceased to tell me that they were proud of me for trying. Sometimes that made all difference in the world. Lastly, and most of all, I thank Mary Hawkins; my best friend, partner, and wife (and soon to be the mother of our first child - Nicholas Paul). Mary strongly believed that coming to MIT was the right thing to do, and even though she had to endure and sacrifice much more than I could have anticipated, her commitment to our goals never wavered. Mary's love and support more than anything else have brought me here today to write the acknowledgments for my doctoral dissertation.

DEDICATION

I dedicate this thesis to the memory of:

Dr. Rudolph F. Nunnemacher
Professor of Zoology at Clark University

who helped me realize my professional goals
and instilled in me the enthusiasm, drive, and perseverance
required to achieve those goals.

And to the memory of my grandparents:

Carolina Ann and Nicholas Paul Rogers

who taught me the importance of hard work.

TABLE OF CONTENTS

CHAPTER 1: INTRODUCTION AND OVERVIEW 19

INTRODUCTION 19

REGIONAL GEOLOGY 20

OVERVIEW 21

REFERENCES 23

FIGURE CAPTIONS 25

FIGURES 27

CHAPTER 2: A U-PB GEOCHRONOLOGIC FRAMEWORK FOR THE PALEOPROTEROZOIC CRUSTAL EVOLUTION OF THE UPPER GRANITE GORGE, GRAND CANYON, ARIZONA 35

ABSTRACT 35

INTRODUCTION 36

REGIONAL GEOLOGY 37

GEOLOGY OF THE UPPER GRANITE GORGE 39

ANALYTICAL METHODS 40

RESULTS 42

Supracrustal Rocks 42

Mafic to Intermediate Intrusions 46

Peraluminous Granite and Pegmatite Intrusions 49

DISCUSSION 53

The Elves Chasm Pluton 53

Volcanism and Sedimentation 54

Arc-Related Magmatism 55

Timing of Deformation 56

Peraluminous Granite and Pegmatite Magmatism 58

Timing of Metamorphism 59

Regional Affinities and Significance 59

SUMMARY 62

REFERENCES 63

FIGURE CAPTIONS 68

FIGURES 71

CHAPTER 3: A CASE STUDY OF MONAZITE (AND XENOTIME) U-PB SYSTEMATICS FROM THE PALEOPROTEROZOIC OF THE GRAND CANYON, ARIZONA.....119

ABSTRACT.....119
INTRODUCTION.....120
GEOLOGIC BACKGROUND.....123
SAMPLE DESCRIPTIONS.....123
ANALYTICAL TECHNIQUES.....125
U-PB GEOCHRONOLOGY.....127
Unfoliated Granite Dike.....127
Sheared Granite Dike.....130
Deformed Pegmatite Stock.....136
DISCUSSION.....142
REFERENCES.....145
FIGURE CAPTIONS.....150
FIGURES.....153

CHAPTER 4: U-PB MONAZITE, XENOTIME AND SPHENE GEOCHRONOLOGICAL CONSTRAINTS ON THE HIGH-TEMPERATURE THERMAL HISTORY OF PALEOPROTEROZOIC MIGMATITES FROM THE GRAND CANYON, ARIZONA.....179

INTRODUCTION.....179
GEOLOGIC BACKGROUND.....181
FIELD OBSERVATIONS FROM MILE 78.0.....182
PREVIOUS U-PB GEOCHRONOLOGY.....183
SAMPLE DESCRIPTIONS.....184
BACK-SCATTERED ELECTRON IMAGING.....187
ANALYTICAL TECHNIQUES.....189
THERMOCHRONOLOGICAL TECHNIQUES.....191
U-PB GEOCHRONOLOGY OF THE MIGMATITE.....194
Paleosomal Schist.....194
Leucosomal Pegmatite.....195
Coupled Melanosomal Selvage and Leucosomal Granite.....195
INTERPRETATION OF THE MIGMATITE DATA.....197
Age Dispersion in the Paleosomal Schist.....197
Age Dispersion in the Leucosomal Pegmatite.....200

Age Dispersion in the Melanosome/Leucosome....201
Origin of the Leucosomes....204
U-PB GEOCHRONOLOGY OF THE CALC-SILICATE GNEISS....205
DISCUSSION....207
A High-Temperature Thermal History for the Mineral Canyon Block....207
Regional Implications....210
CONCLUSIONS....212
REFERENCES....214
FIGURE CAPTIONS....218
FIGURES....221

CHAPTER 5: U-PB GEOCHRONOLOGICAL CONSTRAINTS ON THE SIGNIFICANCE OF THE BLOCK ARCHITECTURE OF THE UPPER GRANITE GORGE, GRAND CANYON, ARIZONA: CONTRASTING THERMAL HISTORIES ACROSS SHEAR ZONES IN PALEOPROTEROZOIC MIDDLE CRUST....259

INTRODUCTION....259
THE BLOCK ARCHITECTURE OF THE UPPER GORGE....260
ANALYTICAL TECHNIQUES....261
THERMOCHRONOLOGICAL APPROACH....262
U-PB GEOCHRONOLOGY....264
Mineral Canyon Block....264
Clear Creek Block....265
Trinity Creek Block....267
Topaz Canyon Block....274
Tuna Creek Block....275
Walthenberg Canyon Block....276
DISCUSSION....277
CONCLUSIONS. 281
REFERENCES....282
FIGURE CAPTIONS....284
FIGURES....287

CHAPTER 1

INTRODUCTION AND OVERVIEW

INTRODUCTION

The ultimate goal of this thesis is to contribute to our understanding of the growth and maturation of continental lithosphere. The area chosen for this study is the Grand Canyon in northern Arizona which exposes a 70 kilometer-long transect through a Paleoproterozoic orogenic system that extends across the southern part of the North American craton. The orogen is composed largely of juvenile island arc crust that was accreted to North America between 1.8 and 1.6 Ga and subsequently incorporated into the North American craton. These rocks, therefore, provide an opportunity to study the growth and maturation of the North American craton during the Paleoproterozoic.

Uranium-lead geochronology provides fundamental constraints on the evolution of continental lithosphere. Geochronological data from carefully chosen samples in metamorphic terrains can be used to establish the absolute timing and duration of deformation, metamorphism, magmatism and post-metamorphic cooling, which provide important clues regarding the processes that create and modify continental lithosphere. The research described in this thesis was designed to develop a temporal framework to characterize the Paleoproterozoic tectonic and thermal history of crust exposed in the Upper Granite Gorge of the Grand Canyon.

The sections that follow are meant to accomplish two goals. The first section briefly describes the Paleoproterozoic orogenic system of the southwestern United States and the second section briefly states the purpose of each chapter.

REGIONAL GEOLOGY

The 1.8 to 1.6 Ga Paleoproterozoic orogen that underlies much of southern North America records a period of crustal growth during which the craton grew by about 20% in only 200 m.y. (Fig. 1). The orogen is well-exposed in the southwestern United States in the Rocky Mountains of Colorado and New Mexico, at the southern margin of the Colorado Plateau and in the Basin and Range province of southern Arizona and southern California (Fig. 2).

Based on the geology in the southwestern United States, the orogen has been divided into two orogenic belts: the Yavapai belt and the Mazatzal belt (e.g., Karlstrom et al., 1987; Karlstrom and Daniel, 1993; Fig. 2). The Yavapai belt is characterized by 1.75 to 1.72 Ga supracrustal rocks intruded by contemporaneous calc-alkaline batholiths that were deformed, metamorphosed to moderate- to high-grades, and intruded by granitic plutons between 1.71 and 1.68 Ga (Karlstrom et al., 1987; Karlstrom and Bowring, 1988). In the Mojave Desert region of southern California, rocks of the Yavapai belt preserve geochemical evidence for the influence of older crust on the development of 1.75 to 1.70 Ga island arcs (Bennett and DePaolo, 1987; Wooden et al., 1988; Wooden and Miller, 1990; Wooden and DeWitt, 1991; Bryant et al., 1994; Wooden et al., 1994). This area is referred to as the Mojave Province and is distinguished from the Yavapai province on geochemical grounds (Fig. 2). The Mazatzal orogenic belt is characterized by 1.72 to 1.68 Ga continental-margin sedimentary rocks and rhyolitic caldera complexes, overlying or intruding 1.76 to 1.72 Ga basement (Dann, 1991), all of which are intruded by 1.66 to 1.60 granitic plutons (Karlstrom et al., 1987; Conway and Silver, 1989).

Tectonic models for the orogen have emphasized the spatial distribution Yavapai-age rocks and Mazatzal-age rocks. Most models interpret the general younging of supracrustal rocks from north to south and to indicate southward accretion of successively younger island arcs (Van Schmus and Bickford, 1981; Condie, 1982;

Anderson, 1989). More recent models, developed as a result of detailed mapping and geochronologic data from central Arizona and northern New Mexico, view the orogen as a collage of shear-zone-bounded crustal blocks characterized by contrasting geologic, tectonic and thermal histories (Karlstrom and Bowring, 1988; Grambling et al., 1988; Bowring and Karlstrom, 1990). In central Arizona, thermochronologic studies reveal that adjacent crustal blocks cooled at different rates and that some blocks cooled very slowly for hundreds of millions of years (Chamberlain and Bowring, 1990; Bowring and Karlstrom, 1990; Hodges et al., 1994; Hodges and Bowring, 1995). These results underscore the importance of major shear zones in the evolution of continental lithosphere in the southwestern United States.

The Upper Granite Gorge of the Grand Canyon exposes Paleoproterozoic rocks that underlie the Colorado Plateau in the northern part of the Yavapai orogenic belt (Figs. 2 & 3). The geology is similar to that of the Yavapai orogenic belt: metasedimentary and metavolcanic rocks intruded by calc-alkaline plutons deformed, metamorphosed and intruded by variably deformed granite plutons. The Upper Gorge transect is divided into six crustal blocks defined by five steeply-dipping shear zones characterized by complex movement histories (Ilg et al., 1996; Fig. 4). This thesis presents U-Pb data from 35 rock samples that constrain the crustal evolution of the Upper Gorge transect and provide a basis for evaluating the significance of the block architecture in the northern Yavapai belt.

OVERVIEW

The four chapters that follow describe results that bear on two main issues: 1) characterization of the U-Pb systematics of monazite, xenotime and sphene in these rocks; and 2) utilization of U-Pb geochronological and thermochronological to constrain the tectonic and thermal evolution of Paleoproterozoic middle crust exposed in the Grand Canyon. Chapter 2 presents a geochronological framework that establishes the

absolute timing of arc-development, deformation and magmatism, as well as the regional affinities of the Upper Gorge transect. Chapter 3 explores in detail the U-Pb systematics of monazite and xenotime granite dikes using an aggressive analytical strategy that includes micro-sampling of previously imaged monazite and xenotime crystals. Chapter 4 utilizes U-Pb data, field observations, petrography, phase relations, compositional data and Pb diffusion models to construct a detailed thermal history spanning 50 m.y. for high-grade rocks in the eastern Upper Gorge. Chapter 5 compares the thermal evolution of the six shear-zone-bounded crustal blocks that compose the Upper Gorge transect.

REFERENCES

Anderson, P., 1989, Proterozoic plate tectonic evolution of Arizona from 1900 to 1600 Ma, in Jenny, J.P., and Reynolds, S.J., eds., Geologic evolution of Arizona: Arizona Geological Society Digest 17, p. 57-148.

Bowring, S.A., and Karlstrom, K.E., 1990, Growth, stabilization and reactivation of Proterozoic lithosphere in the southwestern United States: Geology, v. 18, p. 1203-1206.

Chamberlain, K.R. and Bowring, S.A., 1990, Proterozoic geochronologic and isotopic boundary in NW Arizona: Journal of Geology, v. 98, p. 399-416.

Condie, K.C, 1982, Plate-tectonics model for Proterozoic continental accretion in the southwestern United States: Geology, v. 10, p. 37-42.

Conway, C.M., and Silver, L.T., 1989, Early Proterozoic rocks (1710 - 1615 Ma) in central to southeastern Arizona, *in* Jenney, J.P., and Reynolds, S.J., eds., Geological Evolution of Arizona: Arizona Geological Society Digest 17, p. 165-186.

Dann, J., 1991, A Proterozoic ophiolite in central Arizona: Implications for models of crustal growth: Geology, v. 19, p. 590-593.

Grambling, J.A., Williams, M.L., and Mawer, C.K., 1988, Proterozoic tectonic assemble of New Mexico: Geology, v. 16, p. 724-727.

Hodges, K.V., and Bowring, S.A., 1995, $^{40}Ar/^{39}Ar$ thermochronology of isotopically zoned micas: Insights from the southwestern USA Proterozoic orogen: Geochimica et Cosmochimica Acta, v. 59, p. 3205-3220.

Hodges, K.V., Hames, W.E., and Bowring, S.A., 1994, $^{40}Ar/^{39}Ar$ age gradients in micas from a high temperature-low pressure metamorphic terrain: Evidence for very slow cooling and implications for the interpretation of age spectra: Geology, v. 22, p. 55-58.

Hoffman, P.F., 1989, Precambrian geology and tectonic history of North America, *in* Bally, A.W., and Palmer, A.R., eds., The Geology of North America — An Overview: Boulder, Colorado, Geological Society of America, The Geology of North America, v. A, p. 447-511.

Ilg, B.R., Karlstrom, K.E., Hawkins, D.P., and Williams, M.L., 1996, Paleoproterozoic rocks of the Upper and Middle Gorges, Grand Canyon, Arizona: New stratigraphic nomenclature, structural geometry and insights into middle crustal processes: Geological Society of America Bulletin, in press.

Karlstrom, K.E., and Bowring, S.A., 1988, Early Proterozoic assembly of tectonostratigraphic terranes in southwestern North America: Journal of Geology, v. 96, p. 561-576.

Karlstrom, K.E., and Bowring, S.A., 1994, Proterozoic orogenic history of Arizona, in Reed, J.C., Jr., Bickford, M.E., Houston, R.S., Link, P.K., Rankin, D.W., Sims, P.K., and

Van Schmus, W.R., eds., Transcontinental Proterozoic provinces, Precambrian: Conterminous United States: Boulder, Colorado, Geological Society of America, The Geology of North America, v. C-2, p. 188-211.

Karlstrom, K.E., and Daniel, C.G., 1993, Restoration of Laramide right-lateral strike-lip in northern New Mexico by using Proterozoic piercing points: Tectonic implications from the Proterozoic to the Cenozoic: Geology, v. 21, p. 1139-1142.

Karlstrom, K.E., Bowring, S.A., and Conway, C., 1987, Tectonic significance of an Early Proterozoic two-province boundary in central Arizona: Geological Society of America, v. 99, p. 529-538.

Van Schmus, W.R., and Bickford, M.E., 1981, Proterozoic chronology and evolution of the midcontinent region, North America, *in* Kröner, A., ed., Precambrian plate tectonics: Amsterdam Elsevier Publishing Company, p. 261-296.

Wooden, J.L., and DeWitt, E., 1991, Pb isotopic evidence for the boundary between the Early Proterozoic Mojave and central Arizona crustal provinces in western Arizona, *in* Karlstrom, K.E., ed., Proterozoic geology and ore deposits of Arizona: Arizona Geological Society Digest 19, p. 27-50.

Wooden, J.L., Nutman, A.P., Howard, K.A., Bryant, B. DeWitt, E., and Mueller, P.A., 1994, Shrimp U-Pb zircon evidence for Late Archean and Early Proterozoic crustal evolution in the Mojave province and central Arizona crustal provinces [Abs.]: Geological Society of America Abstracts with Programs, v. 26, no. 6, p. 69.

Wooden, J.L., and Miller, D.M., 1990, Chronologic and isotopic framework for Early Proterozoic crustal evolution in the eastern Mojave Desert region, SE California: Journal of Geophysical Research, v. 95, p. 20,133-20,146.

FIGURE CAPTIONS

Figure 1 Distribution of Archean and Proterozoic crust in the North American craton. The Paleoproterozoic orogenic system was added to the southern margin of the craton between 1.8 and 1.6 Ga. Note that orogen is juxtaposed with the Archean Wyoming craton to the northwest and slightly older Paleoproterozoic orogenic belts, including the Trans-Hudson orogen, to the north. These areas are interpreted to be the provenance for the detrital zircons from the Grand Canyon described in Chapter 2. Map modified after Hoffman (1989).

Figure 2 Regional map showing the distribution of Paleoproterozoic rocks (dark shading) around the Colorado Plateau (light shading), the location of the Upper Granite Gorge of the Grand Canyon, and the proposed boundaries between the three orogenic belts that comprise the orogen. Modified after Karlstrom and Bowring (1994) and Karlstrom and Daniel (1993).

Figure 3 Regional map showing the major shear zones (solid heavy black lines) and subsurface lineaments (heavy dashed lines beneath the Colorado Plateau) that segment this part of the orogen into crustal blocks. The Upper Granite Gorge of the Grand Canyon, which exposes the Paleoproterozoic rocks that underlie the Colorado Plateau, is divided into six crustal blocks (not shown). Modified after Karlstrom and Bowring (1988).

Figure 4 Simplified geologic map of the Upper Granite Gorge showing the overall block architecture of the transect. The major shear zones are shown as clusters of broken lines projected outside the outcrop area of Paleoproterozoic rocks. Inset shows the location of the Grand Canyon. Abbreviations for the shear zones, from east to west, are translated as follows: VFZ = Vishnu fault zone; BASZ = Bright Angel shear zone; 96-MSZ = Ninety-Six Mile shear zone; CRSZ = Crystal Creek shear zone; BSZ = Bass shear zone.

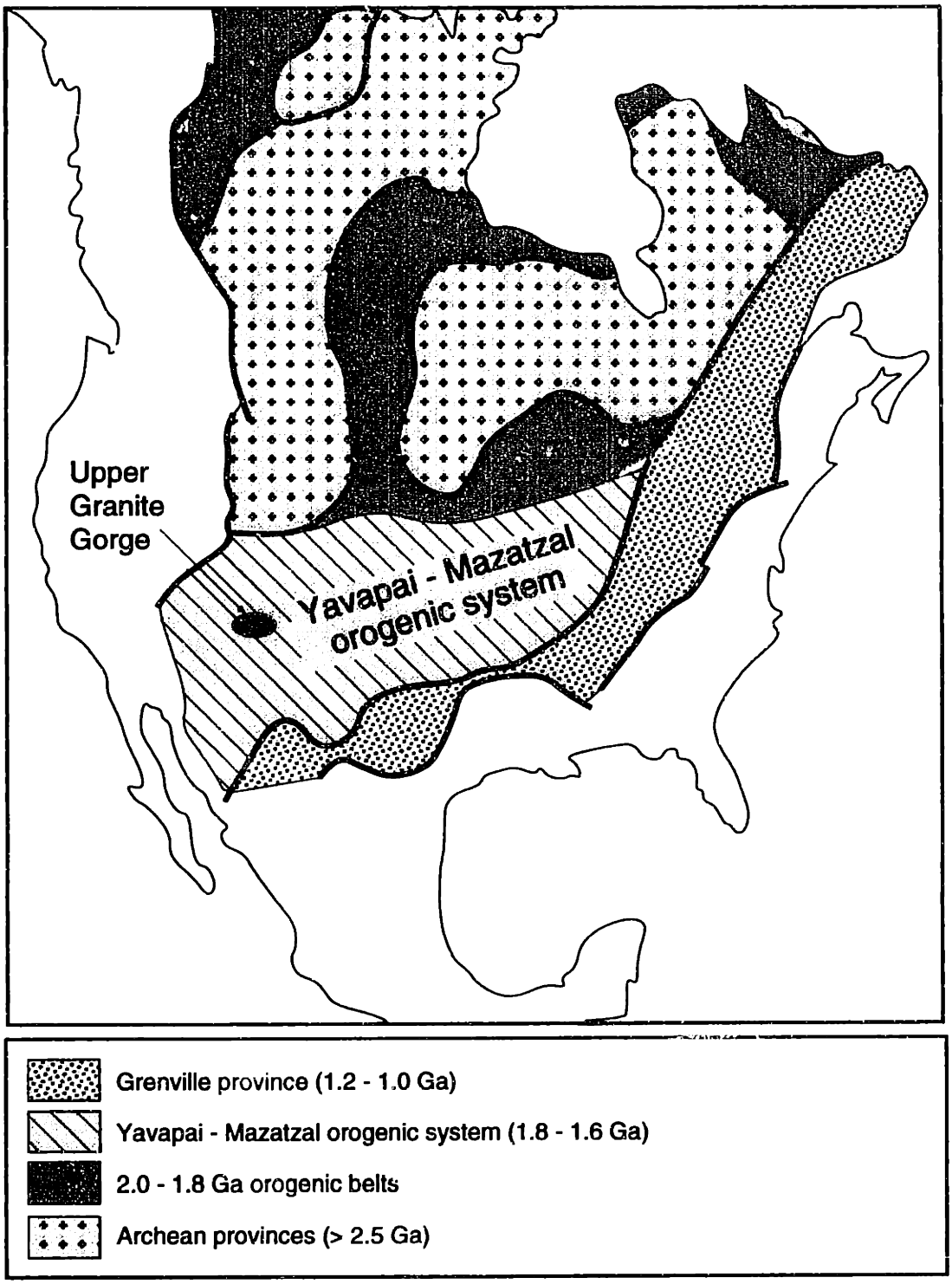
Upper
Granite
Gorge
Yavapai - Mazatzal
orogenic system
Grenville province (1.2 - 1.0 Ga)
Yavapai - Mazatzal orogenic system (1.8 - 1.6 Ga)
2.0 - 1.8 Ga orogenic belts
Archean provinces (> 2.5 Ga)

Figure 1

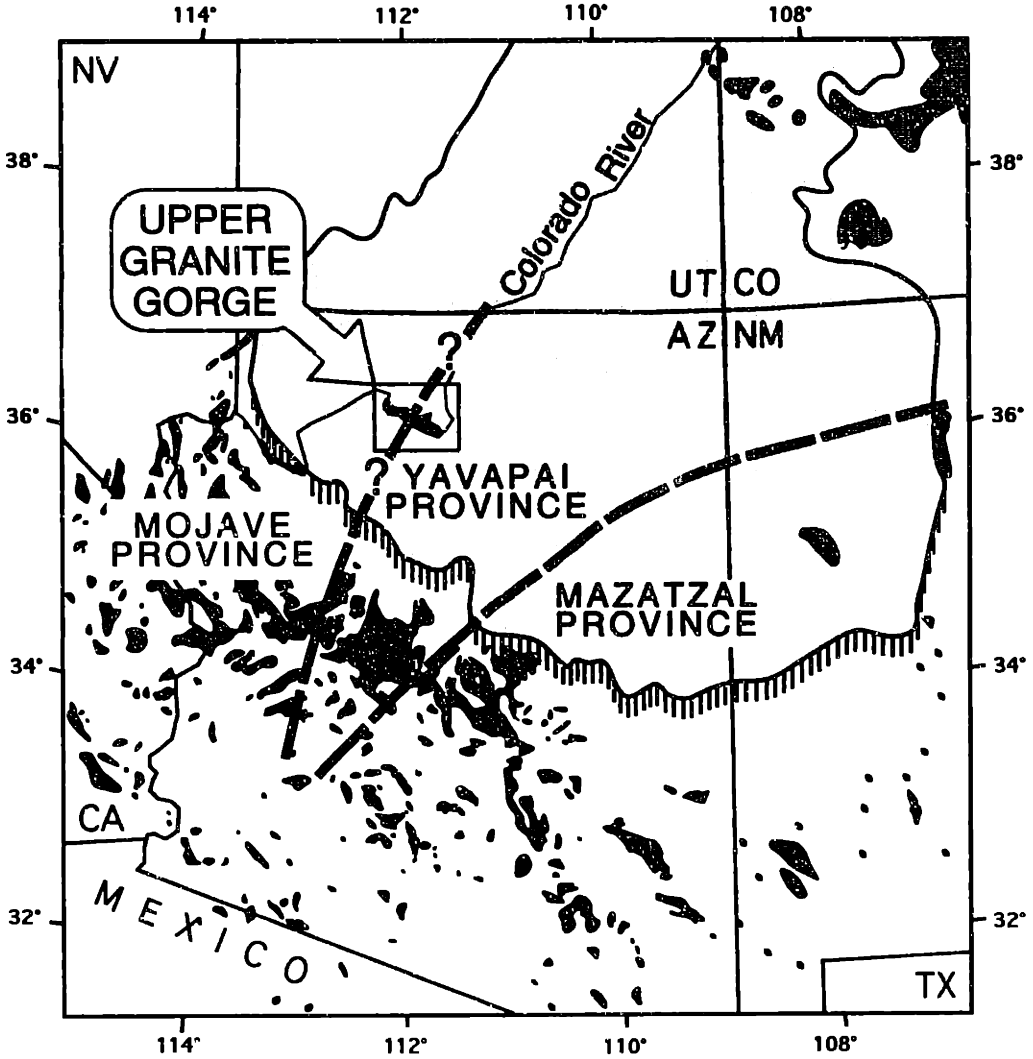
114°
112°
110°
108°
NV
38°
UPPER
GRANITE
GORGE
Colorado River
UT CO
AZ NM
36°
? YAVAPAI
PROVINCE
MOJAVE
PROVINCE
MAZATZAL
PROVINCE
34°
CA
32°
MEXICO
TX

Figure 2

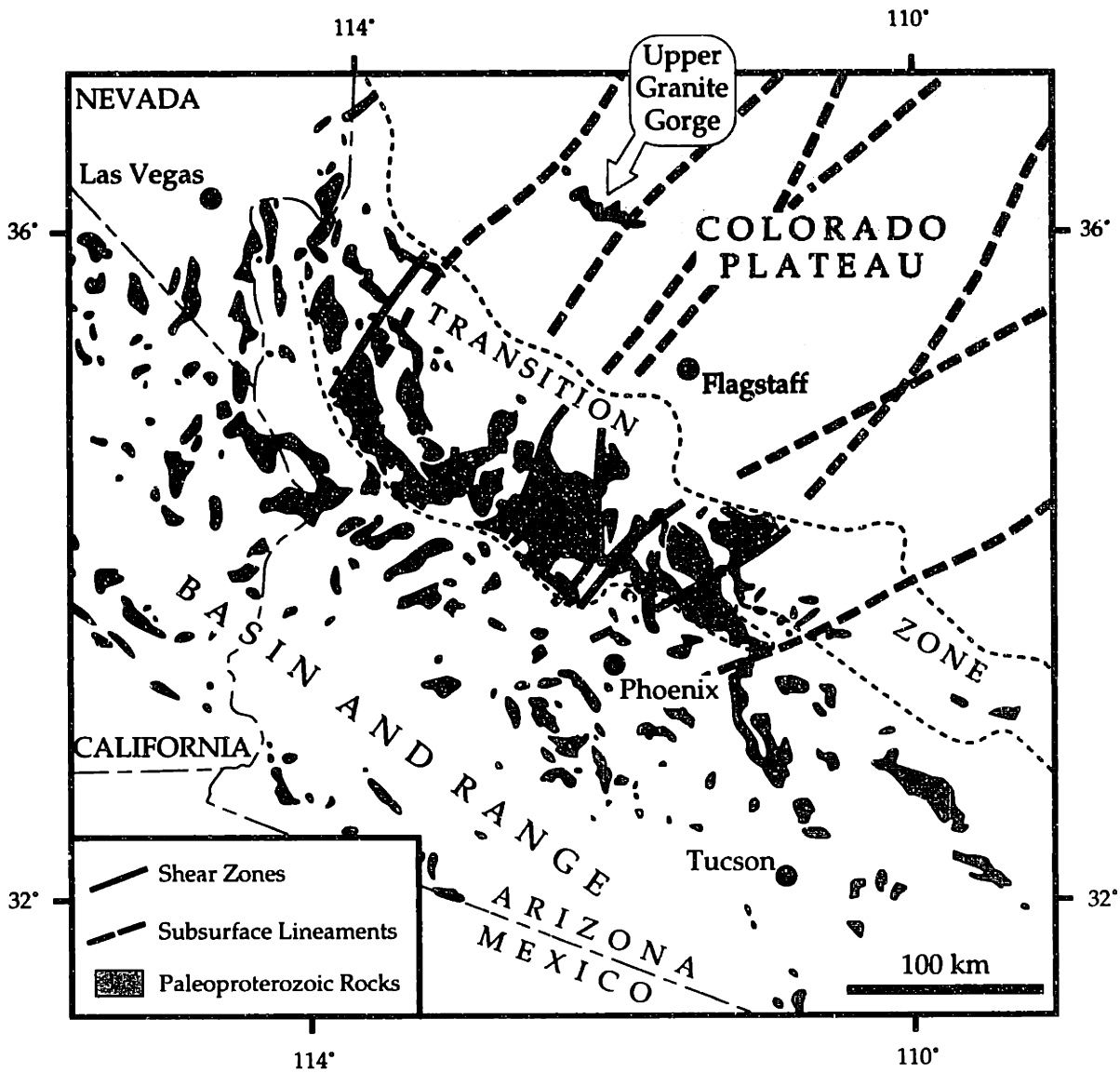
114°
110°
Upper
Granite
Gorge
NEVADA
Las Vegas
36°
COLORADO
PLATEAU
TRANSITION
Flagstaff
BASIN AND RANGE
ZONE
Phoenix
CALIFORNIA
Tucson
ARIZONA
MEXICO
32°
Shear Zones
Subsurface Lineaments
Paleoproterozoic Rocks
100 km

Figure 3

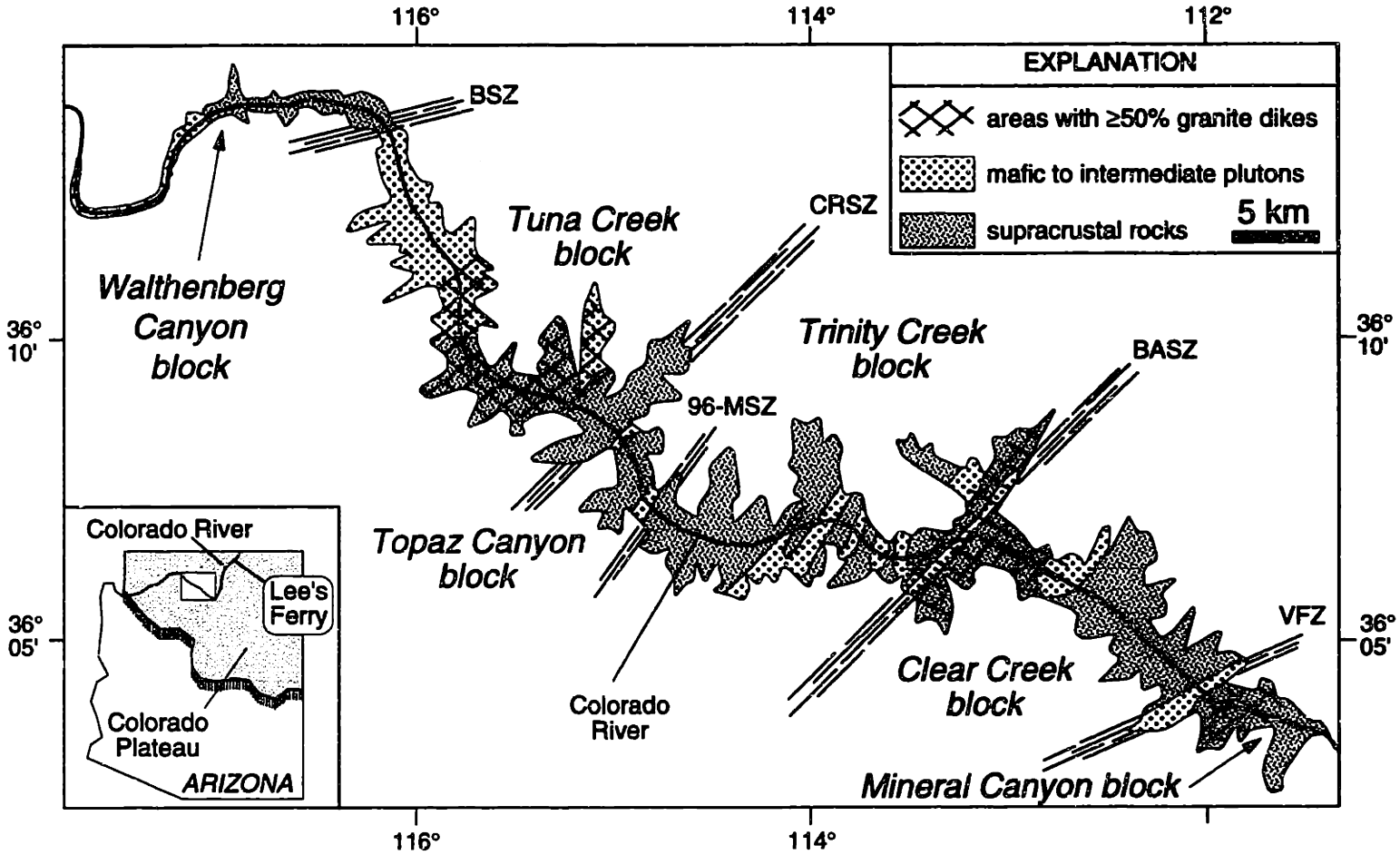
116°
114°
112°
EXPLANATION
areas with ≥50% granite dikes
mafic to intermediate plutons
supracrustal rocks
5 km
BSZ
CRSZ
Tuna Creek block
Walthenberg Canyon block
Trinity Creek block
BASZ
96-MSZ
36° 10'
36° 05'
Topaz Canyon block
Colorado River
Lee's Ferry
Colorado Plateau
ARIZONA
Colorado River
VFZ
Clear Creek block
Mineral Canyon block

Figure 4

CHAPTER 2

A U-PB GEOCHRONOLOGIC FRAMEWORK FOR THE PALEOPROTEROZOIC CRUSTAL EVOLUTION OF THE UPPER GRANITE GORGE, GRAND CANYON, ARIZONA

ABSTRACT

The Upper Granite Gorge of the Grand Canyon exposes three lithotectonic units, including supracrustal rocks, mafic to intermediate plutons and peraluminous granite dikes, that are variably deformed and metamorphosed. U-Pb geochronology indicates that layered supracrustal rocks were deposited or erupted over at least 18 m.y., between 1750 and 1732 Ma, and contain detrital zircons with Pb-Pb dates between 3269 to 1732 Ma. Supracrustal rocks were intruded by calc-alkaline plutons between 1741 and 1713 Ma. Both supracrustal and plutonic rocks were intruded by peraluminous granite and pegmatite dikes between 1698 and 1680 Ma and at about 1662 Ma locally. U-Pb dates of foliated plutonic rocks and cross-cutting granite dikes bracket the timing of fabric development. The oldest fabrics formed between 1730 and 1698 Ma and were overprinted by the predominant northeast-striking fabric between 1713 Ma and 1685 Ma. Local crenulation cleavages and kink bands formed after about 1685 Ma. Metamorphic grade varies across the Upper Gorge from lower amphibolite facies to lower granulite facies. We suggest that 1706 to 1697 Ma metamorphic monazites from a 1741 Ma supracrustal rock directly date the timing of lower granulite facies metamorphism in the eastern Upper Gorge, a suggestion that is consistent with U-Pb ages (1685 to 1680 Ma) of dikes that cross-cut migmatites in the eastern Upper Gorge.

The Paleoproterozoic geologic history of the Upper Granite Gorge is similar to that of juvenile crust of the Yavapai province in central Arizona. However, the occurrence in the western Upper Gorge of the 1840 Ma Elves Chasm tonalite and ca. 2000 Ma inherited zircons in a 1750 to 1710 Ma calc-alkaline pluton indicates that pre-1.8 Ga crustal components participated, at least locally, in the development of the 1740 - 1710 Ma island arcs.

INTRODUCTION

Nearly 20% of the North American craton occurs within a 1300-km wide Paleoproterozoic (1.8 to 1.6 Ga) orogen exposed in the southwestern United States (Fig. 1). The orogen offers an opportunity to examine the geologic record of the processes responsible for the growth and stabilization of crust added to the North American craton. Recent studies in the region have focused on three goals: characterizing the style and timing of deformation across the region (Karlstrom and Bowring, 1988; 1991, and references therein; Wooden and Miller, 1990); reconstructing the thermal history at different crustal levels (Chamberlain and Bowring, 1990; Bowring and Karlstrom, 1990; Williams, 1991, and references therein); and mapping the distribution of reworked continental crust and juvenile continental crust (Bennett and DePaolo, 1987; Wooden and others, 1988; Wooden and DeWitt, 1991; Bryant and others, 1994). The current geologic framework not only provides the basis for proposed tectonic models (see Van Schmus and others, 1993) but also identifies key areas for further study.

The Upper Granite Gorge of the Grand Canyon (Fig. 2) is a key area of the orogen. Much of the north-central portion of the orogen is obscured beneath Phanerozoic rocks of the Colorado Plateau, but the Colorado River has exposed in the Upper Granite Gorge a continuous transect through the Paleoproterozoic basement. The 70 km long transect provides superb exposures across the dominant structural grain of the orogen in an area

that was not significantly overprinted by Phanerozoic tectonic and thermal processes. The Upper Gorge is also important because it spans the proposed northeast-trending boundary between reworked continental crust to the west and juvenile crust to the east (Fig. 2; Bryant and others, 1994). Despite the regional significance of the Upper Gorge and a long history of study (e.g., Noble and Hunter, 1914; Campbell and Maxson, 1938; Babcock and others, 1979; Brown and others, 1979; Clark, 1979), the tectonic affinities of the Upper Gorge are not well known largely due to a paucity of reliable age determinations. Although K-Ar and Rb-Sr isotopic studies established the Proterozoic age of these rocks (Aldrich and others, 1957; Giletti and Damon, 1961; Babcock and others, 1979; Brown and others, 1979; Clark, 1979), only two U-Pb ages have been reported from the Upper Gorge (Pasteels and Silver, 1966).

In this paper, we present 121 precise zircon and monazite U-Pb analyses that constrain the geologic history of these rocks and permit the Upper Granite Gorge to be incorporated into the regional tectonic framework. The ages of variably deformed intrusive rocks indicate that the Upper Gorge shares a similar geologic and tectonic history with rocks in central Arizona, being characterized by deformation and metamorphism associated with the ca. 1.70 Ga Yavapai orogeny. We also present U-Pb zircon and whole rock Pb isotopic data that begin to address long-standing questions about the nature of the basement to the supracrustal rocks exposed throughout the southwestern United States (e.g., Noble and Hunter, 1914, p. 112; Karlstrom and Bowring, 1988).

REGIONAL GEOLOGY

Paleoproterozoic rocks in Arizona and adjacent areas can be divided into three orogenic provinces (Fig. 2) defined by both geologic and geochemical criteria (Karlstrom and Bowring, 1988): from northwest to southeast these are the Mojave, Yavapai and

Mazatzal provinces. The Mojave province is composed of high grade supracrustal rocks intruded by numerous plutonic rocks that were deformed and metamorphosed at ca. 1.70 Ga (Young and others, 1989; Wooden and Miller, 1990). Mojave-type crust characteristically preserves geochronologic and isotopic evidence for pre-1.8 Ga crust (Bennett and DePaolo, 1987; Wooden and others, 1988; Wooden and Miller, 1990; Wooden and DeWitt, 1991). The Yavapai province is characterized by juvenile crust with arc affinities composed of 1.75 to 1.71 Ga moderate to high grade supracrustal rocks that were intruded by 1.75 to 1.70 Ga mafic to intermediate plutonic rocks, and penetratively deformed and metamorphosed during the ca. 1.70 Ga Yavapai orogeny (e.g., Karlstrom and others, 1987; Karlstrom and Bowring, 1988; Williams, 1991). Crust with continental affinities that was deformed during the 1.65 to 1.60 Ga Mazatzal orogeny comprises the Mazatzal province (Karlstrom and others, 1987; Karlstrom and Bowring, 1988; Conway and Silver, 1989). Karlstrom and Bowring (1988) showed that the three orogenic provinces can be subdivided into shear-zone-bounded blocks and suggested a tectonic model involving diachronous accretion, uplift and erosion to produce the present orogenic collage.

The nature of the boundaries that separate the orogenic provinces is particularly important to reconstructing the paleogeography and tectonic history of the orogen. Karlstrom and others (1987) concluded that the Yavapai-Mazatzal boundary is associated with a prominent shear zone. In contrast, geologic expression of the boundary between the Mojave and Yavapai provinces has not been recognized. Instead, the boundary is defined by U-Pb zircon ages and whole rock Pb isotopic signatures indicating that Mojave-type contains a component(s) of pre-1.8 Ga crust (Bennett and DePaolo, 1987; Wooden and others, 1988; Chamberlain and Bowring, 1990; Wooden and DeWitt, 1991; Bryant and others, 1994; Wooden and others, 1994). The Mojave and Yavapai provinces are separated by a 60-km-wide zone in western Arizona in which

Yavapai-type crust, Mojave-type crust and crust with mixed geochemical signatures occur in close proximity (Wooden and DeWitt, 1991). Bryant and others (1994) and Wooden and others (1994) suggested that the province boundary is the eastern limit of this complex boundary zone (Fig. 2).

GEOLOGY OF THE UPPER GRANITE GORGE

Major lithostratigraphic and plutonic units of the Upper Granite Gorge include supracrustal rocks, mafic to intermediate plutons, and peraluminous granitic and pegmatitic intrusions (Fig. 3; see Ilg and others, 1996). Supracrustal rocks include amphibolite and mafic schist of the Brahma schist, quartzofeldspathic gneiss of the Rama schist, and quartzite and pelitic schist of the Vishnu schist. Although primary sedimentary structures and relict pillows provide facing directions locally, the stratigraphic relationship and primary thickness of the supracrustal units are obscured by deformation. The supracrustal rocks are intruded by mafic to intermediate plutons most of which are penetratively deformed. These rocks are, in turn, intruded by peraluminous granite and pegmatite dikes that locally comprise more than 50% of the rock volume.

Deformational structures fall into three groups based on orientation, morphology and relative timing (Ilg and others, 1996). Group 1 structures include penetrative fabrics (S_1) and several generations of folds (F_1). Group 2 structures include the dominant (although heterogeneously developed) subvertical, northeast-striking foliations (S_2) and associated upright, asymmetric F_2 folds. Group 3 structures include a diverse group of crenulation cleavages, kinks and meso-scale m.y.lonite zones that appear to post-date Group 2 structures. It is unclear at present whether these three groups of structures

resulted from multiple deformational events or a single, progressive deformational event (e.g., Albin and Karlstrom, 1991; Ilg and others, 1996).

We also recognize five major northeast-striking shear zones (Fig. 3) that preserve complex movement histories and therefore do not fit neatly into any of the three groups. The shear zones divide the transect into crustal blocks (Fig. 3) characterized by similar rock units and similar fabric overprinting relationships, but metamorphic grade varies from block to block (see Chapter 5). For example, the Vishnu fault zone separates lower granulite facies assemblages in the Mineral Canyon block to the east from lower amphibolite facies assemblages in the Clear Creek block to the west. These observations indicate that significant motion on the shear zones post-dated peak metamorphism and that the block architecture is a fundamental aspect of the geology in the Upper Granite Gorge.

Metamorphic grade varies across the transect. Blocks characterized by lower amphibolite facies mineral assemblages are separated by blocks with upper amphibolite to lower granulite facies assemblages. The higher grade blocks typically contain migmatitic supracrustal rocks and generally expose peraluminous granitoid dikes and sills. Metamorphic grade changes abruptly across the Vishnu, 96-mile and Crystal shear zones, and increases progressively from the Vishnu shear zone to the Bright Angel shear zone (Fig. 3).

ANALYTICAL METHODS

Zircon and monazite were separated by standard crushing, heavy liquid and magnetic techniques. All zircon grains were air abraded (Krogh, 1982) and then washed in warm 30% HNO_3. Monazite grains were washed in both 2% HNO_3 and warm H_2O prior to dissolution. Samples were dissolved in teflon microcapsules and were spiked prior to dissolution with a mixed ^{205}Pb-^{233}U-^{235}U tracer. Zircon was dissolved in

concentrated HF at 220 °C for 40 - 60 hours; monazite was dissolved in 10-11 N HCl in two stages for a total of 60-72 hours at 180 °C. Pb and U were separated using HCl-based ion chromatography procedures modified after Krogh (1973). Lead was analyzed using conventional thermal ionization mass spectrometry either: 1) in static mode using Faraday detectors for all isotopes except ^{204}Pb, which was measured with the Daly detector, or 2) by peak-jumping using a Daly detector in ion counting mode. Uranium was analyzed in static mode using Faraday collectors. Additional analytical details are included in Table 1.

We employ the two statistical methods described by Ludwig (1989; 1990) to interpret the U-Pb data. For discordant data forming a linear array, an upper intercept age is calculated using a linear regression that, unless otherwise noted, assumes all scatter results from the analytical uncertainty (York, 1969). Most of the U-Pb ages are less than 10% discordant resulting in small uncertainties in upper intercept ages and relatively large uncertainties in lower intercept ages. We interpret the zero-age lower intercepts, exhibited by most samples, to reflect recent Pb loss related to interaction with shallow crustal fluids (e.g., Goldich and Mudrey, 1972; Ewing and others, 1982; Eyal and Fleischer, 1985). For samples with U-Pb ages that are concordant or less than 1% discordant, we determine the weighted mean of the Pb-Pb dates of the individual analyses. Both upper intercept and weighted mean ages are evaluated using the mean square of the weighted deviates (MSWD) and evaluated using the criteria derived by Wendt and Carl (1991). Specifically, the linear regression or weighted mean is statistically significant if the MSWD $< [1+2(2/f)^{0.5}]$, where f is the number of data points minus two (Wendt and Carl, 1991).

Several monazite analyses presented below plot above concordia (e.g., Fig. 12, 13, 15). Such reversely discordant dates are typically explained by the presence in the

crystal of ^{206}Pb that is unsupported by ^{238}U (e.g., Schärer, 1984). This excess ^{206}Pb forms from the decay of ^{230}Th, an intermediate daughter in the ^{238}U decay chain (Schärer, 1984). Although this effect can be important in monazites from Phanerozoic rocks, it cannot explain all of the reverse discordance observed in Paleoproterozoic monazites from the Upper Gorge. For example, based on the excess ^{206}Pb correction scheme developed by Schärer (1984), we find that unrealistically low whole rock Th/U ratios (less than 0.05) are required to correct the observed reverse discordance. In addition, we find that reversely discordant analyses from the Upper Gorge lie along best fit linear regressions defined by normally discordant data (e.g., Figs. 15 and 16). These observations suggest that factors other than excess ^{206}Pb produced reverse discordance in these monazites. Chapter 3 includes a detailed discussion of reverse discordance in Upper Gorge monazites.

RESULTS

In this section we describe the field observations and U-Pb data for the 18 samples analyzed in this study. Supracrustal sample are listed by river mile. All other samples are listed by age within each lithostratigraphic unit. The sample numbers include the river-mile at which the rock was collected. For example, sample UG79.6-1 was collected in the Upper Gorge at river-mile 79.6.

Supracrustal Rocks

Rama schist (sample UG79.6-1). The Rama schist consists of quartzofeldspathic schists and gneisses that Ilg and others (1996) interpreted as metavolcanic and metavolcaniclastic rocks. This sample of biotite-muscovite quartzofeldspathic gneiss

was collected from a 2 meter-thick layer in the core of an S_2 antiform in the eastern Upper Gorge (Fig. 3). The sample contained both zircon and monazite. Zircon crystals are euhedral prisms, although some grains are subrounded and have pitted crystal faces, perhaps resulting from partial dissolution during lower granulite facies metamorphism. U-Pb zircon data from four discordant analyses (Fig. 4) yield an upper intercept age of 1741 ± 1 Ma (lower intercept = 43 ± 27 Ma; MSWD = 0.48) which we interpret as the primary crystallization age of zircons from felsic to intermediate volcanic rocks of the Rama Formation.

Monazite U-Pb dates from this sample are significantly younger than 1741 Ma. Monazite grains occur as inclusions in biotite and most crystals are idioblastic. Seven single grains, ranging in size from <10 μm to 150 μm, yield slightly discordant U-Pb dates with Pb-Pb dates ranging from 1706 to 1697 Ma. The variation in Pb-Pb dates can be interpreted in terms of primary processes, such as continuous growth during metamorphism or metamorphic growth around inherited nuclei, and/or secondary processes, such as high-temperature Pb loss (e.g., Parrish, 1990) or fluid-mineral interaction (e.g., Black and others, 1984; DeWolf and others, 1993). Although inheritance of detrital monazite has been interpreted for monazites from moderate to high grade metasedimentary rocks (Parrish, 1990; Suzuki and others, 1991), we consider inheritance of a detrital or primary igneous component to be unlikely because: 1) back scattered electron imaging reveals no evidence for compositionally distinct cores; 2) the monazites from this sample are over 30 m.y. younger than the crystallization age; and 3) the monazites have a limited range of Th/U ratios (3.5 ± 1.1), suggesting that these crystals grew from a common source. We also consider Pb loss near the closure temperature of monazite (inferred to be 725 ± 25 °C: Copeland and others, 1988; Parrish, 1990) to be unlikely. For the small crystals analyzed in this study, high-temperature Pb loss should result in grain-size-dependent variation in Pb-Pb dates, even for cooling rates as high as

50 °C/m.y. (e.g., Suzuki and others, 1995; Smith and Giletti, 1995). However, the observed variation in Pb-Pb dates for these monazites does not correlate with grain size. We tentatively interpret the variation in Pb-Pb dates in this sample to reflect continuous growth of monazite during lower granulite facies metamorphism, as observed in metamorphic monazites from other areas of the Upper Gorge (see Chapter 4).

Vishnu schist (sample UG81.1-1). A one meter-thick layer of muscovite - biotite quartzite, which is interlayered with biotite - muscovite schist in Vishnu Creek, was sampled for geochronology. The sample contains abundant rounded zircons characterized by cracks and dusty inclusions. Four single-crystal analyses yielded discordant U-Pb dates with Pb-Pb dates of 1851, 1855, 1956 and 2365 Ma (Table 1; Fig. 5). These detrital zircons are older than rocks exposed throughout the region with the exception of the Elves Chasm pluton described below.

Brahma schist (sample UG84.4-1). The dominantly amphibolitic Brahma schist locally contains 1-2 meter-thick layers of foliated, very fine-grained, metafelsite containing 2-5 mm porphyroclasts of quartz and plagioclase. These layers are interpreted as felsic metavolcaniclastic strata or hypabyssal sills contained within a sequence of mafic to intermediate metavolcanic and metavolcaniclastic rocks. Five zircon fractions from a 1 meter-thick layer of porphyroclastic metafelsite yielded discordant U-Pb dates (Fig. 4). Linear regression of the data produced an upper intercept age of 1750 ± 2 Ma (lower intercept = 234 ± 82 Ma; MSWD = 0.71) that we interpret as the crystallization age of the metafelsite. Because we cannot distinguish between a shallow intrusive or a volcanic origin for these rocks, we consider 1750 ± 2 Ma as a minimum age for volcanism associated with the Brahma Formation in this part of the Upper Gorge.

Brahma Schist (sample UG90.4-1). Around the margins of the Horn Creek pluton, the Brahma schist includes interlayered amphibolite, locally preserving pillows, and biotite-hornblende quartzofeldspathic gneiss, which we interpret as metamorphosed

intermediate-composition volcanic or volcaniclastic layers. A sample of the quartzofeldspathic gneiss from one of these layers is composed of fine- to medium-grained, equigranular quartz, plagioclase, microcline and less than 10 vol% biotite and hornblende. The rock contains about 5 vol%, 1-2 centimeter, medium-grained felsic pods composed of quartz, plagioclase and microcline that are flattened parallel to the foliation. The pods are mantled by 1-3 mm selvages or reaction rims containing about 50 vol% biotite and hornblende. Both the matrix and the pods are thoroughly recrystallized to form granoblastic texture, suggesting that the rock was annealed at high temperatures following development of the felsic pods. The bulk sample crushed for U-Pb geochronology included both the matrix and the felsic pods because the pods were too small and too widely dispersed to be separated from the matrix prior to crushing.

The gneiss contains abundant <100 μm, euhedral, squat prismatic zircons containing dusty inclusions. Twelve zircon fractions, including both multi- and single-crystal analyses yielded discordant U-Pb dates with Pb-Pb dates ranging from 1735 to 1658 Ma (Table 1; Fig. 6). The data do not define a statistically significant upper intercept age and given the discordance of the U-Pb dates, the dispersion in the Pb-Pb dates is difficult to interpret. However, because these rocks are intruded by the 1713 Ma Horn Creek pluton (described below) the data are consistent with a multi-stage history involving primary crystallization at about 1735 Ma and more than one episode of metamorphic zircon growth: one around 1700 Ma and one or more after 1670 Ma.

Vishnu Schist (sample UG95.7-1). This sample was collected from a 50 centimeter-thick bed of micaceous quartzite in a sequence of quartzofeldspathic schist that preserves relict graded bedding. Zircons are abundant; they occur as rounded, often-frosted crystals varying in size (250 - 50 μm), color (purple, pink, colorless), and quality (clear to cracked and turbid). Seven single-crystal analyses yielded discordant U-Pb

dates with Pb-Pb dates ranging from 1822 Ma to 3267 Ma (Table 1; Fig. 5). Potential source areas for these crystals are discussed below.

Vishnu Schist (sample UG109.9-1). A sample of medium-grained muscovite quartzite from river-mile 109.9 contained abundant large, rounded zircons, ranging in color from light purple to colorless. Eleven single crystal analyses yielded variable discordant U-Pb ages with Pb-Pb ages between 1732 and 2476 Ma. There is no correlation between color and date, although the oldest crystals were light purple. The three youngest fractions define a discordia with an upper intercept age of 1736 ± 2 Ma (lower intercept = 19 ± 34 Ma; MSWD = 0.08; Fig. 5). Regardless of the significance of the discordia, the sandstone protolith of this quartzite was deposited after about 1732 Ma, the Pb-Pb date of the youngest crystal.

Mafic to Intermediate Intrusions

Elves Chasm Pluton (sample UG113.2-1). The Elves Chasm pluton is a lineated medium- to coarse-grained hornblende-biotite tonalite to quartz diorite exposed in the western Upper Gorge (Fig. 3). The sample collected for geochronology was taken 0.3 river miles downstream from (southwest of) the eastern margin of the pluton. Zircon grains are euhedral and are either equant (aspect ratio < 2) or prismatic (aspect ratio > 2). Five zircon fractions, including both equant and prismatic morphologies, define a chord that yields an upper intercept age, anchored by two concordant points, of 1840 ± 1 Ma (lower intercept = -86 ± 126 Ma; MSWD = 1.66; Fig. 7). The weighted mean of the Pb-Pb dates is 1840.6 ± 1.0 Ma (MSWD = 1.74) which is indistinguishable from the upper intercept age. We interpret the crystallization age to be 1840 ± 1 Ma making the Elves Chasm pluton the oldest rock yet described from the southwestern United States.

Zoroaster Pluton (sample UG84.9-1). This foliated medium-grained biotite granite to granodiorite intrudes amphibolite and mafic schist of the Brahma schist. Foliation

within the pluton and compositional layering in the adjacent amphibolite sequence define a south-plunging antiform (Lingley, 1973). The pluton contains screens of both amphibolite and quartzofeldspathic gneiss. Zircons from the Zoroaster granite are colorless, prismatic, doubly-terminated grains. U-Pb data for five single-crystal zircon fractions (Table 1; Fig. 8) range from concordant to 3.6 % normally discordant and yield an upper intercept age of 1741 ± 1 Ma (lower intercept = 133 ± 100; MSWD = 0.79), which we interpret as the crystallization age of the Zoroaster pluton.

Grapevine Camp Pluton (sample UG81.2-3). A narrow body of medium-grained, foliated, highly fractured, biotite granite crops along the Vishnu fault zone (Fig. 3). The fault zone forms the western contact of the pluton, whereas the eastern contact is irregular and cross-cuts compositional layering in the supracrustal rocks. The pluton exhibits textural evidence for both high temperature ductile deformation and low temperature brittle deformation. Zircons are colorless, doubly-terminated grains containing ubiquitous dusty inclusions and fractures. Terminations and crystal edges are rounded slightly and crystal faces are pitted, indicating resorption during either magmatism, recrystallization or deformation. Three single-grain zircon fractions (Table 1; Fig. 9) define a chord with an upper intercept age, anchored by one concordant point, of 1737 ± 1 Ma (lower intercept -52 ± 30 Ma; MSWD = 0.67), which we interpret as the crystallization age.

Trinity Pluton (sample UG91.2-1). The Trinity pluton is a medium- to coarse-grained biotite orthogneiss of granodioritic to granitic composition. The pluton occurs as a kilometer-scale, isoclinally folded sheet and contains tightly folded S_1 fabric. Although contacts with adjacent amphibolites are isoclinally folded and commonly sheared, intrusive relationships are preserved locally (Ilg and others, 1996). A sample of the Trinity pluton yielded a single population of clear, colorless, euhedral, doubly-terminated zircons with aspect ratios of 2 to 4. Four discordant zircon analyses (Table 1; Fig. 9)

yield an upper intercept age of 1730 ± 3 Ma (lower intercept = -52 ± 82 Ma; MSWD = 1.08) which we interpret as the crystallization age.

Tuna Creek Pluton (sample UG99.2-1). A medium-grained, foliated granodiorite that is part of a composite mafic to intermediate pluton in Tuna Creek was sampled for geochronology. The eight zircon fractions analyzed yielded extremely discordant U-Pb dates (Table 1; Fig. 10). Three fractions have Pb-Pb dates between 1946 and 2178 Ma and reflect inheritance of older zircons. The other five points are distinctly younger than 1750 Ma (Pb-Pb between 1706 and 1588 Ma), but do not yield a statistically significant upper intercept age. Despite being complicated by inheritance and extreme Pb loss, the data suggest that the pluton is a member of the 1750 - 1710 Ma arc-related magmatic suite. The results also demonstrate that the pluton contains older (>1998 Ma) crustal components.

Ruby Pluton (sample 104.3-2, AZ-398). The Ruby pluton is a composite body comprising mafic to intermediate intrusive phases exhibiting magma mingling relationships. The pluton contains a poorly developed magmatic fabric consistent in orientation with S_1 fabric in the surrounding supracrustal rocks. The eastern contact of the pluton and is tectonized and obscured by younger pegmatite dikes and stocks. However, dikes and small stocks of Ruby-type granitoids intrude the supracrustal gneisses and schists near the contact, suggesting that the Ruby pluton intruded the adjacent supracrustal rocks. The western contact is overprinted by the Bass shear zone (Fig. 3; Ilg and others, 1996). The unit sampled for U-Pb dating is a medium- to coarse-grained hornblende-biotite granodiorite that makes up most of the pluton. Zircons from the Ruby pluton are large, clear, inclusion-free grains characterized by equant morphologies. Because both single and multi-crystal zircon fractions yield concordant U-Pb ages (Table 1; Fig. 11), ten fractions were analyzed over a 28 month period to evaluate analytical reproducibility. The weighted mean of the ten Pb-Pb dates is 1716.6

± 0.5 Ma (MSWD = 1.35) indicating excellent analytical reproducibility over the course of this study. We interpret 1716.6 ± 0.5 Ma as the crystallization age of the Ruby pluton.

Horn Creek Pluton (sample UG90.6-2). The Horn Creek pluton is a strongly foliated medium-grained hornblende quartz diorite to tonalite containing abundant mafic inclusions. The pluton is a 250 m wide, northeast-striking sheet that intruded parallel to compositional layering in the supracrustal rocks. The pluton contains a northwest-oriented foliation, consistent in orientation with S_1, that is transposed by a prominent, northeast-striking S_2 foliation. Zircon grains are clear and range in morphology from prismatic to equant. Five zircon analyses (Table 1; Fig. 11), including both single and multi-crystal fractions of the two morphological populations, do not yield a statistically significant upper intercept age. However, four of the points define a statistically significant linear regression with an upper intercept age of 1713 ± 2 Ma (lower intercept = 187 ± 232 Ma; MSWD = 1.43). The fifth analysis (fraction Z15), composed of a single equant zircon crystal lacking a visible core in transmitted light, has a Pb-Pb date of 1717 ± 2 Ma and plots to the right of the linear array (Fig. 11). Because numerous studies show that xenocrystic cores are not always revealed in transmitted light (e.g., Hanchar and Rudnick, 1995), we interpret crystal Z15 as a mixture of magmatic and a very small amount of xenocrystic zircon of unknown age and accept 1713 ± 2 Ma as the crystallization age of the Horn Creek pluton.

Peraluminous Granite and Pegmatite Intrusions

Biotite-muscovite granite stock (sample UG85.2-4). Foliation (S_1) in the Zoroaster granite is cross-cut by an irregular stock of fine- to medium-grained biotite - muscovite granite (Fig. 12). The granite is unfoliated except along contacts where it contains weak magmatic fabric, and adjacent to xenoliths of schist where it contains a weak tectonic

fabric that is axial planar to the Zoroaster antiform (Fig. 12). These observations suggest that the stock intruded after the formation of S_1 foliation in the Zoroaster granite and either before or during F_2 folding of the Zoroaster granite.

We analyzed six random fragments of monazite and two multi-grain fractions of zircon (Fig. 12) that do not define a statistically significant upper intercept age because two of the monazite analyses plot to the right of the linear array defined by most of the data. These grains may contain an inherited component: back-scattered electron imaging of monazite crystals from peraluminous granite dikes throughout the Upper Gorge indicates that partially resorbed cores are present in 30 to 60% of the crystals (see Chapters 3 and 4). This observation indicates that inherited monazite is likely to occur in random fragments such as those analyzed from this sample. When these two points are excluded, the other data, including both zircon and monazite analyses, yield an upper intercept age of 1698 ± 1 Ma (lower intercept = -79 ± 270 Ma; MSWD = 0.29), which we interpret as the crystallization age of the granite stock.

Folded Muscovite Pegmatite Dike (sample UG111.8-1). A 5 centimeter-wide, zoned pegmatite dike obliquely cross-cuts NW-striking foliation (S_1) and compositional layering in the Vishnu schist on the west side of the Ruby pluton. Both the dike and the compositional layering in the metamorphic rocks are deformed into small-scale, open folds, and foliation in the adjacent pelitic schist is crenulated to form an S_2 fabric axial planar to the folds (Fig. 13). Solid-state deformational features along both margins of the dike indicate that the pegmatite intruded and crystallized prior to folding (Fig. 13). The dike, therefore, constrains the development of both S_1 and S_2 fabrics as well as the folding event. Five single grain fractions of monazite separated from the pegmatitic portion of the dike yield four concordant and one reversely discordant U-Pb date (Fig

13). The weighted mean of the Pb-Pb dates for all five points is 1697.3 ± 0.4 Ma (MSWD = 0.55). We interpret 1697 ± 1 Ma as the crystallization age of the dike.

Biotite - muscovite granite dike (sample UG80.5-1). Granite and pegmatite dikes comprise about 50% of the rock volume near river mile 80.5. The dikes intrude upper amphibolite facies quartzofeldspathic gneiss and migmatitic schist of the Vishnu schist. This sample was collected from within a 15 centimeter-wide dike of fine-grained biotite - muscovite granite that cross-cuts both compositional layering and the dominant foliation in the adjacent supracrustal sequence. In thin section, the contact is sharp: biotite grains in the gneiss are resorbed and/or overgrown by igneous biotite oriented subparallel to the contact. Zircon grains are clear, colorless and generally lack inclusions and fractures. Most grains have prominent terminations that account for about two-thirds of the total length of the grains. Four concordant zircon fractions (Table 1; Fig. 14) yield a weighted mean of the Pb-Pb dates of 1685.0 ± 0.8 Ma (MSWD = 1.09). One of the concordant analyses, fraction Z9, consists of two crystal terminations broken from two different grains indicating that the sharp crystal terminations are not metamorphic overgrowths. We accept 1685 ± 1 Ma as the crystallization age of the dike.

Unfoliated Muscovite Granite Dike (sample UG78.0-1). This sample was collected from a 20 centimeter-wide dike of fine- to medium-grained, unfoliated granite at the mouth of Mineral Canyon (Fig. 3). The dike cross-cuts the composite S_1/S_2 foliation in the supracrustal rocks and contains partially disagreggated, randomly-oriented xenoliths of foliated schist and gneiss, indicating that the dike post-dates development of S_2 fabric.

We present data from five single grains of monazite (Table 1; Fig. 15). Four nearly-concordant points (M1, M5, M6, M8) have similar Pb-Pb dates, whereas the fifth point (M3) is 18 m.y. older. We interpret fraction M3 as a metamorphic crystal inherited from

the adjacent schist and gneiss, because both the Pb-Pb date and the Th/U ratio are similar to metamorphic monazites in this part of the transect (see Fig. 11 in Chapter 4). Both the weighted mean of the Pb-Pb dates (MSWD = 0.66) and the upper intercept age (MSWD = 0.89) for the four remaining points are 1680 ± 1 Ma. If the reversely discordant point is excluded, the weighted mean of the Pb-Pb dates is 1680 ± 1 Ma (MSWD = 1.12; see sample 87.7-1 below). We interpret the crystallization age of the dike to be 1680 ± 1 Ma.

Phantom pluton (sample UG87.7-1). The Phantom pluton is a fine-to medium-grained biotite-muscovite granite that intrudes migmatitic supracrustal rocks. The pluton locally contains magmatic fabric. Pegmatite dikes cross-cut the pluton and are offset along discrete shear bands. The sample contained both partially metamict zircon and clear, euhedral, equant crystals of monazite. We analyzed five fractions of zircon, containing one to three crystals each, that yielded 18 to 59 % discordant U-Pb dates with Pb-Pb dates ranging from 1541 to 1626 Ma (Table 1; Fig. 16a). The data do not define a statistically significant discordia.

Monazite yielded more coherent results. Five single grains of euhedral monazite yielded 0.4 % reversely discordant to 2.1 % normally discordant U-Pb dates (Table 1; Fig. 16b). The weighted mean of the five Pb-Pb dates is 1661 ± 1 Ma (MSWD = 1.52) and the upper intercept age is 1662 ± 1 Ma (lower intercept = 220 ± 200 Ma; MSWD = 0.31). If the reversely discordant point is excluded from the linear regression, the upper intercept is 1662 ± 1 Ma with a lower intercept of 226 ± 217 Ma and an MSWD of 0.40. Because reversely discordant monazite analyses from two widely separated samples (UG78.0-1, UG87.7-1) are consistent with normally discordant data from the same sample, we suggest that the reverse discordance in these monazites did not result from the incorporation of excess ^{206}Pb (e.g., Schärer, 1984; Parrish, 1990) and that the Pb-Pb dates of the individual analyses are reliable (see Chapter 3 for further discussion of

reverse discordance in Upper Gorge monazites). Because the zircon data scatter about the discordia defined by the monazite data, we interpret the monazite data to record the crystallization age of the pluton. We suggest that the pluton was emplaced at 1662 ± 1 Ma, an age that is significantly younger than other muscovite-bearing granites in the Upper Gorge.

DISCUSSION

In this section we discuss the implications of the new U-Pb ages for the Paleoproterozoic evolution and regional significance of the Paleoproterozoic rocks exposed in the Upper Granite Gorge. Timing constraints are summarized in Figure 17.

The Elves Chasm Pluton

The 1840 Ma Elves Chasm tonalite (sample UG113.2-1) is the oldest rock yet described from the southwestern United States, but its geologic significance is somewhat unclear because the field relationships are equivocal. The pluton intrudes an isolated block of amphibolite near the eastern margin of the pluton, but appears to be intruded by a mafic dike that was subsequently metamorphosed to coarse-grained amphibolite (Karlstrom, personal communication 1996). The pluton also exhibits complex contact relationships with distinctive orthoamphibole-cordierite-garnet gneisses that are restricted to the eastern margin of the pluton (Clark, 1979; Brown and others, 1979). On the east margin of the pluton, the contact appears to be gradational, but Karlstrom (personal communication, 1996) observed an apparent intrusive relationship in Garnet Canyon (Fig. 3). These apparently contradictory field relationships are difficult to interpret. Possible interpretations include: 1) a basement - cover relationship in which case the amphibolite intruded by the pluton is a screen of crust older than 1840 Ma and the supracrustal rocks east of the pluton are younger than 1840 Ma (e.g., Babcock, 1990);

2) an intrusive relationship indicating that the supracrustal sequence is older than 1840 Ma and that a significant volume of pre-1840 Ma crust is present in the western Upper Gorge; or 3) a tectonic relationship that has been overprinted by deformation and metamorphism.

The detrital zircons from the Vishnu schist at mile 109.9 may provide some insight into this problem. Although many of the zircon crystals analyzed yielded Pb-Pb dates older than 1800 Ma, three grains yielded Pb-Pb dates between 1732 and 1736 Ma indicating that the sandstone protolith was deposited after 1732 Ma. To the extent that no unrecognized shear zones or unconformities occur between mile 109.9 and the ortho-amphibole gneisses miles 112.4 to 112.9 on the eastern margin of the pluton, the detrital zircons indicate that the supracrustal sequence east of the Elves Chasm pluton is younger than the pluton. Given the caveats already mentioned, we tentatively interpret the contact between the Elves Chasm pluton and the adjacent supracrustal sequence as either an unconformity or an overprinted shear zone. Regardless of the contact relationships, the age presented here for the pluton demonstrates that pre-1.8 Ga crust is present beneath at least part of the Colorado Plateau.

Volcanism and Sedimentation

Metavolcanic rocks of the Rama and Brahma schists were deposited/erupted at 1750 (sample UG84.4-1), 1741 Ma (sample UG79.6-1) and ca. 1735 Ma (UG90.4-1). The spatial relationship at the time these units formed is unknown because of subsequent deformation and metamorphism and because each of the dated units occurs in a different crustal block (Fig. 3). However, comparable units of the Rama, Vishnu and Brahma Formations are interlayered at several localities in the Upper Gorge transect, suggesting that these units comprise a complex volcanic and sedimentary package characterized by spatial and temporal lithologic variation (Ilg and others, 1996). The U-Pb data

presented here indicate that: 1) protoliths of the Brahma, Rama and Vishnu schists formed between about 1750 and 1732 Ma; 2) protoliths of the Brahma schist formed over at least 15 m.y. between 1750 and 1735 Ma; 3) protoliths of Rama schist formed contemporaneously with protoliths of the Brahma schist; and 4) at least part of the sedimentary precursors to the Vishnu schist were deposited after 1732 Ma.

Detrital zircons from the Vishnu schist throughout the transect (miles 81.1 to 109.9) preserve evidence for a source of sediment that is not exposed in the orogen today. The Pb-Pb dates of 19 pre-Yavapai single-crystal analyses range from 1772 to 3269 Ma. Most of the crystals fall into three narrow age groups: five analyses yielded Pb-Pb dates between 1800 and 1900 Ma; six analyses yielded Pb-Pb dates between 2300 to 2500 Ma; and two analyses yielded Pb-Pb dates older than 2800 Ma. The source of these detrital zircons is not known because there is no regional database for evaluating sedimentary transport directions between 1750 and 1730 Ma. Nonetheless, the distribution of Pb-Pb dates is consistent with sources to the north-northeast within the North American craton: 3300 to 2300 Ma zircons may have been derived from the Wyoming craton; and the 1900 to 1800 Ma zircons may have derived from sources in the Trans-Hudson orogen (Fig. 1). However, the provenance of these grains could also correspond to dispersed elements of Laurentia, such as Baltica or Antarctica (see Hoffman, 1989).

Arc-Related Magmatism

Mafic to intermediate plutons intruded the supracrustal rocks between about 1741 Ma and 1713 Ma. Intrusion of 1750 Ma Brahma schist by the 1741 Ma Zoroaster pluton was contemporaneous with deposition/eruption of part of the Rama schist (1741 Ma). Mafic to intermediate plutonism continued with pluton emplacement at 1737 Ma (Grapevine Camp), 1730 Ma (Trinity), 1716 Ma (Ruby) and 1713 Ma (Horn Creek).

Because several plutons remain undated, the significance of the apparent temporal bimodality (1740 - 1730 Ma and 1720 - 1710 Ma) cannot be evaluated.

Timing of Deformation

Development of Group 1 fabrics is bracketed by the ages of foliated plutons and cross-cutting dikes. The 1740 Ma Zoroaster (sample UG84.9-1), 1730 Ma Trinity (sample UG91.5-1), 1717 Ma Ruby (sample UG104.3-3, AZ-398) and 1713 Ma Horn Creek (sample UG90.6-2) plutons all contain an S_1 fabric. Both the Zoroaster and Trinity plutons exhibit well-developed penetrative S_1 fabrics folded by F_2 folds. The Ruby pluton (miles 102 to 108; sample UG104.3-4, AZ-398) contains a poorly developed northwest-striking magmatic fabric, suggesting that some component of the finite strain associated with S_1 fabric development accumulated at 1717 Ma. Deformation associated with the development of S_1 also outlasted emplacement of the 1713 Ma Horn Creek pluton, which contains a well-developed fabric, consistent in orientation with S_1, that is transposed by S_2. Because of the uncertainty involved in correlating fabrics with similar orientations both across the transect and with respect to absolute time, we adopt 1730 Ma, the age of the Trinity pluton, as a maximum age bracket on the development of S_1 fabrics. Minimum age brackets on S_1 are provided by two muscovite-bearing granitic intrusions: the 1698 Ma muscovite-biotite stock, which cross-cuts S_1 fabric in the Zoroaster pluton (sample UG85.2-4; Fig. 12); and the 1697 Ma folded pegmatite dike (sample UG111.8-1), which cross-cuts S_1 fabric in the Vishnu Formation (Fig. 13). Taken together, these ages and fabric relations indicate that across the transect S_1 fabrics mainly developed after 1730 Ma and ceased to develop by 1698 Ma (Fig. 17).

The timing of S_2 fabric development is constrained by the observation that S_2 overprints S_1 and by U-Pb ages from deformed plutons and cross-cutting dikes. The 1698 Ma granite stock (sample UG85.2-4), which cross-cuts S_1 fabric in the Zoroaster pluton and locally contains an axial planar S_2 fabric (Fig. 12), predated much of the shortening associated with the development of S_2 in the eastern Upper Gorge. The 1713 Ma Horn Creek pluton (sample UG90.6-2) contains an S_1 fabric transposed by an S_2 fabric and therefore provides a maximum timing constraint on the development of S_2 in the central part of the transect. In the western Upper Gorge, the 1697 Ma folded pegmatite dike (sample UG111.8-1), which is associated with an axial planar S_2 crenulation cleavage (Fig. 13), predates much of S_2/ F_2 deformation. Because of the abundant evidence for strain partitioning related to development of S_2 fabrics and the uncertainty involved in correlating fabrics across the transect, we adopt 1713 Ma, the age of the Horn Creek pluton, as a maximum age bracket for S_2 fabrics across the transect. The only minimum timing constraints are provided by two granite dikes from the eastern Upper Gorge, samples UG80.5 (1685 Ma) and UG78.0-1 (1680 Ma), which truncate S_2 fabrics and exhibit little evidence for S_2/ F_2 shortening. We interpret these field relationships and U-Pb ages to bracket S_2 fabric development to between 1713 and 1685 Ma across the transect (Fig. 17).

The timing of Group 3 structures is poorly constrained. These structures probably post-date 1680 Ma, the age of the unfoliated dike from mile 78 (sample UG78.0-1), and also 1662 Ma, as indicated by group 3 shear bands that deform the Phantom pluton

(sample UG87.7-1). More data are required to evaluate whether group 3 deformational structures represent the late stages of a protracted deformational event responsible for group 2 structures, or a temporally distinct (and perhaps locally preserved?) deformational event (see Chapter 5 for further discussion).

Peraluminous Granite and Pegmatite Magmatism

Variably deformed peraluminous granite and pegmatite dikes and stocks intrude high grade supracrustal rocks and deformed mafic to intermediate plutons. East of the Vishnu fault zone, the outcrop volume of these dikes and sills increases from less than 10% at mile 78.0 to greater than 50% near mile 80.5. Notably high volumes (≥ 50 vol%) of dikes occur east of the Vishnu fault zone, immediately west of the Zoroaster pluton, between Tuna Creek and the Ruby pluton, and within the Elves Chasm pluton (Fig. 3). The dikes and sills span a range of ages, as indicated by: 1) cross-cutting relationships between different dikes and sills; 2) variable degrees of deformation; and 3) U-Pb ages spanning 5 m.y. locally (1685 to 1680 Ma, mile 78.0) and about 40 m.y. (1698 to 1662 Ma) across the transect. We envision these bodies as partial melts that formed, accumulated and mobilized at deeper levels of the crust before being emplaced at the current level of exposure. East of the Vishnu shear zone, the dikes cross-cut leucosomes in migmatites suggesting the dikes post-date the peak of lower granulite facies metamorphism at the current level of exposure. The age of the Phantom pluton (1662 Ma) indicates that, immediately west of the Bright Angel shear zone, generation of peraluminous granite melt continued until (?) or occurred 40 - 50 m.y. after partial melting began in the eastern Upper Gorge (see Chapter 5 for further details).

Timing of Metamorphism

U-Pb mineral dates provide insight into the timing of lower granulite facies metamorphism (650-720 °C, ca. 6 kbars; Williams, unpublished data) east of the Vishnu fault zone. We analyzed seven single crystals of monazite from a 1741 Ma biotite-sillimanite quartzofeldspathic rock (sample UG79.6-1) of the Rama Formation. The monazite Pb-Pb dates range from 1706 to 1697 Ma, and are over 35 m.y. younger than the crystallization age for the rock (Fig. 4). We interpret these dates to reflect continuous growth during lower granulite facies metamorphism (see description of data for sample UG79.6-1). This interpretation is consistent with U-Pb ages of granite dikes (1685 Ma, sample UG80.5-1, Fig. 14; 1680 Ma, sample UG78.0-1, Fig. 15) that cross-cut leucosomes in the migmatites.

Two lines of evidence suggest that a significant thermal perturbation occurred between 1670 and 1660 Ma in at least part of the transect. The age of the Phantom pluton (1662 Ma) and the evidence for ca. 1660 Ma metamorphic zircon growth in the Brahma schist at mile 90.4, suggest that metamorphism occurred at about 1662 Ma between the Bright Angel and 96-Mile shear zones (Fig. 3). The relationship between ca. 1660 Ma crustal heating and the ca. 1700 Ma metamorphism documented in the eastern Upper Gorge is explored in Chapter 5.

Regional Affinities and Significance

The evolution of crust in the Upper Granite Gorge is similar to that of the Yavapai Province in central Arizona. The nature and age of the supracrustal sequences, the timing and duration of mafic to intermediate plutonism, and the ca. 1.70 Ga deformational, magmatic and metamorphic histories are characteristic of the Yavapai Province in central Arizona (e.g., Karlstrom and others, 1987; Karlstrom and Bowring, 1988). These results

are consistent with regional correlation of the Upper Gorge with the Yavapai Province (e.g., Karlstrom and Daniel, 1993).

Unlike the Yavapai province, however, the Upper Gorge contains pre-1.80 Ga crust (the 1840 Ma Elves Chasm pluton) and evidence for the involvement of pre-1.8 Ga crustal components in the development of the 1.75 to 1.71 Ga arcs (Fig. 10). Two related questions arise from these findings: 1) does the Upper Gorge transect or some portion thereof, represent Mojave-type crust, Yavapai-type crust or perhaps crust with distinct characteristics?; and 2) does the Upper Gorge expose the boundary between the Mojave and Yavapai provinces? Because the distinction between the crustal provinces is based upon U-Pb zircon dates and, especially, whole rock Pb isotopic data (Wooden and others, 1988; Wooden and Miller, 1990; Wooden and DeWitt, 1991; Bryant and others, 1994; Wooden and others, 1994), we need to consider both types of data.

The Upper Gorge and the Mojave province exhibit similar detrital and inherited zircon populations. Wooden and others (1994) reported 1.80 to 2.70 Ga detrital and inherited zircons from the Mojave province. The Upper Gorge contains 1.77 to 3.27 Ga detrital zircons and inherited zircons between 2.00 and 2.27 Ga. However, the Upper Gorge is distinguished from the Mojave province by exposures of the 1840 Ma Elves Chasm pluton (sample UG113.2-1; Fig. 7), the oldest known rock in the region, but the significance of this unit to the questions at hand cannot be evaluated based on the U-Pb zircon data alone.

Whole rock Pb isotopic data provide a robust indicator of crustal affinities and can be evaluated relative to an extensive regional database (Wooden and DeWitt, 1991; Aleinikoff and others, 1993). To evaluate the regional significance of the Upper Gorge transect, particularly the Elves Chasm pluton, we determined whole rock Pb isotopic data for six samples from the Upper Gorge transect (Table 2). Following the method of Wooden and DeWitt (1991), the data are normalized to the Pb isotopic composition of

galena from Jerome, Arizona (Table 2). The normalized value, ΔJerome, highlights differences in the $^{207}Pb/^{204}Pb$ ratio of the whole rock samples (Wooden and DeWitt, 1991). As shown in figure 18, Mojave-type crust has high $^{207}Pb/^{204}Pb$ ratios (ΔJerome values > +3.0) and highly variable Th/U ratios, whereas Yavapai-type crust has low $^{207}Pb/^{204}Pb$ ratios (ΔJerome values < +3.0) and Th/U ratios less than about 3.5. Mojave-type crust includes rocks from the Mojave province and northern Colorado, whereas Yavapai-type crust is exposed in southern Colorado and central Arizona (Fig. 18).

The ΔJerome values of rocks from the Upper Gorge span much of the range exhibited by rocks from throughout the orogen. Most of the data plot within the Mojave and Yavapai fields, but there is no correlation between river mile and the ΔJerome value (Fig 18). This observation suggests that the distribution of crust with Mojave-type Pb isotopic signatures is complex and that any boundary between the Mojave and Yavapai provinces should be exposed east of river mile 84.4. However, several features of the data suggest that the Upper Gorge exposes crust with distinctive characteristics. The Tuna Creek pluton and the Elves Chasm pluton have some of the highest ΔJerome values observed in the orogen. The Tuna Creek pluton plots outside of the Mojave-type field. Unlike most of the rocks considered to be Mojave-type crust, rocks from the Upper Gorge have very low Th/U ratios, particularly the Elves Chasm pluton (Fig. 18). Given the broad range of Th/U ratios observed in Mojave-type crust, it is tempting to speculate that the range in Th/U ratio within the Mojave-type crust field represents mixing between an uncharacterized reservoir with high ΔJerome values and high Th/U ratios and ca. 1.84 Ga crust with high ΔJerome values and low Th/U ratios. Such a scenario suggests that older crust is present beneath much of the orogen and significantly reduces the volume of juvenile crust represented by the orogen.

SUMMARY

The Upper Gorge contains 1750 to ca. 1732 Ma supracrustal rocks that were intruded by ca. 1740 to 1710 Ma mafic to intermediate plutons. These rocks were penetratively deformed resulting in two groups of structures that formed at 1730 to 1698 Ma, and 1713 and 1685 Ma, respectively. A third, more diverse group of fabrics and structures developed after 1680 Ma and is present in the 1662 Ma Phantom pluton. Based on these timing brackets, we cannot distinguish whether these structures reflect a continuum of deformation or discrete deformational events. Metamorphic monazites from a 1741 Ma quartzofeldspathic schist yield a range of Pb-Pb dates between 1706 and 1697 Ma which we interpret to indicate the timing of prograde to peak metamorphism in the eastern Upper Gorge. Peraluminous granitic melt production and emplacement largely occurred between 1698 Ma and 1680 Ma, but local melt production occurred as late as 1662 Ma.

The tectonic and thermal history of crust in the Upper Gorge is similar to that of rocks in the Yavapai province of central Arizona. Unlike the Yavapai province, however, rocks in the western Upper Gorge exhibit the following evidence for the involvement of pre- 1.75 Ga crust: 1) the occurrence of the 1840 Ma Elves Chasm pluton, the oldest plutonic rock from the Paleoproterozoic of the southwestern United States; 2) the presence of inherited zircons, with minimum ages of 1998 and 2178 Ma, in a granodiorite pluton from the 1740 -1710 Ma arc-related magmatic suite; and 3) radiogenic whole rock Pb isotopic data. These data indicate that, at least locally, pre-1.8 Ga crust was involved in the development of the 1740 - 1710 Ma arc-related magmatic suite.

REFERENCES

Albin, A.L., and Karlstrom, K.E., 1991, Orthogonal fabrics in northwestern Arizona: Multiple orogenic events or progressive deformation during continental assembly, in Karlstrom, K.E., ed., Proterozoic geology and ore deposits of Arizona: Arizona Geological Society Digest 19, p. 67-84.

Aldrich, L.T., Wetherill, G.W., and Davis, G.L., 1957, Occurrence of 1350 million-year-old granitic rocks in the western United States: Geological Society of America Bulletin, v. 68, p. 655-656.

Aleinikoff, J.N., Reed, J.C., Jr., and Wooden, J.L., 1993, Lead isotopic evidence for the origin of Paleo- and Mesoproterozoic rocks of the Colorado Province, U.S.A.: Precambrian Research, v. 63, p. 97-122.

Babcock, R.S., 1990, Precambrian crystalline core, in Bues, S., and , eds., Geology of the Grand Canyon: Flagstaff, Museum of Northern Arizona, p. 11-28.

Babcock, R.S., Brown, E.H., Clark, M.D., and Livingston, D.E., 1979, Geology of the older Precambrian rocks of the Grand Canyon: Part II. The Zoroaster plutonic complex and related rocks: Precambrian Research, v. 8, p. 243-275.

Bennett, V.C., and DePaolo, D.J., 1987, Proterozoic crustal evolution of the western United States as determined by neodymium isotopic mapping: Geological Society of America Bulletin, v. 99, p. 674-685.

Black, L.P., Fitzgerald, J.D., and Harley, S.L., 1984, Pb isotopic composition, colour, and microstructure of monazites from a polymetamorphic rock in Antarctica: Contributions to Mineralogy and Petrology, v. 85, p. 141-148.

Bowring, S.A., and Karlstrom, K.E., 1990, Growth, stabilization and reactivation of Proterozoic lithosphere in the southwestern United States: Geology, v. 18, p. 1203-1206.

Brooks, C., Hart, S.R., and Wendt, I., 1972, Realistic use of two-error regression treatments as applied to rubidium-strontium data: Reviews of Geophysics and Space Physics, v. 10 p. 551-577.

Brown, E.H., Babcock, R.S., Clark, M.D., and Livingston, D.E., 1979, Geology of the older Precambrian rocks of the Grand Canyon: Part I. Petrology and structure of the Vishnu complex: Precambrian Research, v. 8, p. 219-241.

Bryant, B., DeWitt, E., Wooden, J.L., and Conway, C.M., 1994, The boundary between the Early Proterozoic Mojave and central Arizona crustal provinces, western Arizona [Abs.]: Geological Society of America Abstracts with Programs, v. 26, no. 6, p. 6.

Campbell, Ian and Maxson, J.H., 1938, Geological studies of the Archean rocks at Grand Canyon: Carnegie Institution of Washington Yearbook No. 37, p.359-364.

Chamberlain, K.R., and Bowring, S.A., 1990, Proterozoic geochronologic and isotopic boundary in northwestern Arizona: Journal of Geology, v. 98, p. 399-416.

Clark, M.D., 1979, Geology of the older Precambrian rocks of the Grand Canyon: Part III. Petrology of the mafic schists and amphibolites: Precambrian Research, v. 8, p. 277-302.

Conway, C.M., and Silver, L.T., 1989, Early Proterozoic rocks (1710 - 1615 Ma) in central to southeastern Arizona, in Jenney, J.P., and Reynolds, S.J., eds., Geological Evolution of Arizona: Arizona Geological Society Digest 17, p. 165-186.

Copeland, P., Parrish, R.R., and Harrison, T.M., 1988, Identification of inherited radiogenic Pb in monazite and its implications for U-Pb systematics: Nature, v. 333, p. 760-763.

DeWolf, C.P., Belshaw, N. and O'Nions, R.K., 1993, A metamorphic history from micron-scale $^{207}Pb/^{206}Pb$ chronometry of Archean monazite: Earth and Planetary Science Letters, v. 120, p. 207-220.

Ewing, R.C., Haaker, R.F., and Lutze, W., 1982, Leachability of zircon as a function of alpha dose, in Lutze, W., ed., Scientific Basis for Radioactive Waste Management - V: Amsterdam, Elsevier Science Publishing Co., p. 389-397.

Eyal, Y., and Fleischer, R.L., 1985, Timescale of natural annealing in radioactive minerals affect retardation of radiation-damage-induced leaching: Nature, v. 314, p. 518-520.

Giletti, B.J. and Damon, P.E., 1961, Rubidium-strontium ages of some basement rocks from Arizona and northwestern Mexico: Geological Society of America Bulletin, v. 72, p. 639-644.

Goldich, S.S., and Mudrey, M.G., 1972, Dilatancy model for discordant U-Pb zircon ages, in Tugarinov, A.I., ed. Contributions to Recent Geochemistry and Analytical Chemistry: Moscow, Nauka Publications, p. 415-418.

Hanchar, J.M., and Rudnick, R.L., 1995, Revealing hidden structures: The application of cathodoluminescence and back-scattered electron imaging to dating zircons from lower crustal xenoliths: Lithos, in press.

Hoffman, P.F., 1989, Precambrian geology and tectonic history of North America, in Bally, A.W., and Palmer, A.R., eds., The Geology of North America — An Overview: Boulder, Colorado, Geological Society of America, The Geology of North America, v. A, p. 447-511.

Ilg, B.R., Karlstrom, K.E., Hawkins, D.P., and Williams, M.L., 1996, Paleoproterozoic rocks of the Upper and Middle Gorges, Grand Canyon, Arizona: New stratigraphic nomenclature, structural geometry and insights into middle crustal processes: Geological Society of America Bulletin, in press.

Karlstrom, K.E., and Bowring, S.A., 1988, Early Proterozoic assembly of tectonostratigraphic terranes in southwestern North America: Journal of Geology, v. 96, p. 561-576.

Karlstrom, K.E., and Bowring, S.A., 1991, Styles and timing of Early Proterozoic deformation in Arizona, in Karlstrom, K.E., ed., Proterozoic geology and ore deposits of Arizona: Arizona Geological Society Digest 19, p. 1-10.

Karlstrom, K.E., and Daniel, C.G., 1993, Restoration of Laramide right-lateral strike-lip in northern New Mexico by using Proterozoic piercing points: Tectonic implications from the Proterozoic to the Cenozoic: Geology, v. 21, p. 1139-1142.

Karlstrom, K.E., Bowring, S.A., and Conway, C., 1987, Tectonic significance of an Early Proterozoic two-province boundary in central Arizona: Geological Society of America, v. 99, p. 529-538.

Krogh, T.E., 1973, A low contamination method for hydrothermal decomposition of zircon and extraction of U and Pb for isotopic age determination: Geochimica et Cosmochimica Acta, v. 37, p. 488-494.

Krogh, T.E., 1982, Improved accuracy for U-Pb zircon ages by creation of more concordant systems using an air abrasion technique: Geochimica et Cosmochimica Acta, v. 46, p. 637-649.

Lingley, W.S., 1973, Some structures in older Precambrian rocks in the vicinity of Clear Creek and Zoroaster Canyon, Grand Canyon, Arizona [M.S. Thesis]: Western Washington University, 78p.

Livingston, D.E., Brown, E.H., Babcock, R.S., and Clark, M.D., 1974, Rb-Sr whole rock isochron ages for "Older" Precambrian plutonic and metamorphic rocks of the Grand Canyon, Arizona[Abs.]: Geological Society of America Abstracts with Programs, v. 6, p. 848-849.

Ludwig, K.R., 1989, Pb.dat: A computer program for processing raw Pb-U-Th isotope data: U.S. Geological Survey Open-File Report 88-557.

Ludwig, K.R., 1990, Isoplot: A plotting and regression program for radiogenic-isotope data: U.S. Geological Survey Open-File Report 90-91.

Noble and Hunter, 1914, Reconnaissance of the Archean complex of the Granite Gorge, Grand Canyon, Arizona: United States Geological Survey Professional Paper 98I, p. 95-113.

Overstreet, W.C., 1967, The geologic occurrence of monazite: United States Geological Survey Professional Paper 530, 164p.

Parrish, R.R., 1990, U-Pb dating of monazite and its application to geological problems: Canadian Journal of Earth Sciences, v. 27, p. 1435-1450.

Pasteels, P., and Silver, L.T., 1966, Geochronologic investigations in the crystalline rocks of the Grand Canyon, Arizona [Abs.]: Geological Society of America Special Papers No. 87, p. 124.

Schärer, U., 1984, The effect of initial ^{230}Th disequilibrium on young U-Pb ages: The Makalu case, Himalaya: Earth and Planetary Science Letters, v. 67, p. 191-204.

Smith, H.A., and Barreiro, B.A., 1990, U-Pb dating of staurolite grade metamorphism in pelitic schists: Contributions to Mineralogy and Petrology , v. 105, p. 602-615.

Smith, H.A., and Giletti, B.J., 1995, Pb loss in monazite via diffusion and other transport processes [Abs.]: Geological Society of America Abstracts with Programs, v. 27, no. 6, p. A36.

Stacey, J.S., and Kramers, J.D., 1975, Approximation of terrestrial lead isotopes evolution by a two-stage model: Earth and Planetary Science Letters, v. 26, p. 207-221.

Suzuki, K., and Adachi, M., and Tanaka, T., 1991, Middle Precambrian provenance of Jurassic sandstone in the Mino Terrane, central Japan: Th-U-total Pb evidence from an electron microprobe monazite study: Sedimentary Geology, v. 75, p. 141-147.

Van Schmus, W.R., Bickford, M.E., Anderson, J.L., Bender, E.E., Anderson, R.R., Bauer, P.W., Robertson, J.M., Bowring, S.A., Condie, K.C., Denison, R.E., Gilbert, M.C., Grambling, J.A., Mawer, C.K., Shearer, C.K., Hinze, W.J., Karlstrom, K.E., Kisvarsanyi, E.B., Lidiak, E.G., Reed, J.C., Jr. Sims, P.K., Tweto, O., Silver, L.T., Treves, S.B., Williams, M.L., Wooden, J.L., 1993, Transcontinental Proterozoic provinces, in Reed, J.C., Jr., Bickford, M.E., Houston, R.S., Link, P.K., Rankin, D.W., Sims, P.K., and Van Schmus, W.R., eds., Precambrian: Conterminous United States: Boulder, Colorado, Geological Society of America, The Geology of North America, v. C-2, p. 171-333.

Wendt, I. and Carl, C., 1991, The statistical distribution of the mean squared weighted deviation: Chemical Geology, v. 86, p. 275-285.

Williams, M.L., 1991, Early Proterozoic low-pressure high-temperature metamorphism in Arizona, in Karlstrom, K.E., ed., Proterozoic geology and ore deposits of Arizona: Arizona Geological Society Digest 19, p. 11-26.

Wooden, J.L., and DeWitt, E., 1991, Pb isotopic evidence for the boundary between the Early Proterozoic Mojave and central Arizona crustal provinces in western Arizona, in Karlstrom, K.E., ed., Proterozoic geology and ore deposits of Arizona: Arizona Geological Society Digest 19, p. 27-50.

Wooden, J.L., and Miller, D.M., 1990, Chronologic and isotopic framework for Early Proterozoic crustal evolution in the eastern Mojave Desert region, SE California: Journal of Geophysical Research, v. 95, p. 20133-20146.

Wooden, J.L., Nutman, A.P., Howard, K.A., Bryant, B. DeWitt, E., and Mueller, P.A., 1994, Shrimp U-Pb zircon evidence for Late Archean and Early Proterozoic crustal evolution in the Mojave province and central Arizona crustal provinces [Abs.]: Geological Society of America Abstracts with Programs, v. 26, no. 6, p. 69.

Wooden, J.L., Stacey, J.S., and Howard, K.A., Doe, B.R., and Miller, D.M., 1988, Pb isotopic evidence for the formation of Proterozoic crust in the southwestern United States, in Ernst, W.G., ed., Metamorphism and Crustal Evolution of the Western United States: Rubey Volume VII, p. 69-86.

York, D., 1969, Least-squares fitting of a straight line with correlated errors: Earth and Planetary Science Letters, v. 5, p. 320-324.

Young, E.D., Anderson, J.L., Clarke, H.S., and Thomas, W.M., 1989, Petrology of biotite-cordierite-garnet gneiss of the McCullough Range, Nevada I: Evidence for Proterozoic low pressure fluid-absent granulite-grade metamorphism in the southern Cordillera: Journal of Petrology, v. 30, p. 39-60.

FIGURE CAPTIONS

Figure 1 Generalized tectonic map of the North American craton showing the distribution of Archean provinces, 2.0 to 1.8 Ga orogenic belts, the Yavapai-Mazatzal orogenic system, and the Grenville province. Note that the Yavapai-Mazatzal system represents about 20% of the pre-Grenville craton. Also shown are the location of potential sources for detrital zircons: the Archean Wyoming province and the Trans-Hudson orogen. Modified after Hoffman (1989).

Figure 2. Regional map showing the distribution of Paleoproterozoic rocks (dark shading) around the Colorado Plateau (light shading), the location of the Upper Granite Gorge, the boundary between the Mojave and Yavapai provinces (as suggested by Wooden and others, 1994 and Bryant and others, 1994), and the boundary between the Yavapai and Mazatzal provinces (as suggested by Karlstrom and Daniel, 1993). The inset map shows the location of Lee's Ferry. Modified after Van Schmus and others (1993) and Karlstrom and Daniel (1993).

Figure 3. Generalized geologic map of the Upper Granite Gorge transect showing the sample localities. Although the shear zones cut the Paleoproterozoic rocks, for clarity they are represented as foliation traces projected outside of the Paleoproterozoic exposures. The inset shows the location of Lee's Ferry, the reference point for all locations along the Colorado River. Abbreviations: 96-MSZ—96-mile shear zone; BASZ—Bright Angel shear zone; BSZ—Bass shear zone; CSZ—Crystal shear zone; ECP—Elves Chasm pluton; GCP—Grapevine Camp pluton; HP—Horn Creek pluton; PhP—Phantom pluton; RP—Ruby pluton; TP—Trinity pluton; TuP—Tuna pluton; VFZ—Vishnu fault zone; ZP—Zoroaster pluton.

Figure 4 U-Pb concordia plot for metamorphosed supracrustal rocks from the Upper Granite Gorge. Two points for sample UG79.6-1 that plot along the best fit line (MSWD = 0.33) are normally discordant beyond the plot frame shown. The inset shows monazite data for sample UG79.6-1.

Figure 5 U-Pb concordia diagram for detrital zircons from three samples of the Vishnu schist. Labels indicate the river-mile and fraction number. Note that the zircons fall roughly into three groups: 1750 - 1950 Ma (9 crystals); 2300 - 2500 Ma (6 crystals); and >2800 Ma (2 crystals).

Figure 6 U-Pb concordia diagram for zircons from the biotite-hornblende quartzofeldspathic gneiss interlayered with Brahma schist amphibolites at mile 90.4. Note that fractions Z1 and Z7 have Pb-Pb dates that are comparable to the age of the Phantom pluton (see Fig. 16).

Figure 7. Concordia plot for U-Pb zircon data from the Elves Chasm pluton (sample UG113.2-1). The data include two different morphologies and both single and multi-grain analyses. The MSWD of the linear regression is 1.66.

Figure 8. Concordia diagram for U-Pb data from the Zoroaster granite (sample UG84.9-1). The five zircon analyses yield a best-fit chord with an MSWD of 0.79.

Figure 9. Concordia plot for U-Pb zircon data for the Grapevine Camp (sample UG81.2-3) and Trinity plutons (sample UG91.5-1). One very discordant analysis for the Grapevine Camp pluton plots off the diagram on the best fit line (MSWD = 0.67).

Figure 10. Concordia diagram for U-Pb zircon data from the Tuna Creek granodiorite (sample UG99.2-1). Note that the 2-sigma error ellipses are smaller than the points shown. The data are extremely discordant and do not yield a statistically significant chord (the line is shown for reference only). The three points that plot to the right of the reference line include two single grain analyses with Pb-Pb ages of 1998 and 2175 Ma.

Figure 11. Concordia diagram for U-Pb zircon data from the Ruby (sample UG104.3-4) and Horn Creek (sample UG90.6-2) plutons. Ten analyses from the Ruby pluton are concordant. We interpret the one outlying analysis from the Horn Creek pluton to contain an inherited component and exclude it from the linear regression.

Figure 12. Field sketch and U-Pb concordia plot for the biotite granite stock (sample UG85.2-4) that intrudes the Zoroaster pluton. Inset is a field sketch of a river-polished rock face sloping 28° to bearing 028°. The granite stock (X's) cross-cuts S_1 fabric in the Zoroaster granite (foliation traces) and contains a weakly developed S_2 fabric, axial planar to a large-scale F_2 fold, near xenoliths of schist and gneiss (dark gray). Note that the best fit line on the concordia plot (MSWD = 0.29) is defined by both monazite and zircon analyses.

Figure 13. Field sketch and U-Pb concordia plot for a folded pegmatite dike at river mile 111.8. Inset shows a detailed field sketch of fabric relations and solid state deformational features, represented by two dimensional strain ellipses shown in black. The aplitic margin of the dike exhibits normal-sense offset resulting in thinning in the hinge region. The margin of the dike exhibits numerous fractures along which reverse-sense offset resulted in thickening in the hinge region. We interpret these observations to indicate that the dike solidified prior to the folding event and therefore provides a maximum age bracket to F_2 folding. The weighted mean of the Pb-Pb ages of the individual analyses has an MSWD of 0.55.

Figure 14. Concordia plot of U-Pb zircon data from a biotite granite dike at river mile 80.5. The weighted mean of the Pb-Pb ages of the individual analyses has an MSWD of 1.09.

Figure 15. Concordia plot of U-Pb monazite data from an unfoliated muscovite granite dike at river mile 78.0. We interpret the ca. 1700 Ma point as an inherited metamorphic grain from the supracrustal rocks the dike intrudes (the dike contains numerous partially disaggregated xenoliths from the adjacent schists and gneisses). The ages obtained with or without the reversely discordant analysis are identical and statistically significant (see text for discussion).

Figure 16. Concordia plots for U-Pb zircon (a) and monazite (b) data from the Phantom pluton (sample UG87.7-1). a. Note that the discordant zircon data lie close to the discordia defined by the monazite data. b. Close-up view of the monazite data. The upper intercept ages obtained with and without the reversely discordant analysis are identical and statistically significant (see text for discussion).

Figure 17. Summary of U-Pb ages for samples from the Upper Granite Gorge showing the processes they bracket in time. The position of the each vertical black bar corresponds to the age and the width of each bar corresponds to the 2-sigma uncertainty in the age. Arrows indicate the type of age bracket represented by specific samples. Arrows pointing to the right represent a sample that provides a maximum age bracket, whereas arrows pointing to the left represent samples that provide minimum a age bracket. The age of the Elves Chasm pluton is not shown.

Figure 18. Plot of Th/U ratio versus ΔJerome for whole rock Pb isotopic data from the Proterozoic of the southwestern United States. The data define two types of crust: Mojave-type crust, which is characterized by ΔJerome values greater than +3.0; and Central-Arizona-type crust, which has ΔJerome values less than +2.5 and Th/U ratios less than 4.0. Note that whole rock leads from the Upper Gorge span much of the regional compositional range and that the three samples from the western Upper Gorge have some of the highest ΔJerome values observed. Note also that the sample from mile 84.4 plots well within the Mojave-type crust field. We speculate that the compositional variation exhibited by Mojave-type crust may represent mixing between reservoirs with similar ΔJerome values, but contrasting Th/U ratios. The older crust from the western Upper Gorge may represent an end member of such a mixture.

TABLE 1. U-PB ANALYTICAL DATA

Sample	Fractions/Description	Wgt (µg)	Composition U (ppm)	Pb (ppm)	(Pb)c (pg)	Th U	Atomic Ratios $^{206}Pb/^{204}Pb$	$^{208}Pb/^{206}Pb$	$^{206}Pb/^{238}U$	$^{207}Pb/^{235}U$	$^{207}Pb/^{206}Pb$	rho	Ages (Ma) $^{206}Pb/^{238}U$	$^{207}Pb/^{235}U$	$^{207}Pb/^{206}Pb$
(1)		(2)	(3)	(3)	(4)	(5)	(6)	(7)	(8)	(8)	(8)	(9)			(10)
Biotite-Muscovite Quartzofeldspathic Gneiss of Rama schist (UG79.6-1)															
Z1	22, aa	20.2	248	74	19.4	0.28	4507	0.087	0.29050 (0.07)	4.26553 (0.11)	0.10649 (0.09)	0.614	1644	1687	1740 ± 2
Z3	1, aa	2.4	283	87	6.1	0.29	2122	0.086	0.30091 (0.47)	4.42122 (0.47)	0.10656 (0.07)	0.988	1696	1716	1741 ± 1
Z8	1, aa	3.2	361	100	18.2	0.26	1040	0.086	0.27007 (0.27)	3.96138 (0.28)	0.10638 (0.08)	0.961	1541	1626	1738 ± 1
Z21	1, aa	4.7	150	48	16.3	0.29	818	0.085	0.30934 (0.29)	4.54330 (0.32)	0.10652 (0.13)	0.910	1737	1739	1741 ± 2
M1	1, eu	1.2	7310	4645	38.2	4.56	4077	1.340	0.30092 (0.17)	4.32338 (0.19)	0.10420 (0.07)	0.932	1696	1698	1700 ± 1
M2	1, eu	0.6	11989	5832	19.6	2.60	6568	0.764	0.30169 (0.08)	4.34465 (0.10)	0.10445 (0.05)	0.847	1700	1702	1705 ± 1
M3	1, eu	2.4	8994	3731	23.7	1.67	16260	0.493	0.30135 (0.15)	4.34206 (0.15)	0.10450 (0.05)	0.953	1698	1701	1706 ± 1
M4	1, eu	1.4	6578	3714	76.9	3.62	2134	1.062	0.30179 (0.12)	4.34162 (0.13)	0.10434 (0.06)	0.904	1700	1701	1703 ± 1
M5	1, res	2.1	10984	6730	45.9	4.28	8866	1.260	0.29996 (0.14)	4.30758 (0.14)	0.10415 (0.04)	0.953	1691	1695	1699 ± 1
M7	1, res	1.7	11502	7205	227.8	4.45	1526	1.303	0.30124 (0.29)	4.32123 (0.30)	0.10404 (0.07)	0.969	1697	1697	1697 ± 1
Muscovite - Biotite Quartzite from Vishnu schist (UG81.1-1)															
Z1	1, aa	6.9	24	9	2.5	0.67	1429	0.198	0.32619 (0.25)	5.10225 (0.28)	0.11345 (0.12)	0.896	1820	1836	1855 ± 2
Z2	1, aa	7.2	22	8	3.4	0.74	965	0.222	0.32212 (0.28)	5.02587 (0.39)	0.11316 (0.26)	0.758	1800	1824	1851 ± 5
Z3	1, aa	6.4	78	27	3.4	0.36	3112	0.113	0.32914 (0.19)	5.44488 (0.20)	0.11998 (0.06)	0.957	1834	1892	1956 ± 1
Z4	1, aa	6.1	81	37	2.9	0.38	4482	0.116	0.41413 (0.18)	8.65966 (0.19)	0.15166 (0.06)	0.954	2234	2303	2365 ± 1
Porphyroclastic Gnieiss in Brahma schist (UG84.4-1)															
Z7	2, aa	10.1	166	51	15.6	0.28	1971	0.085	0.30205 (0.17)	4.44854 (0.19)	0.10682 (0.06)	0.950	1701	1721	1746 ± 1
Z8	1, aa	8.4	284	89	11.3	0.29	3904	0.086	0.30420 (0.14)	4.48296 (0.15)	0.10688 (0.05)	0.946	1712	1728	1747 ± 1
Z10	1, aa	3.3	477	146	22.0	0.30	1279	0.093	0.29607 (0.20)	4.35690 (0.23)	0.10673 (0.10)	0.889	1672	1704	1744 ± 2
Z13	1, aa	3.1	351	111	3.3	0.30	6579	0.090	0.30613 (0.16)	4.51524 (0.18)	0.10697 (0.07)	0.911	1722	1734	1748 ± 1
Z14	1, aa	1.6	656	208	19.5	0.28	1004	0.083	0.30966 (0.17)	4.57028 (0.20)	0.10704 (0.08)	0.906	1739	1744	1750 ± 2
Biotite - Hornblende Quartzofeldspathic Gneiss from the Brahma schist (UG90.4 -1)															
Z1	7,aa	13.1	1155	316	81.3	0.06	3060	0.018	0.27915 (0.05)	3.91908 (0.07)	0.10182 (0.05)	0.753	1587	1618	1658 ± 1
Z3	5,aa	16.3	348	110	77.5	0.24	1298	0.073	0.29947 (0.06)	4.37983 (0.08)	0.10607 (0.05)	0.768	1689	1709	1733 ± 1
Z6	4,aa	5.4	559	162	17.4	0.14	2992	0.044	0.28899 (0.10)	4.14302 (0.11)	0.10398 (0.06)	0.865	1636	1663	1696 ± 1
Z7	8,aa	6.0	935	263	20.6	0.05	4687	0.016	0.28982 (0.08)	4.08892 (0.09)	0.10232 (0.05)	0.828	1641	1652	1667 ± 1
Z9	1, aa	1.1	754	204	13.6	0.08	988	0.027	0.26655 (0.40)	3.78688 (0.41)	0.10304 (0.08)	0.982	1523	1590	1680 ± 1
Z10	1, aa	2.4	421	123	8.0	0.31	2154	0.097	0.27887 (0.20)	3.97805 (0.21)	0.10346 (0.06)	0.962	1586	1630	1687 ± 1
Z11	3,aa	0.4	1065	261	2.5	0.12	2776	0.042	0.24924 (0.15)	3.52412 (0.17)	0.10255 (0.08)	0.871	1435	1533	1671 ± 2
Z12	5,aa	0.6	702	198	2.9	0.17	2526	0.053	0.28286 (0.15)	4.06424 (0.18)	0.10421 (0.09)	0.861	1606	1647	1700 ± 2
Z15	1, aa	1.3	254	89	20.3	0.24	308	0.073	0.30013 (0.77)	4.39376 (0.82)	0.10618 (0.25)	0.951	1692	1711	1735 ± 5

TABLE 1 — continued

Sample	Fractions/Description	Wgt (µg)	Composition U (ppm)	Pb (ppm)	(Pb)c (pg)	Th/U	Atomic Ratios $^{206}Pb/^{204}Pb$	$^{208}Pb/^{206}Pb$	$^{206}Pb/^{238}U$	$^{207}Pb/^{235}U$	$^{207}Pb/^{206}Pb$	rho	Ages (Ma) $^{206}Pb/^{238}U$	$^{207}Pb/^{235}U$	$^{207}Pb/^{206}Pb$
(1)		(2)	(3)	(3)	(4)	(5)	(6)	(7)	(8)	(8)	(8)	(9)			(10)
Z16	1, aa	1.1	337	102	5.7	0.23	1242	0.069	0.29607 (0.70)	4.32808 (0.71)	0.10602 (0.13)	0.984	1672	1699	1732 ± 2
Z20	1, aa	0.4	1032	285	2.7	0.12	2802	0.036	0.28166 (0.18)	4.03299 (0.25)	0.10385 (0.18)	0.724	1600	1641	1694 ± 3
Z21	1, aa	0.3	1007	279	2.3	0.15	2349	0.047	0.28011 (0.58)	4.05173 (0.66)	0.10491 (0.30)	0.887	1592	1645	1713 ± 6
Biotite - Muscovite Quartzite from the Vishnu schist (UG95.7-1)															
Z1	1, aa	2.5	164	58	10.2	0.51	764	0.155	0.31196 (0.47)	4.79060 (0.49)	0.11138 (0.11)	0.976	1750	1783	1822 ± 2
Z2	1, aa	32.1	449	213	29.0	0.37	12043	0.113	0.43183 (0.10)	9.55549 (0.11)	0.16049 (0.04)	0.931	2314	2393	2461 ± 1
Z3	1, aa	11.1	513	406	20.2	0.60	10714	0.166	0.64107 (0.12)	23.30368 (0.13)	0.26364 (0.04)	0.948	3193	3240	3269 ± 1
Z4	1, aa	23.3	581	244	385.9	0.28	717	0.098	0.36345 (0.13)	7.85025 (0.14)	0.15665 (0.05)	0.934	1999	2214	2420 ± 1
Z5	1, aa	4.3	1991	1003	107.4	0.63	1671	0.248	0.39206 (0.12)	11.26752 (0.13)	0.20843 (0.04)	0.941	2132	2546	2893 ± 1
Z6	1, aa	4.9	241	116	7.1	0.38	4352	0.112	0.43910 (0.18)	9.53950 (0.21)	0.15756 (0.09)	0.894	2347	2391	2430 ± 2
Z7	1, aa	10.4	176	89	4.6	0.47	11288	0.135	0.45532 (0.10)	10.02828 (0.11)	0.15974 (0.05)	0.909	2419	2437	2453 ± 1
Muscovite Quartzite from Vishnu schist (UG109.9-1)															
Z1	1, aa	5.1	117	38	6.2	0.45	1836	0.134	0.30276 (0.34)	4.43528 (0.35)	0.10625 (0.07)	0.977	1705	1719	1736 ± 1
Z2	1, aa	3.9	235	81	11.0	0.34	1616	0.101	0.32123 (0.19)	4.92356 (0.20)	0.11116 (0.06)	0.952	1796	1806	1819 ± 1
Z3	1, aa	2.7	273	84	2.3	0.16	6573	0.047	0.31128 (0.13)	4.65260 (0.14)	0.10837 (0.05)	0.942	1747	1759	1772 ± 1
Z4	1, aa	3.6	371	138	7.2	0.29	4004	0.087	0.35394 (0.15)	6.01233 (0.16)	0.12320 (0.05)	0.942	1953	1978	2003 ± 1
Z5	1, aa	1.7	71	21	2.0	0.35	1069	0.115	0.27516 (0.32)	4.02941 (0.35)	0.10621 (0.14)	0.923	1567	1640	1735 ± 2
Z6	1, aa	5.0	198	46	10.1	0.48	1173	0.222	0.19589 (1.33)	2.86367 (1.40)	0.10603 (0.39)	0.960	1153	1372	1732 ± 7
Z7	1, aa	3.4	501	160	6.7	0.27	4906	0.082	0.31076 (0.15)	4.67761 (0.17)	0.10917 (0.06)	0.931	1744	1763	1786 ± 1
Z8	1, aa	5.4	176	90	4.5	0.44	6079	0.124	0.46317 (0.16)	10.34244 (0.17)	0.16195 (0.05)	0.947	2454	2466	2476 ± 1
Z9	1, aa	3.3	262	133	3.3	0.37	7907	0.104	0.46534 (0.14)	10.36671 (0.17)	0.16157 (0.09)	0.828	2463	2468	2472 ± 2
Z10	1, aa	2.0	136	59	1.2	1.12	5286	0.324	0.35090 (0.09)	5.74783 (0.14)	0.11880 (0.10)	0.703	1939	1939	1938 ± 2
Z11	1, aa	6.2	282	100	20.9	0.38	1623	0.112	0.32580 (0.19)	5.01701 (0.21)	0.11169 (0.09)	0.915	1818	1822	1827 ± 2
Elves Chasm Pluton (UG113.2-1)															
Z1	3, eq, aa	6.7	137	45	7.5	0.17	2456	0.052	0.32490 (0.19)	5.04160 (0.20)	0.11254 (0.06)	0.953	1814	1826	1841 ± 1
Z2	2, pr, aa	4.1	127	41	5.3	0.17	1971	0.050	0.32531 (0.33)	5.04874 (0.34)	0.11256 (0.06)	0.985	1816	1828	1841 ± 1
Z6	2, pr, aa	2.6	378	125	3.8	0.19	5423	0.054	0.33019 (0.17)	5.11895 (0.19)	0.11244 (0.07)	0.931	1839	1839	1839 ± 1
Z17	3, pr, aa	3.4	248	81	3.1	0.19	5625	0.056	0.32351 (0.19)	5.02041 (0.21)	0.11255 (0.07)	0.935	1807	1823	1841 ± 1
Z18	5, pr, aa	5.2	189	63	3.2	0.17	6639	0.050	0.33020 (0.16)	5.12425 (0.17)	0.11255 (0.06)	0.937	1839	1840	1841 ± 1
Zoroaster Pluton (UG84.9-1)															
Z8	1, aa	2.6	500	160	27.9	0.32	868	0.093	0.30988 (0.19)	4.54987 (0.25)	0.10649 (0.15)	0.806	1740	1740	1740 ± 3

TABLE 1 — continued

Sample Fractions/Description (1)		Wgt (µg) (2)	Composition U (ppm) (3)	Pb (ppm) (3)	(Pb)c (pg) (4)	Th U (5)	Atomic Ratios $^{206}Pb/^{204}Pb$ (6)	$^{208}Pb/^{206}Pb$ (7)	$^{206}Pb/^{238}U$ (8)	$^{207}Pb/^{235}U$ (8)	$^{207}Pb/^{206}Pb$ (8)	rho (9)	Ages (Ma) $^{206}Pb/^{238}U$	$^{207}Pb/^{235}U$	$^{207}Pb/^{206}Pb$ (10)
Z9	1, aa	2.6	466	143	5.4	0.30	4172	0.092	0.29850 (0.18)	4.37932 (0.20)	0.10640 (0.07)	0.925	1684	1708	1739 ± 1
Z12	1, aa	2.9	927	296	33.2	0.34	3135	0.099	0.30736 (0.09)	4.51507 (0.12)	0.10654 (0.08)	0.767	1728	1734	1741 ± 1
Z10	1, aa	2.9	346	108	6.0	0.30	1485	0.089	0.30355 (0.18)	4.45571 (0.19)	0.10646 (0.07)	0.935	1709	1723	1740 ± 1
Z14	1, aa	2.5	807	251	8.6	0.31	4317	0.091	0.30227 (0.11)	4.43470 (0.12)	0.10641 (0.06)	0.884	1703	1719	1739 ± 1
Grapevine Camp Pluton (UG81.1-3)															
Z4	1, aa	2.5	224	62	15.3	0.27	608	0.090	0.27015 (0.35)	3.96655 (0.37)	0.10649 (0.11)	0.952	1542	1627	1740 ± 2
Z7	2, aa	4.4	695	223	12.6	0.34	4492	0.099	0.30870 (0.09)	4.52359 (0.10)	0.10628 (0.05)	0.897	1734	1735	1737 ± 1
Z9	1, aa	3.1	531	164	8.0	0.31	3786	0.094	0.29915 (0.13)	4.38676 (0.14)	0.10635 (0.05)	0.929	1687	1710	1738 ± 1
Trinity Pluton (UG91.2-1)															
Z2	2, aa	15.1	221	63	18.0	0.19	643	0.061	0.28452 (0.10)	4.15876 (0.13)	0.10601 (0.08)	0.798	1614	1666	1732 ± 1
Z4	1, aa	8.4	263	75	25.5	0.21	1472	0.066	0.28232 (0.18)	4.13213 (0.25)	0.10615 (0.16)	0.755	1603	1661	1734 ± 3
Z10	2,aa	2.2	143	43	17.9	0.19	3168	0.058	0.30246 (0.28)	4.41574 (0.39)	0.10588 (0.23)	0.799	1704	1715	1730 ± 4
Z14	2,aa	1.4	144	43	6.0	0.16	332	0.049	0.30057 (0.46)	4.39193 (0.49)	0.10597 (0.14)	0.955	1694	1711	1731 ± 3
Ruby Pluton (AZ-398, UG104.3-4)															
Z3	1, aa	32.5	60	20	3.1	0.56	12342	0.163	0.30495 (0.10)	4.42021 (0.11)	0.10513 (0.05)	0.893	1716	1716	1717 ± 1
Z5	1, aa	15.2	70	23	4.3	0.57	4770	0.166	0.30498 (0.18)	4.41938 (0.19)	0.10510 (0.06)	0.952	1716	1716	1716 ± 1
Z6	1, aa	28.5	67	23	4.1	0.59	9119	0.172	0.30476 (0.11)	4.41612 (0.13)	0.10510 (0.05)	0.911	1715	1715	1716 ± 1
Z7	1, aa	16.2	129	44	8.9	0.62	4357	0.181	0.30523 (0.15)	4.42454 (0.16)	0.10513 (0.07)	0.915	1717	1717	1717 ± 1
Z8	1, aa	10.5	121	41	8.6	0.60	3884	0.175	0.30494 (0.15)	4.41842 (0.17)	0.10509 (0.07)	0.918	1716	1716	1716 ± 1
Z9	1, aa	9.8	212	71	10.3	0.57	2748	0.168	0.30505 (0.16)	4.42168 (0.18)	0.10513 (0.07)	0.928	1716	1716	1717 ± 1
Z10	2, aa	8.1	135	46	5.4	0.67	3715	0.195	0.30505 (0.20)	4.42106 (0.21)	0.10511 (0.05)	0.968	1716	1716	1716 ± 1
Z11	2, aa	10.0	178	60	11.3	0.59	2893	0.172	0.30500 (0.13)	4.42077 (0.15)	0.10512 (0.07)	0.891	1716	1716	1716 ± 1
Z13	4, aa	7.2	221	74	4.6	0.57	6653	0.167	0.30473 (0.13)	4.41892 (0.14)	0.10517 (0.05)	0.920	1715	1716	1717 ± 1
Z14	1, aa	8.2	196	67	6.0	0.65	7322	0.191	0.30507 (0.12)	4.42430 (0.13)	0.10518 (0.05)	0.932	1716	1717	1718 ± 1
Granodiorite from Tuna Creek (UG99.2-1)															
Z1	8,aa	11.4	485	136	65.5	0.34	1235	65.476	0.24933 (0.06)	4.10166 (0.09)	0.11931 (0.06)	0.740	1435	1655	1946 ± 1
Z6	1,aa	0.4	1453	391	8.4	0.23	1015	8.417	0.24346 (0.39)	4.56779 (0.40)	0.13607 (0.08)	0.979	1405	1743	2178 ± 1
Z7	1,aa	3.0	1565	220	48.8	0.18	699	48.802	0.12502 (0.15)	1.69068 (0.20)	0.09808 (0.12)	0.789	759	1005	1588 ± 2
Z8	1,aa	1.0	1458	368	23.3	0.31	829	23.328	0.22670 (0.20)	3.26500 (0.23)	0.10446 (0.09)	0.914	1317	1473	1705 ± 2
Z10	1,aa	0.5	1961	298	13.7	0.19	582	13.651	0.13542 (0.41)	1.86812 (0.45)	0.10005 (0.14)	0.949	819	1070	1625 ± 3
Z11	1,aa	0.4	1179	285	6.9	0.31	936	6.874	0.22267 (0.53)	3.17566 (0.55)	0.10344 (0.11)	0.979	1296	1451	1687 ± 2
Z12	1,aa	0.6	1621	340	16.3	0.10	687	16.321	0.19449 (0.40)	3.29507 (0.42)	0.12287 (0.12)	0.957	1146	1480	1998 ± 2

TABLE 1 — continued

Sample Fractions/Description		Wgt (µg)	Composition U (ppm)	Pb (ppm)	(Pb)c (pg)	Th U	Atomic Ratios $^{206}Pb/^{204}Pb$	$^{208}Pb/^{206}Pb$	$^{206}Pb/^{238}U$	$^{207}Pb/^{235}U$	$^{207}Pb/^{206}Pb$	rho	Ages (Ma) $^{206}Pb/^{238}U$	$^{207}Pb/^{235}U$	$^{207}Pb/^{206}Pb$
(1)		(2)	(3)	(3)	(4)	(5)	(6)	(7)	(8)	(8)	(8)	(9)			(10)
Z13	4,aa	0.4	1018	318	5.4	0.45	1376	5.363	0.28793 (0.53)	4.14922 (0.56)	0.10451 (0.19)	0.941	1631	1664	1706 ± 4
Horn Pluton (UG90.6-2)															
Z9	1, aa, eq	6.5	133	44	5.3	0.52	2215	0.154	0.30334 (0.22)	4.38678 (0.23)	0.10489 (0.07)	0.959	1708	1710	1712 ± 1
Z10	1, aa, eq	8.2	126	41	4.6	0.51	4277	0.150	0.30150 (0.22)	4.36042 (0.23)	0.10489 (0.07)	0.958	1699	1705	1712 ± 1
Z13	2, aa, pr	5.8	168	55	4.5	0.57	6419	0.170	0.30077 (0.19)	4.35074 (0.22)	0.10491 (0.09)	0.902	1695	1703	1713 ± 2
Z15	1, aa, eq	4.6	179	57	6.9	0.44	4158	0.131	0.29950 (0.26)	4.34263 (0.28)	0.10516 (0.09)	0.940	1689	1701	1717 ± 2
Z16	1, aa, eq	8.4	204	66	5.1	0.51	3102	0.151	0.29998 (0.14)	4.33524 (0.15)	0.10482 (0.05)	0.935	1691	1700	1711 ± 1
Biotite Granite Stock that intrudes the Zoroaster pluton (UG85.2-4)															
Z3	2, aa	2.0	717	231	6.6	0.49	3995	0.145	0.30018 (0.18)	4.30818 (0.19)	0.10409 (0.06)	0.944	1692	1695	1698 ± 1
Z4	1, aa	4.3	561	174	72.6	0.38	595	0.111	0.29744 (0.10)	4.27033 (0.22)	0.10413 (0.18)	0.587	1679	1688	1699 ± 3
M1	1, eq	1.6	4012	6070	62.2	15.98	1845	4.673	0.30242 (0.06)	4.34788 (0.08)	0.10427 (0.06)	0.732	1703	1702	1702 ± 1
M2	1, frag	1.2	7770	10851	20.2	14.47	8295	4.240	0.30182 (0.07)	4.33989 (0.08)	0.10429 (0.04)	0.834	1700	1701	1702 ± 1
M3	1, frag	0.9	4707	8587	23.6	20.12	3194	5.937	0.29908 (0.08)	4.29305 (0.09)	0.10411 (0.05)	0.841	1687	1692	1699 ± 1
M4	1, frag	1.8	3643	5097	40.4	14.54	2893	4.261	0.30122 (0.06)	4.32257 (0.08)	0.10408 (0.05)	0.783	1697	1698	1698 ± 1
M5	1, frag	1.6	3251	4442	64.2	14.13	1437	4.168	0.29927 (0.12)	4.29608 (0.14)	0.10411 (0.07)	0.873	1688	1693	1699 ± 1
M6	1, frag	0.9	11309	16977	55.8	15.88	3234	4.657	0.30089 (0.06)	4.31943 (0.08)	0.10412 (0.05)	0.786	1696	1697	1699 ± 1
Folded Muscovite Pegmatite dike (UG111.8-1)															
M1	1, eu	1.0	34785	2530	8.2	5.81	77154	1.703	0.30053 (0.17)	4.30911 (0.17)	0.10399 (0.04)	0.968	1694	1695	1697 ± 1
M2	1, eu	1.1	23168	15958	8.4	5.26	55229	1.542	0.30124 (0.20)	4.32326 (0.21)	0.10409 (0.05)	0.966	1697	1698	1698 ± 1
M6	1, eu	0.2	39863	21565	6.7	3.33	22101	0.973	0.30166 (0.08)	4.32706 (0.09)	0.10403 (0.04)	0.878	1700	1699	1697 ± 1
M7	1, eu	0.4	24887	20043	8.5	6.79	21545	1.988	0.30123 (0.08)	4.32061 (0.09)	0.10403 (0.04)	0.887	1697	1697	1697 ± 1
M8	1, frag	1.4	29085	19168	13.2	4.88	55429	1.428	0.30124 (0.07)	4.32149 (0.08)	0.10405 (0.04)	0.848	1697	1697	1698 ± 1
Biotite Granite Dike that cross-cuts S2 fabric and migmatites (UG80.5-1)															
Z8	2, aa	25.3	31	10	5.7	0.69	2558	0.201	0.29823 (0.28)	4.24531 (0.33)	0.10324 (0.16)	0.865	1683	1683	1683 ± 3
Z9	2, tips, aa	4.5	211	72	8.8	0.73	1964	0.215	0.29841 (0.28)	4.25036 (0.35)	0.10330 (0.20)	0.822	1683	1684	1684 ± 4
Z10	1, frag, aa	6.8	102	34	21.7	0.63	579	0.184	0.29836 (0.34)	4.24876 (0.36)	0.10328 (0.12)	0.942	1683	1683	1684 ± 2
Z11	1, frag, aa	11.7	109	37	5.1	0.75	4657	0.220	0.29765 (0.43)	4.24205 (0.44)	0.10336 (0.05)	0.993	1680	1682	1685 ± 1
Muscovite Granite dike that cross-cuts S2 fabric and migmatites (UG78.0-1)															
M1	1, eu	5.0	3455	6205	15.8	20.00	19351	5.888	0.29657 (0.11)	4.21488 (0.12)	0.10308 (0.05)	0.912	1674	1677	1680 ± 1
M3	1, eu	5.0	3904	3558	12.3	8.17	28570	2.394	0.30115 (0.07)	4.32183 (0.08)	0.10408 (0.04)	0.866	1697	1698	1698 ± 1
M5	1, eu	1.9	4544	5297	28.6	11.67	5322	3.424	0.29755 (0.13)	4.22708 (0.15)	0.10304 (0.07)	0.782	1679	1679	1680 ± 1
M6	1, eu	0.8	26794	57968	261.0	24.88	1450	7.247	0.29902 (0.05)	4.25151 (0.10)	0.10312 (0.07)	0.644	1686	1684	1681 ± 1

TABLE 1 — continued

Sample Fractions/Description (1)	Wgt (2)	Composition U (ppm) (3)	Pb (ppm) (3)	(Pb)c (pg) (4)	Th U (5)	Atomic Ratios $^{206}Pb/^{204}Pb$ (6)	$^{208}Pb/^{206}Pb$ (7)	$^{206}Pb/^{238}U$ (8)	$^{207}Pb/^{235}U$ (8)	$^{207}Pb/^{206}Pb$ (8)	rho (9)	Ages (Ma) $^{206}Pb/^{238}U$	$^{207}Pb/^{235}U$	$^{207}Pb/^{206}Pb$ (10)
M8 1, eu	0.3	9698	13577	16.6	14.76	3121	4.328	0.29770 (0.09)	4.23161 (0.11)	0.10309 (0.07)	0.860	1680	1680	1681 ± 1
Phantom Pluton (UG87.8-1)														
Z1 1,aa	2.5	3550	614	126.7	0.05	681	0.027	0.16400 (0.11)	2.26334 (0.13)	0.10009 (0.07)	0.862	979	1201	1626 ± 1
Z2 2,aa	1.2	2080	527	70.3	0.10	518	0.035	0.23312 (0.16)	3.20811 (0.19)	0.09981 (0.09)	0.869	1351	1459	1620 ± 2
Z3 3,aa	1.4	2697	666	200.0	0.10	242	0.041	0.20025 (0.42)	2.67979 (0.48)	0.09706 (0.22)	0.893	1177	1323	1568 ± 4
Z4 1,aa	0.8	1676	435	25.9	0.07	733	0.025	0.24980 (0.24)	3.43517 (0.28)	0.09974 (0.13)	0.882	1437	1512	1619 ± 2
Z6 1,aa	11.4	2521	282	119.0	0.06	1580	0.041	0.11040 (0.33)	1.45608 (0.35)	0.09566 (0.12)	0.943	675	912	1541 ± 2
M1 1, eu	0.6	3492	6027	49.1	19.44	737	5.824	0.28768 (0.29)	4.04469 (0.38)	0.10197 (0.23)	0.803	1630	1643	1660 ± 4
M2 1, res	0.7	7890	13329	132.0	18.84	738	5.502	0.29534 (0.32)	4.15605 (0.35)	0.10206 (0.13)	0.926	1668	1665	1662 ± 2
M3 1, eu	1.6	3851	7007	20.2	20.59	5345	6.039	0.29409 (0.15)	4.13810 (0.16)	0.10205 (0.05)	0.953	1662	1662	1662 ± 1
M4 1, eu	1.9	5229	7884	30.1	16.47	5702	4.866	0.29177 (0.52)	4.10186 (0.53)	0.10196 (0.13)	0.971	1650	1655	1660 ± 2
M5 1, res	4.2	4689	7908	32.3	18.86	10499	5.580	0.29138 (0.52)	4.09644 (0.52)	0.10196 (0.06)	0.993	1648	1654	1660 ± 1

(1) fractions analyzed include mineral, Z = zircon and M = monazite, followed by analysis number. fraction descriptions include the number of crystals analyzed followed by descriptive abbreviations: aa = air abraded, eq = equant, eu = euhedral, frag = fragment, pr = prismatic, res = resorbed, tips = crystal terminations.

(2) sample weights estimated using a video monitor with a gridded screen are known to within 40%.

(3) expressed as ppm U and ppm radiogenic Pb.

(4) picograms total common Pb in the analysis.

(5) present day values calculated from the 208Pb concentration using the 207Pb/206Pb age.

(6) measured ratio corrected for fractionation: Pb fractionation correction is 0.12% ± 0.04% per atomic mass unit (amu) for multicollector analyses and 0.15% ± 0.04% per amu for single collector analyses.

(7) radiogenic Pb.

(8) corrected for fractionation, spike, blank, and initial common Pb: U blank = 1 pg ± 50%; Pb blanks ranged from 5 to 2 pg during this study and most analyses were reduced using a blank of 3.5 pg ± 50% — for analyses with less than 3.5 pg common Pb the total common Pb was assumed to be blank; initial common Pb composition calculated from Stacey and Kramers (1975) using the interpreted age of the sample. Numbers in parentheses are analytical uncertainties reported in percent at the two-sigma confidence interval.

(9) correlation coefficient

(10) uncertainty in My at the two-sigma confidence interval.

Table 2: WHOLE ROCK Pb ISOTOPIC DATA.

Sample (1)	$^{206}Pb/^{204}Pb$ (2)	$^{207}Pb/^{204}Pb$ (2)	$^{208}Pb/^{204}Pb$ (2)	ΔJerome (3)
1. UG79.6-1	23.016	16.025	40.359	-0.5
2. UG84.4-4	19.418	15.705	37.890	5.0
3. UG84.9-1	27.555	16.468	40.889	-3.4
4. UG90.6-2	18.099	15.529	37.748	1.1
5. UG96.0-1	19.157	15.653	36.675	2.6
6. UG99.2-1	20.506	15.880	38.147	11.2
7. UG113.2-1	21.886	16.004	37.222	9.2
8. UG117.1-2, AZ-399	22.936	16.114	38.328	9.3

(1) samples are listed by river mile see Fig. 2 for localities.

(2) corrected for fractionation only: Pb fractionation correction = 0.12%±0.03% per amu.

(3) calculated using measured values for galena from ore at Jerome, AZ: 206Pb/204Pb = 15.72, 207Pb/204Pb = 15.27, 208Pb/204Pb = 35.34, following the method of Wooden and DeWitt (1991).

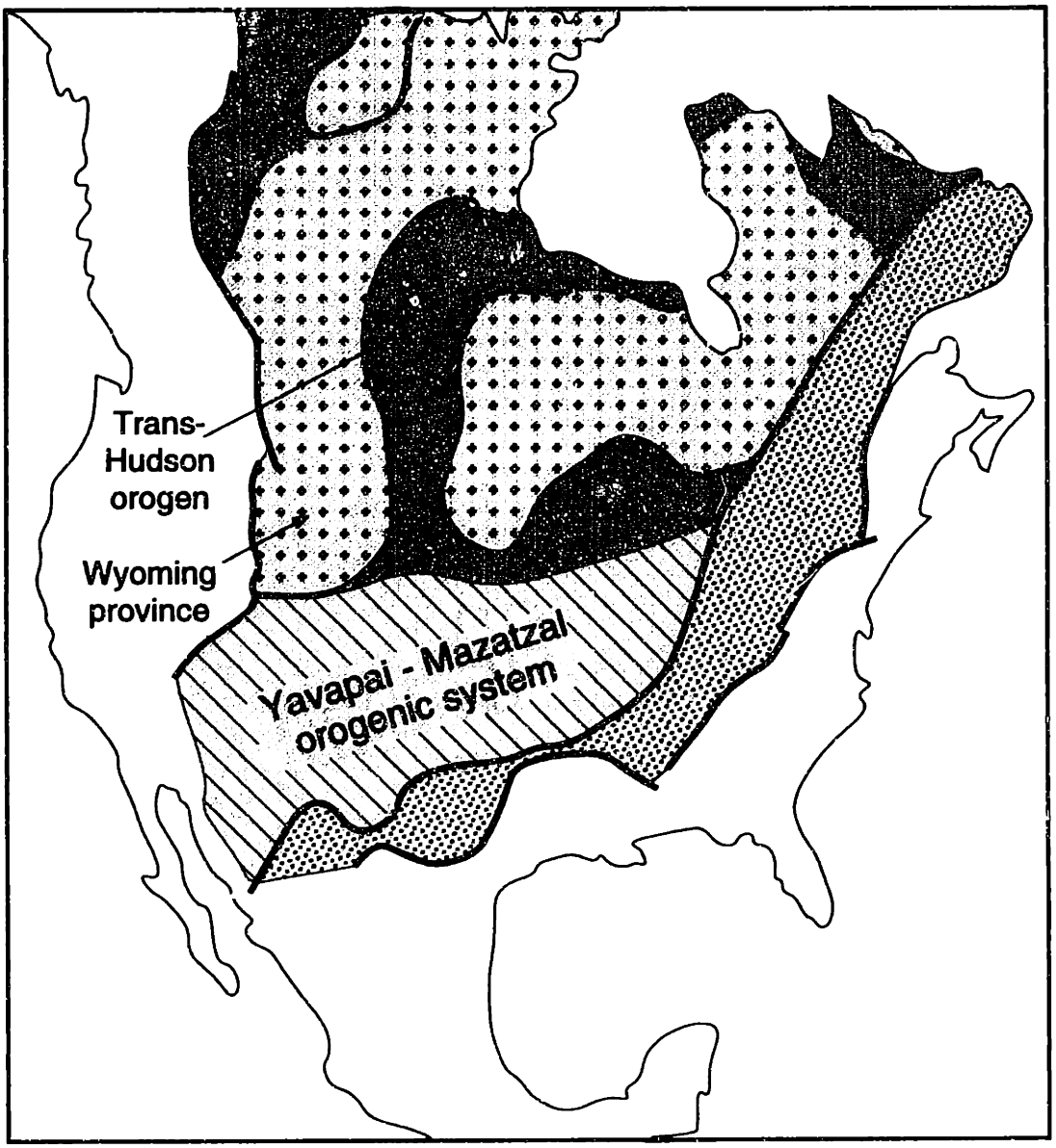
Trans-
Hudson
orogen
Wyoming
province
Yavapai - Mazatzal
orogenic system
Grenville province (1.2 - 1.0 Ga)
Yavapai - Mazatzal orogenic system (1.8 - 1.6 Ga)
2.0 - 1.8 Ga orogenic belts
Archean provinces (> 2.5 Ga)

Figure 1

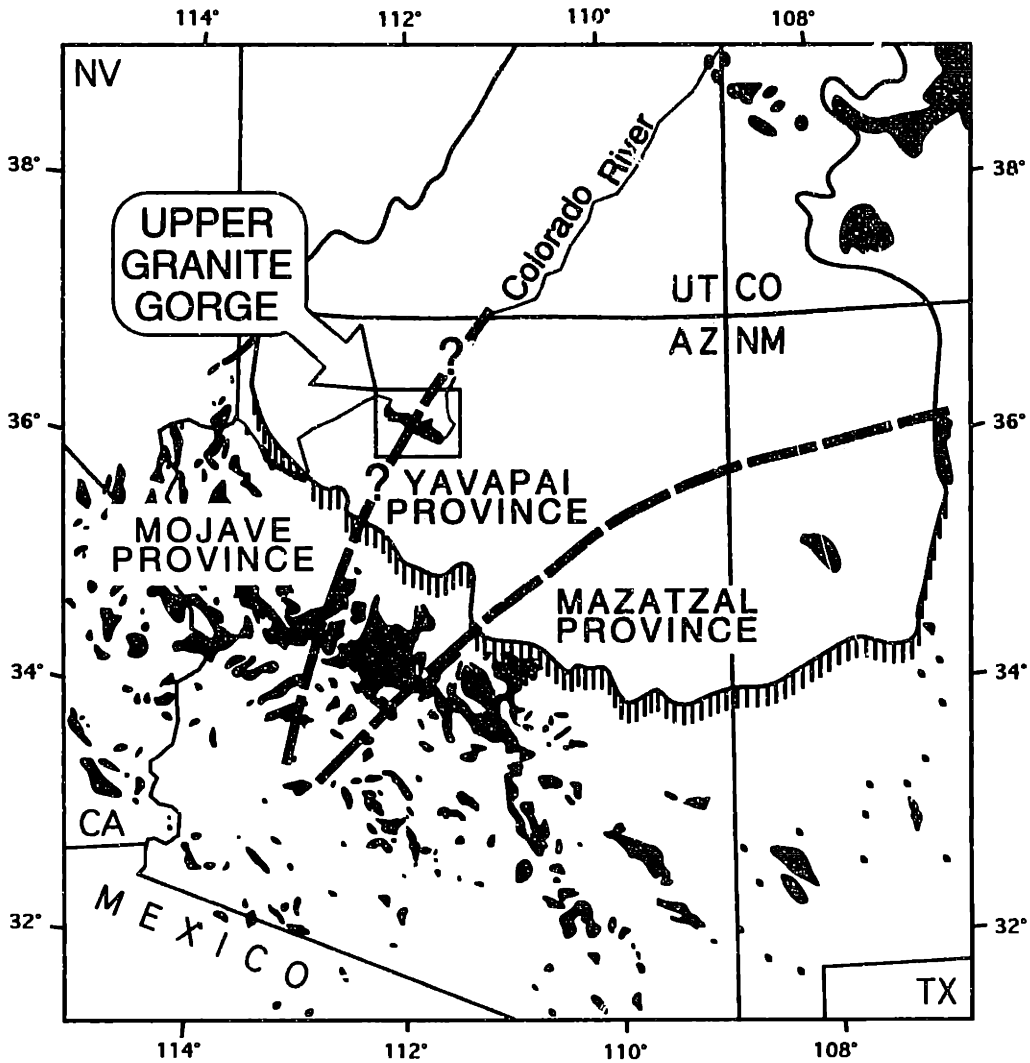
114°
112°
110°
108°
NV
38°
UPPER
GRANITE
GORGE
Colorado River
UT CO
AZ NM
36°
? YAVAPAI
PROVINCE
MOJAVE
PROVINCE
MAZATZAL
PROVINCE
34°
CA
32°
MEXICO
TX

Figure 2

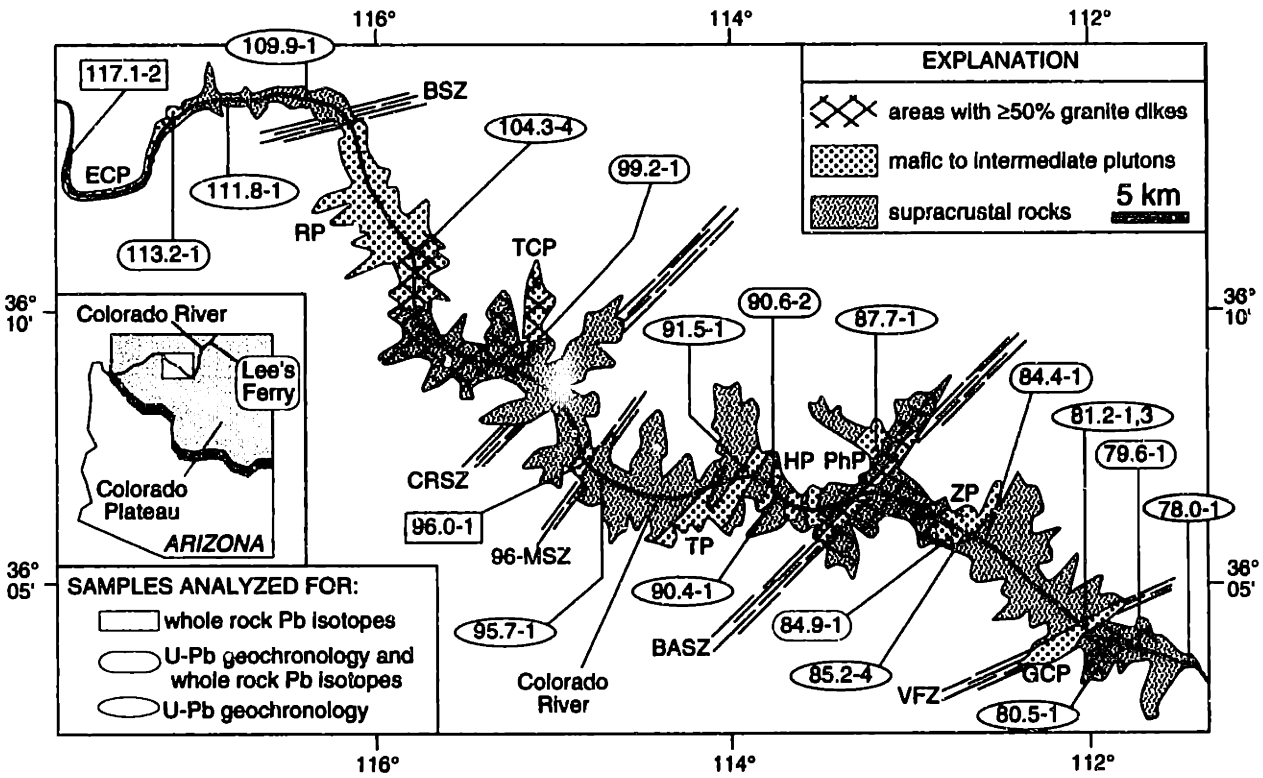
116°
114°
112°
36° 10'
36° 05'
109.9-1
117.1-2
ECP
111.8-1
113.2-1
BSZ
104.3-4
RP
99.2-1
TCP
90.6-2
91.5-1
87.7-1
84.4-1
81.2-1,3
79.6-1
78.0-1
HP PhP
ZP
CRSZ
96.0-1
96-MSZ
TP
90.4-1
95.7-1
BASZ
84.9-1
85.2-4
VFZ
GCP
80.5-1
Colorado River
Lee's Ferry
Colorado Plateau
ARIZONA
EXPLANATION
areas with ≥50% granite dikes
mafic to intermediate plutons
supracrustal rocks
5 km
SAMPLES ANALYZED FOR:
whole rock Pb isotopes
U-Pb geochronology and whole rock Pb isotopes
U-Pb geochronology
Colorado River

Figure 3

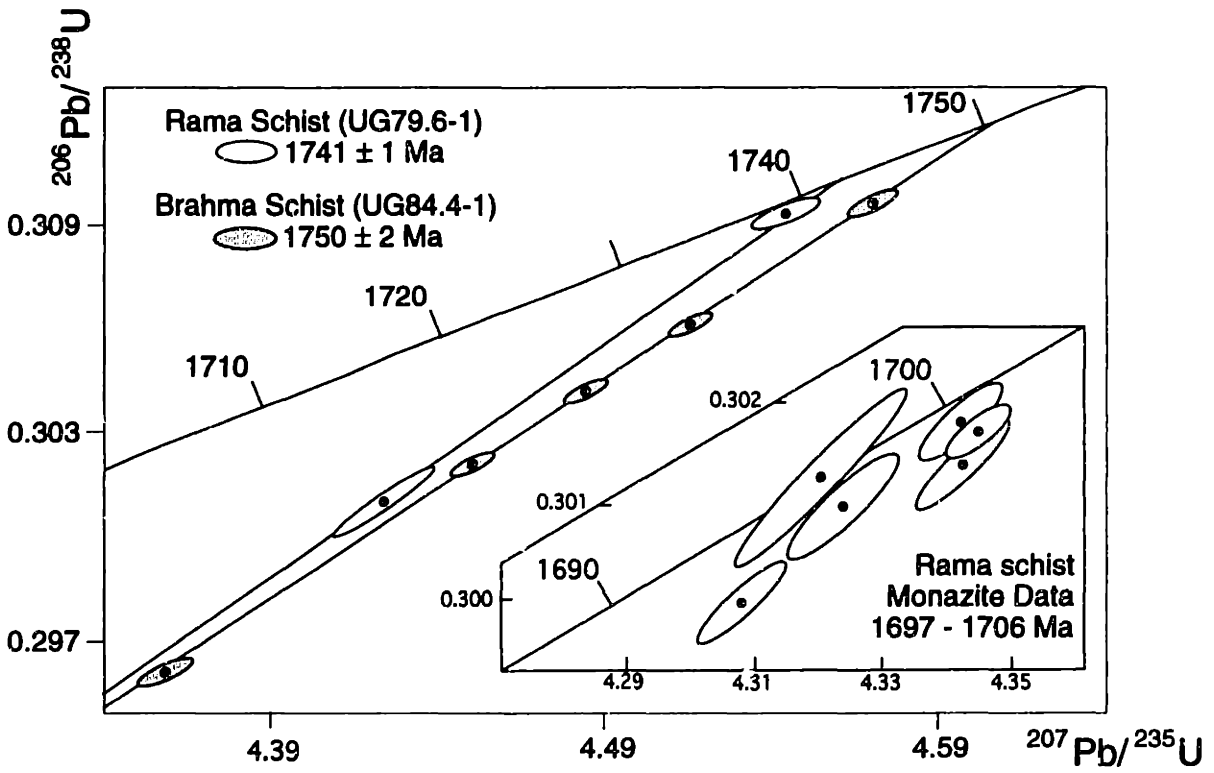
Rama Schist (UG79.6-1)
1741 ± 1 Ma
Brahma Schist (UG84.4-1)
1750 ± 2 Ma
1750
1740
1720
1710
1700
1690
0.309
0.303
0.297
0.302
0.301
0.300
Rama schist
Monazite Data
1697 - 1706 Ma
4.29
4.31
4.33
4.35
4.39
4.49
4.59
206Pb/238U
207Pb/235U

Figure 4

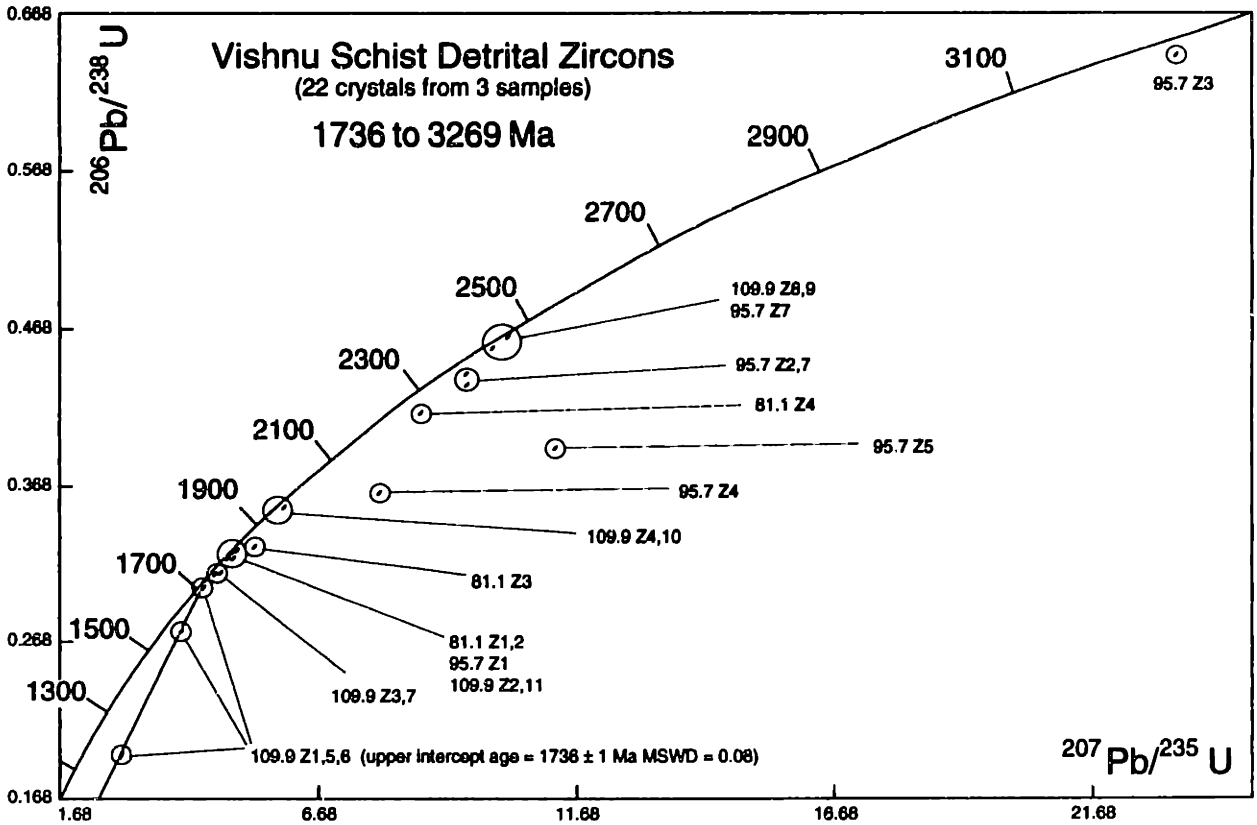
Vishnu Schist Detrital Zircons
(22 crystals from 3 samples)
1736 to 3269 Ma
206Pb/238U
207Pb/235U
0.668
0.568
0.468
0.368
0.268
0.168
1.68
6.68
11.68
16.68
21.68
3100
2900
2700
2500
2300
2100
1900
1700
1500
1300
95.7 Z3
109.9 Z8,9
95.7 Z7
95.7 Z2,7
81.1 Z4
95.7 Z5
95.7 Z4
109.9 Z4,10
81.1 Z3
81.1 Z1,2
95.7 Z1
109.9 Z2,11
109.9 Z3,7
109.9 Z1,5,6 (upper intercept age = 1736 ± 1 Ma MSWD = 0.08)

Figure 5

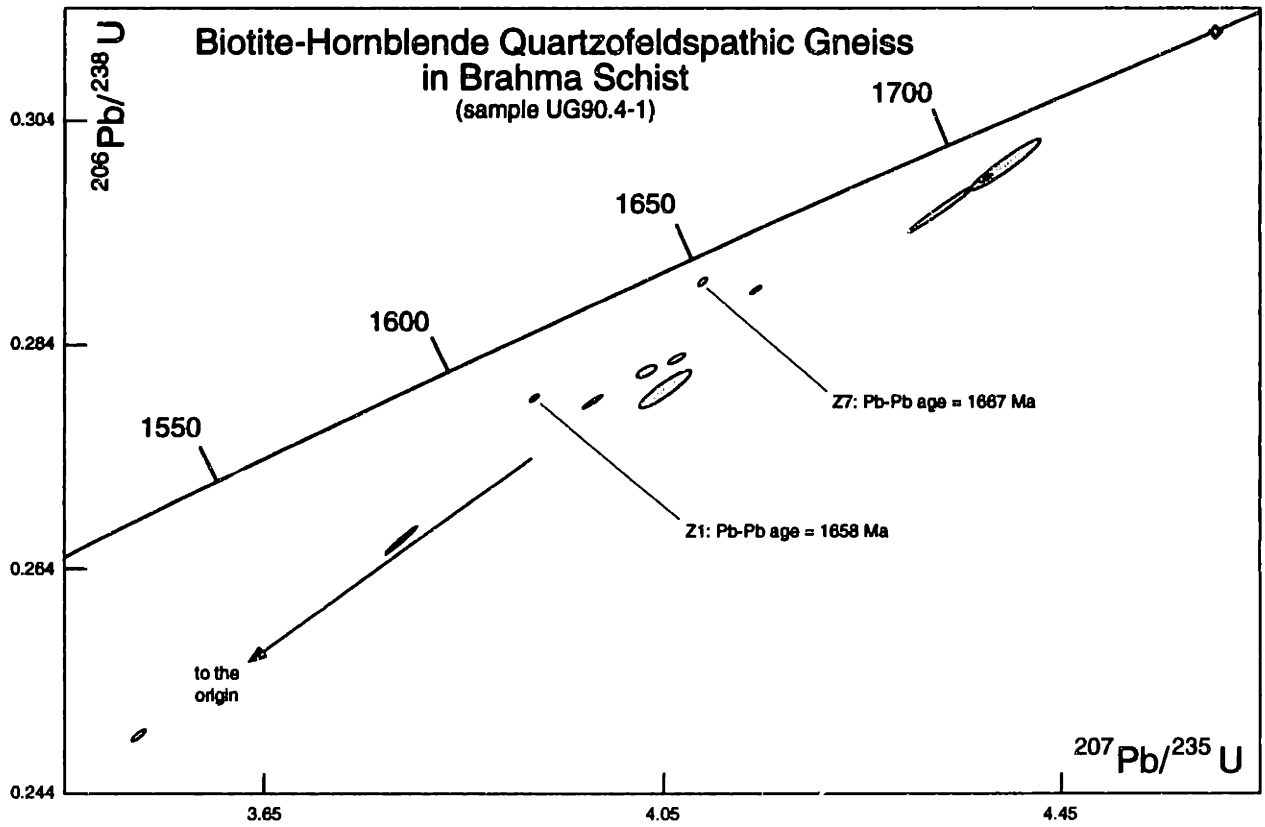
Biotite-Hornblende Quartzofeldspathic Gneiss
in Brahma Schist
(sample UG90.4-1)
206Pb/238U
207Pb/235U
0.304
0.284
0.264
0.244
3.65
4.05
4.45
1700
1650
1600
1550
Z7: Pb-Pb age = 1667 Ma
Z1: Pb-Pb age = 1658 Ma
to the
origin

Figure 6

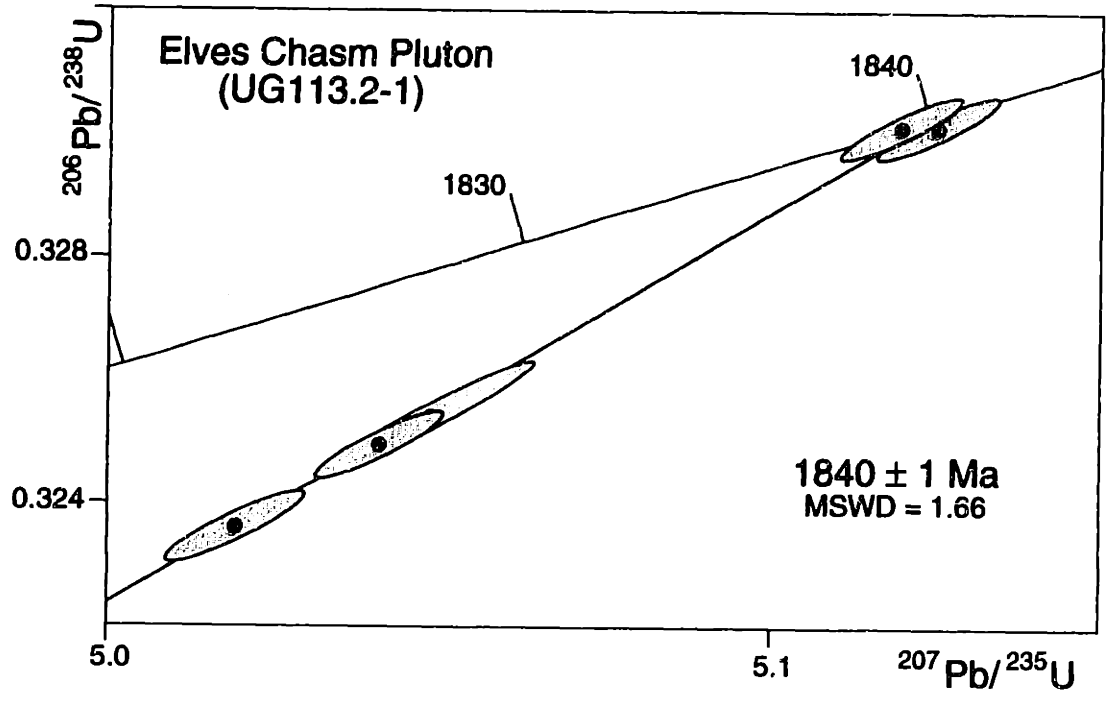
Elves Chasm Pluton
(UG113.2-1)
1840
1830
0.328
0.324
1840 ± 1 Ma
MSWD = 1.66
5.0
5.1
$^{206}Pb/^{238}U$
$^{207}Pb/^{235}U$

Figure 7

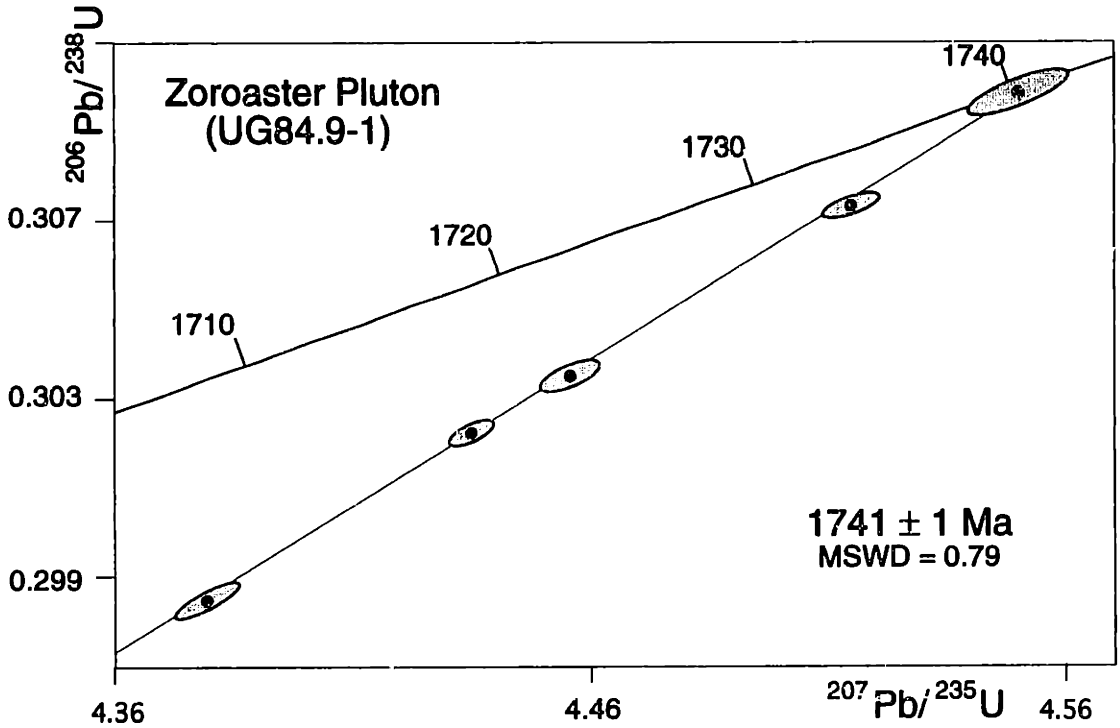
Zoroaster Pluton
(UG84.9-1)
1740
1730
1720
1710
0.307
0.303
0.299
1741 ± 1 Ma
MSWD = 0.79
4.36
4.46
4.56
206Pb/238U
207Pb/235U

Figure 8

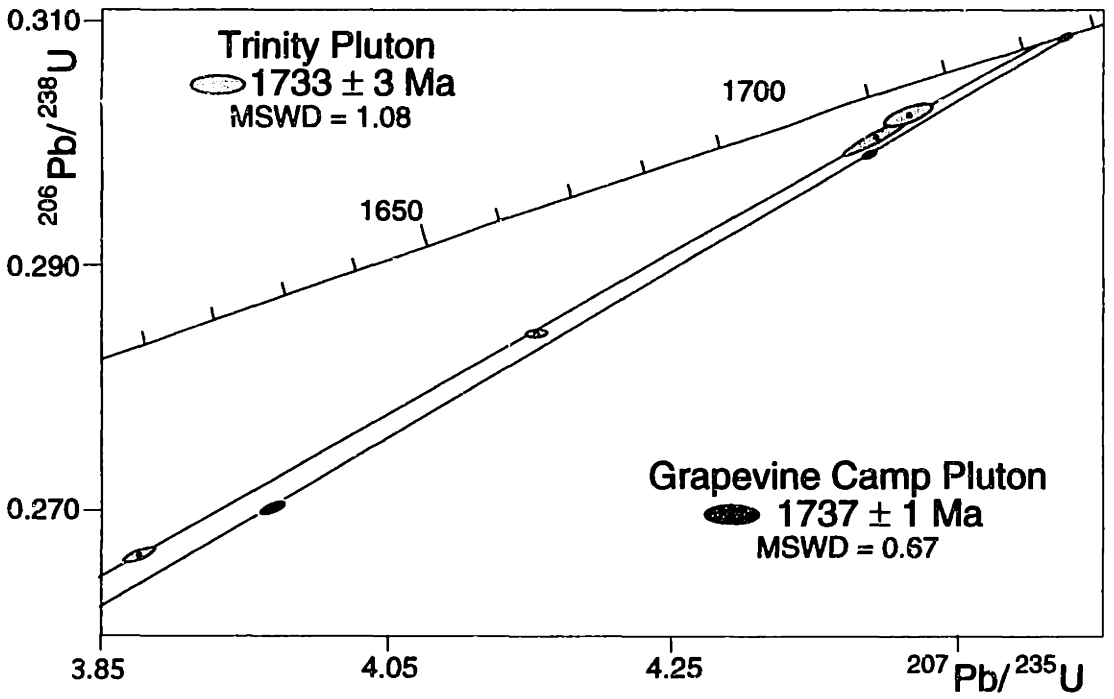
Trinity Pluton
1733 ± 3 Ma
MSWD = 1.08
1700
1650
Grapevine Camp Pluton
1737 ± 1 Ma
MSWD = 0.67
0.310
0.290
0.270
206Pb/238U
3.85
4.05
4.25
207Pb/235U

Figure 9

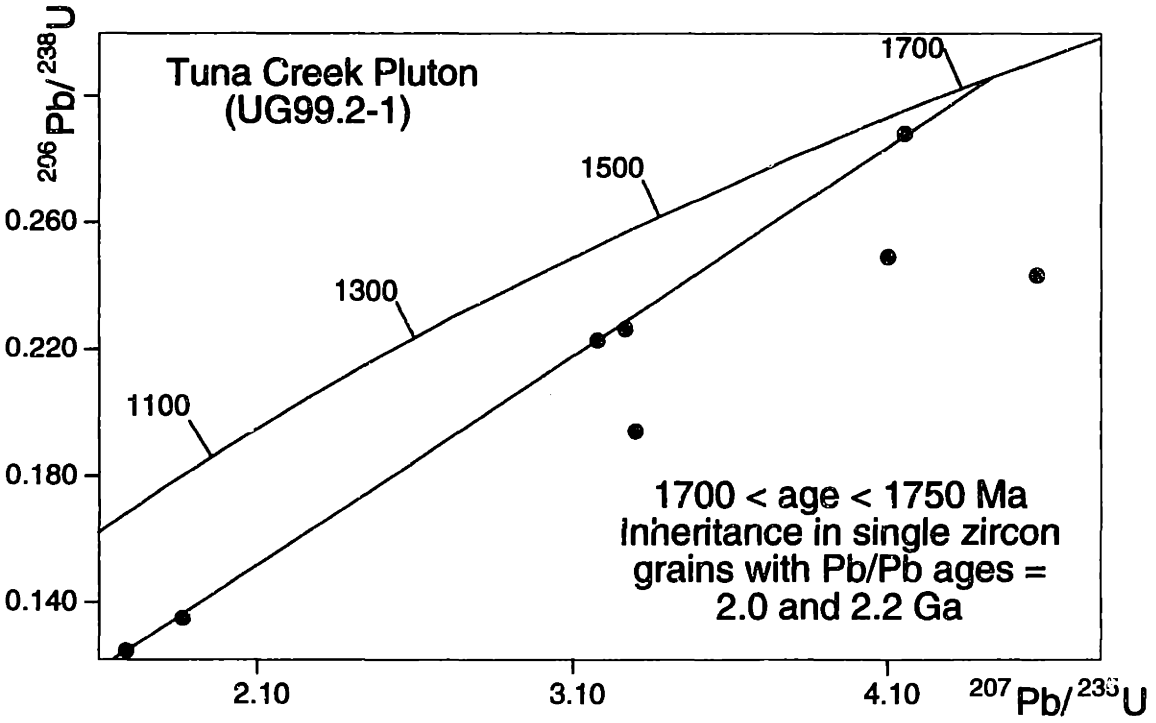
Tuna Creek Pluton
(UG99.2-1)
1700
1500
1300
1100
0.260
0.220
0.180
0.140
2.10
3.10
4.10
206Pb/238U
207Pb/235U
1700 < age < 1750 Ma
Inheritance in single zircon
grains with Pb/Pb ages =
2.0 and 2.2 Ga

Figure 10

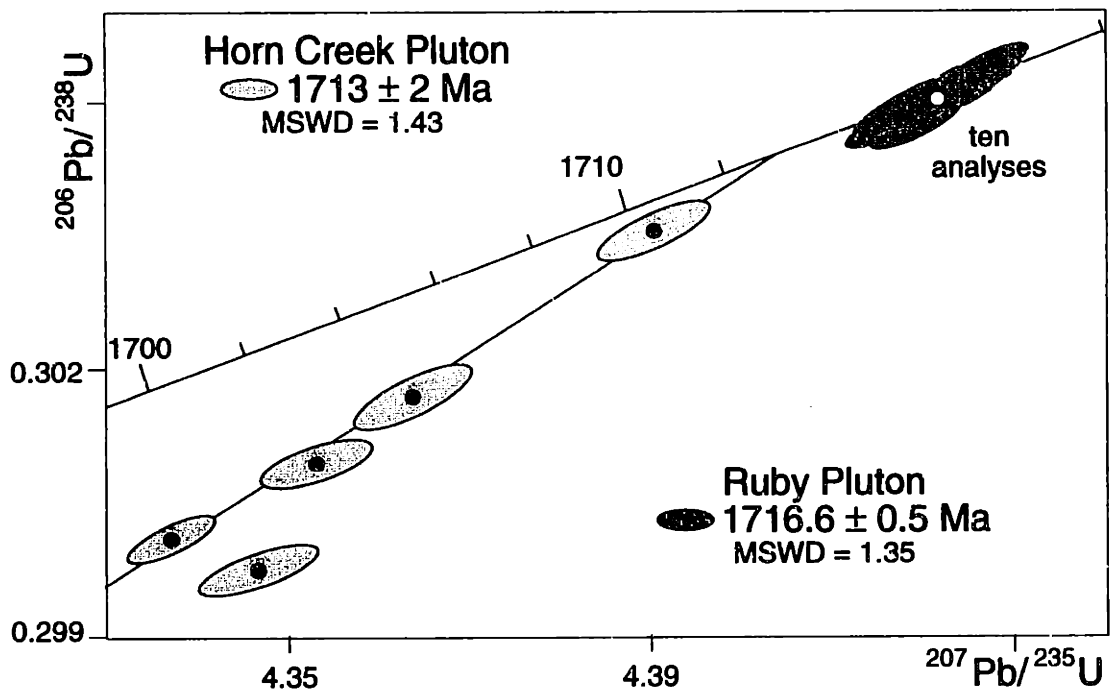
Horn Creek Pluton
1713 ± 2 Ma
MSWD = 1.43
ten
analyses
1710
1700
0.302
0.299
Ruby Pluton
1716.6 ± 0.5 Ma
MSWD = 1.35
4.35
4.39
$^{206}Pb/^{238}U$
$^{207}Pb/^{235}U$

Figure 11

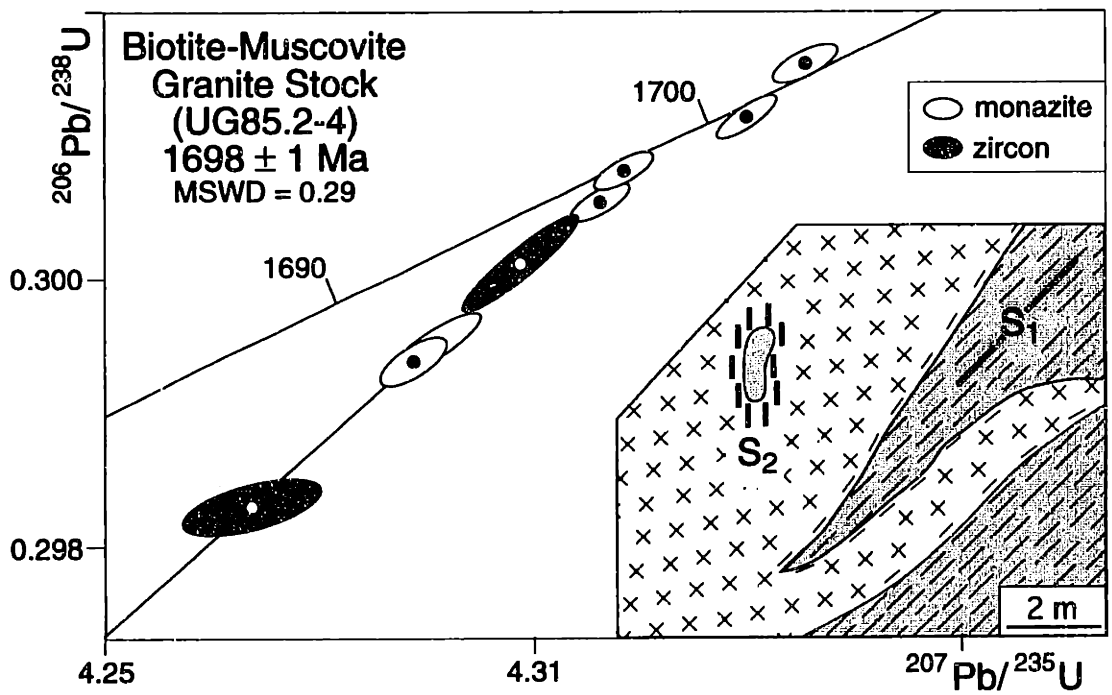
Biotite-Muscovite
Granite Stock
(UG85.2-4)
1698 ± 1 Ma
MSWD = 0.29
1700
1690
monazite
zircon
S_1
S_2
2 m
0.300
0.298
4.25
4.31
$^{206}Pb/^{238}U$
$^{207}Pb/^{235}U$

Figure 12

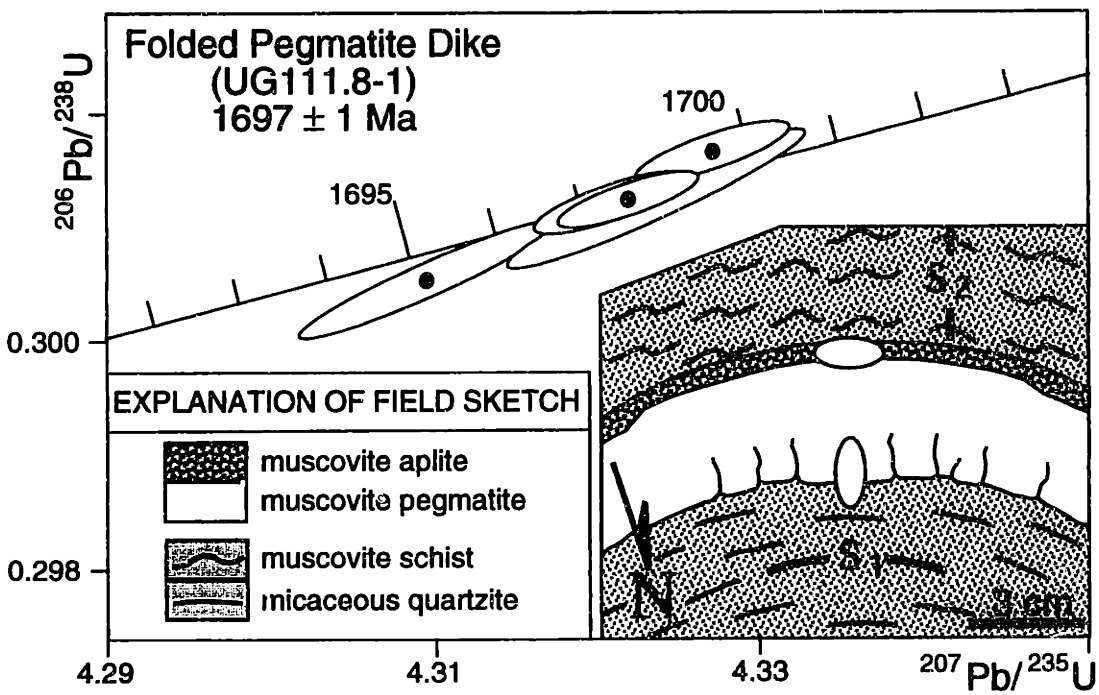
Folded Pegmatite Dike
(UG111.8-1)
1697 ± 1 Ma
1700
1695
0.300
0.298
206Pb/238U
EXPLANATION OF FIELD SKETCH
muscovite aplite
muscovite pegmatite
muscovite schist
micaceous quartzite
S2
S1
N
1 cm
4.29
4.31
4.33
207Pb/235U

Figure 13

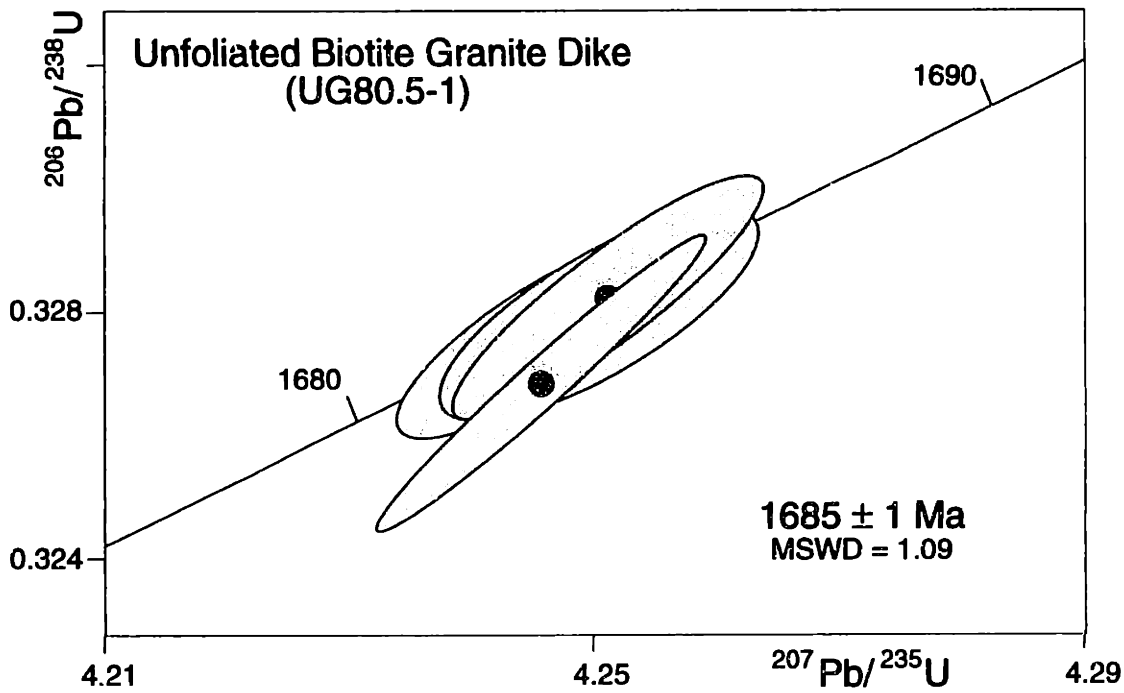
Unfoliated Biotite Granite Dike
(UG80.5-1)
1690
1680
1685 ± 1 Ma
MSWD = 1.09
0.328
0.324
4.21
4.25
4.29
206Pb/238U
207Pb/235U

Figure 14

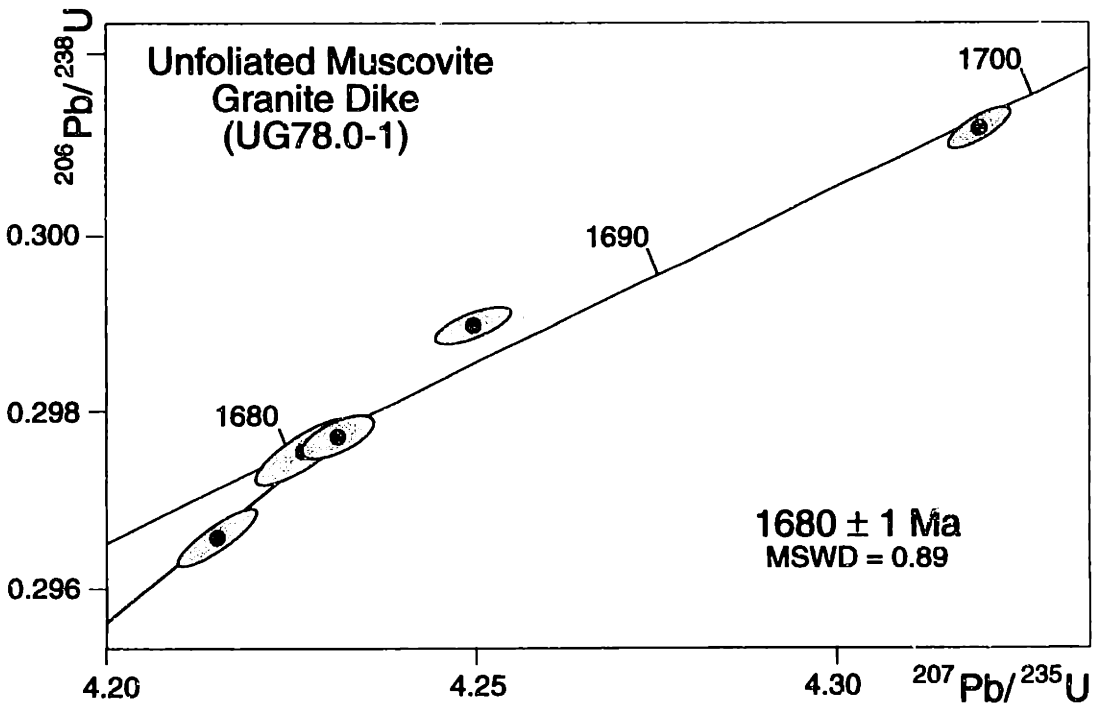
Unfoliated Muscovite
Granite Dike
(UG78.0-1)
1700
1690
1680
1680 ± 1 Ma
MSWD = 0.89
0.300
0.298
0.296
4.20
4.25
4.30
206Pb/238U
207Pb/235U

Figure 15

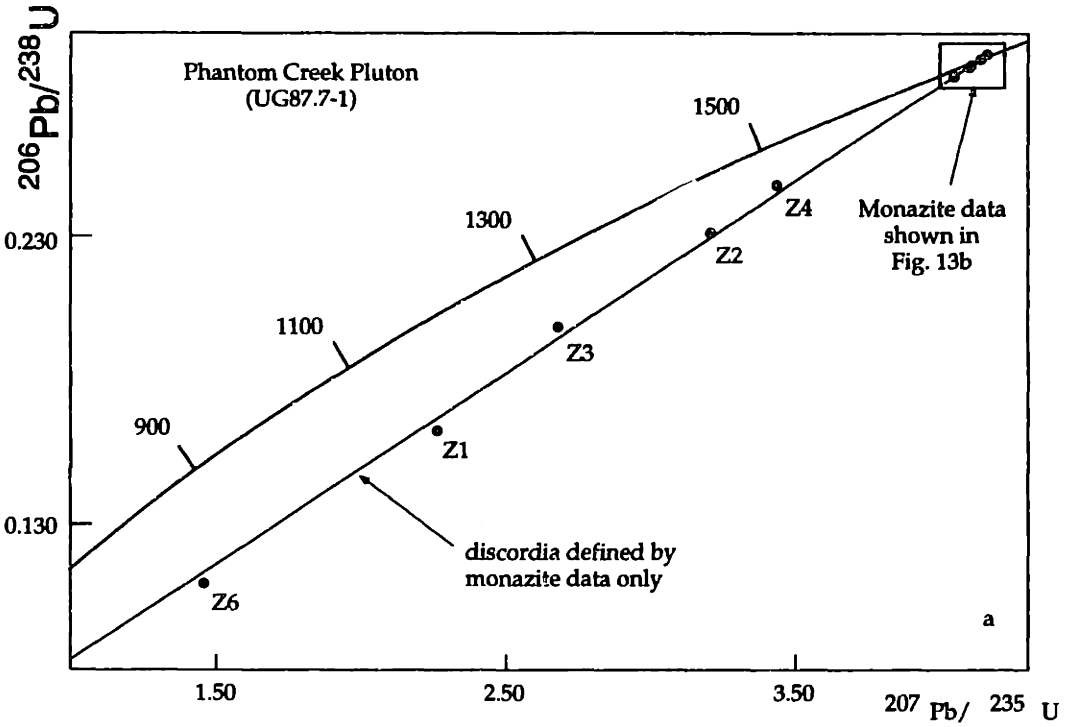
Phantom Creek Pluton
(UG87.7-1)
1500
1300
1100
900
Z4
Z2
Z3
Z1
Z6
Monazite data
shown in
Fig. 13b
discordia defined by
monazite data only
a
0.230
0.130
1.50
2.50
3.50
207 Pb/ 235 U
206Pb/238U

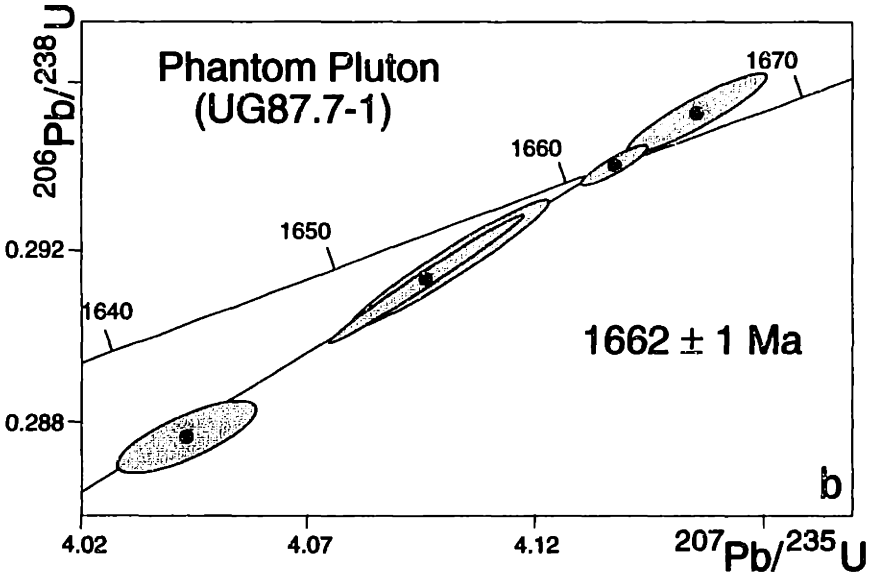
Phantom Pluton
(UG87.7-1)
1670
1660
1650
1640
1662 ± 1 Ma
b
0.292
0.288
4.02
4.07
4.12
207Pb/235U
206Pb/238U

Figure 16

Sample Numbers
84.2-4
79.6-1
84.9-1
81.2-3
109.9-1
91.5-1
104.3-4
90.6-2
111.8-1
85.2-4
80.5-1
78.0-1
87.7-1
Peraluminous Granite Magmatism
Prograde to Peak Metamorphism
six single-crystal monazite Pb-Pb dates from 79.6-1
Group 2 Fabrics and Structures
Group 1 Fabrics
Mafic to Inter-mediate Plutonism
Sedimentation & Volcanism
monazite ages
zircon ages
1.76
1.74
1.72
1.70
1.68
1.66
Age (Ga)

Figure 17

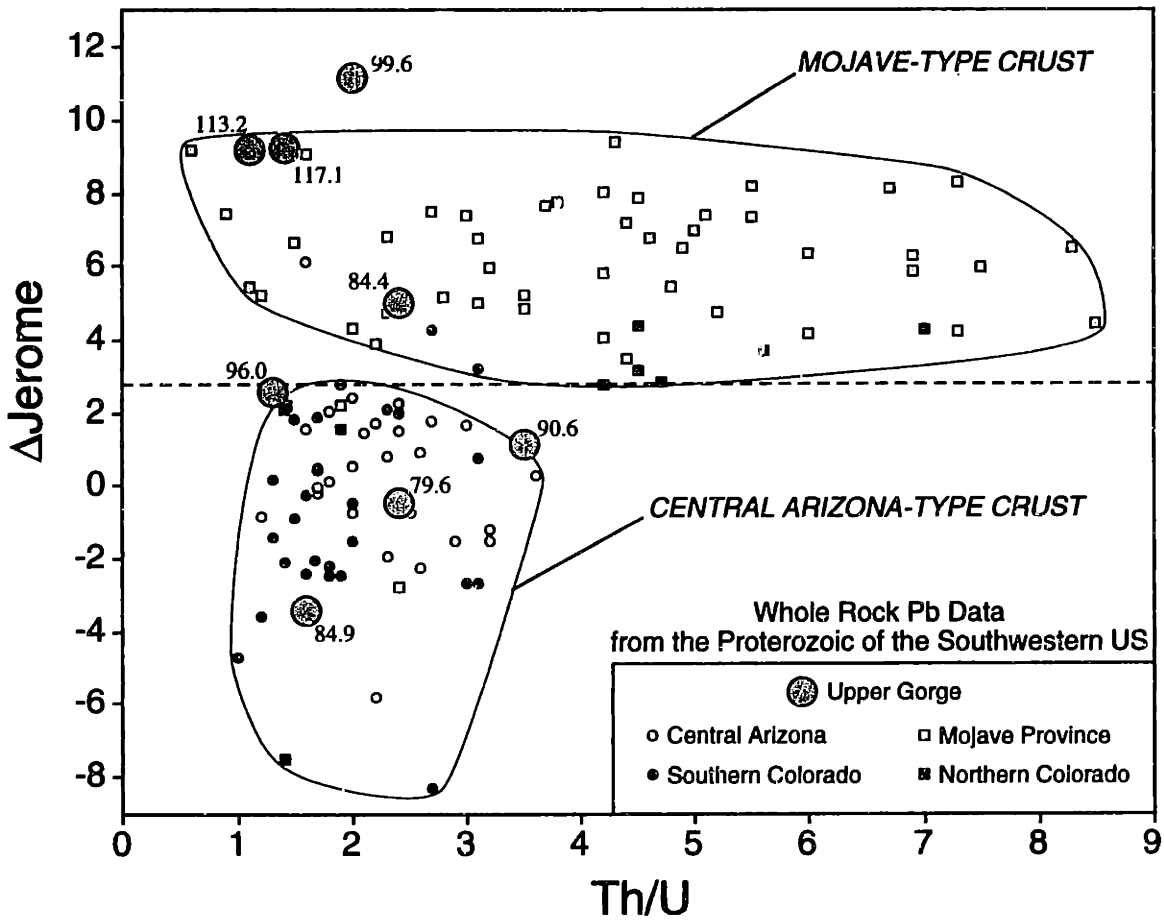
MOJAVE-TYPE CRUST
CENTRAL ARIZONA-TYPE CRUST
99.6
113.2
117.1
84.4
96.0
90.6
79.6
84.9
Whole Rock Pb Data
from the Proterozoic of the Southwestern US
Upper Gorge
Central Arizona
Mojave Province
Southern Colorado
Northern Colorado
ΔJerome
Th/U
12
10
8
6
4
2
0
-2
-4
-6
-8
0
1
2
3
4
5
6
7
8
9

Figure 18

CHAPTER 3

A CASE STUDY OF MONAZITE (AND XENOTIME) U-PB SYSTEMATICS FROM THE PALEOPROTEROZOIC OF THE GRAND CANYON, ARIZONA

ABSTRACT

Monazite is widely accepted as an important U-Pb geochronometer in metamorphic terrains because it potentially preserves prograde crystallization ages. However, recent studies have shown that the U-Pb isotopic system in monazite can be influenced by a variety of processes that partially obscure the early growth history. In this paper, we attempt to interpret complex monazite and xenotime U-Pb data from three Paleoproterozoic granite dikes exposed in the Grand Canyon. Single crystal monazite analyses from an unfoliated granite dike spread out along concordia from the crystallization age of the dike (defined by U-Pb zircon data to be 1685 ± 1 Ma) to 1659 ± 2 Ma, a span of 26 m.y. Back-scattered electron (BSE) imaging reveals that magmatic domains within most crystals from this sample are truncated by secondary domains associated with prominent embayments at the grain margin. Fragments of a single crystal yield contrasting, concordant dates and fragments from the edges and tips of crystals yield the youngest dates. Based on these observations we suggest that the secondary domains formed at least 26 m.y. after the crystal formed. Monazite and xenotime dates from the second sample, a sheared dike that cross-cuts the previous dike, spread out along concordia over 16 m.y. and range up to 2.4 % normally discordant. Again, BSE imaging reveals secondary domains that truncate both magmatic zoning and xenocrystic cores. Fragments sliced from specific domains of a previously imaged monazite crystal demonstrate that the secondary domain is 13 m.y. younger than the core domain.

Textures revealed in BSE images suggest that the secondary domains formed by fluid-mineral interaction. Normal discordance appears to result from both radiation damage accumulated at temperatures below 300 °C and water-mineral interaction. Monazite data from the third sample exhibit dispersion in both the Pb-Pb dates (1677 to 1690 Ma) and discordance (+ 1.6% to - 3.1%). Reverse discordance in these monazites cannot be explained by incomplete dissolution or excess (thorogenic) ^{206}Pb. Sliced fragments from several crystals reveal dramatic intragrain U-Pb disequilibrium that does not correlate with either Th or U concentration or position within the crystal. We suggest that reverse discordance resulted from mechanisms that involve exchange or fractionation of elemental U or elemental Pb, and that neither the U-Pb dates or the Pb-Pb dates are reliable indicators of the rock's crystallization age. Given the large number of processes proposed in the recent literature to explain monazite U-Pb systematics from rocks of all ages, our results can be viewed as another cautionary note for single-crystal and multi-crystal monazite geochronometry. However, we suggest that because individual crystals can preserve a temporal record of primary and secondary monazite growth, micro-sampling of individual monazite crystals may provide precise absolute ages on a variety of processes that operate during the prograde, peak and/or retrograde history of metamorphic terrains.

INTRODUCTION

An important goal of tectonic studies is to determine the rates and duration of the processes that operate during orogenesis. Processes such as heat transfer, ductile deformation, anatexis and metamorphic mineral reactions operate over 10^6 to 10^8 years, and absolute ages with uncertainties of ± 1 m.y. or less are required to resolve their timing and interdependence (e.g., Zeitler, 1989). Absolute ages determined by U-Pb

geochronology are both reliable and precise: isotope dilution thermal ionization mass spectrometric (IDTIMS) analysis of geochronometers such as zircon and monazite can achieve analytical uncertainties of better than 0.15% for U-Pb dates and better than 0.1% for Pb-Pb dates. In many cases, the high analytical precision results in crystallization ages for metamorphic and igneous rocks with uncertainties of ± 1 m.y. In other cases, however, the high analytical precision reveals variation in the Pb-Pb dates of different crystals from the same rock that exceed the uncertainty of the individual analyses. Understanding this variation depends largely on our knowledge of the paragenesis of the minerals used to determine the ages and the factors that control and influence the U-Pb isotopic systematics of those minerals.

The U-Pb geochronometers most widely used in moderate- to high-grade metamorphic terrains are zircon, sphene and monazite. Of these, monazite is particularly important because it grows as a metamorphic mineral over a broad stability range (e.g., Overstreet, 1967; Smith and Barreiro, 1990), and retains U-Pb isotopic signatures up to about 725 °C (Copeland et al., 1988; Parrish, 1990). As such, U-Pb dates from monazite provide the opportunity to bracket the timing of not only the thermal peak of metamorphism, but also some segment of the prograde pressure-temperature path. Monazite also occurs as an accessory phase, often with xenotime (YPO_4), in peraluminous granitoids, dikes of which generally provide key timing constraints on structures and fabrics. However, zircons from peraluminous granites tend to be complicated by both inheritance and Pb loss (Harrison and Watson, 1983; Parrish, 1990), thus monazite and xenotime geochronology provide the best opportunity to determine crystallization ages on these rocks.

Although monazite tends to yield concordant U-Pb dates (e.g., Parrish, 1990), recent studies show that a variety of primary and secondary processes can influence the age and discordance of monazite U-Pb dates. Primary processes include: 1) growth on

xenocrystic nuclei resulting in inheritance (Copeland et al, 1988; Aleinikoff and Grauch, 1990; Parrish, 1990; Suzuki and Adachi, 1991; 1994; Smith et al., 1992; Childe et al., 1993; Kingsbury et al., 1993; Suzuki et al., 1994); 2) protracted or episodic growth (Parrish, 1990; Lanzirotti and Hanson, 1995; Hawkins and Bowring, 1995a,b); 3) high-temperature diffusive Pb loss near the closure temperature interval (Parrish and Tirrul, 1989; Parrish, 1990; Krogh and Moser, 1994); and 4) U-Th disequilibrium, resulting in reverse discordance (Schärer, 1984; Schärer, et al., 1986). Secondary processes include: 1) fluid-mineral interaction (Black et al, 1984; Parrish, 1990; DeWolf et al, 1993); 2) secondary overgrowth or hydrothermal growth (Aleinikoff and Grauch, 1990; DeWolf et al., 1993; Davis et al., 1994); and 3) Pb loss (Parrish and Carr, 1993; Harrison et al., 1995); and 4) deformation (Getty and Gromet, 1992; Krogh and Moser, 1994). Given the large number of processes that can potentially influence the U-Pb isotopic system in monazite, monazite U-Pb data may be complicated and difficult to interpret.

This paper is a summary of our attempts to decipher complex monazite and xenotime U-Pb data from three Paleoproterozoic peraluminous granite intrusions in the Grand Canyon. Our study is an outgrowth of a larger effort to characterize the absolute timing and duration of fabric development, magmatism and metamorphism on a regional scale. The crystallization ages of these granite intrusions contribute to the broader goal by bracketing the timing of deformation and metamorphism locally. Despite an aggressive analytical strategy, however, the data from these samples did not yield precise monazite or xenotime crystallization ages because the U-Pb analyses from individual samples yielded variably discordant U-Pb dates with contrasting Pb-Pb dates. The purpose of this paper is to evaluate the processes that influenced the U-Pb systematics of monazite and xenotime in these rocks by combining field observations, petrography, back-scattered electron (BSE) imaging, compositional data and U-Pb data from micro-samples of previously imaged monazite and xenotime crystals. Our results indicate that

the U-Pb isotopic system in these monazites have been affected by a variety of primary and secondary processes over a wide temperature range that partially or wholly obscure the crystallization ages.

GEOLOGIC BACKGROUND

The Upper Granite Gorge of the Grand Canyon exposes ca. 1750 Ma metasedimentary and metavolcanic supracrustal rocks intruded by 1710 - 1740 Ma mafic- to intermediate-composition plutonic rocks, which together comprise the remnants of a magmatic arc (Fig. 1; Ilg et al., 1996b; Hawkins et al., 1996). The rocks contain multiple generations of fabrics and structures (Ilg et al., 1996b) and preserve metamorphic field gradients comprised of lower amphibolite to lower granulite facies mineral assemblages (Ilg et al., 1996b). Peraluminous granitic magmatism was associated in time and space with deformation but largely post-dated development of peak metamorphic mineral assemblages (Hawkins et al., 1996). Preliminary thermochronology (Hawkins and Bowring, unpublished data) and P-T path determination (Williams, 1994) suggest that, following a short period of relatively rapid cooling, the rocks in the eastern Upper Gorge underwent an extended period of relatively slow cooling until unroofing and near-surface residence by about 1250 Ma (e.g., Elston, 1989). The rocks remained at shallow crustal levels, at temperatures below about 250 °C, until late Cenozoic uplift and of the Colorado Plateau (e.g., Naeser and Elston, 1987) when the rocks were exposed at the surface.

SAMPLE DESCRIPTIONS

We present U-Pb data from three samples collected from two exposures in the eastern part of the Upper Granite Gorge; two samples from river mile 78.0 and one sample from river mile 85.6 (Fig. 1). The exposure at river mile 78.0 (Fig 1a) comprises

ca. 1740 Ma metasedimentary rocks (Vishnu schist) intruded by variably deformed 1680 to 1685 Ma granite and pegmatite dikes (Hawkins et al., 1996). The migmatitic metasedimentary rocks yielded U-Pb monazite dates that Hawkins and Bowring (1995a,b) interpreted to bracket the timing of peak metamorphism between 1710 and 1685 Ma. Peak metamorphic conditions in this part of the Upper Gorge are approximately 700 °C and 6 kbars (Ilg et al., 1996b). The granite and pegmatite dikes and unfoliated dikes cross-cut compositional layering, foliation, isoclinal folds and leucosomal pegmatite (Hawkins et al., 1996).

The first sample from river mile 78.0 (sample UG78.0-5) was collected from a one meter wide dike composed of medium-grained, equigranular muscovite-biotite granite. The dike cross-cuts both compositional layering and foliation and contains partially disaggregated, randomly-oriented xenoliths of foliated quartzofeldspathic gneiss and migmatitic schist, indicating the dike post-dated both the peak of metamorphism and fabric development in the adjacent schists and gneisses. The granite is unfoliated and the margins are not strained. Biotite within the dike is partially replaced by chlorite and hematite occurs along many grain boundaries.

The second sample from mile 78.0 was collected from a 2.5-meter-wide muscovite - biotite granite dike containing a sheared interior (UG78.0-2A,B). The dike grades from a medium-grained, equigranular unsheared granite at the margin (UG78.0-2B) to a medium-grained, inequigranular sheared granite in the interior (UG78.0-2A). The sheared granite is deformed along discrete, anastomosing shear planes spaced 1-3 cm apart. We interpret the strain gradient within the dike to indicate that shearing occurred prior to final crystallization, such that the partially molten interior of the dike accumulated strain preferentially to the solidified margin of the dike. There is no evidence for multiple intrusion within the dike, and dikes with similar orientations in this part of the transect (mile 78.0 to mile 80.5) also contain internal shear zones. Biotite is replaced by chlorite

throughout the dike, suggesting alteration occurred in the presence of fluids at temperatures below the granite solidus.

The third sample (UG85.6-2) was collected at river mile 85.6 from a muscovite-garnet pegmatite stock that intrudes interlayered biotite - amphibole schist and amphibolite (Brahma schist) on the west margin of the 1740 Ma Zoroaster granite (Fig. 1c; Ilg et al., 1996b; Hawkins et al., 1996). The pegmatite stock exhibits centimeter-scale high-strain zones, cuspate-lobate folds along the contacts, and alignment of coarse-grained muscovite books locally.

ANALYTICAL TECHNIQUES

Monazite and xenotime were separated by standard crushing, heavy liquid and magnetic techniques. Individual crystals, some of which were air abraded (Krogh, 1982), were measured, photographed and washed in acetone and warm H_2O prior to dissolution. Samples were dissolved in 300 µl teflon nanocapsules containing 11 - 12 N HCl and a mixed ^{205}Pb-^{233}U-^{235}U tracer solution in two 30- to 48-hour steps at 180 °C. Lead and uranium were separated using HCl-based ion chromatography procedures modified after Krogh (1973). The samples were analyzed using conventional thermal ionization mass spectrometry on a VG Sector 54 mass spectrometer at the Massachusetts Institute of Technology. Lead was analyzed either: 1) in static mode, using Faraday detectors for all isotopes except ^{204}Pb, which was measured simultaneously with the Daly detector in ion counting mode; or 2) by peak-jumping using a Daly detector in ion counting mode. Uranium was analyzed as a metal in static mode using Faraday collectors. The linear regression of zircon data from the unfoliated granite dike was generated using the model 1 algorithm of Ludwig (1989). Additional analytical details are presented in Table 1.

Some of the U-Pb dates presented in this paper exhibit dramatic normal or reverse discordance. For consistency, we describe the magnitude of both normal and reverse discordance as a percentage of the total distance from the origin to concordia at the Pb-Pb date . This approach is equivalent to measuring discordance as the difference between the $^{207}Pb/^{206}Pb$ date and $^{206}Pb/^{238}U$ date. As such, we refer to reversely discordant dates as having negative discordance and normally discordant dates as having positive discordance. Detailed discussions of discordance are presented in the U-Pb geochronology section for the sheared granite dike (sample UG78.0-2A,B) and for the deformed pegmatite stock (sample UG85.6-2).

To investigate intracrystalline variations in the U-Pb systematics of both monazite and xenotime, we sliced several crystals into fragments, carefully recording the original spatial relationships, and analyzed the fragments separately. These analyses are identified in Table 1 by a lower case letter at the end of the fraction name and are shown along with drawings of the crystals in Figures 2, 4 and 10. Our slicing technique produces fragments as small as 20 x 10 x 10 μm (≈ 100 ng total sample weight)— similar to the dimensions of the pit produced by an ion probe analysis (e.g., DeWolf et al., 1993; Harrison, et al., 1995) — that yield analytical uncertainties (2σ) of better than 0.4% for the U-Pb dates and 0.25% for the Pb-Pb date (see fractions M37c and M39c in table 1). The fourteen fragment analyses from the pegmatite stock (sample UG85.6-2) have absolute common Pb contents (4.4 to 37.0 pg) that are similar to the absolute common Pb contents of whole grain and random fragment analyses (4.8 to 59.1). Furthermore, the uranogenic Pb to common Pb ratios of all but two of the sliced fragment analyses (M37c = 6 and M37b = 14) range from 19 to 396, indicating that the common Pb correction for these analyses is not significant.

Back-scattered electron (BSE) imaging was carried out on a JEOL Superprobe 733 at the Massachusetts Institute of Technology operating at an accelerating voltage of 15 to 20 kV and a beam current of 10 to 15 nA. The images reveal internal compositional variations that reflect differences in the average atomic number (Z) of the material (e.g., Fig. 3). Areas of a crystal with higher average Z appear brighter than areas with lower average Z. Based on several quantitative electron microprobe analyses on Grand Canyon monazites (John Hanchar, personal communication) we determined that differences in average Z of monazites from the Grand Canyon largely reflect variations in the concentration of the LREE, Th and U.

U-PB GEOCHRONOLOGY

Unfoliated Granite Dike

Both zircon and monazite were recovered from a sample of the unfoliated granite dike (sample UG78.0-5). We began by analyzing the monazites to avoid problems of inheritance and discordance typical of zircon U-Pb data from peraluminous granites (e.g., Parrish, 1990). Monazites from this sample are yellow, euhedral to subhedral crystals with equant morphologies. The ten fractions analyzed yielded nearly concordant (+ 0.15% to - 0.15% discordant) U-Pb dates with Pb-Pb dates that span 24 m.y., from 1659 ± 2 to 1683 ± 1 Ma (Table 1 and Figure 2). The youngest Pb-Pb date corresponds to the tip of a euhedral crystal (M11), whereas the two oldest Pb-Pb dates are from a random fragment (M10) and the core region of a sliced crystal (M9a). Analyses of two whole single crystals (M8, M17), two random fragments (M4, M16), an air abraded crystal (M3), the rim of a euhedral crystal (M18) and a second fragment sliced from the core region of a single crystal (M9b) yielded intermediate Pb-Pb dates (1668 ± 2 to 1679 ± 1 Ma). There is no correlation between the Pb-Pb dates and either U concentration or

Th/U ratio. These data indicate that both different crystals and different domains within individual crystals preserve contrasting age information and, without independent constraints, the crystallization age of the dike is not apparent.

Two related questions arise from the monazite results: 1) which, if any, of the monazite dates represents the crystallization age of the unfoliated dike?; and 2) what is the origin of the dispersion of monazite dates along concordia? To answer the first question we analyzed zircon, despite the potential complications. Five single-crystal fractions, composed of clear, euhedral, subequant to prismatic crystals yielded normally discordant (+0.7 to +7.7 %) U-Pb dates with Pb-Pb dates ranging from 1685 to 1704 Ma (Table 1; Fig.2a). The oldest fraction (Z7) is interpreted to be a physical mixture of magmatic zircon and xenocrystic zircon that underwent minor post-crystallization Pb loss. The remaining fractions have identical Pb-Pb dates and define an upper intercept age of 1685 ± 1 Ma (MSWD = 0.72; lower intercept = -25 ± 40 Ma), which we interpret as the crystallization age of the dike.

In addition to yielding the crystallization age, the zircon data provide an independent constraint on possible explanations for the age dispersion in the monazite data. Only two of the monazite dates (M9a and M10) overlap with the upper intercept age. Most of the monazite dates are younger than 1685 Ma, indicating that the age dispersion resulted from a post-crystallization process(es). One possibility, given that the peak metamorphic temperature (ca. 725 °C) was close to the nominal closure temperature of monazite (725 ± 25 °C), is that the monazites underwent high temperature Pb loss and therefore preserve cooling ages. Minerals that yield cooling ages formed above their closure temperature, which for monazite is defined by Pb diffusion, and resided at or above the closure temperature for a protracted time interval (Dodson, 1973; 1979). We cannot use the monazite data from the unfoliated granite dike to evaluate this hypothesis because most of the data were obtained from crystal fragments. However,

several lines of evidence argue against high temperature Pb loss. First, crystallization ages, spanning 30 m.y. of the prograde to post-peak thermal history, based on monazite dates from seven samples of migmatitic supracrustal rocks and cross-cutting dikes in this outcrop are all consistent with the field observations (Hawkins et al., 1996; Hawkins and Bowring, 1995a,b; unpublished data). Second, monazite and xenotime from the sheared granite dike (discussed below) do not preserve cooling ages.

A second possible explanation for the spread in monazite dates is that the magmatic monazites were variably overgrown, replaced or reset at approximately 1659 Ma, the Pb-Pb date of the youngest grain. To evaluate this hypothesis, we obtained BSE images of thirteen monazite grains. All of the crystals preserve a relatively low-Th, sector-zoned core domain surrounded by a relatively high-Th rim domain. The rim domain is characterized by oscillatory-zoning parallel to rational crystal faces (Fig. 3a-d). In some grains, the sector-zoned core domains were slightly resorbed prior to crystallization of the oscillatory-zoned rims. We interpret the sector-zoned core domains and the rim domains to reflect primary growth zones that formed during crystallization from the granitic melt. In most of the crystals we imaged, the magmatic domains are truncated by irregular, heterogeneous domains that invariably occur at the edge of the crystal. Based on these textures, we interpret these domains to reflect late- or post-magmatic development of secondary monazite. Since a crystal termination (M11) yielded the youngest date (1659 Ma), we suggest that the secondary domain formed either episodically after 1659 Ma or perhaps during a protracted interval between 1685 Ma and sometime after 1659 Ma.

A closer look at the BSE images provides insight into the origin of the secondary domains. In each of the crystals we imaged, the grain margin adjacent to the secondary domain is embayed (Fig. 3c,d). Detailed petrography reveals that prominently embayed crystals are restricted to the interstices of the rock, whereas euhedral crystals, lacking

evidence for resorption, occur as inclusions in quartz and feldspar. This relationship suggests that the secondary domains resulted from fluid-mineral interaction: monazite crystals that resided along grain boundaries in the rock were exposed to fluids, whereas monazite crystals occluded by other phases were protected from fluid interaction. Thus, both individual crystals and random fragments are physical mixtures of primary and secondary growth domains. Similar observations have been reported from monazites by DeWolf et al. (1993).

The 24 m.y. spread in concordant U-Pb monazite dates (1659 to 1683 Ma) appears to reflect fluid-mineral interaction that occurred or persisted from 1685 to sometime after 1659 Ma. This interpretation is consistent with the following observations: 1) alteration of biotite to chlorite within the unfoliated dike and locally in the surrounding biotite-sillimanite schist; 2) textural evidence for late or post-magmatic development of secondary monazite domains that truncate primary igneous growth zones; 3) residence of embayed crystals in the interstices between the rock-forming minerals (i.e., along fast fluid pathways); and 4) contrasting Pb-Pb dates within a single crystal of monazite (fractions M9a,b; Fig. 2b). We see no evidence for inheritance, protracted magmatic crystallization, deformation or high-temperature Pb loss, although we cannot rule out the possibility that more than one process was involved.

Sheared Granite Dike

Monazite and xenotime were separated from both the deformed interior (sample UG78.0-2A) and the undeformed margin (sample UG78.0-2B) of the sheared granite dike (Fig.1). Monazite occurs as yellow, euhedral, equant to prismatic crystals, and xenotime occurs as yellow, dipyramidal crystals. The crystal morphology of grains from the two samples are identical, although both monazite and xenotime crystals from the center of the dike are generally larger.

We analyzed a total of twelve monazite crystals and eight xenotime crystals from these two samples (Table 1; Figure 4). Eight analyses yielded concordant U-Pb dates with Pb-Pb dates ranging from 1667 ± 1 Ma to 1683 ± 1 Ma, and twelve analyses yielded normally discordant (0.1% to 3.5%) U-Pb dates with Pb-Pb dates ranging from 1664 ± 1 Ma to 1681 ± 1 Ma (Fig. 4). Monazite and xenotime from the sheared interior show a greater spread in Pb-Pb dates and more extensive discordance than monazites and xenotimes from the unsheared dike margin, although fewer analyses were obtained from the latter. The discordant data do not define a single statistically significant discordia, and without independent constraints, the crystallization age of the dike cannot be interpreted from these data.

Collectively, the data from this dike present two related problems: a spread of concordant dates that spans 16 m.y. (1667 to 1683 Ma), and variable normal discordance (up to 3.5%). We first consider the spread in Pb-Pb dates along concordia for which we have an important constraint. As shown in Figure 1, the sheared dike must be younger than 1685 ± 1 Ma because it crosscuts the 1685 Ma granite unfoliated dike (sample UG78.0-5). Therefore, of the possible explanations for the spread in Pb-Pb dates, four are likely: high temperature Pb loss; inheritance; dynamic recrystallization; and secondary overgrowth or recrystallization. Distinguishing between these explanations is critical because each can lead to different interpretations of the crystallization age of the dike.

High temperature Pb loss can be evaluated directly from the monazite data by examining the relationship between grain size and age for each crystal analyzed. The diffusion studies of Suzuki et al. (1994) and Smith and Giletti (1995) suggest that the effective diffusion dimension (with respect to Pb diffusion) in monazite is equivalent to the size of the crystal. Therefore, if diffusive Pb loss controls the dispersion in concordant dates, then larger crystals should preserve older dates than smaller crystals

and the data should vary predictably for a given cooling rate (e.g., Dodson, 1973; 1979; Cherniak, 1993; Suzuki et al., 1994). Using the closure temperature equation (Dodson, 1973) and the diffusion data of Smith and Giletti (1995), we calculated the predicted curves for grain size as a function of 'cooling age' for several cooling rates (Fig. 5). The calculation assumes a spherical diffusion geometry, a magma temperature of 725 °C and a crystallization age for the dike of 1685 Ma. As shown in figure 5, the data do not exhibit the predicted behavior, suggesting that factors other than high temperature Pb loss must have contributed to the spread in mineral dates observed in these monazites. This result is independent of the diffusion parameters used in the calculation, because different sets of diffusion parameters produce curves with similar shapes (Fig 5). Likewise, the general shape of the curve is insensitive to the choice of diffusion geometry, crystallization age and magma temperature.

To distinguish between inheritance and secondary processes (dynamic recrystallization and secondary replacement), we analyzed fragments of crystals previously imaged at high magnification by BSE. The BSE images reveal three types of monazite and xenotime crystals which we interpret as: 1) magmatic crystals lacking xenocrystic cores (Fig. 3e); 2) magmatic crystals containing xenocrystic cores of either igneous or metamorphic origin (Fig. 3f); and 3) magmatic crystals that were partially replaced by a second generation of monazite (Fig. 3g). Most of the crystals we examined preserve fine-scale zoning patterns, indicating that these grains were not dynamically recrystallized during shearing. Two sliced fragments of the crystal shown in Fig. 3f (fraction B-X3; Table 1 and Fig. 4b) yielded identical Pb-Pb dates (1680 ± 1 Ma) indicating that either: the core and rim domains have resolvable age differences and were present in the same relative proportions; the core is xenocrystic and it's U-Pb isotopic system was reset; or the core and rim domains have indistinguishable ages.

Two fragments from the monazite crystal shown in Fig. 3g (fraction B-M11) yielded contrasting Pb-Pb dates (Table 1 and Fig. 4b). The fragment collected from an area with a high proportion of core domain (B-M11a) yielded slightly discordant U-Pb dates and a Pb-Pb date of 1685 ± 1 Ma, whereas the fragment collected from the rim domain (B-M11d) yielded a concordant date of 1670 ± 2 Ma. The Pb-Pb date of the fragment from the core domain (B-M11a) is indistinguishable from the crystallization age of the unfoliated granite dike that the sheared dike cross-cuts. However, the BSE image (Fig. 3g) shows that the core domain contained inclusions of sillimanite and biotite, suggesting that it contained an inherited metamorphic monazite (ca. 1700-1710 Ma; Hawkins and Bowring, 1995a,b). The micro-sample of the rim domain, which included material within 15 μm of the imaged surface, yielded a date that is 15 m.y. younger than that of the core domain. Considering the textures shown in Fig. 3g, the small sample size, and the contrasting dates yielded by core and rim, we conclude that the rim domain represents a distinct generation of monazite that formed at 1670 Ma. The simplest way to form the second generation is by dissolution and reprecipitation. We suggest that the spread in Pb-Pb dates exhibited by monazite and xenotime from the sheared dike appears to result from post-magmatic fluid-mineral interaction.

The crystallization ages of the magmatic and secondary components are only partly constrained. Fragment B-M11d was composed predominantly of rim domain and yet did not yield the youngest date. Thus, fluid-mineral interaction must have occurred over at least 3 m.y. between 1667 Ma, the youngest concordant date (A-M3), and 1670 Ma, the date yielded by fragment B-M11d. The crystallization age of the magmatic component is constrained to be between 1685 Ma, the age of the unfoliated granite dike, and 1670 Ma, the Pb-Pb date of the secondary domain from B-M11d. Because the fragments from crystal B-X3 yielded identical Pb-Pb dates (1680 ± 1 Ma) and the

fragment from the core domain of crystal B-M11 probably contained an inherited component, we estimate the crystallization age of the sheared dike to be 1682 ± 3 Ma.

The second problem presented by the U-Pb data from the sheared dike is the normal discordance exhibited by both monazite and xenotime. Although normal discordance is common in zircon U-Pb dates, numerous studies have shown that monazites, Precambrian monazites in particular, tend to yield concordant U-Pb dates (Holmes, 1954; Gulson and Krogh, 1973; Köppel and Grünenfelder, 1975; Parrish, 1990; Davis et al., 1994; Krogh and Moser, 1994). Discordance in zircon is generally attributed to enhanced Pb diffusion resulting from damage to the crystal lattice caused by the recoil of daughter nuclei during alpha particle emission in the decay series of ^{238}U, ^{235}U and ^{232}Th (e.g., Silver and Deutsch, 1963; Wasserburg, 1963; Goldich and Mudrey, 1972). Radiation damage of sufficient density ultimately transforms the zircon crystal lattice into a disordered, metamict state (Murakami et al., 1991). In contrast to zircon, metamict monazite is rare, even though monazite contains much higher concentrations of Th and U (Overstreet, 1967; Mitchell, 1973). This observation led to the proposed use of monazite as a mineral host for storing high-level nuclear waste (McCarthy et al., 1978; Floran et al., 1981; Roy and Vance, 1981), but subsequent laboratory studies showed that alpha recoil damage in the monazite is annealed at temperatures above about 300 °C (Karioris et al., 1981; Cartz et al., 1981; Ehlert et al., 1983). Thus, the apparent retentivity of monazite with respect to Pb appears to depend on the thermal history of the rocks; those rocks that resided at temperatures below 300 °C for extended periods of time should contain radiation damaged monazites exhibiting detectable Pb loss.

The normally discordant monazite and xenotime U-Pb dates from the sheared dike can be used to evaluate the enhanced Pb loss hypothesis described above. The rocks at river mile 78.0 were at the surface by about 1.2 Ga, when the overlying Grand Canyon Supergroup was deposited (Elston, 1989), and remained at temperatures below about

250 °C until the present (e.g., Naeser and Elston, 1987). Therefore, we would expect monazite and xenotime to have accumulated radiation damage, and, if the discordance in these monazites resulted from enhanced Pb loss resulting from radiation damage, the total Th and U concentration of each grain should correlate with the degree of U-Pb discordance. As shown in Figure 6a, seven monazite and xenotime analyses from the sheared center of the dike exhibit (to first-order) a positive correlation between the total Th and U concentration and discordance, whereas the three most discordant points show a first-order negative correlation. Thus, although monazite and xenotime data from the sheared interior of the dike reflect two different mechanisms for Pb loss, the majority of the data are consistent with Pb loss enhanced by radiation damage.

There are two problems with this interpretation. First, despite having identical total Th and U concentrations, not all of the monazites and xenotimes from the sheared dike are discordant. Second, only those monazites from foliated granite dikes at mile 78.0 exhibit normal discordance (Fig. 6b). These observations indicate that radiation damage is not sufficient for Pb loss; another mechanism is required that is crystal-specific and more efficient in foliated rocks than unfoliated rocks. We speculate that this mechanism involves water in a similar fashion to the dilatancy model of Pb loss in zircons (Goldich and Mudrey, 1972). We suggest that water accessed damaged domains of crystals along micro-fractures or micro-channels and mobilized Pb that had accumulated in damaged domains. The crystals that occupied impermeable sites in the rock escaped interaction with water and retained their Pb despite having damaged domains in the crystal lattice.

Two additional features of the data are noteworthy. First, despite containing 1 to 27 wgt% total Th and U and residence for over one billion years at temperatures below the nominal annealing temperature for alpha recoil damage, monazite U-Pb dates from mile 78.0 are no more than 2.4% discordant and not all of the crystals yield discordant dates. Perhaps the Pb retentivity of these monazites indicates that alpha recoil damage

in the monazite crystal lattice anneals at temperatures below 300 °C over geologic time scales, as suggested for zircon by Murakami et al. (1991) and for sphene by Cherniak (1993). Second, the similar age dispersion and discordance exhibited by monazite and xenotime suggest that xenotime and monazite have very similar U-Pb systematics, as suggested by Aleinikoff and Grauch (1990), Childe et al. (1993), and Sevigny and Hanson (1995).

Deformed Pegmatite Stock

A sample of the deformed pegmatite stock (UG85.6-2) yielded euhedral to subhedral monazite crystals ranging in size from 200 μm to 50 μm. Euhedral grains were either prismatic, equant or discoidal. subhedral had similar overall shapes, but were pitted, embayed and subrounded. Only clear, euhedral, inclusion-free crystals were selected for BSE imaging and U-Pb analysis.

Back-scattered electron images of optically clear crystals revealed several important observations. First, all of the grains preserve oscillatory zoning parallel to rational crystal faces, suggesting that some component of the monazite crystallized from the melt. Second, most of the crystals are variably embayed, suggesting that they were resorbed either late in the magmatic history or during the post-magmatic history. Third, many grains contain compositionally distinct (higher Th concentrations), deeply embayed core domains mantled by oscillatory-zoned rim domains. The core domains invariably contain mono- and polymineralic inclusions of quartz, alkali feldspar, sillimanite and biotite, whereas the rim domains either lack inclusions or contain inclusions of quartz + plagioclase + biotite ± alkali feldspar. This suggests that the core domains are xenocrystic, metamorphic monazite that may represent an inherited component. Finally, the core domains contain prominent inclusions of uraninite (UO_2) and/or thorite ($ThSiO_4$; huttonite?), identified qualitatively by energy dispersive X-ray spectra. The position and

distribution of the inclusions does not appear to be crystallographically controlled, as would be expected if the inclusions exsolved from the monazite. In some grains, the inclusions occur amongst polymineralic inclusions of quartz, sillimanite, alkali feldspar and biotite, suggesting that they may be xenocrystic. Collectively, these observations suggest that monazites from this sample are physical mixtures of magmatic and metamorphic domains that contain inclusions of inherited uranium-bearing phases.

We determined a total of 34 monazite U-Pb dates from the pegmatite stock (Table 1; Fig. 7). Uranium-lead data from twelve whole single crystals of monazite vary from +1.6 % to -1.5 % discordant and yielded Pb-Pb dates ranging from 1677 to 1690 Ma (Table 1 and Fig. 7). Analyses of eight random fragments broken during sample preparation exhibit similar ranges in discordance (+0.31 % to -3.1 %) and Pb-Pb dates (1679 to 1688 Ma). The remaining fourteen analyses are discussed below. Together the whole grain and random fragment data have Pb-Pb dates that span 13 m.y. and exhibit discordance ranging from + 1.6% to - 3.1%. The discordance severely limits any attempt to precisely constrain the crystallization age of the pegmatite stock, but the data provide an opportunity to evaluate the origin of discordance in these monazites.

Monazite dates from the pegmatite stock exhibit the now familiar problems of normal discordance and a spread in Pb-Pb dates, but reverse discordance is an additional problem. Reverse discordance requires that the crystal either lost U or gained Pb. Uranium loss seems unlikely because U is bound in the crystal structure and Pb gain by diffusion-related processes is difficult to envision. Nonetheless, the most discordant (-1.5%) single crystal analysis (M14) contains an excess of Pb atoms or a deficit of U atoms equal to 1.4% of the total number of atoms of each element. Therefore, any proposed mechanism for the reverse discordance must result in an excess of about 30 ppm Pb or a deficit of about 100 ppm U.

Two types of explanations have been proposed for reverse discordance in U-bearing minerals: incomplete dissolution in the laboratory and excess ^{206}Pb. Incomplete dissolution in the laboratory results in fractionation of U and Pb between the sample and the acid solution to produce reverse discordance (e.g., Tilton, 1956; Tilton and Nicolaysen, 1957; Krogh and Davis, 1974; 1975; Todt and Büsch, 1981; Mattinson, 1994; Mattinson et al., 1996). To evaluate this problem, we first increased the duration of acid digestion from 48 hours to 60 hours. This change had no affect on the reverse discordance. We also included monazites from other Grand Canyon samples in the same pressure vessel as monazites from the pegmatite stock. In every case, the only monazites to display reverse discordance were from the pegmatite stock, regardless of crystal size. There is also no evidence for inclusions of insoluble U-bearing phases such as zircon. These observations suggest that incomplete dissolution is probably not the cause of the discordance. We can also eliminate as possibilities such analytical problems as poor spike calibration, inappropriate fractionation corrections, and inaccurate common Pb corrections and turn, instead to geologic explanations.

The most widely invoked geologic mechanism for producing reverse discordance involves the accumulation ^{206}Pb that is unsupported by ^{238}U (Schärer, 1984). Schärer (1984) explained the excess ^{206}Pb by the decay of ^{230}Th, an intermediate daughter in the ^{238}U decay chain, that was incorporated in the crystal during monazite crystallization from the magma. Because this mechanism does not affect the $^{207}Pb/^{235}U$ ratio, the $^{207}Pb/^{235}U$ date is considered to be most reliable and the magnitude of discordance is measured as the difference between the $^{207}Pb/^{235}U$ date and the $^{206}Pb/^{238}U$ date (Schärer, 1984; Parrish, 1990). Since elemental Th contains less than a tenth of a percent

of ^{230}Th, and since ^{230}Th has a short half-life (7.54×10^4 yrs) relative to ^{238}U (4.47×10^9 yrs), thorogenic ^{206}Pb is eventually swamped-out by uranogenic ^{206}Pb. As such, this mechanism can account for reverse discordance in Phanerozoic and younger monazites, although Parrish (1990) showed that thorogenic ^{206}Pb can also influence precise analyses of monazites as old as 1.4 Ga.

There are several reasons that excess ^{206}Pb is probably not the dominant cause of the reverse discordance in the Paleoproterozoic monazites from the pegmatite dike. First, we do not observe a correlation between the degree of discordance, and either the concentration of Th or the Th/U (Fig. 8). Second, single crystal monazite analyses from both the pegmatite stock and the sheared granite dike at mile 78.0 have similar Th concentrations, but the monazites from the sheared granite dike, despite having higher Th/U ratios, are not reversely discordant (Fig. 8). Third, using the correction scheme derived by Schärer (1984), we calculate that the whole rock Th/U ratio required to displace the reversely discordant whole crystal dates to concordia is 0.06, almost two orders of magnitude lower than the lowest whole rock Th/U ratios measured for Paleoproterozoic rocks throughout the southwestern United States (Th/U = 1 - 45; Wooden and DeWitt, 1991; Aleinikoff et al., 1993; Hawkins et al., 1996). Nonetheless, the effects of excess ^{206}Pb may be obscured by inheritance or post-magmatic alteration of the monazites.

To further characterize the discordance of these grains we determined U-Pb dates for fourteen fragments sliced from five monazite crystals (Table 1; Fig. 7b). Four of the five grains have contrasting intragrain U-Pb systematics. Two fragments from crystal M9 are both about 1% reversely discordant, but the fragment from the termination of the crystal yielded a Pb-Pb date that is 10 m.y. older than the fragment from the core. In

contrast, fragments from crystal M39 exhibit limited a limited spread in Pb-Pb dates (4 m.y.) and instead display a wide range of discordance (+2.7 to -2.4 %). The two normally discordant fragments include more of the grain interior than the reversely discordant fragment (M39c). Fragments from crystals M37 and M38 show dispersion in both Pb-Pb dates (11 m.y. and 6 m.y., respectively) and discordance (+ 1.9 to -2.3 % and -0.2 to -1.5 %, respectively). Finally, crystal M36 yielded three concordant Pb-Pb dates ranging from 1687 to 1691 Ma and one normally discordant fragment with a Pb-Pb date of 1686 Ma. The fragment data reveal no predictable relationship between the magnitude or sign of U-Pb discordance and the position in the crystal (i.e., core versus rim) or the composition (Th/U).

Collectively, the data from the pegmatite stock provide several fundamental constraints on any mechanism proposed to explain the reverse discordance in Paleoproterozoic monazites from the Grand Canyon. Any proposed mechanism must account for: 1) sample specificity; 2) up to 1.43 atom% fractionation of U-Pb on the scale of single crystals and as much as 2.3 atom% fractionation on the subgrain scale; and 3) lack of correlation at the scale of a single crystal between discordance and either grain size, grain shape, Th and U concentration, or Th/U ratio; and 4) lack of correlation at the subgrain scale between discordance and Th or U concentration, Th/U ratio, or position within the crystal.

We suggest several mechanisms that are consistent with these constraints. One possibility stems from the observation that uraninite and thorite inclusions have only been observed in monazites from the pegmatite stock. Infiltrating crustal fluids may have leached U from uraninite inclusions. A second possibility is portrayed in the BSE image in Fig 3f, a xenotime crystal from the sheared granite dike. Note that the low Z core domain is surrounded by a partially resorbed high Z rim. If the high Z rim had a very high U concentration relative to the core domain and was in contact with the core for a

significant period of time prior to resorption, daughter nuclides and radiogenic Pb atoms could be implanted in to the core domain via alpha recoil. Upon dissolution of the rim, the implanted radiogenic Pb would be unsupported by U and thus result in reverse discordance (e.g., Mattinson et al., 1996). Another possibility is that the Pb incorporated in the crystal during magmatic precipitation was highly radiogenic due to local dissolution in the melt of xenocrystic uraninite. Finally, we suggest that reverse discordance could result from preferential leaching of U from undissolved monazite, in a manner analogous to incomplete dissolution in the laboratory, during fluid-mineral interaction in the crust.

All of these mechanisms involve disequilibrium partitioning or fractionation of elemental U or elemental Pb. This implies that the effect of the disequilibrium mechanism on the U-Pb and Pb-Pb dates will depend on both the isotopic composition of the U lost or the Pb gained and the time at which the partitioning or fractionation occurred. In all of these cases, regarding the $^{207}Pb/^{235}U$ date as the most reliable estimate of the monazite growth age is not justified. For many samples from the Grand Canyon, we interpret the $^{207}Pb/^{206}Pb$ date as being reliable for slightly (< 0.5%) reversely discordant monazite U-Pb dates for two reasons. First, reversely discordance monazites from several samples in the Grand Canyon plot along discordia defined by linear regression analysis of concordant and normally discordant monazites and/or zircons (Hawkins et al., 1996). Second, if the spread in monazite Pb-Pb dates from the samples described in this paper was defined on the basis of the $^{207}Pb/^{235}U$ date, the results would not be consistent with independent geologic and geochronologic constraints. However, we must conclude that both the U-Pb dates *and* the Pb-Pb date of monazites from the pegmatite stock are unreliable estimates of the rock's crystallization age.

DISCUSSION

Geochronologic data potentially constrain the rates and duration of deformation, metamorphism and thermal relaxation in orogenic belts. As thermal and mechanical models for orogenic belts become more sophisticated, it is essential that geochronometers and thermochronometers be exploited to resolve very small increments of time (10^6 years). Regional studies in the Proterozoic orogenic belt of the southwestern United States have shown that deformation and metamorphism are diachronous on length scales of ten to one hundred kilometers, the differences largely representing the contrasting crustal levels exposed today (Bowring and Karlstrom, 1990; Karlstrom and Bowring, 1993). Detailed studies on a local scale document the degree of diachroneity, provide insight into the tectonic processes responsible for the Proterozoic crustal architecture, and form a foundation for deducing regional plate tectonic models.

Our work in the Grand Canyon represents a local study focusing on the diachroneity of fabric formation and metamorphism. Detailed studies of representative outcrops from different areas within the transect form the basis for constructing local deformational and thermal histories and for comparing results from different areas. The dikes described in this paper provide essential timing constraints on peak metamorphism and fabric development in two of these areas. The complexity of the monazite data from these intrusions required the development of new analytical strategies and techniques for U-Pb monazite geochronology and resulted in new insights into the utility of monazite as a chronometer of crustal processes.

The results presented in this paper have influenced our approach to analyzing and interpreting U-Pb monazite data from all samples in the Proterozoic of the southwestern U.S., and other orogens as well. Several observations prompted us to adopt an aggressive analytical strategy. First, all of the monazites and xenotimes from these samples are optically clear, contain no visible cores, and are indistinguishable optically

from monazites that yield well-behaved U-Pb systematics. These observations indicate that monazites with complex systematics cannot be identified under the optical microscope. Second, both multi-crystal and single crystal analyses of monazite and xenotime can potentially yield average dates that are significantly different than the 'age of interest' (e.g., the crystallization age of a dike). Third, a concordant date from a single crystal of monazite (i.e., apparent closed system behavior) is not necessarily representative of the rock's crystallization age. Finally, lithologies yielding monazites with complex U-Pb systematics occur in close proximity to lithologies with monazites exhibiting well-behaved U-Pb systematics, suggesting that the U-Pb systematics of monazites from one sample may not be representative of contemporaneous monazites from a particular region. For these reasons, we now routinely analyze enough single crystal fractions (6 to 10) to determine if intra-grain age dispersion is an issue in a given sample.

Our approach to the interpretation of monazite U-Pb data also changed as a result of this study. In the dikes from river-mile 78.0, we observe magmatic monazite crystals that were partially replaced by significantly younger secondary monazite. The secondary monazite apparently formed during the post-magmatic history at temperatures well below the closure temperature of the crystal. Therefore, volume diffusion of Pb at magmatic conditions does not control the U-Pb systematics of that grain and, more importantly, factors other than volume diffusion can significantly affect the U-Pb systematics of monazite.

An important question regarding our results can be framed as follows: do the complex U-Pb systematics from three Paleoproterozoic granite dikes have any general implications for the U-Pb systematics of monazite? We cannot answer this question completely. However, given the large number of processes that have been proposed to explain the U-Pb systematics of monazite (Schärer, 1984; Copeland et al., 1988; Parrish

and Tirrul, 1989; Aleinikoff and Grauch, 1990; Getty and Gromet, 1992; DeWolf et al., 1993; Krogh and Moser, 1994; Harrison et al., 1995), our results can be viewed as another cautionary note for interpreting monazite U-Pb data.

However, our findings also indicate that monazites with complex U-Pb systematics may yield important temporal information about a variety of processes that operate throughout the metamorphic history of orogenic belts. We suggest that the U-Pb system in monazite may be a more powerful geochronometer than previously thought. Not only can single crystals preserve a temporal record of xenocrystic monazite growth, prograde to peak metamorphic growth, and fluid-mineral interaction under retrograde conditions, but different crystals in the same rock can preserve different portions of the rock's geologic or thermal history. In addition, the susceptibility of monazite to fluid-mineral interaction at high temperatures may provide a critical link between metamorphic reactions and absolute time (cf. Lanzirotti and Hanson, 1995). Monazite may also offer a precise geochronologic tool for dating fluid flow during moderate- to high-grade metamorphism, one of the most elusive crustal processes for precise geochronology. To exploit the full potential of the U-Pb system in monazite, it is necessary to characterize both the paragenesis of each generation of monazite present in a given rock, and the processes which influence the U-Pb systematics. Accomplishing this goal requires high precision analysis of monazite on the subgrain scale.

REFERENCES

Aleinikoff JN, Grauch RI (1990) U-Pb geochronologic constraints on the origin of a unique monazite-xenotime gneiss, Hudson Highlands, New York. Am J Sci 290:522-546

Aleinikoff JN, Reed JC, Jr, Wooden JL (1993) Lead isotopic evidence for the origin of Paleo- and Mesoproterozoic rocks of the Colorado Province, U.S.A. Precamb Res 63: 97-122

Black LP, Fitzgerald JD, Harley SL (1984) Pb isotopic composition, colour, and microstructure of monazites from a polymetamorphic rock in Antarctica. Contrib Mineral Petrol 85:141-148

Bowring, SA, Karlstrom, KE (1990) Growth and reactivation of Proterozoic lithosphere in the southwestern United States. Geology 18: 1203-1206

Cartz L, Karioris FG, Fournelle RA, Gowda KA, Ramasami K, Sarkar G, Billy M (1981) Metamictization by heavy ion bombardment of α quartz, zircon, monazite and nitride structures. In: Moore JG (ed) Scientific Basis for Nuclear Waste Management Vol 3. Plenum Press, New York, pp 421-427

Cherniak DJ (1993) Lead diffusion in sphene and preliminary results on the effects of radiation damage on Pb transport. Chem Geol 110:177-194

Childe F, Doig R, Gariepy C (1993) Monazite as a metamorphic chronometer, south of the Grenville Front, western Quebec. Can J Earth Sci 30:1056-1065

Copeland P, Parrish RR, Harrison TM (1988) Identification of inherited radiogenic Pb in monazite and its implications for U-Pb systematics. Nature 333:760-763

Davis DW, Schandl ES, Wasteneys HA (1994) U-Pb dating of minerals in alteration halos of Superior Province massive sulfide deposits: syngenesis versus metamorphism. Contrib Mineral Petrol 115:427-437

DeWolf CP, Belshaw N, O'Nions RK (1993) A metamorphic history from micron-scale $^{207}Pb/^{206}Pb$ chronometry of Archean monazite. Earth Planet Sci Lett 120:207-220

Dodson MH (1973) Closure temperature in cooling geochronological and petrological systems. Contrib Mineral Petrol 40:259-274

Dodson MH (1979) Theory of cooling ages. In: Jäger E, Hunziker JC (eds) Lectures in Isotope Geology. Springer-Verlag, Berlin, pp 194-202

Ehlert TC, Gowda KA, Karioris FG, Cartz L (1983) Differential scanning calorimetry of heavy ion bombarded synthetic monazite. Rad Effects 70:173-181

Elston DP (1989) Grand Canyon Supergroup, northern Arizona: startigraphic summary and preliminary paleomagnetic correlations with parts of other North American

Proterozoic successions. In: Jenney JP, Reynolds SJ (eds) Geologic Evolution Of Arizona. Arizona Geological Society Digest 17, Tucson, pp 259-272.

Floran RJ, Abraham MM, Boatner LA, and Rappaz M (1981) Geological stability of monazite and its bearing on the immobilization of actinide wastes. In: Moore JG (ed) Scientific Basis for Nuclear Waste Management Vol 3. Plenum Press, New York, pp 507-514

Getty SR, Gromet LP (1992) Geochronological constraints on ductile deformation, crustal extension, and doming about a basement-cover boundary, New England Appalachians. Am J Sci 292:359-397

Goldich SS, Mudrey MG (1972) Dilatancy model for discordant U-Pb zircon ages. In: Tugarinov AI (ed) Contributions to Recent Geochemistry and Analytical Chemistry. Nauka Publishing Office, Moscow, pp 415-418

Gulson BL, Krogh TE (1973) Old lead components in the young Bergill Massif, south-East Swiss Alps. Contrib Mineral Petrol 40:239-252

Harrison TM, Watson EB (1983) Kinetics of zircon dissolution and zirconium diffusion in granitic melts of variable water content. Earth Planet Sci Lett 64:295-304

Harrison TM, McKeegan KD, LeFort P (1995) Detection of inherited monazite in the Manaslu leucogranite by $^{208}Pb/^{232}Th$ ion microprobe dating: crystallization age and tectonic implications. Earth Planet Sci Lett 133:271-282

Hawkins DP, Bowring SA, Ilg BE, Karlstrom KE, Williams ML (1996) U-Pb geochronological constraints on the Paleoproterozoic crustal evolution of the Upper Granite Gorge, Grand Canyon, Arizona. Geol Soc Am Bull (in press)

Hawkins DP, Bowring SA (1995a) U-Pb constraints on the origin of Paleoproterozoic migmatites from the grand canyon, Arizona, USA: implications for the timing and duration of peak metamorphism in a high grade terrain (abstract). International Conference Tectonics and Metallogeny of Early/Mid Precanbrian Orogenic Belts, Precambrian '95 Abstracts and Programs, p 259

Hawkins DP, Bowring SA (1995b) Age variation in U-Pb monazite data from Paleoproterozoic migmatites in the Grand Canyon: implicationms for U-Pb monazite geochronometry (abstract). EOS, Trans Am Geophys Union 76:F707

Heaman L, Parrish RR (1991) U-Pb geochronology of accessory minerals. In: Heaman L, Ludden JN (eds) Application of Radiogenic Isotope Systems to Problems in Geology. Mineralogical Society of Canada Short Course Handbook 19, Toronto, pp 59-102

Holmes, A (1954) The oldest dated minerals of the Rhodesia Shield. Nature 173:612-617

Ilg BE, Karlstrom KE, Williams ML, Hawkins DP (1996a) Precambrian crystalline rocks In: Huntoon PW (ed) Geologic Map of the Eastern Part of the Grand Canyon National Park, Arizona (geologic map). Grand Canyon Association, Grand Canyon, Arizona

Ilg BE, Karlstrom KE, Hawkins DP, Williams ML (1996b) Tectonic evolution of Paleoproterozoic rocks in the Grand Canyon: Insights into middle crustal processes. Geol Soc Am Bull (in press)

Karlstrom KE, Bowring SA (1993) Transcontinental Proterozoic provinces In: Reed JC Jr, Bickford ME, Houston RS, Link PK, Rankin DW, Sims PK, Van Schmus WR (eds) Precambrian: Conterminous United States. Geological Society of America, The Geology of North America C-2, Boulder, pp 171-333.

Karioris FG, Gowda KA, Cartz L, (1981) Heavy ion bombardment of monoclinic $ThSiO_4$, ThO_2 and monazite, Rad Effects Lett 58:1-3

Kingsbury JA, Miller CF, Wooden JL, Harrison TM (1993) Monazite paragenesis and U-Pb systematics in rocks of the eastern Mojave Desert, California, U.S.A.: implications for thermochronometry. Chem Geol 110:147-167

Köppel V, Grünenfelder M (1975) Concordant U-Pb ages of monazite and xenotime from the Central Alps and the timing of the high temperature Alpine metamorphism, a preliminary report. Schweiz Mineral Petrogr Mitt 55: 129-132

Krogh TE (1973) A low-contamination method for hydrothermal decomposition of zircon and extraction of U and Pb for isotopic age determination. Geochim Cosmochim Acta 37:485-494

Krogh TE (1982) Improved accuracy of U-Pb ages by the creation of more concordant systems using an air abrasion technique. Geochim Cosmochim Acta 46:637-649

Krogh TE, Davis GL (1974) Alteration in zircons with discordant U-Pb ages. Carnegie Inst Washington Yearb 73:560-567

Krogh TE, Davis GL (1975) Alteration in zircons and differential dissolution of altered and metamict zircon. Carnegie Inst Washington Yearb 74:619-623

Krogh TE, Moser DE (1994) U-Pb zircon and monazite ages from the Kapuskasing uplift: age constraints on deformation within the Ivanhoe Lake fault zone. Can J Earth Sci 31:1096-1103

Lanzirotti A, Hanson GN (1995) U-Pb dating of major and accessory minerals formed during metamorphism and deformation of metapelites. Geochim Cosmochim Acta 59:2513-2526

Ludwig KR, (1989) Pb.Dat: A computer program for processing raw Pb-U-Th isotope data. US Geol Surv Open-File Rep 88-557

Mattinson JM (1994) A study of complex discordance in zircons using step-wise dissolution techniques. Contrib Mineral Petrol 116:117-129

Mattinson JM, Graubau CM, Parkinson, DL, McLelland, WC (1996) U-Pb reverse discordance in zircons: the role of fine-scale oscillatory zoning and sub-micron

transport of Pb. Basu A, Hart SR (eds) Earth Processes: Reading the Isotopic Code. Geophysical Monograph 95, pp 355-370

McCarthy GJ, White WB, Pfoertsch DE (1978) Synthesis of nuclear waste monazites, ideal actinide hosts for geologic disposal. Mat Res Bull 13:1239-1245

Mitchell RS (1973) Metamict minerals: a review. Min Record 4:214-223

Murakami T, Chakoumakos BC, Ewing RC, Lumpkin GR,Weber WJ (1991) Alpha-decay event damage in zircon. Am Mineral 76:1510-1532

Naeser CW, Elston DP (1987) Fission-track dates from the Grand Canyon, Arizona (abstract). Geol Soc Am Abs Prog 19:784

Overstreet WC (1967) The geologic occurrence of monazite. US Geol Surv Prof Paper 530:327p

Parrish RR (1990) U-Pb dating of monazite and its application to geological problems. Can J Earth Sci 27:1435-1450

Parrish RR, Carr SD (1994) U-Pb problematics of very high-U accessory minerals: examples from the Himalaya and Cordillera and implications for U-Pb geochronology (abstract). US Geol Surv Circ 1107:243.

Parrish RR, Tirrul R (1989) U-Pb age of the Baltoro granite, northwest Himalaya, and implications for monazite U-Pb systematics. Geology 17:1076-1079

Roy R, Vance ER (1981) Irradiated and metamict materials: relevance to radioactive waste science. J Mat Sci 16:1187-1190.

Schärer U (1984) The effect of initial ^{230}Th disequilibrium on young U-Pb ages: the Makalu case, Himalaya. Earth Planet Sci Lett 67:191-204

Schärer U, Xu RH, Allegre CJ (1986) U-(Th)-Pb systematics and ages of Himalayan leucogranites, South Tibet. Earth Planet Sci Lett 77, 35-48

Sevigny JH, Hanson GN (1995) Late-Acadian and Pre-Acadian history of the New England Appalachians of southwestern Connecticut. Geol Soc Am Bull 107:487-498

Silver LT, Deutsch S (1963) Uranium lead isotopic variations in zircons: a case study. J Geol 71:721-758.

Smith HA, Barreiro BA (1990) Monazite U-Pb dating of staurolite grade metamorphism in pelitic schists. Contrib Mineral Petrol 105:602-615

Smith HA, Chamberlain CP, Zeitler PK (1992) Documentation of Neogene regional metamorphism in the Himalayas of Pakistan using U-Pb in monazite. Earth Planet Sci Lett 113:93-105

Smith HA, Giletti BJ (1995) Pb loss in monazite by diffusion and other transport processes (abstract). Geol Soc Am Abs Prog 27:A-36.

Stacey JS, Kramers JD (1975) Approximation of terrestial lead isotope evolution by a two-stage model. Earth Planet Sci Lett 26:207-221

Suzuki K, Adachi M (1991) Precambrian provenance and Silurian metamorphism of the Tsubonosawa paragneiss in the South Kitakami terrane, Northeast Japan, revealed by the chemical Th-U-total Pb isochron ages of monazite, zircon and xenotime. Geochem J 25:357-376

Suzuki K, Adachi M (1994) Middle Precambrian detrital monazite and zircon from the Hida gneiss in the Oki-Dogo Island, Japan: their origin and implications for the correlation of basement gneiss of Southwest Japan and Korea. Tectonophysics 235:277-292

Suzuki K, Adachi M, Kajizuka I (1994) Electron microprobe observations of Pb diffusion in metamorphosed detrital monazites. Earth Planet Sci Lett 128:391-405

Tilton GR (1956) The interpretation of lead-age discrepancies by acid-washing experiments. Trans Am Geophys Union 37:224-230

Tilton GR, Nicolaysen LO (1957) The use of monazites for age determination. Geochim Comochim Acta 11:28-40

Todt WA, Büsch W (1981) U-Pb investigations of zircons from pre-Variscan gneisses-I. A study from the Schwarzwald, West Germany. Geochim Cosmochim Acta 45:1789-1810

Williams MW (1994) Conflicting P-T-t paths from Proterozoic rocks of the southwestern USA: The problem is plagioclase (abstract). EOS, Trans Am Geophys Union 75: 185.

Wasserburg GJ (1963) Diffusion processes in lead-uranium systems. J Geophys Res 68:4823-4846

Wooden JL, DeWitt E, (1991) Pb isotopic evidence for the boundary between the Early Proterozoic Mojave and central Arizona crustal provinces in western Arizona. In: Karlstrom KE (ed) Proterozoic Geology and Ore Deposits. Arizona Geological Society Digest 19, pp 11-26

Zeitler PK (1989) The geochronology of metamorphic processes. In: Daly JS, Cliff RA, Yardley BWD (eds) Evolution of Metamorphic Belts. Geological Ssociety Special Publication No. 43, pp 131-147

FIGURE CAPTIONS

Figure 1 Simplified geologic map of Paleoproterozoic rocks in the eastern Grand Canyon between river miles 77 and 86. River miles are the standard spatial reference in the Grand Canyon for travel along the Colorado River. They are measured along the course of the river from Lees Ferry in northern Arizona (see inset). Sketch maps of the geology and sample localities in this study. **a** Exposure on the north side of the river at river 78.0. Note that the sheared granite dike on the east side of the exposure is offset by the brittle normal fault. Lithologic units as indicated for the eastern Upper Gorge map. **b** Exposure at river mile 85.6. Note the scale for the two outcrop maps. Modified after Ilg et al. (1996a,b).

Figure 2 Concordia diagrams for the unfoliated granite dike (sample UG78.0-5) at river mile 78.0. (a) Shows both zircon and monazite data including the linear regression of four zircon analyses. (b) Close-up view of the monazite data. Note that the monazite analyses spread out along concordia from the zircon upper intercept age to younger dates. The inset shows the position spatial relationship of fragments sliced from crystal M9. Labels: aa = air abraded; rf = random fragment.; g = whole grain.

Figure 3a-j Back-scattered electron images of monazite and xenotime crystals from the unfoliated granite dike (**a-d**), the sheared granite dike (**e-g**) and the pegmatite stock (**h-j**). **a,b** Euhedral monazite fragments displaying sector-zoned core domains and prominent high Th rim domains parallel to rational crystal faces. There is evidence in both crystals for minor resorption prior to development of the rim domain. Preservation of the delicate zoning patterns precludes dynamic recrystallization. **c** Subhedral monazite crystal with prominent embayment adjacent to a low Th domain that truncates zoning in the magmatic rim and core domains. The dark area is a hole in the crystal. **d** Euhedral monazite crystal exhibiting a complex, secondary domain that truncates and distorts magmatic growth zones. Note that the crystal is resorbed adjacent to the recrystallized domain. Dark areas are inclusions of quartz. **e** Partially resorbed xenotime crystal with prominent oscillatory zoning parallel to relict crystal faces. Dark areas are holes and both quartz and alkali feldspar inclusions. **f** Subhedral xenotime crystal (B-X3) with a complex core domain surrounded by a partially resorbed high Th and U rim which, in turn, is overgrown an oscillatory-zoned low Th and U rim. This crystal was sliced for U-Pb analysis (B-X3a,b in Table 1 and Fig. 4b). **g** Subhedral, partially resorbed monazite crystal (A-M11) showing two distinct domains with complex contact relationships. Dark areas are inclusions quartz, sillimanite and biotite. This crystal was sliced for U-Pb analysis (A-M11a,d in Table 1 and Fig. 4b). **h,i** Subhedral monazite crystals containing partially resorbed core domains with inclusions of quartz, sillimanite, biotite, and alkali feldspar, overgrown by oscillatory rim domains with few inclusions. Note that both crystals are partially resorbed. **j** Subhedral, highly embayed monazite crystal containing an irregular core domain and complexly zoned rim domain. The core domain has inclusions of quartz, alkali feldspar, biotite, sillimanite, biotite, apatite and uraninite (bright).

Figure 4a,b Concordia diagrams for monazite and xenotime from the sheared granite dike at mile 78.0. **a** concordia diagram showing that the most discordant points are monazite and xenotime analyses from sheared center of the dike. The arrow points in the direction of the origin. **b** Close-up of data points near concordia. The inset shows the

spatial relationships between fragments sliced from crystals B-X3 and B-M11. BSE images of these two grains are shown in figures 3f and 3g, respectively. Note that fragments B-X3a and B-X3b have identical Pb-Pb dates, but that fragments B-M11a and B-M11d have contrasting Pb-Pb dates. See text for discussion. Labels: A = sample UG78.0-2A, the sheared center of the dike; B = sample UG78.0-2B, the unfoliated margin of the dike.

Figure 5 Grain size (smallest dimension of the crystal) versus cooling age (Pb-Pb date) for *concordant* monazite analyses from the sheared granite dike. Curves are the locus of cooling ages expected for different cooling rates. There is no correlation between grain size and cooling age indicating that some other process(es) produced the age dispersion in these monazites.

Figure 6 a-b Plots of Th + U concentration versus percent discordance. **a** Normally discordant monazite and xenotime dates from the sheared granite. Note that seven monazite and xenotime analyses exhibit a first order, positive correlation, suggesting that radiation damage resulted in reverse discordance. **b** Data for 48 monazite and xenotime analyses from five granite and pegmatite samples at mile 78.0 (Hawkins et al., 1996; this paper; Hawkins and Bowring unpublished data). Note that despite having similar total Th and U concentrations, monazites and xenotimes from foliated dikes are more discordant than monazites from unfoliated dikes. Representative errors in concentration (20%) are shown for two points; the points exceed the error at values below about 40,000 ppm.

Figure 7a,b Concordia diagrams, shown at the same scale, for monazites from the deformed pegmatite stock. **a** Data for whole crystals and random fragments. **b** Data for fragments sliced from individual crystals. Inset drawings, shown at the same scale, portray the position of the fragments in each crystal. Note that the fragment data have more variable Pb-Pb dates and discordance than whole grains and random fragments.

Figure 8a,b (**a**) Th concentration versus % discordance for samples with discordant monazite dates. representative errors in Th concentration (20%) are shown for two points. Note that reverse discordance is not a function of Th concentration and that monazites with comparable Th contents exhibit contrasting U-Pb discordance. and Th/U ratio versus % discordance (**b**) for monazites from the shared granite dike and the deformed pegmatite stock. Despite having comparable total Th and U concentrations and higher Th/U ratios, monazites from the sheared granite dike do not exhibit reverse discordance.

Table 1 U-Pb analytical results for monazite, xenotime and zircon from the Grand Canyon

		Composition						Isotopic Ratios						Dates (Ma)		
Fractions	Estimated Wgt (µg)	U (ppm)	Th (ppm)	Pb (ppm)	Th U	Mol% ^{208}Pb	Com Pb (pg)	^{208}Pb ^{204}Pb	^{206}Pb ^{204}Pb	^{208}Pb ^{232}U	^{207}Pb ^{235}U	^{207}Pb ^{206}Pb	corr. coef.	^{208}Pb ^{232}U	^{207}Pb ^{235}U	^{207}Pb ^{206}Pb
(1)	(2)	(3)	(3)	(3)	(3)		(4)	(5)	(6)	(7)	(7)	(7)				(8)
GRANITE SILL (sample UG78.0-5)																
M3 *aa*	30.2	783	12765	1211	16.73	81.7	6.1	71107.12	4.9135	0.29700 (.08)	4.21754 (.09)	0.10299 (.04)	0.887	1676.4	1677.4	1678.7 ±0.8
M4 *rf*	15.5	1840	42484	3825	23.69	86.3	6.1	85575.38	6.9497	0.29798 (.09)	4.24047 (.10)	0.10321 (.04)	0.911	1681.3	1681.9	1682.7 ±0.8
M8 *wg*	0.8	12058	126304	13196	10.74	74.1	6.5	26381.59	3.1514	0.29716 (.06)	4.21875 (.08)	0.10296 (.05)	0.808	1677.2	1677.7	1678.2 ±0.8
M9a *sf*	2.7	4241	95649	8645	23.14	86.0	9.1	22719.52	6.7757	0.29857 (.10)	4.25041 (.11)	0.10325 (.04)	0.914	1684.2	1683.8	1683.3 ±0.8
M9b *sf*	2.3	2462	57668	5162	24.03	86.5	9.9	10250.74	7.0457	0.29678 (.09)	4.20711 (.11)	0.10281 (.05)	0.889	1675.3	1675.4	1675.5 ±0.9
M10 *rf*	1.1	4664	129133	11368	28.40	88.3	7.4	12601.66	8.3103	0.29872 (.10)	4.25135 (.11)	0.10322 (.05)	0.893	1685.0	1684.0	1682.8 ±0.9
M11 *tip*	0.4	2528	45249	4173	18.36	83.0	4.4	4316.39	5.3881	0.29355 (.20)	4.12414 (.22)	0.10190 (.10)	0.898	1659.2	1659.1	1658.9 ±1.8
M16 *rf*	2.4	2099	54648	4834	26.71	87.7	15.8	5638.84	7.8371	0.29702 (.11)	4.21572 (.13)	0.10294 (.07)	0.822	1676.5	1677.1	1677.8 ±1.4
M17 *wg*	0.5	3189	27907	3052	8.98	70.5	7.4	3606.66	2.6367	0.29499 (.16)	4.16540 (.19)	0.10241 (.10)	0.838	1666.4	1667.2	1668.3 ±1.9
M18 *rim*	0.6	8880	40112	5594	4.63	55.2	3.9	23522.86	1.3579	0.29634 (.09)	4.19249 (.12)	0.10261 (.08)	0.766	1673.1	1672.6	1671.8 ±1.4
Z1 *aa*	12.4	179	135	60	0.77	18.2	39.2	936.03	0.2457	0.27569 (.13)	3.92946 (.15)	0.10337 (.08)	0.859	1569.6	1619.8	1685.6 ±1.4
Z5 *aa*	11.6	249	187	85	0.77	17.1	6.4	8182.68	0.2280	0.29556 (.11)	4.21107 (.13)	0.10333 (.06)	0.884	1669.3	1676.2	1684.8 ±1.1
Z6 *aa*	4.1	204	87	64	0.44	10.5	4.5	3529.59	0.1293	0.29682 (.24)	4.22993 (.27)	0.10336 (.11)	0.913	1675.5	1679.8	1685.3 ±2.0
Z7 *aa*	3.1	313	51	91	0.17	4.4	2.9	6236.26	0.0509	0.29342 (.12)	4.22388 (.14)	0.10440 (.08)	0.832	1658.6	1678.7	1703.9 ±1.4
Z8 *aa*	7.1	415	228	130	0.56	13.7	8.8	5729.31	0.1745	0.28280 (.10)	4.03220 (.12)	0.10341 (.06)	0.851	1605.5	1640.7	1686.2 ±1.2
SHEARED GRANITE DIKE (samples UG78.0-2A,B)																
A-M1 *wg*	5.4	462	37668	3042	83.62	95.8	9.5	4614.62	25.1206	0.28937 (.11)	4.09779 (.13)	0.102704 (.08)	0.817	1638.4	1653.9	1673.6 ±1.4
A-M3 *wg*	2.9	841	20486	1814	25.00	86.9	4.3	10471.79	7.3428	0.29481 (.14)	4.16073 (.15)	0.102359 (.05)	0.947	1665.5	1666.3	1667.3 ±0.9
A-M5 *wg*	1.3	2150	46516	4208	22.20	85.6	10.1	4926.09	6.5625	0.29444 (.11)	4.17463 (.14)	0.102829 (.09)	0.797	1663.7	1669.1	1675.8 ±1.6
A-M7 *wg*	1.7	3972	60169	5767	15.54	80.5	7.0	17556.74	4.5573	0.29615 (.09)	4.19076 (.10)	0.102632 (.05)	0.879	1672.2	1672.2	1672.2 ±0.9
A-M9 *wg*	3.0	403	25714	2110	65.46	94.6	8.9	2444.30	19.2998	0.29578 (.17)	4.19948 (.19)	0.102972 (.07)	0.930	1670.4	1673.9	1678.4 ±1.3
A-M10 *wg*	2.7	310	41829	3333	138.29	97.4	15.1	997.40	40.5501	0.29695 (.23)	4.21073 (.24)	0.102844 (.08)	0.949	1676.1	1676.1	1676.1 ±1.4
A-M13 *wg*	1.2	2133	57349	5021	27.59	88.2	7.2	6324.11	8.2121	0.29154 (.12)	4.12254 (.14)	0.102557 (.08)	0.834	1649.2	1658.8	1670.9 ±1.4
A-X2 *wg*	1.1	29696	17317	9581	0.60	13.9	7.1	82128.55	0.1775	0.29275 (.05)	4.14234 (.07)	0.102624 (.04)	0.786	1655.2	1662.7	1672.1 ±0.8
A-X3 *wg*	0.9	38202	26106	12552	0.70	15.9	7.8	78418.29	0.2089	0.29099 (.07)	4.11062 (.09)	0.102455 (.04)	0.877	1646.5	1656.4	1669.1 ±0.8
A-X4 *wg*	1.1	17457	9991	5517	0.59	13.9	7.1	47255.42	0.1776	0.28673 (.07)	4.05153 (.09)	0.102483 (.04)	0.869	1625.1	1644.6	1669.6 ±0.8
A-X5 *wg*	2.6	18035	11019	5926	0.63	14.3	8.8	95415.26	0.1844	0.29647 (.13)	4.20933 (.13)	0.102976 (.04)	0.951	1673.8	1675.8	1678.4 ±0.8
A-X6 *wg*	1.4	5445	3346	1729	0.63	14.8	11.0	11875.14	0.1917	0.28430 (.08)	4.00658 (.09)	0.102211 (.04)	0.882	1613.0	1635.5	1664.7 ±0.8
A-X7 *wg*	2.2	8099	5208	2695	0.66	14.9	14.5	21841.87	0.1936	0.29755 (.07)	4.23023 (.09)	0.103110 (.04)	0.873	1679.2	1679.9	1680.8 ±0.8
B-M1 *wg*	1.8	597	12559	1152	21.57	85.2	19.9	967.82	6.3289	0.29722 (.19)	4.22033 (.24)	0.102982 (.14)	0.815	1677.5	1678.0	1678.5 ±2.5
B-M3 *wg*	0.2	6886	100134	9733	14.92	79.8	5.9	4063.44	4.3669	0.29801 (.16)	4.23428 (.18)	0.103049 (.08)	0.909	1681.4	1680.7	1679.8 ±1.4
B-M4 *wg*	0.8	2552	65709	5814	26.41	87.5	8.3	4444.23	7.7417	0.29697 (.12)	4.21069 (.15)	0.102833 (.09)	0.806	1676.3	1676.1	1675.9 ±1.6
B-M11a *sf*	1.0	13425	193067	18827	14.75	79.7	14.7	16196.73	4.3383	0.29748 (.22)	4.23809 (.23)	0.103325 (.06)	0.959	1678.8	1681.4	1684.7 ±1.2
B-M11d *sf*	1.0	1473	66719	5570	46.47	92.5	9.9	2664.49	13.6398	0.29557 (.16)	4.17848 (.20)	0.102531 (.11)	0.843	1669.3	1669.8	1670.4 ±2.0

Table 1 — continued

Fractions	Estimated Wgt (µg)	Composition U (ppm)	Th (ppm)	Pb (ppm)	Th U	Mol% ^{206}Pb	Com Pb (pg)	Isotopic Ratios ^{206}Pb ^{204}Pb	^{208}Pb ^{206}Pb	^{206}Pb ^{238}U	^{207}Pb ^{235}U	^{207}Pb ^{206}Pb	corr. coef.	Dates (Ma) ^{206}Pb ^{238}U	^{207}Pb ^{235}U	^{207}Pb ^{206}Pb
(1)	(2)	(3)	(3)	(3)	(3)		(4)	(5)	(6)	(7)	(7)	(7)				(8)
B-M21 *wg*	0.4	3397	73416	6629	22.17	85.5	3.2	7567.27	6.5189	0.29551 (.11)	4.18383 (.14)	0.102683 (.08)	0.795	1669.0	1670.9	1673.2 ±1.5
B-M22 *wg*	0.4	6007	86155	8401	14.71	79.6	3.6	12137.92	4.3109	0.29832 (.14)	4.24534 (.16)	0.103211 (.07)	0.892	1683.0	1682.8	1682.6 ±1.3
B-X1 *wg*	1.6	16000	9088	5223	0.58	13.4	7.7	60667.67	0.1711	0.29757 (.07)	4.23173 (.08)	0.103140 (.04)	0.851	1679.3	1680.2	1681.4 ±0.8
B-X2 *wg*	1.7	12189	7191	4009	0.61	13.9	7.0	53815.59	0.1774	0.29825 (.17)	4.24414 (.18)	0.103206 (.05)	0.964	1682.6	1682.6	1682.6 ±0.9
B-X3a *sf*	8.2	9217	5712	3014	0.64	14.6	18.2	72653.31	0.1888	0.29389 (.10)	4.17622 (.11)	0.103060 (.04)	0.925	1661.0	1669.4	1680.0 ±0.7
B-X3b *sf*	5.7	8579	4485	2767	0.54	12.5	9.1	96932.25	0.1576	0.29718 (.16)	4.22388 (.17)	0.103083 (.04)	0.970	1677.3	1678.7	1680.4 ±0.7
PEGMATITE STOCK (sample UG85.6-2)																
M1 *wg*	1.7	4948	32528	3961	6.74	64.1	15.0	10062.13	1.9667	0.30110 (.07)	4.30103 (.08)	0.10360 (.04)	0.841	1696.7	1693.6	1689.6 ±0.8
M2 *wg*	2.3	3886	37598	4037	9.93	72.2	4.9	34148.87	2.8704	0.30214 (.07)	4.29757 (.08)	0.10316 (.04)	0.849	1701.9	1692.9	1681.8 ±0.8
M3 *wg*	5.0	2443	32000	3177	13.44	78.2	57.8	3680.02	3.9600	0.29568 (.23)	4.19530 (.25)	0.10291 (.08)	0.944	1669.8	1673.1	1677.2 ±1.5
M5 *wg*	0.8	9088	54207	6829	6.12	61.8	6.9	19411.36	1.7819	0.30110 (.13)	4.29619 (.14)	0.10348 (.06)	0.894	1696.8	1692.6	1687.5 ±1.2
M7 *wg*	0.8	2372	24846	2619	10.75	73.9	8.5	4107.89	3.1235	0.30120 (.11)	4.29137 (.12)	0.10333 (.06)	0.882	1697.2	1691.7	1684.9 ±1.1
M8 *wg*	4.0	3046	44218	4309	14.89	79.7	7.0	32156.93	4.3307	0.30061 (.06)	4.27800 (.08)	0.10321 (.04)	0.833	1694.3	1689.1	1682.7 ±0.8
M10 *wg*	2.2	4139	4247	1496	1.05	21.9	8.2	20013.56	0.3102	0.29650 (.10)	4.21709 (.13)	0.10316 (.07)	0.820	1673.9	1677.4	1681.6 ±1.3
M12 *wg*	1.1	30536	200233	24050	6.73	64.5	19.7	29616.14	2.0033	0.29305 (.16)	4.16659 (.17)	0.10312 (.07)	0.911	1656.8	1667.5	1681.0 ±1.3
M14 *wg*	6.0	6761	79298	8113	12.03	75.9	59.1	12197.18	3.4758	0.30243 (.16)	4.30201 (.17)	0.10317 (.04)	0.964	1703.4	1693.7	1681.9 ±0.8
M17 *wg*	2.0	10362	82813	9376	8.20	68.5	10.7	34740.58	2.4034	0.29821 (.20)	4.24407 (.20)	0.10322 (.05)	0.969	1682.4	1682.6	1682.8 ±0.9
M26 *wg*	0.2	4853	63301	6432	13.38	77.9	34.7	587.59	3.8769	0.30094 (.22)	4.27350 (.30)	0.10299 (.18)	0.787	1696.0	1688.3	1678.7 ±3.4
M27 *wg*	0.3	4401	37089	4117	8.64	69.8	4.8	4944.59	2.5489	0.29579 (.29)	4.20028 (.30)	0.10299 (.07)	0.971	1670.4	1674.1	1678.7 ±1.3
M15 *rf*	6.2	5654	59266	6232	10.75	74.0	25.2	24663.52	3.1405	0.29997 (.12)	4.27688 (.13)	0.10341 (.04)	0.945	1691.2	1688.9	1686.1 ±0.8
M16 *rf*	5.8	7979	115004	11261	14.79	79.2	52.3	15959.39	4.2041	0.30691 (.10)	4.36178 (.11)	0.10307 (.04)	0.925	1725.5	1705.1	1680.2 ±0.8
M18 *rf*	1.4	4148	65210	6270	16.13	81.0	27.2	3803.19	4.6898	0.30055 (.10)	4.27631 (.12)	0.10319 (.06)	0.867	1694.0	1688.8	1682.3 ±1.1
M20 *rf*	0.2	7425	99775	9957	13.78	78.4	20.3	1324.63	3.9994	0.30099 (.15)	4.28028 (.18)	0.10314 (.09)	0.876	1696.2	1689.6	1681.3 ±1.6
M22 *rf*	0.2	5709	71146	7175	12.78	77.4	8.6	2398.53	3.7800	0.29622 (.22)	4.22297 (.35)	0.10340 (.25)	0.701	1672.5	1678.5	1685.9 ±4.6
M30 *rf*	1.3	5611	36942	4461	6.75	64.2	9.9	13225.13	1.9749	0.29842 (.11)	4.23975 (.12)	0.10304 (.06)	0.887	1683.5	1681.8	1679.6 ±1.0
M31 *rf*	1.0	5736	82107	8009	14.68	79.7	27.8	3636.51	4.3181	0.29659 (.10)	4.21234 (.11)	0.10301 (.06)	0.861	1674.4	1676.4	1679.0 ±1.0
M32 *rf*	2.1	7376	94032	9478	13.08	77.4	36.7	7564.86	3.7775	0.30361 (.29)	4.33346 (.30)	0.10352 (.06)	0.980	1709.2	1699.8	1688.1 ±1.1
M9c *sf*	2.4	3353	49734	4812	15.22	80.0	9.1	16002.14	4.4123	0.30042 (.09)	4.26172 (.10)	0.10289 (.05)	0.889	1693.4	1685.0	1676.8 ±0.9
M9b *sf*	1.4	11593	129066	13380	11.42	75.0	11.8	24913.56	3.3189	0.30142 (.07)	4.29804 (.08)	0.10342 (.04)	0.872	1698.3	1693.0	1686.4 ±0.8
M36a *sf*	3.4	6013	18312	3146	3.12	45.4	15.9	22872.40	0.9163	0.29970 (.12)	4.28493 (.13)	0.10369 (.04)	0.944	1689.8	1690.5	1691.3 ±0.8
M36b *sf*	1.9	5737	31174	4076	5.57	59.7	29.5	6522.58	1.6325	0.29948 (.10)	4.27339 (.12)	0.10349 (.06)	0.843	1688.7	1688.3	1687.6 ±1.1
M36c *sf*	0.9	7161	40288	5182	5.77	60.6	14.0	7852.80	1.6942	0.29854 (.12)	4.25747 (.14)	0.10343 (.07)	0.848	1684.1	1685.2	1686.6 ±1.3
M36d *sf*	0.4	8668	36972	5393	4.38	54.1	37.0	1477.54	1.3031	0.29415 (.16)	4.19334 (.19)	0.10339 (.11)	0.838	1662.2	1672.7	1685.9 ±2.0
M37a *sf*	0.3	2779	34139	3446	12.61	77.3	9.5	1622.64	3.7653	0.29264 (.24)	4.16394 (.26)	0.10320 (.09)	0.942	1654.7	1667.0	1682.4 ±1.6
M37b *sf*	0.3	4390	48759	5146	11.39	74.7	28.1	888.85	3.2636	0.30535 (.18)	4.34744 (.21)	0.10326 (.11)	0.857	1717.8	1702.4	1683.5 ±2.0

Table 1 — continued

		Composition						Isotopic Ratios						Dates (Ma)		
Fractions	Estimated Wgt (µg)	U (ppm)	Th (ppm)	Pb (ppm)	Th U	Mol% ^{208}Pb	Com Pb (pg)	^{206}Pb ^{204}Pb	^{208}Pb ^{206}Pb	^{208}Pb ^{232}U	^{207}Pb ^{235}U	^{207}Pb ^{206}Pb	corr. coef.	^{208}Pb ^{232}U	^{207}Pb ^{235}U	^{207}Pb ^{206}Pb
(1)	(2)	(3)	(3)	(3)	(3)		(4)	(5)	(6)	(7)	(7)	(7)				(8)
M37c *sf*	0.1	5275	76612	7644	14.90	79.7	34.8	390.32	4.3243	0.29937 (.27)	4.23797 (.38)	0.10267 (.23)	0.795	1688.2	1681.4	1672.9 ±4.3
M38a *sf*	0.5	3953	47018	4789	12.20	76.2	11.0	3146.51	3.5259	0.30139 (.25)	4.27526 (.29)	0.10288 (.14)	0.877	1698.2	1688.6	1676.7 ±2.5
M38b *sf*	0.3	3497	45446	4531	13.33	77.9	4.4	4973.92	3.9001	0.29893 (.19)	4.25550 (.21)	0.10325 (.08)	0.930	1686.0	1684.8	1683.3 ±1.4
M39a *sf*	0.7	2302	23687	2476	10.56	74.3	18.8	1395.17	3.1841	0.28724 (.20)	4.05552 (.26)	0.10240 (.15)	0.815	1627.7	1645.4	1668.1 ±2.8
M39b *sf*	0.5	1850	24436	2407	13.55	78.5	12.8	1226.18	4.0279	0.29061 (.26)	4.09285 (.28)	0.10215 (.11)	0.918	1644.6	1652.9	1663.5 ±2.1
M39c *sf*	0.2	3109	31853	3358	10.51	73.2	8.7	1586.39	3.0129	0.30142 (.29)	4.24542 (.30)	0.10215 (.09)	0.955	1698.4	1682.9	1663.6 ±1.7

(1) fractions analyzed include the type of mineral, M=monazite, Z=zircon,X=xenotime, followed by analysis number. fraction descriptions include the following abbreviations: aa = air abraded; rf = random fragment; sf =

wg = whole grain. prefix before fraction name represent sample from the sheared dike: A = sheared interior off the sliced fragment; dike; B = unsheared margin of the dike

(2) sample weights, estimated using a dimensions determined from a gridded video monitor, an ellipsoidal geometry and a nominal density of 5.0 g/cc, are known to within 20% based on comparisons of estimated and measured weights

(3) expressed as ppm U and Th and ppm radiogenic Pb. Th concentration and Th/U ratio calculated from the radiogenic ^{208}Pb and $^{208}Pb/^{206}Pb$ ratios, respectively, assuming concordance between the Th-Pb and U-Pb systems.

(4) total common in each analysis

(5) measured ratio corrected for fractionation: Pb fractionation correction is 0.12% ± 0.04% per atomic mass unit (amu) for multicollector analyses and 0.15% ± 0.04% per amu for single collector analysis based on repeated analyses of NBS 981

(6) radiogenic Pb

(7) Pb/U isotopic ratios corrected for fractionation, spike, blank, and initial common Pb: U blank = 1 pg ± 50%; Pb blanks ranged from 5.2 to 1.1 pg during the course of this study and the data were reduced using a Pb blank of 3.5 pg ± 50% — for analyses with less than 3.5 pg total common Pb the total common Pb was assumed to be blank; initial common Pb was calculated using the two-stage model of Stacey and Kramers (1975) using the interpreted age of the sample. Numbers in parentheses are the % error reported at the 2 sigma confidence interval.

(8) uncertainty in the Pb-Pb date in My at the 2 sigma confidence interval

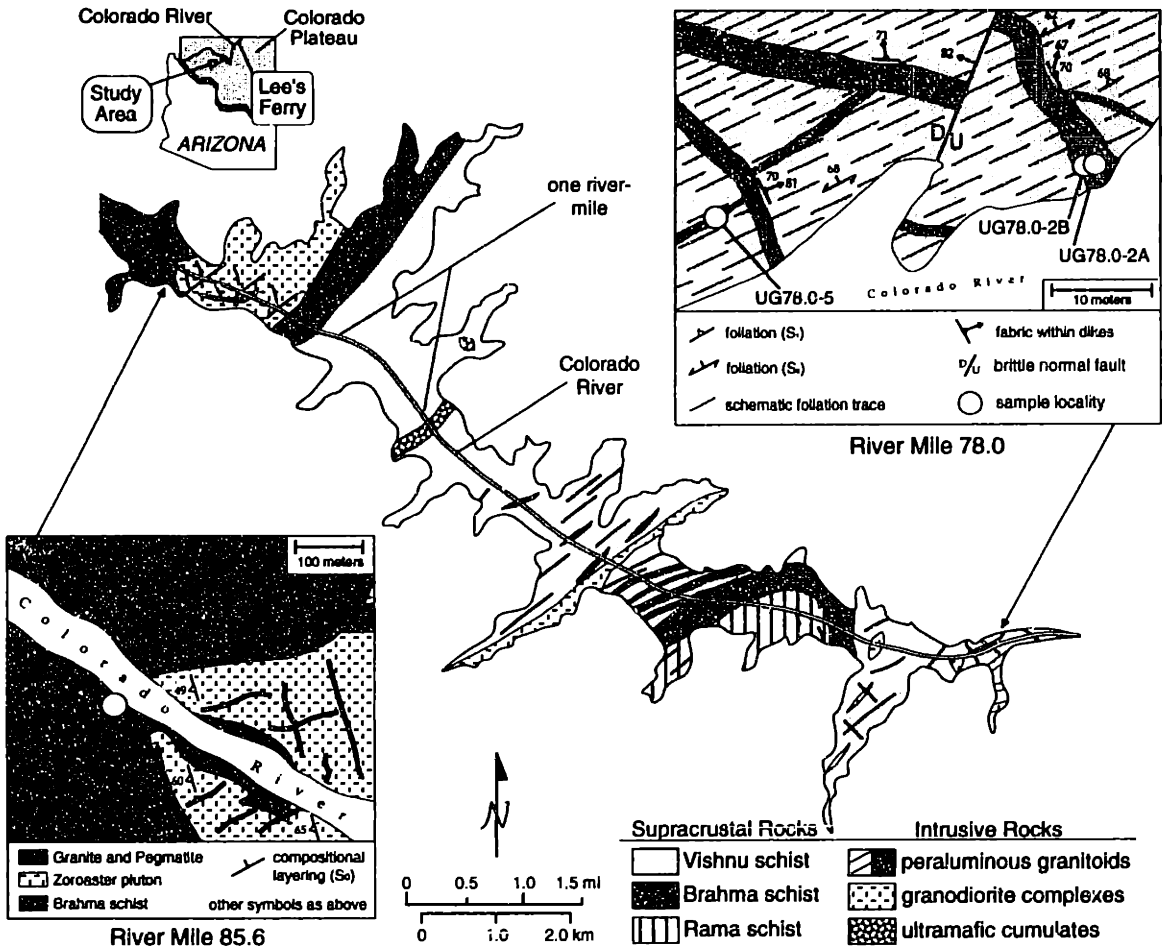
Colorado River
Colorado Plateau
Study Area
Lee's Ferry
ARIZONA
one river-mile
Colorado River
River Mile 78.0
UG78.0-5
UG78.0-2B
UG78.0-2A
Colorado River
10 meters
foliation (S1)
foliation (S2)
schematic foliation trace
fabric within dikes
brittle normal fault
sample locality
River Mile 85.6
100 meters
Granite and Pegmatite
Zoroaster pluton
Brahma schist
compositional layering (So)
other symbols as above
0 0.5 1.0 1.5 mi
0 1.0 2.0 km
Supracrustal Rocks
Vishnu schist
Brahma schist
Rama schist
Intrusive Rocks
peraluminous granitoids
granodiorite complexes
ultramafic cumulates

Figure 1

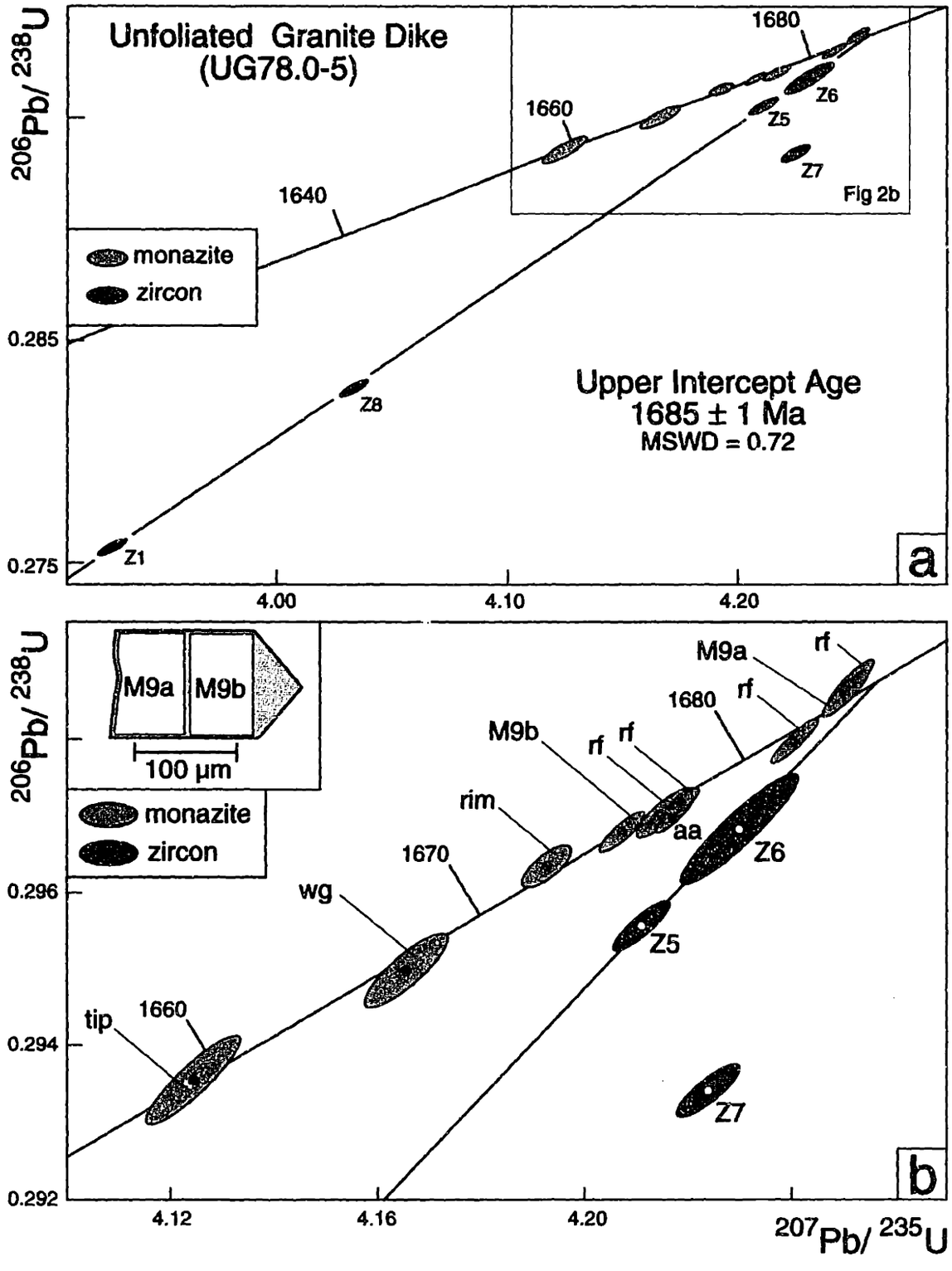
Unfoliated Granite Dike
(UG78.0-5)
1680
1660
1640
Z6
Z5
Z7
Fig 2b
monazite
zircon
Z8
Z1
Upper Intercept Age
1685 ± 1 Ma
MSWD = 0.72
a
0.285
0.275
4.00
4.10
4.20
M9a
M9b
100 µm
rf
rim
aa
wg
1670
tip
1660
b
0.296
0.294
0.292
4.12
4.16
4.20
206Pb/238U
207Pb/235U

Figure 2

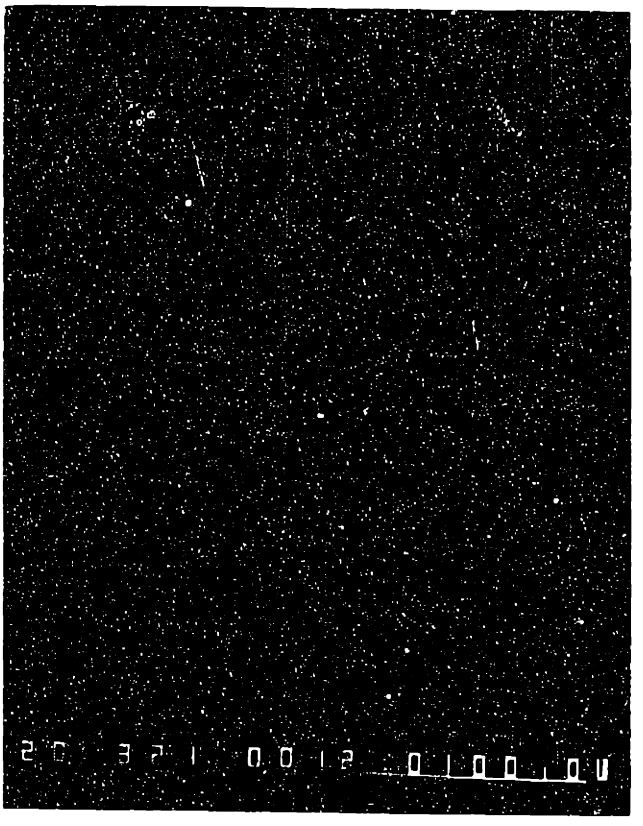

a

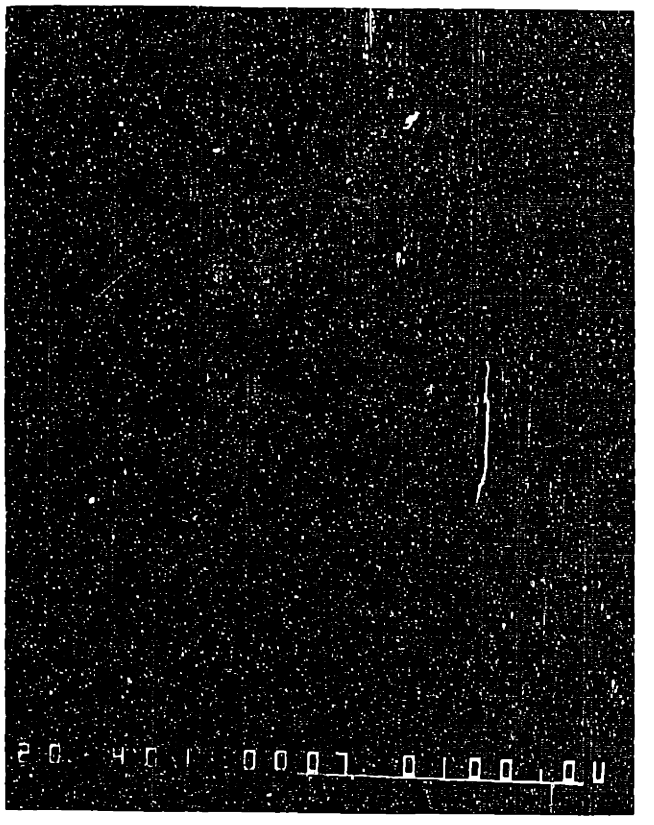

b

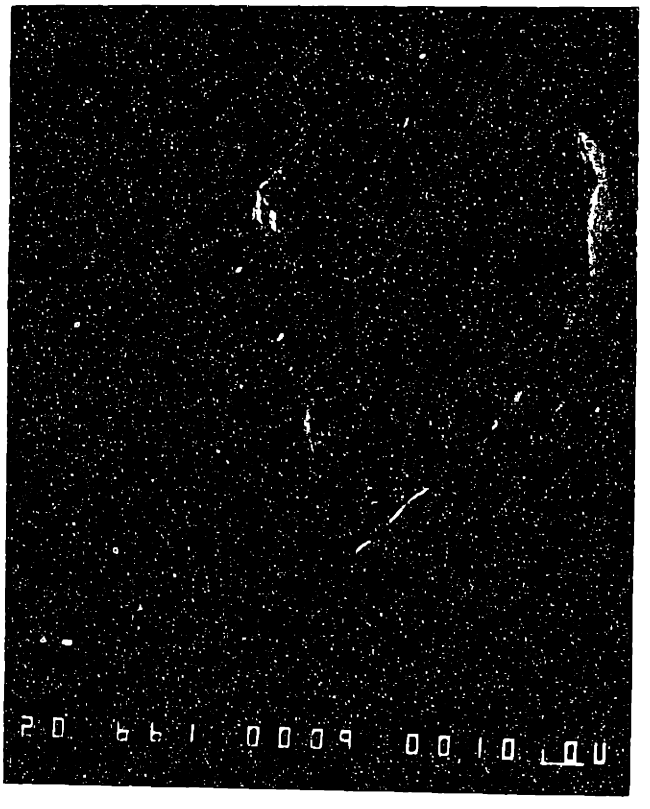

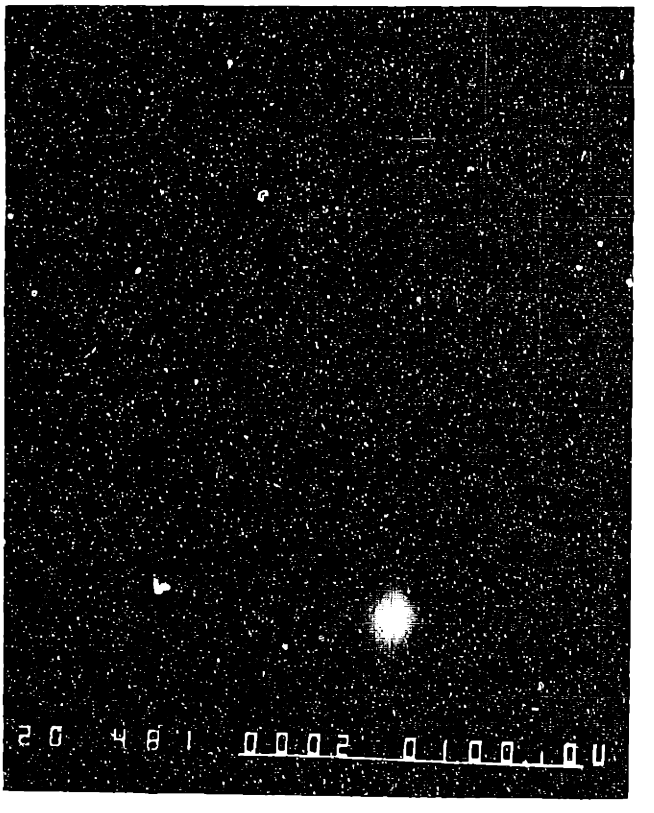

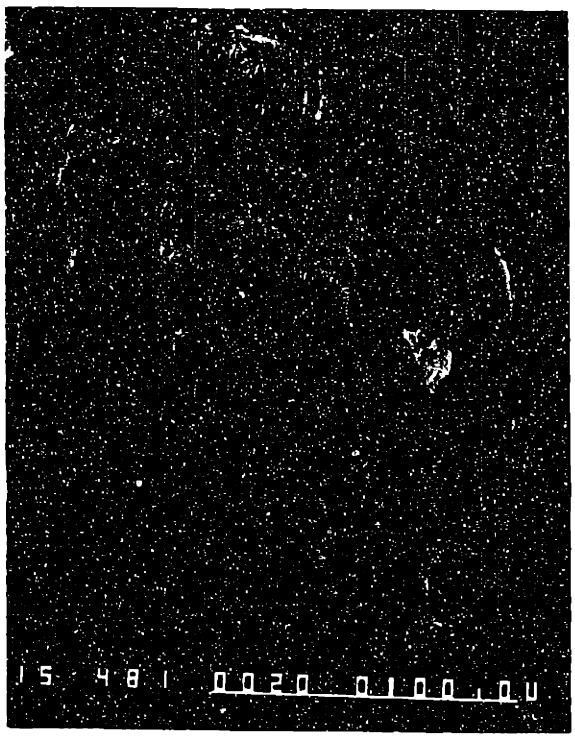

e

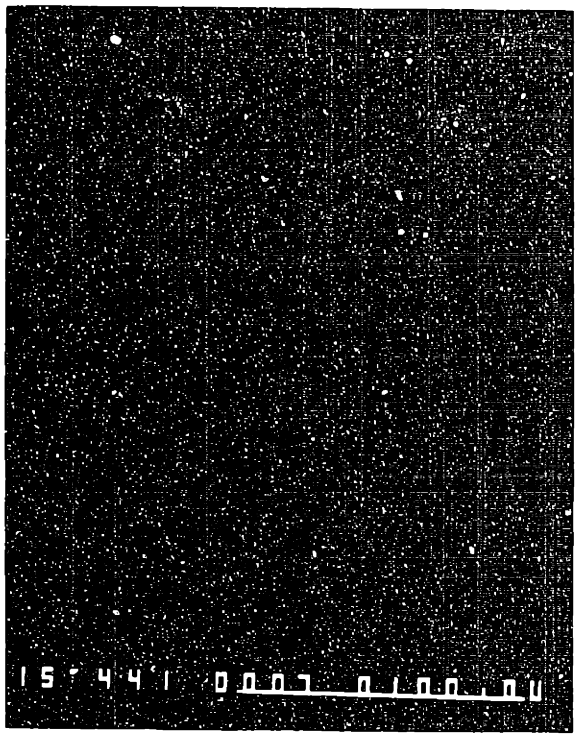

f

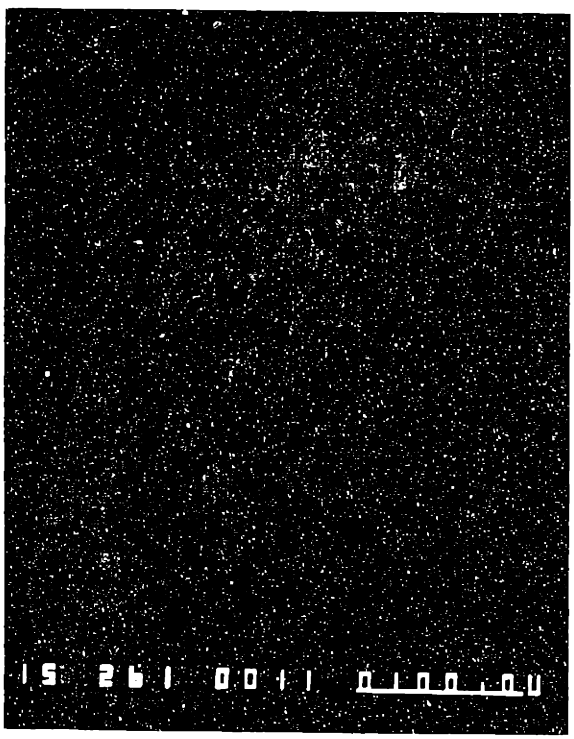

g

Figure 4

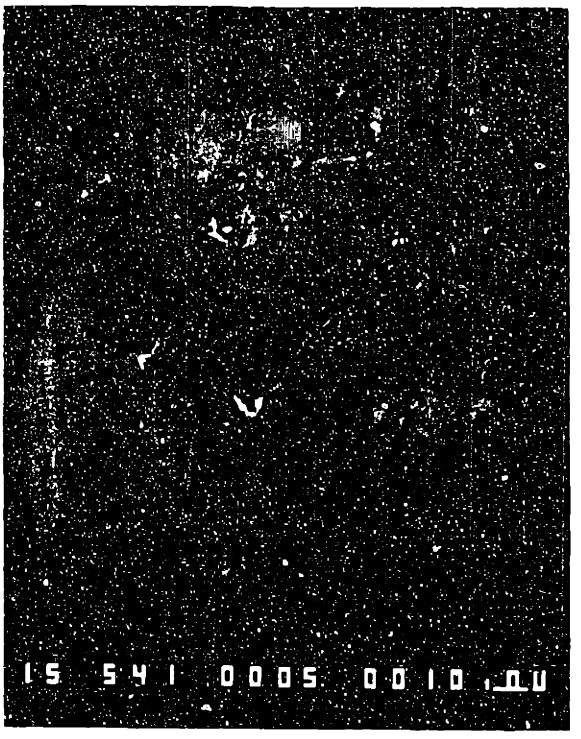
IS 541 0005 0010 DU

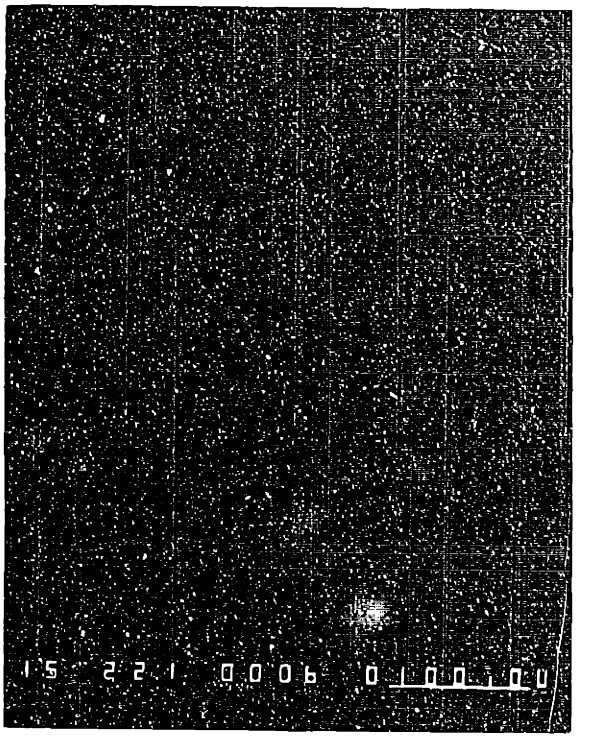
IS 221 0006 0100 DU

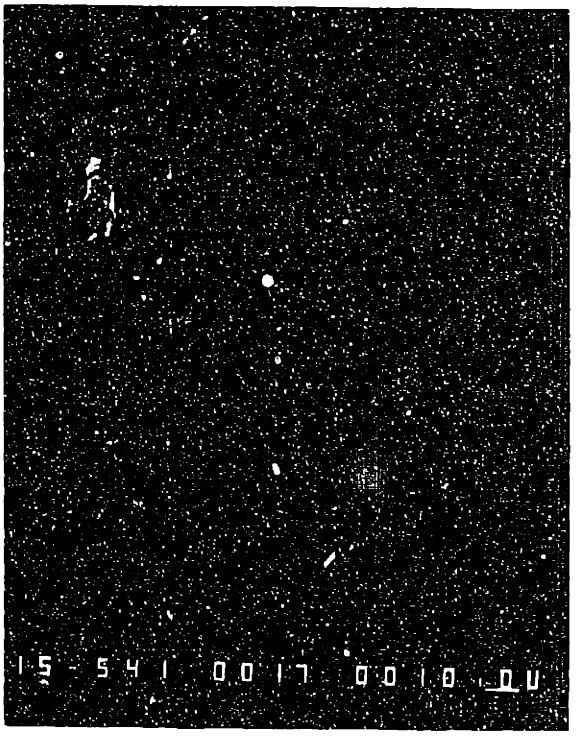
IS 541 0017 0010 DU

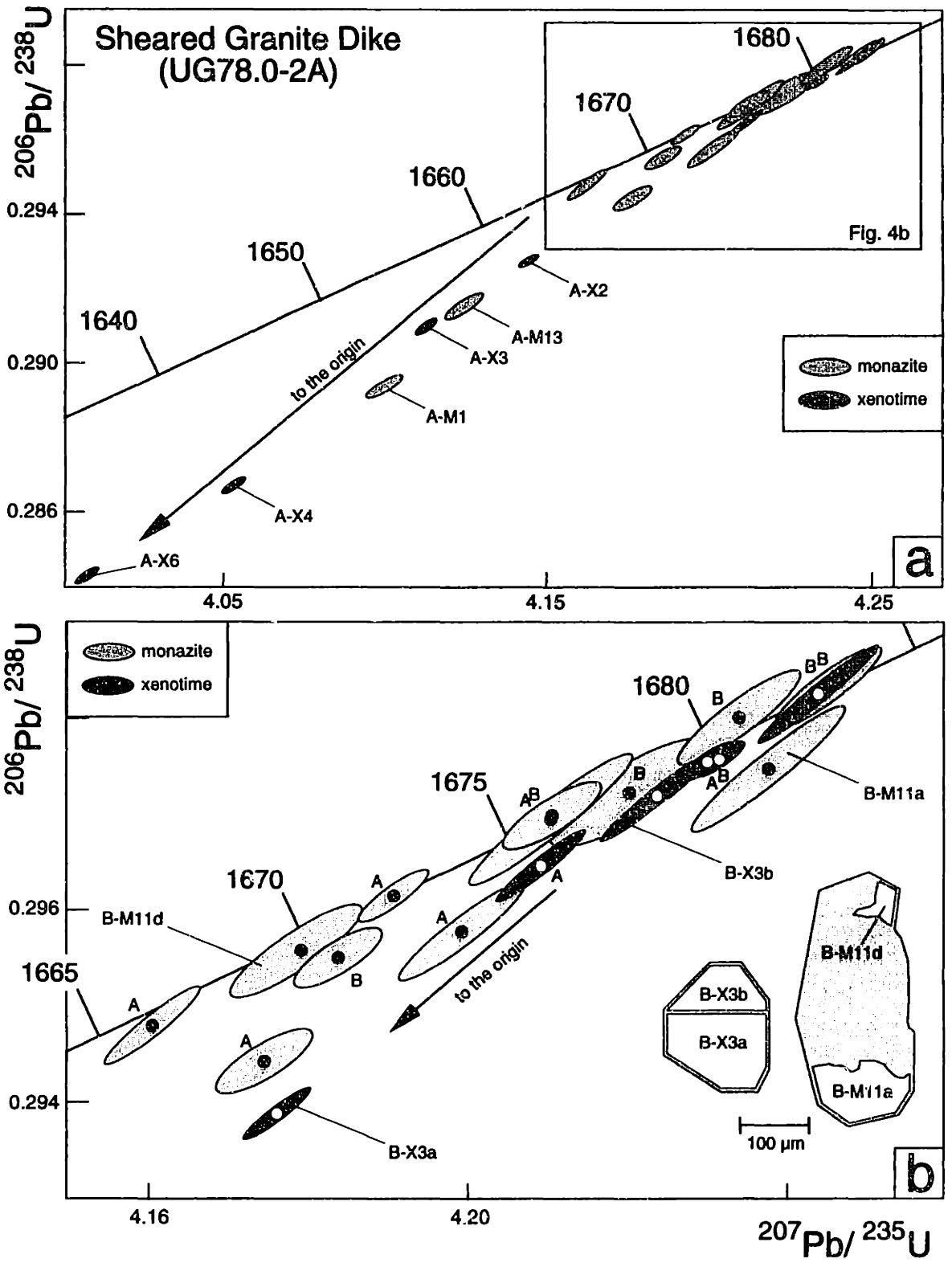
Sheared Granite Dike
(UG78.0-2A)
1680
1670
1660
1650
1640
Fig. 4b
A-X2
A-M13
A-X3
A-M1
A-X4
A-X6
to the origin
monazite
xenotime
0.294
0.290
0.286
4.05
4.15
4.25
a
206Pb/238U
monazite
xenotime
1680
1675
1670
1665
B
A
AB
BB
B-M11a
B-X3b
B-M11d
B-X3a
to the origin
100 µm
0.296
0.294
4.16
4.20
207Pb/235U
b

Figure 4

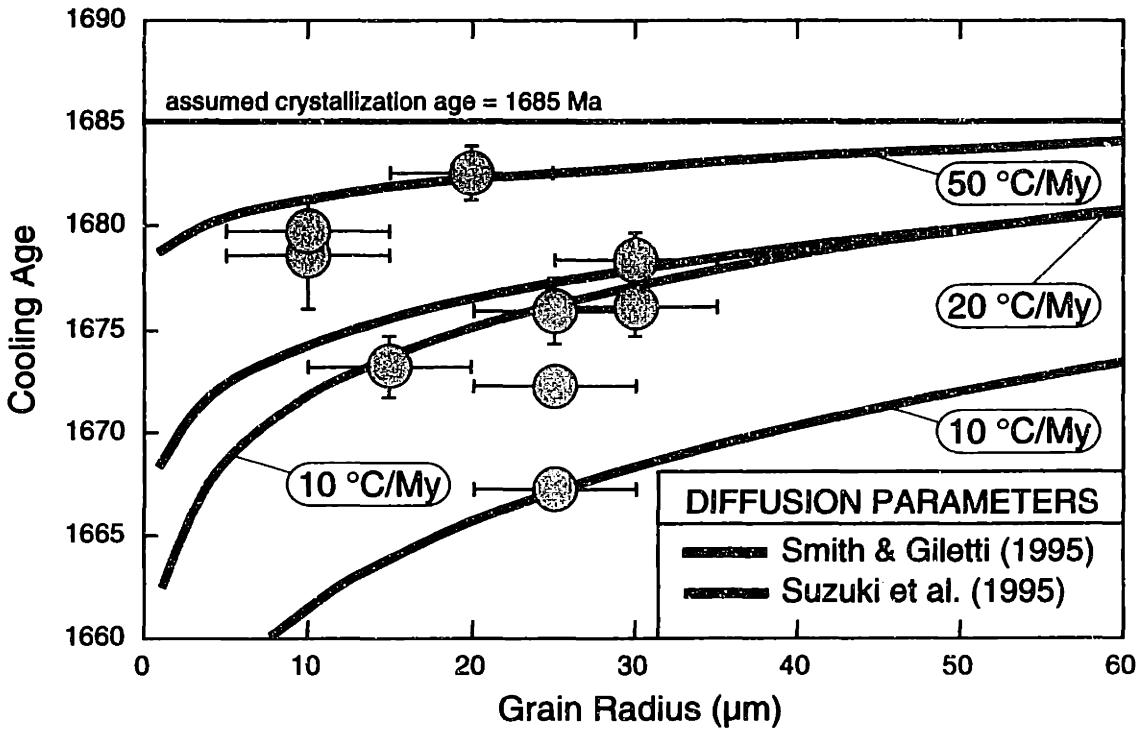
1690
1685
1680
1675
1670
1665
1660
Cooling Age
assumed crystallization age = 1685 Ma
50 °C/My
20 °C/My
10 °C/My
10 °C/My
DIFFUSION PARAMETERS
Smith & Giletti (1995)
Suzuki et al. (1995)
0
10
20
30
40
50
60
Grain Radius (μm)

Figure 5

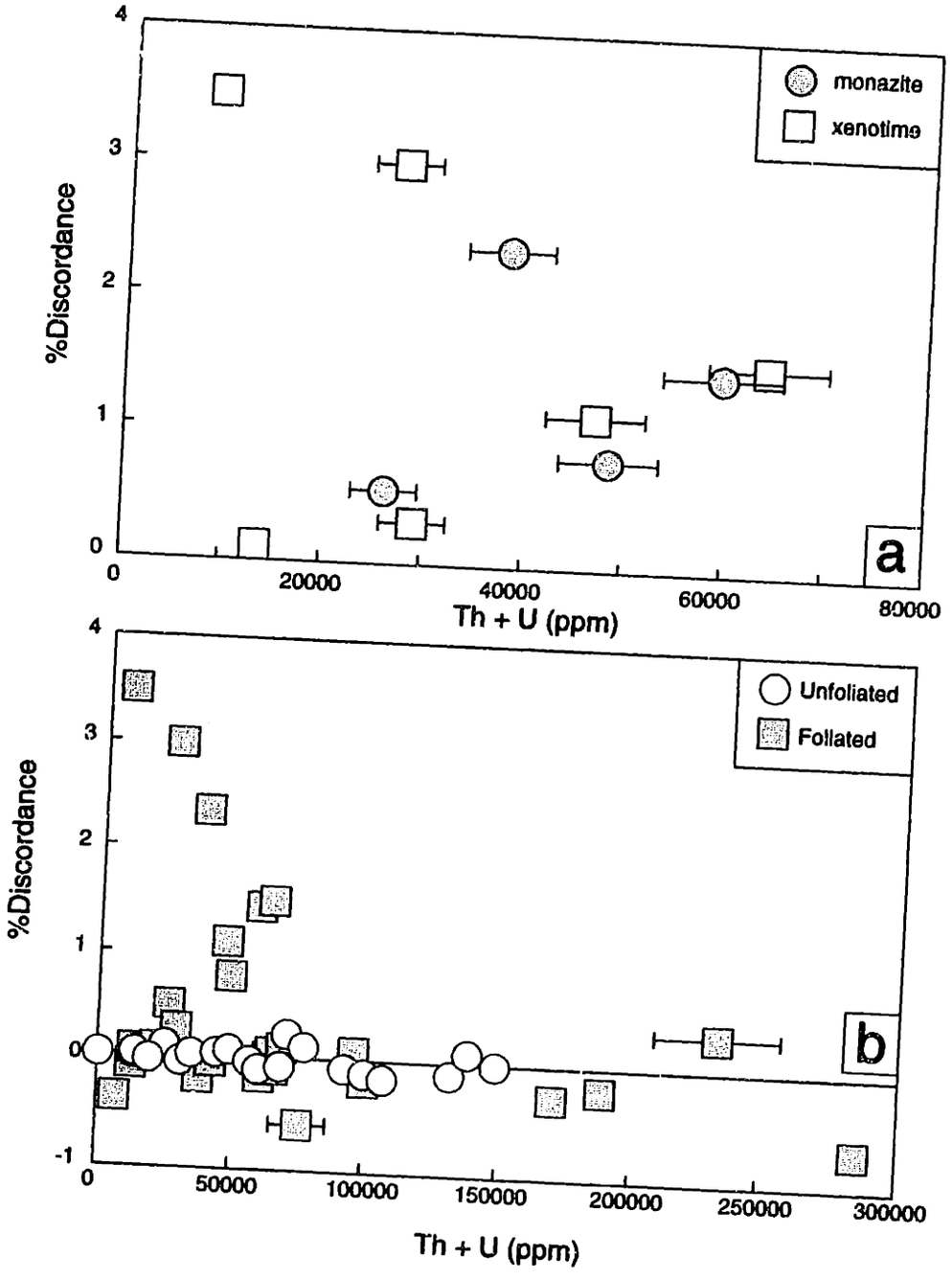
monazite
xenotime
%Discordance
Th + U (ppm)
a
Unfoliated
Foliated
%Discordance
Th + U (ppm)
b

Figure 6

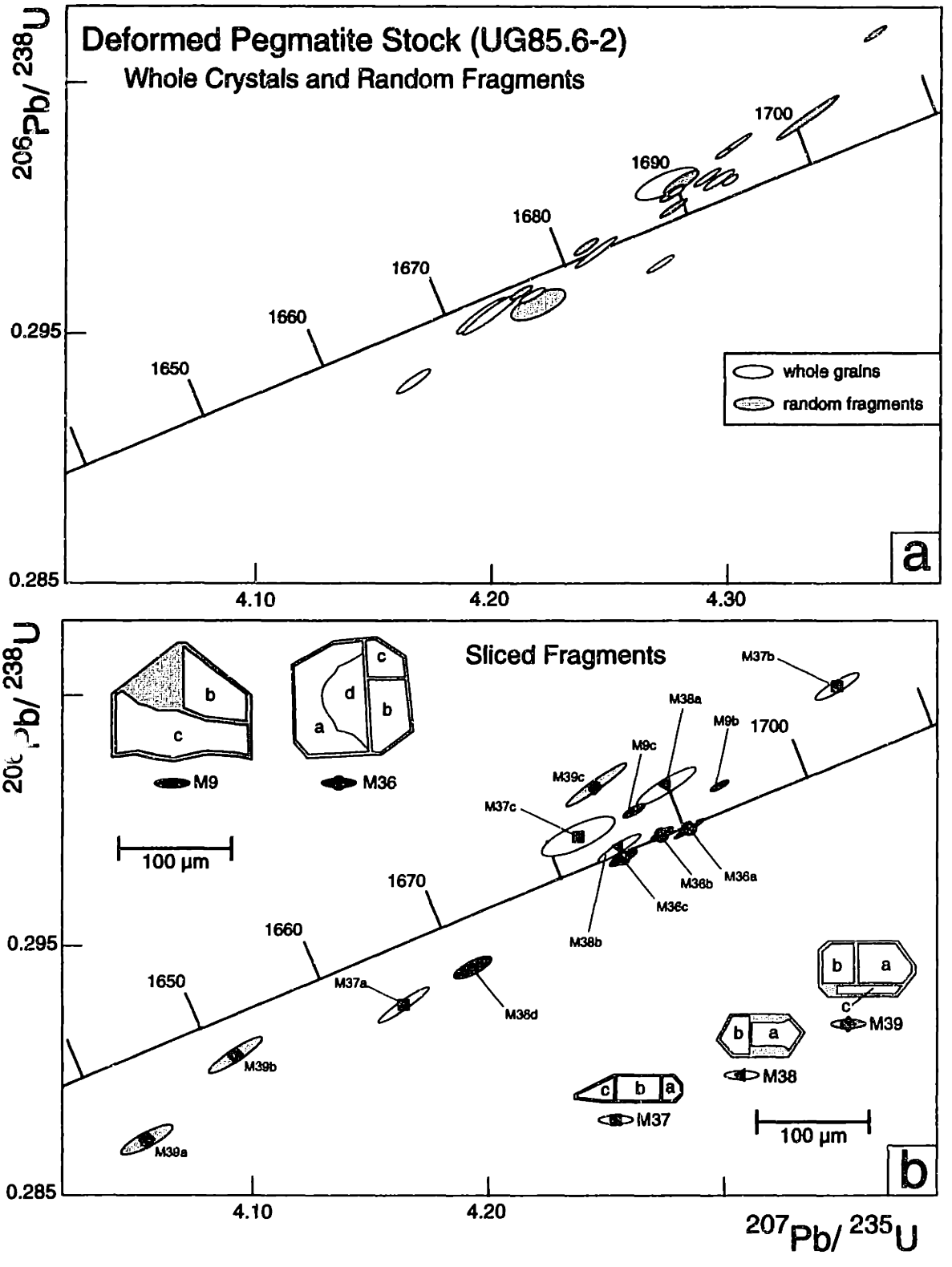
Deformed Pegmatite Stock (UG85.6-2)
Whole Crystals and Random Fragments
206Pb/238U
207Pb/235U
1700
1690
1680
1670
1660
1650
0.295
0.285
4.10
4.20
4.30
whole grains
random fragments
a
Sliced Fragments
M9
M36
100 µm
M37b
M38a
M9b
M9c
M39c
M37c
M38b
M36a
M36c
M38d
M37a
M39b
M39a
M39
M38
M37
b
4.10
4.20

Figure 7

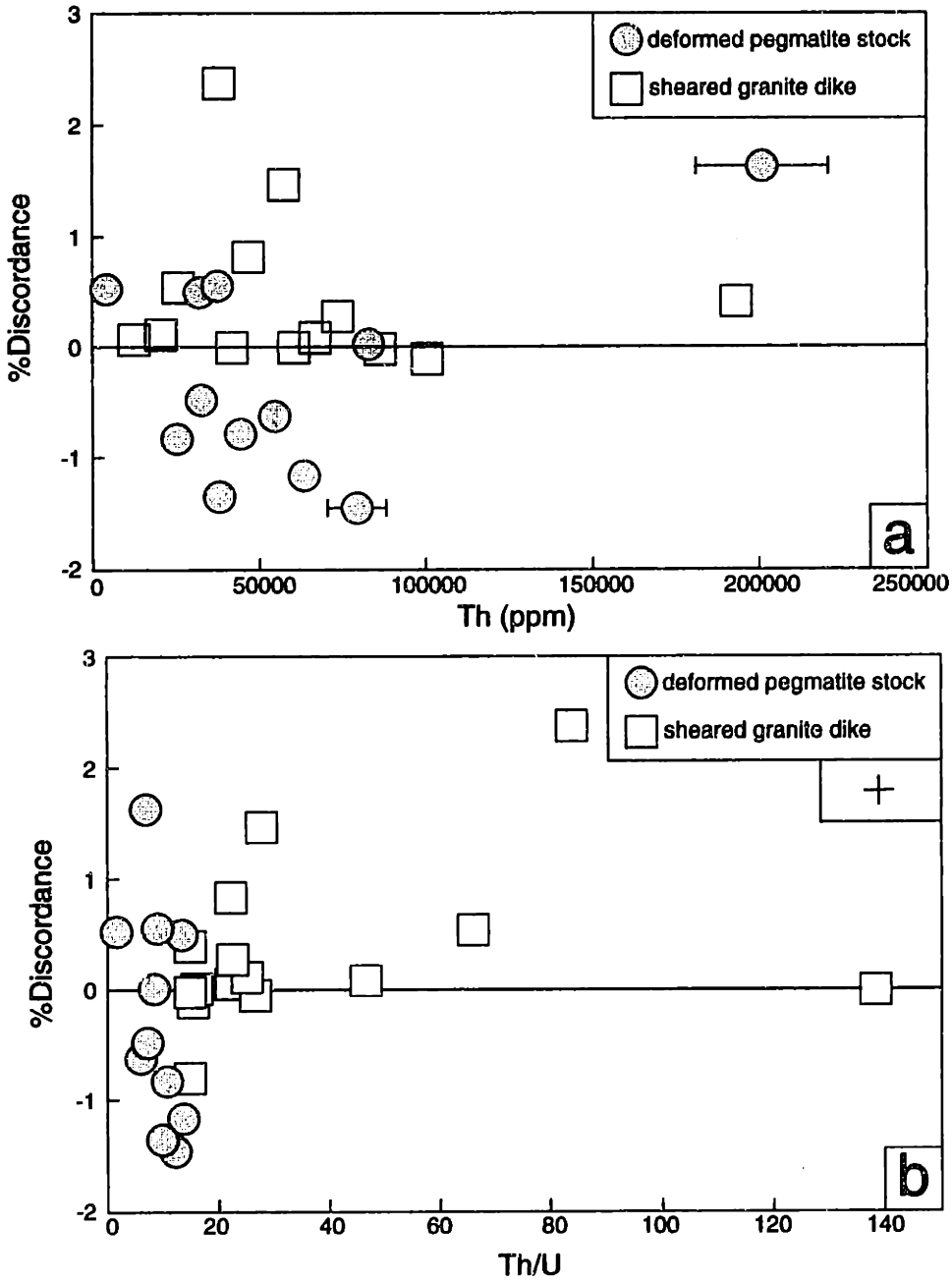
deformed pegmatite stock
sheared granite dike
%Discordance
Th (ppm)
a
b
Th/U

Figure 8

CHAPTER 4

U-PB MONAZITE, XENOTIME AND SPHENE GEOCHRONOLOGICAL CONSTRAINTS ON THE HIGH-TEMPERATURE THERMAL HISTORY OF PALEOPROTEROZOIC MIGMATITES FROM THE GRAND CANYON, ARIZONA

INTRODUCTION

Partial melting of pelitic schists during metamorphism represents an important mechanism for chemical differentiation, heat transfer and redistribution of heat-producing elements within continental crust. Many deeply eroded orogenic belts contain large volumes of peraluminous leucogranite that represent both the products of partial melting and the vehicles for much of the mass and heat transfer associated with orogenesis. Whereas the petrogenesis of peraluminous granites is well known, the rates and duration of the metamorphic heating, partial melting, melt accumulation and melt emplacement are only broadly known in most orogenic belts. Such rates reflect the tectonic processes responsible for deformation and metamorphism. Therefore, a precise chronology of deformation, metamorphism and magmatism reveals insight into the tectonic processes operative during orogenesis in deeply eroded metamorphic terrains. These constraints can be invaluable to reconstructing the tectonic and thermal history of ancient mountain belts where the upper crustal and surficial geology are not preserved.

Intrusive bodies of peraluminous granite are ideal for constraining the timing and duration of metamorphism, anatexis and deformation during orogenesis. The metamorphic reactions responsible for partial melting of metasedimentary source rocks are well-characterized (e.g., Clemens and Wall 1981; LeBreton and Thompson, 1988; Vielzeuf and Holloway, 1988) and the relative volumes of melt produced by these

reactions are well known (Vielzeuf and Holloway, 1988). Furthermore, both peraluminous granites and the metamorphic source rocks contain monazite ($LREEPO_4$) and/or xenotime (YPO_4) (e.g., Harrison and Watson, 1983; Watson et al. 1989; Watt and Harley, 1993; Vidal et al. 1984; Nabelek and Glascock 1995) which are both ideal U-Pb geochronometers because they both have high closure temperatures (Copeland et al., 1988; Childe et al., 1993) and often yield concordant U-Pb dates (Parrish, 1990; Heaman and Parrish, 1991). Therefore, a detailed U-Pb geochronological study of monazite and xenotime from migmatites and peraluminous granite intrusions in deeply eroded metamorphic terrains can provide insight into the high-temperature thermal history and absolute timing constraints on the processes that drive metamorphism in the middle to lower crust during orogenesis.

Migmatites and peraluminous granite dikes are important components of the high-grade crustal blocks in the Grand Canyon transect. The Mineral Canyon block in the easternmost Upper Granite Gorge (Fig. 1) contains both migmatitic metasedimentary rocks and abundant peraluminous granite dikes that are ideal for reconstructing the high-temperature thermal evolution. This paper describes a detailed U-Pb geochronological study of Paleoproterozoic migmatites and granite dikes exposed in a single outcrop in the Mineral Canyon block. We use field, petrographic and U-Pb monazite, xenotime and sphene geochronologic data from different components of the migmatites and the cross-cutting leucogranite dikes to construct a chronology of prograde to peak metamorphism, melt-generation, post-peak cooling, leucogranite emplacement, and retrograde metamorphism that spans 50 m.y. The resulting chronology forms the basis for evaluating the interdependence of magmatism, deformation and metamorphism in space and time at mid-crustal levels during arc accretion.

GEOLOGIC BACKGROUND

Paleoproterozoic igneous and metamorphic rocks are exposed for approximately 70 km along the Colorado River in the Upper Granite Gorge in Grand Canyon National Park. These rocks are the remnants of island arcs and continental margin arcs that were accreted to the southern margin of Laurentia during the ca. 1.7 Ga Yavapai orogeny. The geology of the Upper Gorge is characterized by three dominant lithostratigraphic units: 1) 1750 to 1740 Ma metasedimentary and metavolcanic supracrustal rocks; 2) 1740 - 1710 Ma mafic- to intermediate-composition plutonic rocks; and 3) peraluminous granite and pegmatite intrusive rocks (Fig. 1; Ilg et al., 1996b; Hawkins et al., 1996). The supracrustal rocks and mafic to intermediate composition plutons contain multiple generations of fabrics and structures and preserve lower amphibolite to lower granulite facies mineral assemblages (Ilg et al., 1996b). The peraluminous granite and pegmatite intrusions were associated in time and space with deformation but largely post-dated development of peak metamorphic mineral assemblages (Hawkins et al., 1996).

Five northeast-striking shear and fault zones divide the Upper Gorge transect into crustal blocks that preserve contrasting metamorphic and thermal histories (Fig. 1; Ilg et al., 1996b; Hawkins and Bowring, unpublished data). Preliminary thermochronology (Hawkins and Bowring, unpublished data) and P-T path determination (Williams, 1994; unpublished data) suggest that after a short period of relatively rapid (but spatially heterogeneous) post-peak cooling, the rocks underwent an extended period of relatively slow cooling until final unroofing and near-surface residence by about 1250 Ma (e.g., Elston, 1989). The rocks remained at shallow crustal levels (at temperatures below about 250 °C) until late Cenozoic uplift and of the Colorado Plateau (e.g., Naeser and Elston, 1987) when the rocks were exposed at the surface.

The samples described in this study were collected from a single outcrop in the Mineral Canyon crustal block in the eastern Upper Gorge. Figure 1 shows that the

dominant structure is a kilometer-scale antiform (Sockdolager antiform; F_2) that folds both compositional layering (S_o) and early tectonite fabric (S_1). The pervasive northeast-striking tectonite fabric (S_2) is axial planar to F_2 folds in their core regions and subparallel to S_1 on sheared fold limbs where they form a composite S_1/S_2 fabric (Ilg et al., 1996b). The core of the Sockdolager antiform is occupied by metavolcanic rocks of the Rama schist which yielded a U-Pb zircon crystallization age of 1741 ± 1 Ma as well as near-concordant U-Pb dates between 1706 and 1697 Ma from metamorphic monazites (Hawkins et al., 1996). The supracrustal rocks are intruded by peraluminous granite and pegmatite dikes, locally comprising 50 % of the rock volume (Fig 1), that yield crystallization ages between 1685 and 1680 Ma (Hawkins et al., 1996; Chapter 3). The field relationships and U-Pb ages provide broad constraints consistent with fabric formation and metamorphism at about 1700 Ma followed by widespread intrusion of peraluminous granite dikes between 1685 and 1680 Ma contemporaneous with continued heterogeneous shortening (Chapters 2-3). The rocks exposed at river-mile 78.0 are representative of the geology in the Mineral Canyon crustal block which is characterized by migmatitic Vishnu and Rama schist intruded by peraluminous granite and pegmatite dikes (Fig. 1). Mineral assemblages are consistent with lower granulite facies conditions estimated by Ilg et al. (1996b) to be 720 °C and 6 kbars.

FIELD OBSERVATIONS FROM MILE 78.0

The following field observations provide: 1) fundamental constraints on the nature and origin of the migmatites at river-mile 78.0; 2) a basis for our sampling rationale; and 3) important observations with which to evaluate the U-Pb data.

The outcrop at river mile 78.0 exposes isoclinally folded metasedimentary rocks of the Vishnu schist intruded by variably deformed 1685 to 1680 Ma granite and pegmatite

dikes (Fig. 1). The Vishnu schist in this area is composed of interlayered (centimeter- to meter-scale layers) biotite schist, quartzofeldspathic schist and calc-silicate gneiss which contain composite S_1/S_2 fabric. Of these, only the biotite schist is migmatitic; layers of biotite schist contain decimeter- to meter-scale, highly-strained pods and stringers of medium- to coarse-grained granite and pegmatite that make up less than 10% of the rock volume (Fig. 2a). The pods are lozenge-shaped in three dimensions and exhibit medium- to coarse-grained, hypidiomorphic textures. Each leucosomal pod is mantled by prominent, centimeter-scale selvages that are strongly depleted in quartz, alkali feldspar and plagioclase relative to paleosomal schist (Fig. 2). The melanosomal selvages may represent reaction rims around migrating melt pods or restite from *in situ* melting. The absence of selvages at the margins of granite dikes that cross-cut the migmatite suggests that the selvages are genetically related to the leucosomes. Although there are local examples of melt migration, most of the leucosomes occur as isolated pods.

Peraluminous granite dikes provide minimum time brackets on the formation of both the migmatites and the composite fabric; they also preserve evidence for retrograde metamorphism. The dikes cross-cut compositional layering, composite S_1/S_2 fabric, and deformed leucosome pods, and some dikes contain randomly-oriented xenoliths of foliated schist and migmatite. The dikes themselves are variably deformed, but the foliated xenoliths indicate that the dikes post-date the development of the composite fabric.

PREVIOUS U-PB GEOCHRONOLOGY

Three granite dikes from this outcrop yielded U-Pb (zircon, monazite and/or xenotime) crystallization ages of 1680 ± 1 Ma, 1682 ± 3 Ma, 1685 ± 1 Ma (Hawkins et al., 1996; Chapter 3) which are consistent with cross-cutting relationships among the

dikes (Fig. 1). These ages also overlap with the U-Pb ages of other dikes in the Mineral Canyon block (Hawkins et al. 1996). In addition to yielding crystallization ages, U-Pb data from two of these dikes preserve evidence, within individual crystals of monazite, for a subsolidus disturbance in the U-Pb system (Chapter 3). Based on textural observations, compositional data and U-Pb micro-sampling of monazite crystals that were previously imaged under the electron microscope, Hawkins and Bowring (in review) interpreted these secondary domains to result from fluid-mineral interaction under retrograde conditions around 1660 Ma. In summary, the U-Pb data from three dikes at river-mile 78.0 indicate that the migmatites and the composite fabric formed prior to 1685 Ma and that retrograde fluid-rock interaction occurred around 1660 Ma.

SAMPLE DESCRIPTIONS

Our sampling strategy was designed to bracket the timing of peak metamorphism by dating metamorphic monazite from the schist and magmatic monazite from the leucosomes and to constrain post-peak metamorphic cooling using U-Pb data from metamorphic sphene. Five samples were collected to meet these goals (localities shown in Fig. 1) : a paleosomal schist (UG78.0-4), a meter-scale leucosomal pegmatite (UG78.0-6), a coupled leucosome and melanosome pair (crushed separately as samples UG78.0-9A & -9B) and a calc-silicate gneiss (UG78.0-3). The petrographic descriptions of these samples that follow provide additional independent constraints for evaluating both the U-Pb data and the nature and origin of the migmatites.

The paleosomal biotite-sillimanite schist was collected from a 10 centimeter-thick layer that contained few leucosomal pods and melanosomal selvages. The rock is composed of biotite, sillimanite, muscovite, quartz, plagioclase, and alkali feldspar. Muscovite and sillimanite reaction textures are well-preserved; throughout the rock,

medium-grained crystals of muscovite are partially replaced by prismatic and fibrolitic sillimanite (Fig. 3) indicating progress of the reaction:

muscovite + quartz ± plagioclase = sillimanite + alkali feldspar + vapor/melt.

Sillimanite also occurs along the grain boundaries between adjacent biotite crystals and, in some parts of the rocks, dense mats of fibrolite completely envelope isolated biotite grains. However, cordierite and garnet are not present in the rock, indicating that the apparent reaction textures between biotite and sillimanite reflect the tendency of sillimanite to nulceate on biotite crystals (Williams, personal communication, 1995). Plagioclase crystals are not altered. Monazite is an abundant accessory phase that occurs as prominent inclusions in biotite and plagioclase and as smaller crystals in the interstices of the rock. Chlorite partially replaces biotite locally.

The melanosomal selvages are pretrographically similar to the paleosomal schist, although the modal mineralogy is different. The selvages comprise biotite and sillimanite, with minor amounts of quartz, alkali feldspar and plagioclase. Sillimanite occurs as both dense mats of fibrolite and isolated prismatic crystals associated with biotite. Muscovite occurs as deeply embayed crystals in contact with sillimanite, showing similar textures to muscovite in the paleosomal schist. Rare plagioclase grains in the melanosome are invariably altered to sausserite. Monazite is an abundant accessory mineral that occurs as prominent inclusions in biotite and as smaller crystals in the interstices. Chlorite, which partially replaces biotite, is restricted to biotite crystals adjacent to leucosomes and is more abundant than in the paleosomal schist.

The textural and mineralogical observations from the paleosomal schist and melanosomal selvages place general but significant constraints on the P-T conditions during peak metamorphism. Both the paleosomal schist and the melanosomal selvage

preserve textural evidence for progress of the reaction muscovite breakdown reaction shown above. The mineral assemblages and reaction textures place the metamorphic conditions in the P-T space bounded by the sillimanite stability field at or above the muscovite breakdown (second sillimanite) reaction boundary. Phase relationships in the Ca-K-Na-Al-Si-H_2O (CKNASH) and K-Fe-Mg-Al-Si-H_2O (KFMASH) compositional subsystems indicate that most of the P-T space defined by the petrographic observations lie above the water-saturated pelite solidus (Fig. 4). In other words, the P-T conditions were probably appropriate for partial melting of the biotite schist via the breakdown of muscovite to sillimanite. As shown in figure 4, this interpretation of the petrographic data is consistent with thermobarometric estimates from a garnet-bearing assemblage at river-mile 78.9 that yielded peak conditions of 720 °C and 6 kbars (Ilg et al., 1996b).

The leucosomal granite and pegmatite pods appear to be composed of the mineral assemblage that is depleted in the melanosomal selvages; the pods are composed of quartz, alkali feldspar, and plagioclase with minor biotite and/or muscovite. Quartz exhibits undulatory extinction, but there is no evidence for grain size reduction or subgrain development; the textures are hypidiomorphic inequigranular. Both discrete crystals and exsolved lamellae of plagioclase are partially altered to sausserite.

Many leucosome pods contain selvage material that is either contiguous with the selvage or isolated as xenoliths (Fig. 2b). In general, the isolated xenoliths are partially disaggregated and chemically altered. The chemical alteration is expressed as extensive alteration of biotite to ilmenite and quartz. Unreacted biotite is partially altered to chlorite.

Monazite and xenotime in the leucosomes occur as euhedral crystals in the interstices, and as xenocrysts in association with xenoliths of the selvage. Many crystals contain optically distinct cores and some crystals, especially xenotime crystals, exhibit oscillatory zoning in thin section.

The calc-silicate gneiss collected for U-Pb sphene dating contained abundant, idioblastic sphene crystals. The calc-silicate gneisses are distinctive rocks with variable mineralogy, generally exhibiting both textural and mineralogical zoning. The sample, which was a 30-centimeter-long discontinuous lens, was collected from a one-meter-thick layer of biotite quartzofeldspathic schist about 5 meters from a sheared granite dike (Fig. 1). The rock consists of two distinct zones with identical mineralogy: quartz + tremolitic amphibole + garnet + plagioclase. The outer zone, in contact with the quartzofeldspathic schist, is fine-grained and contains less garnet and amphibole than the medium-grained core zone. Sphene is present in both zones but is much more abundant in the medium-grained zone. There is no textural evidence for the sphene-producing mineral reaction — sphene occurs as idioblastic, lentil-shaped, randomly-oriented crystals ranging in grain size (long dimension) from 40 to 350 μm. The crystals are brown and the color is homogeneous: there is no textural evidence in thin section or in the mineral separates for core-overgrowth relationships or multiple generations of growth.

BACK-SCATTERED ELECTRON IMAGING

Back-scattered electron imaging of monazite and xenotime permit petrographic observations at high magnification. The images provide an invaluable means of evaluating textural relationships between the datable accessory phases and the mineral reactions preserved in the rock-forming minerals. Such observations have important implications for the paragenesis of the accessory minerals and provide a means of linking that paragenesis to metamorphic reactions and magmatic crystallization sequences. This section describes the textural observations in the migmatite samples.

Monazite crystals in the paleosomal schist (UG78.0-4) and the melanosomal schist have two end-member morphologies: idioblastic crystals with well defined crystal faces; and embayed, xenoblastic crystals. Idioblastic crystals invariably occur as inclusions in

biotite, plagioclase and quartz, whereas xenoblastic crystals occur along grain boundaries between the rock-forming minerals, especially in association with muscovite, sillimanite and quartz. (Fig. 5a,b,c). These relationships imply that only those crystals that occupied interstitial sites in the rock were partially resorbed during melt-production. Further evidence for the partial dissolution of monazite in the presence of melt is provided by the textural relationships shown in figure 5c. Note that the monazite crystal in this image has rational crystal faces against biotite and resorbed margins against intergrowths of alkali feldspar and sillimanite near biotite grain boundaries, muscovite and quartz. Xenotime crystals from the melanosomal selvage exhibit similar textural relationships. We interpret the textural relationships among these minerals to indicate that: 1) growth of monazite spanned the interval of sillimanite growth; and 2) those crystals which grew prior to the development of sillimanite were partially resorbed during sillimanite growth (Figs. 5b,c).

Regardless of the morphology, monazite crystals from the paleosomal schist and melanosomal selvage preserve evidence for a protracted growth history. Monazite crystals have internal compositional variation characterized by local truncations of discontinuous growth zones which we interpret to reflect cyclic precipitation and dissolution over the course of the growth history (Fig. 5d). These growth cycles may indicate that the fluids from which the monazite crystallized were buffered at conditions close to monazite saturation. There is no textural evidence in the paleosomal schist that monazite crystals were reactive during alteration of biotite to chlorite, however most monazites from the melanosomal selvage in contact with chlorite are embayed and have secondary domains that truncate primary growth zoning. Hawkins and Bowring (1996) demonstrated that similar secondary domains in monazite crystals from the cross-cutting dikes in this outcrop formed 15 to 25 m.y. after the dikes crystallized.

Back-scattered electron images of monazite and xenotime crystals from the leucosomal granite (sample UG78.0-6) and pegmatite (UG78.0-9A) show clear textural evidence for magmatic growth and, in some monazite crystals, xenocrystic cores. Most xenotime crystals and many monazite crystals exhibit core-to-rim oscillatory zoning parallel to rational crystal faces (Fig. 5e). Some monazite and xenotime grains exhibit more complex growth histories involving periods of resorption prior to continued precipitation (Fig. 5f). We interpret both types of textures as evidence for magmatic crystallization. In other grains, however, oscillatory-zoned rims overgrow compositionally distinct, deeply embayed cores characterized by irregular compositional zoning (Fig. 5f). We suggest that the resorbed domains are xenocrystic because: 1) many contain inclusions of sillimanite; 2) they are deeply embayed; and 3) they have distinct compositions relative to rim domains (higher Th concentrations).
Monazites from xenoliths of selvage material within the leucosomes are deeply embayed and many of these crystals have external morphologies similar to compositionally distinct core domains in magmatic crystals (Fig 5h).

ANALYTICAL TECHNIQUES

Monazite, xenotime and sphene were separated by standard crushing, heavy liquid and magnetic techniques. Hand-picked crystals were measured, photographed and washed in acetone and warm H_2O (monazite and xenotime) or acetone and 30% HNO_3 (zircon and sphene) prior to dissolution. Samples were dissolved in 300 µl teflon nanocapsules containing 11 - 12 N HCl (monazite and xenotime) or 50% HF + 14N HNO_3 (sphene) and a mixed ^{205}Pb-^{233}U-^{235}U tracer solution. Lead and uranium were separated from monazite, xenotime and zircon using HCl-based ion chromatography modified after Krogh (1973). Sphene ion chromatography used HBr chemistry for

separation of Pb and HCl chemistry for separation of U. The samples were analyzed using conventional thermal ionization mass spectrometry on a VG Sector 54 mass spectrometer at the Massachusetts Institute of Technology. Lead was analyzed either: 1) in static mode, using Faraday detectors for all isotopes except ^{204}Pb, which was measured simultaneously with the Daly detector in ion-counting mode; or 2) by peak-jumping using a Daly detector in ion-counting mode. Uranium was analyzed as a metal in static mode using Faraday collectors. Statistical analysis of the data relies on the algorithms of Ludwig (1989). Additional analytical details are presented in Table 1.

For the purpose of description, we report the magnitude of U-Pb discordance, for both normally and reversely discordant analyses, as the difference between $^{207}Pb/^{206}Pb$ date and the $^{206}Pb/^{238}U$ date and use the Pb-Pb date as a minimum age for each analysis. Reversely discordant dates have negative discordance and normally discordant dates have positive discordance. The degree of discordance is calculated as a percentage of the total distance from the origin to the Pb-Pb age along concordia.

To investigate intracrystalline variations in the U-Pb systematics of both monazite and xenotime, we sliced several crystals into fragments, carefully recording the original spatial relationships, and analyzed the fragments separately. These analyses are identified in Table 1 by a lower case letter at the end of the fraction name and are shown along with drawings of the crystals in Figures 7 and 9. Our slicing technique can produce fragments as small as 20 x 10 x 10 μm (≈ 100 ng total sample weight)— similar to the dimensions of the pit produced by an ion probe analysis (e.g., DeWolf et al., 1993; Harrison, et al., 1995) — that yield analytical uncertainties of better than 0.15% for the U-Pb dates and 0.04% for the Pb-Pb date (Table 1). The size of the fragment is limited by both the concentration of Pb in the mineral —- which for these monazites and xenotimes is generally >1000 ppm — and, more importantly, the $^{208}Pb/^{206}Pb$ ratio of the

monazite lead, which together dictate the amount of uranogenic Pb present in the fragment.

Back-scattered electron (BSE) imaging was carried out on a JEOL Superprobe 733 at the Massachusetts Institute of Technology operating at an accelerating voltage of 15 to 20 kV and a beam current of 10 to 15 nA. The images reveal internal compositional variations that reflect differences in the average atomic number (Z) of the material (e.g., Fig. 5). Areas of a crystal with higher average Z appear brighter than areas with lower average atomic numbers. Based on several quantitative analyses on Grand Canyon monazites (John Hanchar, personal communication) we determined that differences in average Z of monazites from the Grand Canyon largely reflect variations in the concentration of the LREE, Th and U.

THERMOCHRONOLOGICAL TECHNIQUES

We employ a simple method to determine whether the mineral dates from a particular sample represent cooling ages. Because monazite and sphene appear to have very large effective diffusion dimensions (Suzuki et al., 1994; Mezger et al., 1991; Cherniak, 1993), crystals that preserve cooling ages should exhibit a predictable relationship between the grain size and age (Dodson, 1973). Based on the closure temperature equations of Dodson (1973; 1976), Wright et al. (1991) derived a convenient linear expression that describes the relationship between grain size and age for crystals that cooled through their closure temperatures:

$$t_c = \tau \ln\left(A\tau D(0)\right) - 2\tau \ln(a) \qquad (1)$$

where t_c is the apparent cooling age (seconds), τ is the cooling time constant (seconds) of Dodson (1976), a is the effective diffusion dimension (cm), A is the dimensionless diffusion geometry (A = 55 for the spherical diffusion geometry used here), and D(0) is the diffusion coefficient at time zero (the time when the crystal formed; $cm^2\ s^{-1}$). This equation is linear in ln(a) versus t_c and can be used to evaluate whether a set of U-Pb data records cooling ages. If the data define a statistically significant line (MSWD ≈ 1.0), then the slope and y-intercept define τ and D(0), respectively. These parameters, combined with experimentally determined diffusion parameters, can be used to calculate a hyperbolic cooling curve that is valid over the time interval represented by the observed mineral dates. Wright et al. (1991) derived the following relationship between temperature and time:

$$T = \frac{E/R}{t/\tau + \ln\left(\frac{D(0)}{D_o}\right)} \qquad (2)$$

where the T is the temperature (K), E is the activation energy for thermally activated diffusion (cal/mol), R is the universal gas constant (cal/mol K), t is time (sec) and D_o is the frequency factor (cm^2/sec). These parameters also allow calculation of the closure temperature of each crystal analyzed using the parameterized form of Dodson's (1976) equation

$$T_c = \frac{E/R}{\ln\left[\frac{A\tau D_o}{a^2}\right]} \qquad (3)$$

where T_c is the closure temperature. Equations 1, 2, and 3 are subject to the assumptions and approximations made by Dodson (1973; 1976).

Practical application of these equations to the data presented below proceeded as follows. For single-grain fractions, the selected crystal was measured along three orthogonal axes prior to dissolution. Multi-grain fractions were composed of crystals with identical size and shape represented by a single set of dimensions. The effective diffusion dimension was calculated as the average of the three orthogonal measurements expressed as a radius. The Pb-Pb date, which is the best estimate of the mineral's age for Proterozoic rocks, was used for the 'cooling age' to be tested. The relationship between the natural logarithm of the grain radius and the Pb-Pb date, presented on a Wright diagram, was analyzed by linear regression analysis using the algorithm of Ludwig (1989). If the MSWD was statistically significant (Wendt and Carl, 1991), then τ was calculated as one-half the slope and D(0) was calculated from the y-intercept. These values were used to calculate the cooling curve and closure temperature profile according to equations 2 and 3, respectively.

The uncertainty in the calculated cooling curve was estimated by making a series of simplifications. The uncertainties of four factors in equation 2 contribute to the uncertainty in the cooling rate: $\sigma_{D(0)}$; σ_t; σ_E; and σ_{Do}. Of these the values of $\sigma_{D(0)}$ and σ_{Do} are vary large (50 - 100%) compared to the values of σ_t and σ_E (3-5%), so the first simplification is to ignore the contribution from E and τ. The uncertainty in D_o is systematic and therefore does not change the relative cooling rates calculated for comparative purposes. Although the magnitude of the uncertainty in Do can be large (e.g., 83% average error for the diffusion parameters determined by for sphene by Cherniak, 1993), we have chosen to ignore the uncertainty in D_o for calculating T-t and T-

a profiles because any set of mineral data will be subject to the same systematic error. Therefore the uncertainties reported in figure 13 and in the text reflect only the quality of the linear regression (one-half of the uncertainty in the slope, σ_t). The consistency of the calculated temperatures and cooling rate for the sphene data from the calc-silicate gneiss with independent P-T constraints (described below) suggests that our results are geologically reasonable. The error bar for the calculated temperatures shown in figure 14 is an attempt to approximate the error contribution from both τ and D_o.

U-PB GEOCHRONOLOGY OF THE MIGMATITE

In this section we describe the U-Pb isotopic data from each of the four samples from the migmatite. The data are presented in table 1 and in concordia diagrams in figures 6 -11. Interpretation of the data is described in a separate section that draws upon the field, mineralogical and textural observations discussed above. The sphene data from the calc-silicate gneiss is described in a separate section.

Paleosomal Schist

The paleosomal (sample UG78.0-4) yielded abundant clear, yellow monazite crystals that ranged from faceted, idioblastic grains to pitted and embayed, xenoblastic grains. Fifteen single-crystal analyses yielded 0.16% reversely discordant to 0.8 % normally discordant U-Pb dates with Pb-Pb dates ranging from 1697 ± 1 to 1708 ± 1 Ma, including four concordant points with Pb-Pb dates between 1708 and 1702 Ma (Table 1; Fig. 6). As a whole, the data do not define a single, statistically significant upper intercept age. However, idioblastic grains yielded older Pb-Pb dates (1708 to 1702 Ma) than xenoblastic grains (1702 to 1697 Ma).

Leucosomal Pegmatite

Monazite separated from the deformed biotite-muscovite pegmatite pod (sample UG78.0-6) occurs as clear, yellow crystals ranging from well-faceted, euhedral grains to slightly resorbed subhedral grains. The sparse inclusions of quartz, alkali feldspar, sillimanite and biotite revealed in the BSE images were not apparent under the optical microscope. We analyzed a total of fifteen monazite fractions (Fig. 7). Five whole single crystals yielded 0.16% reversely discordant to 0.39% normally discordant U-Pb dates with Pb-Pb dates ranging from 1701 Ma to 1679 Ma, although four grains have Pb-Pb dates between 1701 and 1693 Ma (note that whole grain fraction M7 is younger than the dikes that cross-cut the migmatite in this outcrop; see Fig. 1). Six air abraded crystals yielded generally older Pb-Pb dates ranging from 1706 to 1698 Ma. Four fragments, sliced from a single crystal, yielded concordant to slightly discordant (-0.25% to +0.39%) U-Pb dates with Pb-Pb dates of 1693 ± 1, 1692 ± 1, 1689 ± 1 and 1691 ± 1 Ma (Fig. 7). The fragments exhibit limited age dispersion relative to the entire data set. There is no predictable correlation between the position of the fragments in the crystal and either the Pb-Pb dates or the degree of discordance (Fig. 7).

The U-Pb data from the leucosomal pegmatite do not define a single, statistically significant upper intercept age. Given the textural evidence for compositionally distinct, xenocrytsic cores and the observation that air abraded crystals yield older Pb-Pb dates, the monazites in this sample can be interpreted as physical mixtures of a magmatic component and a slightly older inherited component. Without further constraints, however, the exact ages of the end member components in this mixture are unclear.

Coupled Melanosomal Selvage and Leucosomal Granite

Monazites from the melanosomal selvage (sample UG78.0-9B) are all sub- to anhedral, yellow crystals with irregular shapes and pitted surfaces. Ten single crystal

analyses yielded normally discordant (0.18% to 2.35%) U-Pb dates with Pb-Pb dates ranging from 1700 to 1682 Ma (Table 1; Fig. 8). The data do not define a single statistically significant upper intercept age. The youngest data point (fraction M10) is apparently younger than the dikes that cross-cut the migmatite in this outcrop (Fig. 1). Furthermore, most of the monazites have Pb-Pb dates that are younger than monazites from the paleosomal schist. These data present three characteristics that complicate interpretation: 1) age dispersion; 2) normal discordance; and 3) apparent ages that are young relative to monazites from the paleosomal schist and leucosomal granite described above.

The adjacent leucosomal granite (sample UG78.0-9A) contained both monazite and xenotime. Monazite occurs as euhedral to subhedral, yellow crystals with equant to discoidal morphologies. Xenotime crystals are pale yellow to pale brown, euhedral crystals with prismatic to discoidal morphologies. Four whole single crystals of euhedral monazite yielded slightly discordant (up to 0.38%) U-Pb dates with Pb-Pb dates of 1698.0 ± 0.8 1698.0 ± 0.8, 1700.8 ± 0.7 and 1700.9 ± 0.8 Ma (Table 1, Fig. 9).

Xenotime yielded similar results (Table 1, Fig. 9). Three single crystal xenotime analyses (X1 - X3) are 0.13% to 0.75% normally discordant and have Pb-Pb dates of 1695.5 ± 0.9, 1700.3 ± 0.9 and 1701.4 ± 1.1 Ma. We also analyzed fragments sliced from three xenotime crystals. Three fragments from a discoidal grain (X4) are variably discordant (0.34% to 2.67%) but yield an upper intercept age of 1695.6 ± 0.8 Ma (MSWD = 0.33). In contrast, fragments from a prismatic crystal (X5) have contrasting Pb-Pb dates. Fragment X5c from the core of the crystal has a Pb-Pb date of 1700.5 ± 0.8 Ma, whereas a euhedral, epitaxial crystal (X5a) and the termination (X5d) adjacent to it have Pb dates of 1697 ± 1 and 1697.8 ± 0.8 Ma, respectively. The BSE image of the other crystal termination revealed oscillatory zoning parallel to rational crystal faces (identical to the crystal shown Fig. 5f), suggesting that this crystal preserves about 4 m.y. of

magmatic growth or perhaps a Pb diffusion gradient. Finally, two fragments from a prismatic grain (X6), characterized by regular oscillatory zoning from core to rim (based on BSE imaging), have identical Pb-Pb dates (1701.1 ± 0.8 and 1700.7 ± 0.8 Ma) and therefore no significant intra-grain age dispersion. The monazite and xenotime data suggest that these minerals either: 1) crystallized from melt between from 1701 to 1697 Ma; 2) preserve cooling ages; or 3) preserve disturbed U-Pb systematics perhaps by Pb loss early in the rock's history.

INTERPRETATION OF THE MIGMATITE DATA

Age Dispersion in the Paleosomal Schist

The monazite data from the paleosomal schist do not define a single, statistically significant upper intercept age; instead they preserve a multi-stage history involving dispersion along concordia followed by recent Pb loss. Of the possible explanations for the dispersion along concordia (e.g., Black et al., 1984; Copeland et al., 1988; Aleinikoff and Grauch, 1990; Parrish, 1990; Getty and Gromet, 1992; DeWolf et al., 1993; Hawkins and Bowring, in review), four are likely: inheritance of ca. 1740 Ma detrital monazite; high temperature Pb loss (e.g., Parrish and Tirrul, 1989; Parrish, 1990); protracted growth during metamorphism; and secondary growth or recrystallization (e.g., DeWolf et al., 1993). Each of these interpretations is considered below.

Inheritance of a detrital monazite component is unlikely for several reasons. First, there is no evidence for compositionally distinct, xenocrystic cores in the BSE images. Detrital crystals would probably have diverse parageneses and, therefore, variable compositions. Whereas, the lack of compositionally distinct cores is not sufficient to rule out inheritance, we would expect to see significant compositional contrast between detrital cores and metamorphic overgrowths in the BSE images if such cores were present. The fact that monazites from this rock have remarkably similar Th/U ratios (9.0 ± 1.7;

Table 1) suggests a second argument against inheritance of detrital monazite: monazites with such homogeneous compositions probably formed from a common source. Of course, detrital monazites from a single source might also exhibit limited compositional variation. Finally, detrital monazite is not commonly preserved in high grade metamorphic rocks (Overstreet, 1967; Parrish, 1990; Smith and Barreiro, 1990; Kingsbury et al., 1993), although several examples have been reported in moderate grade rocks (e.g., Suzuki and Adachi, 1991; 1994).

High-temperature Pb loss could also explain the age dispersion in the schist, especially since the temperature estimated for the peak of metamorphism (720 °C; Ilg et al., 1996b) is close to the empirically-determined nominal closure temperature of monazite (725 ± 50 °C; Copeland et al., 1988; Parrish, 1990). However, the data do not exhibit a correlation between grain size and Pb-Pb date (Fig. 10). For example, crystals with a mean radius of 20 ± 3 μm have Pb-Pb dates of 1699.7 ± 1.2 and 1701.2 ± 1.3 Ma, and crystals with a mean radius of 28.3 ± 3 μm have Pb-Pb dates of 1697.0 ± 0.8 and 1697.4 ± 0.9 Ma. In fact, the oldest grain (1708.0 ± 1.3 Ma; fraction M7) has a mean radius of only 21.7 ± 3 μm. Therefore, factors other than Pb diffusion are the main cause of the age dispersion in monazites from the paleosomal schist.

The textures observed in the BSE images provide a useful means of distinguishing between the last two possibilities, protracted growth during metamorphism and secondary growth of monazite or secondary disturbance of the U-Pb system. The latter interpretation, does not fit the observations. The BSE images reveal no textural evidence for the development of secondary monazite, even at reaction fronts between biotite and retrograde chlorite (compare Figs. 5b,d). In addition, there is no evidence in the U-Pb data for a monazite component that is younger than the cross-cutting dikes, as exhibited by monazites from the melanosomal selvages, the leucosomes, and the dikes themselves (see below; Chapter 3). Considering these factors and the above arguments for

preservation of growth ages, we suggest that an interpretation involving either secondary monazite growth or partial disturbance of the U-Pb system is not viable.

In contrast, the body of textural evidence suggests the monazites preserve primary growth ages reflecting a complex growth history. Most monazite grains preserve complex internal zoning suggestive of a growth history involving cyclic precipitation and resorption (Fig. 5d). In xenoblastic crystals, these growth zones are truncated by embayments that represent partial dissolution in the presence of melt. Such embayments invariably occur in monazites that occur at or near boundaries in association with reactants and products of the melt-producing muscovite reaction. This means that monazite grew prior to the development of sillimanite and these grains that occurred in the interstices of the rock reacted with melt generated by the breakdown of muscovite to sillimanite. Based on these textural relationships, we predict that idioblastic crystals should preserve older integrated ages than xenoblastic crystals.

The U-Pb data are consistent with this prediction and suggest that the single crystal monazite analyses preserve integrated ages corresponding to primary metamorphic growth. As shown in figure 7, idioblastic grains generally have older Pb-Pb dates (1708 - 1702 Ma) than xenoblastic grains (1703 - 1697 Ma) regardless of grain size. The consistency between the textural setting and the Pb-Pb dates independent of crystal size indicates that the crystals are preserving primary ages. The overlap in age between idioblastic and xenoblastic grains at about 1702 Ma provides a useful maximum age bracket on the formation of sillimanite and melt. We suggest that monazite began to precipitate from metamorphic fluids at about 1710 Ma, prior to recrystallization of biotite and plagioclase. The textures shown in figure 5d indicate a protracted growth history characterized by repeated growth and dissolution. Those monazites that were overgrown by prograde biotite and plagioclase between 1710 and 1700 Ma were 'protected' from further reaction, whereas interstitial monazites continued to react with

fluids, and subsequently with melt, during development of sillimanite at peak conditions over the interval 1702 to 1697 Ma. Therefore, we interpret the monazite data from the paleosomal schist to record prograde to peak metamorphic ages.

Age Dispersion in the Leucosomal Pegmatite

Several independent lines of evidence provide insight into the origin of the age variation in this sample. Back-scattered electron imaging indicates that monazites contain deeply embayed, compositionally distinct cores. The cores contain inclusions of sillimanite suggesting a metamorphic origin. In addition, the tendency of air abraded crystals to yield older Pb-Pb dates strongly suggests that the cores retain radiogenic Pb. Based on quantitative microprobe analyses and compositional mapping (John Hanchar, personal communication 1995), the cores of these crystals have higher Th and lower U concentrations than the magmatic rims.

The difference in composition between monazite cores and rims can be portrayed using the Th/U calculated for each analysis (Table 1; Fig. 11). As noted above, monazites from the paleosomal schist have a mean Th/U ratio of 9.0 ± 1.7. Monazites from the leucosomal pegmatite, on the other hand, exhibit wide variation in Th/U ratios (1.7 to 8.0) that correlates with the Pb-Pb dates — air abraded crystals have the oldest Pb-Pb dates and the highest Th/U ratios, whereas the fragments from the sliced crystal (M21) have the youngest Pb-Pb dates, with the exception of fraction M7, and the lowest Th/U ratios. The data form a broad linear trend that we interpret as a mixing array between a magmatic component represented by the sliced fragments from fraction M21 and an inherited component from the paleosomal schist. Based on this compositional relationship, the apparently low degrees of partial melting (Fig. 2a), the absence of evidence for extensive melt migration (Fig. 2a), the evidence for incorporation and reaction of selvage into the leucosomes, and the distinct composition of metamorphic

monazites from the Rama schist at river-mile 79.6 (Fig. 11), we suggest that the melts comprising the leucosomal pegmatite pod formed by *in situ* partial melting of the surrounding schist.

Fraction M7 does not fall along the mixing array described above (Pb-Pb date = 1679 and Th/U = 5.6; Table 1; Fig. 11). The Pb-Pb date of this grain is younger than the crystallization age of the cross-cutting granite dikes and must, therefore, preserve evidence for post-magmatic disturbance of the U-Pb system. Based on the textures observed in monazites from the leucosomal granite and the evidence for secondary growth domains in monazites from the granite dikes (Chapter 3), we suggest that this crystal also contains secondary growth domains probably resulting from fluid-mineral interaction under retrograde conditions. We therefore envision this grain as a physical mixture between magmatic (and perhaps inherited) and secondary monazite components.

Age Dispersion in the Coupled Melanosome/Leucosome

Several observations suggest that the 18 m.y. spread in Pb-Pb dates of monazites from the melanosomal selvage appears to reflect, at least in part, melt-mineral interaction during anatexis. The grains analyzed from this sample were xenoblastic, and based on textural evidence from BSE imaging, occupied the interstices of the rock. Mineralogical, textural and thermobarometric data as well as the compositional evidence from the leucosomal pegmatite are consistent with *in situ* melting of the schist during the peak of metamorphism. Watson et al. (1989) established that accessory phases occurring along grain boundaries in a rock containing partial melt will interact with that melt. The degree of interaction will depend on the solubility of the accessory phase in the attendant melt. Such mineral-melt interaction with interstitial could explain the deeply embayed morphology of monazites and xenotimes in the selvage. Mineral-melt interaction would

not completely dissolve large (> 50 μm) monazite or xenotime over the duration of the melting event (< 10 m.y.?) because of the sluggish dissolution kinetics of monazite and xenotime in peraluminous granite melt (Rapp and Watson, 1986; Montel, 1986; 1993; Rapp et al., 1987; Wolf and London, 1995). Most importantly, however, seven monazites from the melanosomal selvage (M1,2,6,13,15) yielded Pb-Pb dates (1692.7 ± 1.4 to 1699.7 ± 1.1) that are indistinguishable from the Pb-Pb dates of monazites and xenotimes (1694.4 ± 0.8 to 1701.4 ± 1.1 Ma) from the adjacent leucosome. To the extent that the leucosome was derived by *in situ* melting of the schist and that the monazites and xenotimes record primary crystallization ages, these data indicate that monazites in the selvages co-existed with partial melt.

Mineral-melt interaction cannot account for all of the age dispersion in the melanosomal selvage. The remaining five analyses yielded Pb-Pb dates that are younger than the Pb-Pb dates of monazites and xenotimes from both the adjacent leucosome and the paleosomal schist. In fact, fraction M10 yielded a Pb-Pb date (1682 Ma) that is younger than the oldest cross-cutting dike (Fig. 1). These results indicate that some monazite crystals contain secondary monazite that formed after 1682 Ma. The association of resorbed crystals that exhibit secondary domains with biotite-chlorite 'reaction fronts' suggests that the secondary domains formed during alteration of biotite to chlorite. The compositional data shown in figure 11b provide further support for this suggestion. Monazites from the melanosomal selvage form a broad array between monazites from the paleosomal schist and fraction M7 from the leucosomal pegmatite, which we interpret to contain a secondary monazite component formed by fluid-mineral interaction prior to 1682 Ma. We tentatively suggest that monazites from the selvage with Pb-Pb dates younger than about 1692 Ma are physical mixtures of primary metamorphic monazite and secondary monazite formed during retrograde conditions.

Monazite and xenotime from the leucosomal granite have Pb-Pb dates that vary over 3 m.y. and 6 m.y., respectively. The critical question for this sample is whether the grains preserve primary crystallization ages or cooling ages. Unfortunately there are not enough whole crystal analyses to rigorously address this question. However, these crystals are all larger than monazites from the paleosomal schist and yet preserve Pb-Pb dates that are younger than the majority of the metamorphic monazites. Therefore, it is reasonable to interpret these monazites as recording primary igneous ages.

If monazites and xenotimes from the leucosomal granite preserve magmatic crystallization ages, several observations suggest that magmatic crystallization occurred over at least 6 m.y. First, the total range of Pb-Pb dates from whole crystals ranges over 6 m.y. and the sliced fragments from crystals X4 and X6 indicate that these grains grew over less than 2 m.y. over 5 m.y. apart. For example, the three fragments from crystal X4 define a single-grain discordia with an upper intercept age of 1695.5 ± 0.8 Ma (MSWD = 0.32), whereas two fragments from X6 have indistinguishable Pb-Pb dates of 1700.7 ± 0.8 and 1701.1 ± 0.8 Ma. This observation implies that different crystals grew at distinctly different times. Second, the fragments from crystal X5, an oscillatory-zoned crystal imaged under BSE prior to analysis, preserve growth history of at least 3.5 m.y. years from the core to both the rim and an epitaxial overgrowth (Fig. 9). Therefore, some crystals grew over protracted intervals. In addition, the textures shown in figure 5f suggest that some grains had growth histories involving periods of dissolution within the magma. Our preferred interpretation of these results is that the leucosome is composed of small batches of melt that were variably saturated— probably due to variable modal abundance of monazite and xenotime along the pathway traveled by the melt — with respect to monazite and xenotime as they accumulated. We suggest that the melt batches comprising this leucosomal pod accumulated between 1701 and 1695 Ma.

Origin of the Leucosomes

Many of the observations presented in the preceding pages form the basis for several conclusions regarding the origin of the leucosomes. The leucosomes are restricted to layers of biotite schist and are invariably and uniquely mantled by melanosomal selvages. The selvages are depleted in quartz, alkali feldspar and plagioclase and enriched in biotite and sillimanite relative to the paleosomal biotite schist. Mineral assemblages, reaction textures and thermobarometric estimates of peak conditions indicate that conditions were appropriate for partial melting through the breakdown of muscovite to sillimanite. Even the volume of the leucosome component in outcrop (approximately 10 %) is consistent with estimates for the volume of melt produced through muscovite breakdown based on phase relations in the KFMASH compositional subsystem (Vielzeuf and Holloway, 1988). Finally, there is little field evidence for melt migration during melting. All of these observations are consistent with an interpretation that the leucosomes formed by *in situ* partial melting of the adjacent schist, but they do not require this conclusion.

Another line of evidence from the paleosomal schist and the leucosomal pegmatite supports an *in situ* origin for the leucosomes. Monazites from the leucosomal pegmatite preserve textural evidence for xenocrystic cores that contain inclusions of sillimanite, and the U-Pb data indicate that the cores preserve older Pb-Pb dates. There is ample textural evidence for the incorporation in the melt of partially dissolved metamorphic monazites from xenoliths of selvage material (e.g. Fig 5h). Moreover, the composition and age of monazites from the leucosomal pegmatite define a mixing array between metamorphic monazite from the paleosomal schist and magmatic monazite from the leucosome. Finally, metamorphic monazites from the Rama schist at river-mile 79.6 — within the Mineral Canyon crustal block — have a distinct and restricted composition. Taken together, the independent observations from field work, petrography, BSE imaging,

U-Pb geochronology and monazite geochemistry define a self-consistent body of evidence that leads to a single conclusion: at least some component of the leucosomes in this outcrop represent *in situ* partial melts of the adjacent schist.

The results from the leucosomal granite pod are less clear. The age dispersion exhibited by monazites and xenotimes from the granite pod could be interpreted either as representing 5 m.y. of local melt accumulation or perhaps melt accumulated at various structural levels during 5 m.y. of ascent from a deeper structural level. However, one observation suggests an *in situ* origin. Xenotime is present in both the granite pod and the adjacent melanosome, but is absent in the paleosomal schist and leucosomal granite from other parts of the same outcrop. This apparent local control of mineralogy and composition is consistent with experimental investigations of melt-rock interactions under crustal conditions (Watson et al. 1989). Nonetheless, some component of the melt may have been derived from a rock volume that is not represented in this outcrop. We suggest that the most of the leucosomal pods exposed at this crustal level were derived by *in situ* melting of the adjacent schist.

U-PB THERMOCHRONOLOGY OF THE CALC-SILICATE GNEISS

The calc-silicate pod (sample UG78.0-3) yielded abundant pale to light brown, idioblastic, lentil-shaped sphene. We report U-Pb data for nine single-grain and five multigrain analyses, most of which are normally discordant (Table 1, Fig. 12). The Pb-Pb dates range from 1691 to 1676 Ma; however, all but three fractions (S17, S21, S22) form a discordant array that defines an upper intercept age of 1686 ± 2 Ma (MSWD = 4.4) and lower intercept that overlaps the origin. Although the array does not define a statistically significant upper intercept age, the near-zero lower intercept indicates that the discordance reflects recent Pb loss. This observation indicates that the Pb-Pb date is a reliable estimate of the age of each analysis.

The sphene data from the calc-silicate gneiss exhibit a clear relationship between grain size and Pb-Pb date that can be used to derive a time-integrated cooling rate for the time interval immediately following the peak of metamorphism. These sphene data are ideal for this purpose for the following reasons: 1) the crystals appear to represent a single generation of growth; 2) they contain favorable radiogenic Pb to common Pb ratios (7.2 to 27.1) and are, therefore, insensitive to common Pb corrections; 3) more than half of the data are single-crystal analyses and the multi-crystal analyses comprise carefully chosen whole single grains of similar size, shape and color; 4) the analyzed fractions represent a range of grain radii (19 to 105 μm) over which closure temperature is very sensitive to the diffusion radius; 5) although the data are slightly discordant, Pb loss appears to be recent and the Pb-Pb date is a reasonable estimate for the age of each analysis.

The sphene data from the calc-silicate gneiss are consistent with this equation. Using the linear regression of York (1969), the sphene data yield an MSWD of 1.62 (Fig 13), which is statistically significant for a data set of fourteen points (Wendt and Carl, 1992). The resulting values of τ (3.2 ± 0.8 m.y.) and D(0) (3.42 x 10-^{19} cm^2/s) lead to an integrated cooling rate (using the diffusion parameters of Cherniak, 1993) of 5.4 $^{+1.7}_{-0.9}$ °C/m.y. over the interval 1691 to 1676 Ma (Fig. 14). Since temperature decays as a logarithmic function, the cooling rate is not constant over this time interval. The integrated cooling rate for the interval 1690 to 1685 Ma is 5.7 °C/m.y. whereas the integrated cooling rate for the interval 1680 to 1675 Ma is 4.1 °C/m.y.

An alternative interpretation is that the data preserve two different cooling rates. Note in figure 13 that the data define two different slopes. Grains with $ln(a) > 3.50$ have a relatively shallow slope that yields an integrated cooling rate of about 8 °C/m.y. between 1691 and 1685 Ma. The smaller crystals ($ln(a)<3.50$) preserve a steeper slope

that yields a cooling rate of 1.5 °C/m.y. However, the slopes overlap at the extreme of the two-sigma uncertainties; more data in the small grain size range are required to support a two stage cooling model.

DISCUSSION

A High-Temperature Thermal History for the Mineral Canyon Block

The preceding observations and interpretations permit the construction of a temperature-time (T-t) path for these rocks (Fig. 15). By combining the inferred T-t path with the P-T path estimated for the Mineral Canyon block (Fig. 16; Williams, 1994; personal communication, 1995), we can assemble a P-T-t path for the Mineral canyon block. The following discussion is keyed to figures 15 and 16.

The oldest idioblastic monazite crystals (1708 Ma) from the paleosomal schist provide a reasonable estimate for the initiation of monazite growth on the prograde P-T path prior to anatexis. The temperature at the time of prograde monazite growth is unknown because there is no textural evidence for the nature of the monazite-producing reaction, and because little is known about the prograde paragenesis of monazite in metamorphic rocks. The studies by Smith and Barreiro (1990) and Kingsbury et al. (1993), which identify two mechanisms for the development of metamorphic monazite in pelitic schists, deal with rocks differing in bulk composition from the biotite schist studied here. Numerous studies (Sawka et al., 1986; Smith and Barreiro, 1990; Akers et al., 1993; Kingsbury et al.,1993) have shown that metamorphic monazite can develop along a variety of reaction pathways.

Monazite probably continued to grow during prograde heating until the P-T path intersected the muscovite-out reaction boundary signifying the onset of partial melting. The intersection probably occurred between 1702 and 1700 Ma, based on the overlap in

the Pb-Pb dates of idioblastic and xenoblastic monazites from the paleosomal schist, and the oldest monazite and xenotime dates (1701 Ma) from the leucosomal granite. As melt formed and began to migrate along grain boundaries, interstitial monazite and xenotime crystals were partially dissolved in the melt. We envision this mineral-melt interaction in the manner described from experiments of Watson et al. (1989). The degree of dissolution is consistent with experimentally determined dissolution kinetics (Rapp and Watson, 1986; Montel, 1986; 1993; Rapp et al., 1987; Wolf and London, 1995).

Melting continued for about 10 m.y. until final crystallization of the leucosomal pegmatite at about 1692 Ma (Figs. 15). During this time interval, the accumulating melt pods were deformed, and sillimanite needles that previously defined S_1 were transposed into the composite S_1/S_2 fabric. At some point during the peak of metamorphism, which we assume to be about 1700 Ma, sphene crystallized from the calc-silicate mineral assemblage at 1690 Ma and temperatures above about 596 °C, the calculated closure temperature of the largest crystals. Before the largest sphene crystals closed with respect Pb diffusion, the leucosomal pegmatite reached its solidus temperature, which is required to be greater than about 650 °C (e.g., Fig. 16). The cooling rate over the interval 1692 and 1690 Ma depends upon the temperature at which the pelite solidus was crossed. If the leucosomal pegmatite crystallized at 700 °C, then the cooling rate between 1692 and 1690 Ma is about 30 °C/m.y. If, on the other hand, the leucosomal pegmatite crystallized at about 650 °C/m.y., then the cooling rate is about 15 °C/m.y. The cooling rate over this 2 m.y. time interval also depends upon the accuracy of the calculated closure temperature for sphene. Nonetheless, cooling at greater than 15 °C/m.y. is consistent with the geological, petrological, thermobarometric, and geochronological constraints and therefore represents the simplest interpretation. At about 1690 Ma, the cooling rate slowed considerably to 5 °C/m.y., based on the sphene cooling dates.

During the interval of slow cooling (sphene closure), peraluminous granite dikes intruded the migmatite. Documented crystallization ages range from 1685 to 1680 Ma, but some dikes, particularly centimeter-scale, strongly folded dikes, may have intruded as the leucosomes crystallized around 1690 Ma (Fig. 15). The relative timing of metamorphism at mile 78.0 and dike intrusion has two important implications. First, the rocks were cooling throughout the interval of dike intrusion. This means that the dikes did not significantly contribute to the local thermal budget. Second, intrusion of large volumes of peraluminous granite melt between 1690 and about 1680 Ma indicates that melting, melt accumulation and melt emplacement continued at depth for at least 10 m.y. after melting had ceased at the presently exposed crustal level.

Cooling continued at a rate of about 4 °C/m.y. until the smallest analyzed sphene grains reached about 515 °C. The only other constraint along the P-T-t path is recorded in individual crystals of monazite from two of the cross-cutting granite dikes at mile 78.0. In chapter 3, we described U-Pb data from micro-samples of secondary monazite that partially reset magmatic monazite. We interpreted the textures to indicate fluid-mineral interaction at subsolidus conditions, and the micro-samples suggested a maximum date of 1659 Ma for fluid-flow. The temperature is unconstrained and in figure 15 we show two alternative explanations: continued cooling along an exponential decay path; and a short-duration thermal spike. The magnitude and duration of any thermal spike are severely limited by the diffusion kinetics of the sphene data.

The P-T path determined for rocks in the Mineral Canyon crustal block (Williams, personal communication, 1995) is consistent with the thermal history described above and can be used to place broad constraints on the post-peak unroofing rate of these rocks. The P-T loop crosses the muscovite-out reaction boundary at about 7 kbars, reaches peak temperatures at about 6 kbars, and passes below the pelite solidus between 3 and 4 kbars (Fig. 16). Using the observations and interpretations described throughout

this paper, each of these points along the P-T path are constrained in time: the muscovite-out reaction was achieved between 1702 and 1700 Ma; peak conditions were attained at about 1700 Ma; and partial melting ceased by about 1692 ma. Decompression during peak conditions suggests a time-integrated decompression rate of about 0.35 kbars/m.y. which translates to a crude unroofing rate of 1 mm/yr. From 1682 to 1676 Ma, the integrated unroofing rate apparently slowed considerably to less than 0.1 mm/yr.

The P-T-t evolution outlined for the rocks at mile 78.0 is representative of the entire Mineral Canyon block for several reasons. First, the field relations between migmatitic supracrustal rocks and peraluminous granite and pegmatite intrusions are consistent throughout the block, although the lithologies and relative volume of the intrusions varies across strike. Second, metamorphic monazites from the Rama schist in the core of the Sockdolager antiform at river mile 79.6 yielded Pb-Pb dates that overlap with the range of Pb-Pb dates from the paleosomal schist at mile 78.0. Finally, the U-Pb date of a peraluminous granite that cross-cuts migmatites and is, in turn, cross-cut by peraluminous granite dikes at river-mile 80.5 yielded a U-Pb zircon crystallization age (1685 ± 1 Ma) that overlaps with the range of crystallization ages from mile 78.0.

Regional Implications

The P-T-t evolution outlined in the preceding section provides important constraints on models for the tectonic and thermal evolution of the Paleoproterozoic middle crust exposed in the Mineral Canyon block. As summarized by Ilg et al. (1996b), the prograde path was characterized by heating and burial associated with thrusting and formation of penetrative S_1 fabric and F_1 folds. Ilg et al (1996b) argue that sillimanite needles are aligned in both S_1 and S_2 and suggest that the transition from S_1 fabrics and F_1 folding to

S_2 fabrics and F_2 folding occurred during peak metamorphism. These observations imply that initial monazite growth and prograde heating were associated in time with crustal thickening prior to anatexis and that S_1 and F_1 structures were actively forming at about 1710 Ma (the oldest monazite dates from the paleosomal schist).

The onset of crustal melting signified a dramatic change in the structural, thermal and baric evolution of the Mineral Canyon block. This transition is marked by: 1) accumulation of partial melt locally and perhaps input of melt from deeper structural levels; 2) local transposition of S_1 by heterogeneously developed S_2 (Ilg et al. 1996b); 3) folding of S_1 tectonic layering into kilometer-scale and related F_2 folds such as the Sockdolager antiform (Fig. 1); and 4) the change from burial and heating to decompression and cooling (Figs. 15 & 16). The textural relationships and monazite dates indicate that the transition occurred between about 1702 and 1700 Ma. The spatial correlation, throughout the Grand Canyon transect, of a strong S_2 overprint and high-grade metamorphic mineral assemblages (Ilg et al., 1996b) suggests that the change in structural style during peak metamorphism reflects a change in crustal rheology and may signify the onset of accretion.

The apparent contemporaneity of post-peak cooling and decompression from 6 kbars to 3-4 kbars is particularly important from a tectonic perspective. Unroofing of about 11 km of crust (assuming 3.7 km/kbar) in about 10 m.y. requires both rapid uplift rates and rapid erosion rates. This requirement along with the absence of kyanite-bearing assemblages place important constraints on the tectonic mechanism(s) for unroofing. Two possibilities are likely: extensional thinning of the crust and thinning of the mantle lithosphere. Whereas extensional thinning of the crust is an efficient mechanism for unroofing, the absence of kyanite-bearing assemblages implies moderate crustal thickness

and limited topographic gradients both of which are inconsistent with gravity-driven extension. There is also a lack of structural evidence for extension at mid-crustal levels during or following the development of S_2. Thinning of the mantle lithosphere would also result in rapid uplift rates by inducing density-driven isostatic adjustments. Such adjustments would involve vertical motions on short time-scales and perhaps be accommodated along the vertical shear zones that define the crustal architecture along the Grand Canyon transect. However, the time scale of isostatic response is much shorter than the 8-10 m.y. suggested by the geochronological data. Resolving the mechanism responsible for ca. 1700 Ma unroofing is difficult because the upper 22 km of Paleoproterozoic crust has been removed. Detailed studies of the thermal history of other crustal blocks in the region may be the best means of resolving this issue.

Regardless of the driving mechanism for uplift, the Mineral Canyon block stabilized by about 1690 Ma. The dramatic change in cooling rate at about 1690 Ma signifies the beginning of slow, isobaric cooling at about 500 °C and 3 kbars. In some parts of the Mineral Canyon block, this period of isobaric cooling is represented by garnet growth and the development of andalusite (and muscovite ?) at the expense of sillimanite (Ilg et al., 1996b). From a tectonic perspective, the onset of isobaric cooling represents the stabilization of newly accreted continental crust.

CONCLUSIONS

U-Pb geochronologic data from monazite, xenotime and sphene combined with field, petrographic and compositional data provide insights into the origin and thermal evolution of the middle crust in the Mineral Canyon block of the Upper Granite Gorge during the Paleoproterozoic Yavapai orogeny. Metamorphic monazite began to grow on the prograde path by 1710 Ma during thrusting, F_1 folding and S_1 fabric development.

Crustal thickening culminated with partial melting of biotite schist resulting from the breakdown of muscovite to sillimanite. Leucosomes largely represent melt that formed and accumulated *in situ* between about 1692 and 1701 Ma. This period of partial melting was coincident with rapid cooling and decompression from 6 to 3 kbars. Sphene crystals from a calc-silicate gneiss preserve cooling dates that define a change in the cooling rate from 15 -30 °C/m.y. to 5 °C/m.y. at about 1690 Ma. Cooling continued until the smallest sphene crystals closed at 1676 Ma.

The P-T-t path derived from the Mineral Canyon block suggests that the thermal evolution was controlled by tectonic processes. Heating was associated with crustal thickening and both rapid cooling and decompression reflect either crustal thinning or thinning of the mantle lithosphere combined with rapid erosion rates. Although the emplacement of peraluminous granite melt continued until 1680 Ma, the dramatic change in cooling rate at about 1690 Ma signifies the transition from collision to stabilization of newly accreted continental lithosphere.

REFERENCES

Akers WT, Grove M, Harrison, Ryerson FJ (1993) The instability of rhabdophane and its unimportance in monazite paragenesis. Chem Geol 110:169-176

Aleinikoff JN, Grauch RI (1990) U-Pb geochronologic constraints on the origin of a unique monazite-xenotime gneiss, Hudson Highlands, New York. Am J Sci 290:522-546

Black LP, Fitzgerald JD, Harley SL (1984) Pb isotopic composition, colour, and microstructure of monazites from a polymetamorphic rock in Antarctica. Contrib Mineral Petrol 85:141-148

Cherniak DJ (1993) Lead diffusion in sphene and preliminary results on the effects of radiation damage on Pb transport. Chem Geol 110:177-194

Childe F, Doig R, Gariepy C (1993) Monazite as a metamorphic chronometer, south of the Grenville Front, western Quebec. Can J Earth Sci 30:1056-1065

Clemens JD, Wall VJ (1981) Origin and crystallization of some peraluminous (S-type) granitic magmas. Can Mineral 19:111-131

Copeland P, Parrish RR, Harrison TM (1988) Identification of inherited radiogenic Pb in monazite and its implications for U-Pb systematics. Nature 333:760-763

DeWolf CP, Belshaw N, O'Nions RK (1993) A metamorphic history from micron-scale $^{207}Pb/^{206}Pb$ chronometry of Archean monazite. Earth Planet Sci Lett 120:207-220

Dodson MH (1973) Closure temperature in cooling geochronological and petrological systems. Contrib Mineral Petrol 40:259-274

Dodson MH (1976) Kinetic processes and thermal history of slowly cooled solids. Nature 259:551-553

Dodson MH (1979) Theory of cooling ages. In: Jäger E, Hunziker JC (eds) Lectures in Isotope Geology. Springer-Verlag, Berlin, pp 194-202

Getty SR, Gromet LP (1992) Geochronological constraints on ductile deformation, crustal extension, and doming about a basement-cover boundary, New England Appalachians. Am J Sci 292:359-397

Harrison TM, Watson EB (1983) Kinetics of zircon dissolution and zirconium diffusion in granitic melts of variable water content. Earth Planet Sci Lett 64:295-304

Harrison TM, McKeegan KD, LeFort P (1995) Detection of inherited monazite in the Manaslu leucogranite by $^{208}Pb/^{232}Th$ ion microprobe dating: crystallization age and tectonic implications. Earth Planet Sci Lett 133:271-282

Hawkins DP and Bowring SA (in review) A case study of monazite (and xenotime) U-Pb systematics from the Paleoproterozoic of the Grand Canyon, Arizona. Contrib Mineral Petrol

Hawkins DP, Bowring SA, Ilg BE, Karlstrom KE, Williams ML (1996) U-Pb geochronological constraints on the Paleoproterozoic crustal evolution of the Upper Granite Gorge, Grand Canyon, Arizona. Geol Soc Am Bull (in press)

Heaman L, Parrish RR (1991) U-Pb geochronology of accessory minerals. In: Heaman L, Ludden JN (eds) Application of Radiogenic Isotope Systems to Problems in Geology. Mineralogical Society of Canada Short Course Handbook 19, Toronto, pp 59-102

Holdaway MJ (1971) Stability of andalusite and the aluminosilicate phase diagram. Am J Sci 271:97-131

Ilg BE, Karlstrom KE, Williams ML, Hawkins DP (1996a) Precambrian crystalline rocks In: Huntoon PW (ed) Geologic Map of the Eastern Part of the Grand Canyon National Park, Arizona (geologic map). Grand Canyon Association, Grand Canyon, Arizona

Ilg BE, Karlstrom KE, Hawkins DP, Williams ML (1996b) Tectonic evolution of Paleoproterozoic rocks in the Grand Canyon: Insights into middle crustal processes. Geol Soc Am Bull (in press)

Kingsbury JA, Miller CF, Wooden JL, Harrison TM (1993) Monazite paragenesis and U-Pb systematics in rocks of the eastern Mojave Desert, California, U.S.A.: implications for thermochronometry. Chem Geol 110:147-167

Krogh TE (1973) A low-contamination method for hydrothermal decomposition of zircon and extraction of U and Pb for isotopic age determination. Geochim Cosmochim Acta 37:485-494

Krogh TE (1982) Improved accuracy of U-Pb ages by the creation of more concordant systems using an air abrasion technique. Geochim Cosmochim Acta 46:637-649

LeBreton, NL, Thompson AB (1988) Fluid-absent (dehydration) melting of biotite in metapelites in the early stages of crustals anatexis. Contrib Mineral Petrol 99:226-237

Ludwig KR, (1989) Pb.Dat: A computer program for processing raw Pb-U-Th isotope data. US Geol Surv Open-File Rep 88-557

Mezger K, Rawnsley CM, Bohlen SR, Hanson GN (1991) U-Pb garnet, sphene, monazite and rutile ages: Implications for the duration of high-grade metamorphism and cooling histories, Adirondack Mtns. J Geol 99:415-428

Montel J-M (1986) Experimental determination of the solubility of Ce-monazite in SiO_2-Al_2O_3-K_2O-Na_2O melts at 800 °C, 2 kbar, under H_2O-saturated conditions. Geology 14:659-662

Montel J-M (1993) A model for monazite/melt equilibrium and application to the generation of granitic magmas. Chem Geol 110:127-146

Nabalek PI, Glascock MD (1995) REE-depleted leucogranites, Black Hills, South Dakota: a consequence of disequilibrium melting of monazite-bearing schists. J Petrol 36:1055-1071

Naeser CW, Elston DP (1987) Fission-track dates from the Grand Canyon, Arizona (abstract). Geol Soc Am Abs Prog 19:784

Overstreet WC (1967) The geologic occurrence of monazite. US Geol Surv Prof Paper 530:327p

Parrish RR (1990) U-Pb dating of monazite and its application to geological problems. Can J Earth Sci 27:1435-1450

Parrish RR, Tirrul R (1989) U-Pb age of the Baltoro granite, northwest Himalaya, and implications for monazite U-Pb systematics. Geology 17:1076-1079

Rapp RP, Watson EB (1986) Monazite solubility and dissolution knietics: implications for the thorium and light rare earth chemistry of felsic magmas. Contrib Mineral Petrol 94:304-316

Rapp RP, Ryerson FJ, Miller CF (1987) Experimental evidence bearing on the stability of monazite during crustal anatexis. Geophys Res Lett 14:307-310

Sawka WN, Banfield JF, Chappell BW (1986) A weathering-related origin of widespread monazite in S-type granites. Geochim Cosmochim Acta 50:171-175

Smith HA, Barreiro BA (1990) Monazite U-Pb dating of staurolite grade metamorphism in pelitic schists. Contrib Mineral Petrol 105:602-615

Stacey JS, Kramers JD (1975) Approximation of terrestial lead isotope evolution by a two-stage model. Earth Planet Sci Lett 26:207-221

Suzuki K, Adachi M (1991) Precambrian provenance and Silurian metamorphism of the Tsubonosawa paragneiss in the South Kitakami terrane, Northeast Japan, revealed by the chemical Th-U-total Pb isochron ages of monazite, zircon and xenotime. Geochem J 25:357-376

Suzuki K, Adachi M (1994) Middle Precambrian detrital monazite and zircon from the Hida gneiss in the Oki-Dogo Island, Japan: their origin and implications for the correlation of basement gneiss of Southwest Japan and Korea. Tectonophysics 235:277-292

Suzuki K, Adachi M, Kajizuka I (1994) Electron microprobe observations of Pb diffusion in metamorphosed detrital monazites. Earth Planet Sci Lett 128:391-405

Thompson AB (1982) Dehydration melting of pelitic rocks and the generation of H2O-undersaturated granitic liquids. Am J Sci 282:1567-1595

Vidal P, Bernard-Griffiths J, Cocherie A, Le Fort P, Peucat JJ, Sheppards MF (1984) Geochemical comparisons between Himalayan and Hercynian leucogranites. Phys Earth Planet Inter 35:179-190.

Vielzeuf D, Holloway JR (1988) Experimental determination of the fluid-absent melting relations in the pelitic system. Contrib Mineral Petrol 98:257-276

Watson EB, Vicenzi EP, Rapp RP (1989) Inclusion/host relations involving accessory minerals in high-grade metamorphic and anatectic rocks. Contrib Mineral Petrol 101:220-231

Watt GR, Harley SL (1993) Accessory phase controls on the geochemistry of crustal melts and restites produced during water-undersaturated partial melting. Contrib Mineral Petrol 114:550-566

Wendt I, Carl C (1991) The statistical distribution of the mean squared weighted deviation. Chem Geol 86:275-285

Williams MW (1994) Conflicting P-T-t paths from Proterozoic rocks of the southwestern USA: The problem is plagioclase (abstract). EOS, Trans Am Geophys Union 75: 185.

Wolf MB, London D (1995) Incongruent dissolution of REE- and Sr-rich apatite in peraluminous granitic liquids: Differential apatite, monazite, and xenotime solubilities during anatexis. Am Mineral 80:765-775

Wright N, Layer PW, York D (1991) New insights into thermal history from single grain $^{40}Ar/^{39}Ar$ analysis of biotite. Earth Planet Sci Lett 104:70-79

FIGURE CAPTIONS

Figure 1 Simplified geologic map of the Paleoproterozoic rocks in the easternmost Upper Granite Gorge between river-miles 77 and 82.5. River-miles are the standard spatial reference frame in the Grand Canyon for travel along the Colorado River. They are measured along the course of the river from Lees Ferry in northern Arizona (see inset). The main map shows the salient geology of the Mineral Canyon crustal block which is exposed from river-mile 77, the beginning of exposures of the Paleoproterozoic, to the Vishnu fault zone at river-mile 81. The large-scale sketch map shows the geology of the study area at river-mile 78.0. U-Pb ages for the granite dikes are from Chapter 3. The legend applies to both maps. Modified after Ilg et al., 1996a,b).

Figure 2a-b Field photographs of the migmatites at mile 78.0. **a** Distribution of leucosomes in a 4 meter-thick layer of biotite schist. Note that the leucosomes are strongly deformed, decimeter- to meter- scale pods that comprise less than 15 % of the schist layer. **b** Close-up of a single leucosome pod showing the prominent melanosomal selvage and the adjacent paleosomal schist. Partially isolated selvage material extends into the leucosome in the left-center of the image. Note that the grain size does not vary across the pod.

Figure 3 Photomicrograph in crossed polarized light from the paleosomal schist (sample UG78.0-4) showing a deeply embayed muscovite crystal enveloped by fibrolitic sillimanite. The texture clearly indicates that prograde muscovite reacted to sillimanite in the presence of quartz and feldspar. Large prismatic sillimanite crystals show similar textures in other parts of the thin section. Scale bar is 500 μm.

Figure 4 Pressure - temperature diagram showing relevant phase equilibria in the compositional subsystems Ca K Na Al Si H_2O (CKNASH shown as solid curves) and K Fe Mg Al Si H_2O (KFMASH shown as dashed curves). Solid black points are invariant points in the respective subsystems. Reaction boundaries number 1 and 2 are the muscovite breakdown reaction boundaries for the CKNASH and KFMASH compositional subsystems, respectively. Dotted lines about reaction boundary number 1 reflect compositional variations in the reactants and products (Thompson, 1982). The shaded areas represent the P-T space delimited by petrographic observations in the paleosomal schist and melanosomal selvage: the lighter shade of gray corresponds to the CKNASH compositional subsystem and the darker shading corresponds to the KFMASH compositional subsystem. Note that peak P-T estimates determined through thermobarometric calculations (Ilg et al., 1996b) are consistent with the petrographic constraints. CKNASH system after LeBreton and Thompson (1988) and KFMASH system after Vielzeuf and Holloway (1988). Aluminosilicate reaction boundaries from Holdaway (1971).

Figure 5a-g Back-scattered electron images of textural relationships and xenotime and monazite crystals. **a** Contrasting monazite morphologies in the paleosomal schist. Note that the small crystal occluded by the large quartz crystal is idioblastic whereas both the large and small crystals along the grain boundaries are xenoblastic. The grain boundary region is an intergrowth of muscovite, biotite, sillimanite, alkali feldspar, and quartz. **b** Idioblastic monazite from the paleosomal schist. This crystal occurs as an inclusion in a biotite grain that is partially replaced by chlorite along several cleavage planes. Note

that the monazite crystal is not resorbed adjacent to the chlorite. **c** Reaction relationships between monazite and the breakdown of muscovite to sillimanite in paleosomal schist. Note that the monazite crystal is idioblastic against biotite but is embayed near intergrowths of muscovite, sillimanite and alkali feldspar. Such textures are typical of interstitial monazite and xenotime crystals in both the paleosomal schist and the melanosomal selvages. **d** Compositional variation within the idioblastic monazite crystal shown in figure 5b. Note that internal growth zones are truncated locally throughout the growth history. We interpret these textures, which are typical of monazites from the paleosomal schist and melanosomal selvage, to reflect a cyclic history of growth and dissolution during prograde metamorphism. Note that the growth zones are not disrupted or truncated on the side of the crystal adjacent to chlorite. **e** Euhedral xenotime from the leucosomal granite that exhibits oscillatory zoning from core to rim. Most xenotime and monazite crystals from the leucosomal granite exhibit similar magmatic growth zoning. **f** One of the few examples of complex zoning within a xenotime from the leucosomal granite. Earlier growth domains were partially resorbed prior to continued precipitation. Because of the limited compositional variation, we interpret this grain to record evidence for disequilibrium within the magma between xenotime and melt. We suggest that these textures resulted from mixing of magmas within contrasting degrees of xenotime saturation. **g** Monazite crystal from the leucosomal pegmatite containing a compositionally distinct (high Th, low U), partially resorbed core surrounded by an unzoned rim (low Th, high U). Inclusions in the core include sillimanite suggesting that the core is a xenocrystic, metamorphic monazite. **h** Deeply embayed monazite crystal in the leucosomal granite at the margin of a xenolith of selvage material. The grain was clearly out of equilibrium with the surrounding melt and was substantially dissolved prior to crystallization of the melt.

Figure 6 Concordia diagram for monazite analyses from the paleosomal schist. Note that idioblastic crystals have older Pb-Pb dates than xenoblastic crystals.

Figure 7 Concordia diagram for monazite analyses from the leucosomal pegmatite shown at the same scale as the concordia diagram for the paleosomal schist (Fig 6). Inset in left corner shows ellipse for fraction M7 which plots just off the plot frame. Sketch of crystal M21 shows the original morphology of the grain and the location within the crystal of the sliced fragments that were analyzed. Note that air abraded crystals have older Pb-Pb dates than unabraded crystals.

Figure 8 Concordia diagram for monazite data from the melanosomal selvage. Note that these grains yielded Pb-Pb dates that are generally younger than monazites from the paleosomal schist.

Figure 9 Concordia diagram, shown at the same scale as the diagram in figure 8, for monazite and xenotime analyses from the leucosomal granite adjacent to the melanosomal selvage. Note that these grains yielded Pb-Pb dates that overlap with the oldest monazite analyses from the adjacent melanosomal selvage. The inset is a blow-up of the data near concordia that identifies analyses of sliced fragments from crystals X4, X5 and X6.

Figure 10a-c Wright diagram for monazite data from the paleosomal schist (a), and the coupled melanosome/leucosome pair. None of these data define statistically significant correlations, although the number of data points for the latter samples is insufficient to rigorously evaluate the relationship.

Figure 11a-b Pb-Pb date versus Th/U diagrams for monazites from the paleosomal schist and leucosomal pegmatite (**a**) and the melanosomal selvage and leucosomal granite (**b**). a Note that data from the leucosomal pegmatite form an apparent mixing array between metamorphic monazites from the schist and the interpreted magmatic component represented by sliced fragments from crystal M21. Crystal M7 is younger than dikes that cross-cut the migmatite and probably contains a significant secondary monazite component. **b** Note that monazites from the melanosomal selvage form a first order mixing array between metamorphic monazites from the paleosomal schist and fraction M7. This relationship suggests that monazites from the selvage contain secondary monazite components that formed sometime after 1679 Ma. Monazites from the leucosomal granite are similar in composition to monazites from the leucosomal pegmatite.

Figure 12 Concordia diagram showing sphene data from the calc-silicate gneiss. Inset shows the most discordant analysis (fraction S21).

Figure 13 Wright diagram for sphene data from the calc-silicate gneiss. The data define a statistically significant line consistent with grain-size-controlled volume diffusion that indicates these grains preserve cooling ages. The dashed curve about the best-fit line show the error envelope, a graphical representation of uncertainty in the slope of the line.

Figure 14 Calculated radius versus time, radius versus temperature and time versus temperature plots for sphene data from the calc-silicate gneiss over the interval 1691 to 1676 Ma. Dashed lines about the calculated curves graphically portray one-sigma uncertainties calculated by propagating uncertainties in the cooling time constant (τ) determined from the linear regression in figure 13. The radius versus time plot (upper left) shows the best-fit curve calculated using the values of τ and D(0) determined from the linear regression in figure 12b.

Figure 15 Thermal evolution of the Mineral Canyon crustal block based. See text for discussion.

Figure 16 Pressure-temperature-time path for rocks in the Mineral Canyon crustal block. P-T path from Williams (1994; personal communication, 1995). Solid curves are reaction boundaries in the CKNASH compositional subsystem (LeBreton and Thompson, 1988) and dashed curves are reaction boundaries in the KFMASH compositional subsystem (Vielzeuf and Holloway, 1988). The shaded field labeled number 1 represents the P-T conditions for muscovite breakdown to sillimanite and the shaded field labeled number 2 is the P-T space for the pelite solidus. Absolute time assignments are based on based on temperatures (inferred or calculated) shown I figure 14. See text for further discussion.

Table 1 U-Pb analytical results for monazite, xenotime and sphene from mile 78.0 in the Grand Canyon

		Composition						Isotopic Ratios						Dates (Ma)		
Fractions	Estimated Wgt (µg)	U (ppm)	Th (ppm)	Pb (ppm)	Th/U	Mol% ^{206}Pb	Com Pb (pg)	$^{206}Pb/^{204}Pb$	$^{208}Pb/^{206}Pb$	$^{206}Pb/^{238}U$	$^{207}Pb/^{235}U$	$^{207}Pb/^{206}Pb$	corr. coef.	$^{206}Pb/^{238}U$	$^{207}Pb/^{235}U$	$^{207}Pb/^{206}Pb$
(1)	(2)	(3)	(3)	(3)	(3)			(4)	(5)	(6)	(6)	(6)				(7)
PALEOSOMAL SCHIST (sample UG78.0-4)																
M3 *xeno*	1.1	5843	56546	6127	9.93	72.6	15.5	7244.65	2.9279	0.30002 (.07)	4.31487 (.08)	0.104309 (.04)	0.856	1691.4	1696.2	1702.2 ±0.8
M4 *xeno*	0.7	9920	53447	7041	5.53	59.5	9.6	13739.18	1.6723	0.30085 (.09)	4.31940 (.10)	0.104131 (.04)	0.897	1695.5	1697.1	1699.0 ±0.8
M6 *xeno*	0.6	5049	41744	4722	8.48	69.3	7.5	7513.27	2.4932	0.30012 (.08)	4.30527 (.10)	0.104041 (.05)	0.855	1691.9	1694.4	1697.4 ±0.9
M7 *idio*	0.3	10698	95486	11019	9.16	70.8	117.7	483.38	2.6796	0.30336 (.08)	4.37692 (.11)	0.104641 (.07)	0.746	1708.0	1708.0	1708.0 ±1.3
M8 *xeno*	0.2	17903	166206	18311	9.52	71.6	25.8	2371.66	2.7828	0.30218 (.10)	4.34026 (.12)	0.104170 (.07)	0.831	1702.1	1701.0	1699.7 ±1.2
M9 *idio*	0.4	14885	153854	16495	10.60	73.8	28.4	3764.95	3.1042	0.30311 (.17)	4.37248 (.18)	0.104622 (.06)	0.943	1706.7	1707.2	1707.7 ±1.1
M10 *idio*	0.5	14921	159358	16937	10.96	74.4	58.7	2089.06	3.2064	0.30211 (.07)	4.34413 (.08)	0.104288 (.05)	0.807	1701.8	1701.8	1701.8 ±0.9
M11 *xeno*	0.4	14620	130654	14635	9.17	70.8	66.1	1584.60	2.6822	0.30233 (.07)	4.34830 (.09)	0.104314 (.05)	0.844	1702.8	1702.6	1702.2 ±0.9
M16 *xeno*	0.6	6958	33720	4653	4.97	57.1	23.8	3171.03	1.4677	0.29876 (.10)	4.28488 (.11)	0.104018 (.04)	0.917	1685.2	1690.5	1697.0 ±0.8
M18 *xeno*	0.3	5502	56925	6075	10.61	73.8	15.3	2207.77	3.1161	0.30065 (.13)	4.31481 (.16)	0.104087 (.08)	0.855	1694.5	1696.2	1698.2 ±1.5
M22 *xeno*	0.6	7008	64836	7094	9.49	71.6	6.6	10811.55	2.7891	0.30029 (.13)	4.30899 (.14)	0.104072 (.06)	0.900	1692.7	1695.1	1698.0 ±1.2
M23 *idio*	0.5	9568	93185	10101	9.99	72.6	14.0	5697.39	2.9322	0.30160 (.11)	4.33983 (.12)	0.104362 (.06)	0.892	1699.2	1701.0	1703.1 ±1.0
M24 *idio*	0.3	11124	101693	11230	9.38	71.4	14.7	4647.92	2.7553	0.30143 (.09)	4.33960 (.11)	0.104416 (.07)	0.795	1698.4	1700.9	1704.1 ±1.3
M25 *idio*	0.4	7002	65556	7210	9.60	72.0	16.4	3079.30	2.8346	0.30076 (.12)	4.33837 (.15)	0.104618 (.09)	0.811	1695.1	1700.7	1707.6 ±1.6
M29 *xeno*	0.2	11172	82612	9697	7.59	66.9	5.1	9531.85	2.2291	0.30088 (.15)	4.32510 (.17)	0.104255 (.07)	0.910	1695.7	1698.2	1701.2 ±1.3
LEUCOSOMAL PEGMATITE (sample UG78.0-6)																
M4	9.0	3353	8873	1651	2.71	41.9	10.8	50348.55	0.7950	0.30045 (.07)	4.29952 (.08)	0.103788 (.04)	0.861	1693.5	1693.3	1692.9 ±0.7
M6	20.4	10028	27912	5055	2.86	43.1	31.3	115883.89	0.8351	0.30120 (.06)	4.31472 (.07)	0.103895 (.04)	0.839	1697.3	1696.2	1694.8 ±0.7
M7	0.5	18101	99227	12804	5.62	60.0	10.1	17012.11	1.6539	0.29658 (.07)	4.21313 (.08)	0.103028 (.04)	0.837	1674.3	1676.6	1679.4 ±0.8
M8	8.1	10249	54170	7188	5.42	59.0	15.1	98586.03	1.5895	0.30123 (.06)	4.32499 (.07)	0.104131 (.04)	0.827	1697.4	1698.1	1699.0 ±0.7
M9 aa	0.5	8940	51931	6780	5.96	61.2	65.5	1226.46	1.7427	0.30255 (.07)	4.35113 (.09)	0.104306 (.05)	0.798	1703.9	1703.1	1702.1 ±1.0
M11 aa	0.5	14483	53384	8372	3.78	50.0	17.5	7466.83	1.1045	0.30212 (.09)	4.33522 (.11)	0.104072 (.06)	0.813	1701.8	1700.1	1698.0 ±1.2
M12 aa	0.3	7891	61175	7127	7.95	67.9	13.8	3111.15	2.3313	0.30243 (.10)	4.35777 (.12)	0.104504 (.06)	0.858	1703.4	1704.4	1705.6 ±1.1
M13 aa	1.7	10468	55562	7385	5.45	59.1	20.2	15834.02	1.5936	0.30221 (.05)	4.34508 (.06)	0.104276 (.04)	0.769	1702.3	1702.0	1701.6 ±0.8
M14 aa	1.8	8979	54308	6858	6.20	62.2	17.1	17017.50	1.8177	0.30207 (.12)	4.34502 (.12)	0.104324 (.05)	0.929	1701.6	1702.0	1702.4 ±0.9
M21b	0.2	48153	122497	23398	2.61	40.9	25.6	6033.74	0.7625	0.30023 (.08)	4.28682 (.09)	0.103556 (.05)	0.859	1692.5	1690.8	1688.8 ±0.9
M21c	0.1	86434	145419	35935	1.73	31.5	11.2	16594.27	0.5074	0.29883 (.12)	4.27247 (.13)	0.103693 (.04)	0.939	1685.5	1688.1	1691.3 ±0.8
M21d	0.2	58794	130006	27088	2.27	37.5	25.8	6500.26	0.6632	0.30076 (.07)	4.30350 (.08)	0.103776 (.04)	0.840	1695.1	1694.0	1692.7 ±0.8
M21f	0.0	329853	637805	148428	1.98	34.4	50.3	1172.13	0.5795	0.30027 (.09)	4.29549 (.11)	0.103754 (.06)	0.827	1692.6	1692.5	1692.3 ±1.1
M22	0.2	16610	83258	11553	5.14	57.7	47.0	1017.20	1.5037	0.30143 (.16)	4.32141 (.19)	0.103978 (.10)	0.339	1698.4	1697.5	1696.3 ±1.9
M23	0.3	17253	78423	11161	4.66	55.3	19.3	4819.49	1.3670	0.30158 (.09)	4.33510 (.10)	0.104255 (.05)	0.883	1699.1	1700.1	1701.2 ±0.8
MELANOSOMAL SELVAGE (sample UG78.0-9B)																
M1	2.5	4789	44251	4833	9.48	71.7	19.7	10774.62	2.8007	0.29834 (.14)	4.27629 (.17)	0.103956 (.09)	0.851	1683.1	1688.8	1695.9 ±1.6
M2	1.0	6243	53150	5954	8.73	69.9	13.7	8203.95	2.5697	0.29961 (.10)	4.29478 (.11)	0.103965 (.05)	0.894	1689.4	1692.4	1696.1 ±0.9

Table 1 — continued

Fractions	Estimated Wgt (μg)	Composition U (ppm)	Th (ppm)	Pb (ppm)	Th/U	Mol% ^{208}Pb	Com Pb (pg)	Isotopic Ratios $^{208}Pb/^{204}Pb$	$^{208}Pb/^{206}Pb$	$^{206}Pb/^{238}U$	$^{207}Pb/^{235}U$	$^{207}Pb/^{206}Pb$	corr. coef.	Dates (Ma) $^{206}Pb/^{238}U$	$^{207}Pb/^{235}U$	$^{207}Pb/^{206}Pb$
(1)	(2)	(3)	(3)	(3)	(3)			(4)	(5)	(6)	(6)	(6)				(7)
M3	0.6	7437	57214	6590	7.89	67.8	18.6	4244.05	2.3259	0.29757 (.10)	4.24689 (.12)	0.103509 (.07)	0.846	1679.3	1683.1	1688.0 ±1.2
M5	1.1	6970	57606	6492	8.48	69.3	9.0	15444.30	2.4935	0.29912 (.10)	4.28020 (.11)	0.103780 (.05)	0.895	1687.0	1689.6	1692.8 ±0.9
M6	0.9	7868	53525	6501	6.98	65.0	45.7	2751.95	2.0492	0.30087 (.15)	4.32138 (.16)	0.104170 (.06)	0.924	1695.6	1697.4	1699.7 ±1.1
M7	0.6	8820	66756	7804	7.76	67.4	51.3	1827.21	2.2788	0.29936 (.07)	4.27906 (.09)	0.103671 (.05)	0.823	1688.1	1689.3	1690.9 ±0.9
M10	0.2	8339	58783	6904	7.23	66.2	7.1	4213.60	2.1584	0.29276 (.13)	4.16460 (.15)	0.103172 (.06)	0.913	1655.3	1667.1	1682.0 ±1.1
M11	1.0	9185	79321	8768	8.86	70.7	8.8	19189.83	2.6576	0.29321 (.23)	4.19534 (.24)	0.103775 (.08)	0.950	1657.5	1673.1	1692.7 ±1.4
M13	0.7	9428	85371	9344	9.29	71.5	8.7	13309.88	2.7763	0.29499 (.15)	4.22975 (.16)	0.103992 (.06)	0.939	1666.4	1679.8	1696.6 ±1.0
M15	0.3	8913	79743	8782	9.18	71.1	4.9	9841.61	2.7124	0.29825 (.14)	4.27556 (.15)	0.103970 (.06)	0.918	1682.6	1688.7	1696.2 ±1.1
LEUCOSOMAL GRANITE (sample UG78.0-9A)																
M1	3.4	8558	51453	6487	6.17	62.1	13.2	39707.41	1.8086	0.30093 (.18)	4.31820 (.18)	0.104071 (.04)	0.970	1695.9	1696.8	1698.0 ±0.8
M2	6.2	6150	42656	5114	7.11	65.4	17.0	40239.93	2.0914	0.30078 (.12)	4.32274 (.13)	0.104235 (.04)	0.946	1695.2	1697.7	1700.9 ±0.8
M3	1.5	13404	68378	9197	5.23	58.2	12.9	27951.26	1.5370	0.30046 (.12)	4.31142 (.13)	0.104073 (.04)	0.944	1693.6	1695.5	1698.0 ±0.8
M7	6.9	11959	45944	7033	3.94	51.2	17.1	86784.04	1.1573	0.30106 (.08)	4.32664 (.09)	0.104230 (.04)	0.885	1696.6	1698.5	1700.8 ±0.7
X1	5.2	6298	1116	1872	0.18	4.6	4.5	137500.03	0.0536	0.29858 (.09)	4.27873 (.11)	0.103932 (.05)	0.883	1684.3	1689.3	1695.5 ±0.9
X2	1.8	11980	2178	3579	0.19	4.7	7.4	53519.64	0.0550	0.29955 (.10)	4.30382 (.11)	0.104204 (.05)	0.903	1689.1	1694.1	1700.3 ±0.9
X3	2.7	2971	539	913	0.19	4.7	57.9	2467.15	0.0546	0.30165 (.09)	4.33660 (.11)	0.104265 (.06)	0.846	1699.5	1700.3	1701.4 ±1.1
X4a	1.6	8751	925	2561	0.11	2.8	2.4	111456.68	0.0319	0.29973 (.11)	4.29435 (.11)	0.103911 (.04)	0.925	1690.0	1692.3	1695.1 ±0.8
X4b	0.9	7677	720	2201	0.10	2.6	20.8	5775.97	0.0290	0.29190 (.24)	4.17257 (.26)	0.103674 (.11)	0.904	1651.0	1668.6	1690.9 ±2.1
X4c	0.9	7639	715	2225	0.10	2.5	3.9	33749.90	0.0283	0.29914 (.06)	4.28444 (.08)	0.103875 (.05)	0.789	1687.1	1690.4	1694.5 ±0.9
X5a	0.4	9450	1010	2758	0.11	2.8	2.2	30723.24	0.0324	0.29875 (.14)	4.28456 (.15)	0.104016 (.05)	0.939	1685.1	1690.4	1697.0 ±0.9
X5c	2.3	6271	827	1852	0.14	3.5	1.3	216022.41	0.0398	0.30023 (.16)	4.31398 (.17)	0.104213 (.04)	0.968	1692.4	1696.0	1700.5 ±0.8
X5d	1.0	8255	615	2405	0.08	2.0	2.1	77757.70	0.0224	0.30086 (.15)	4.31675 (.16)	0.104061 (.04)	0.964	1695.6	1696.6	1697.8 ±0.8
X6a	4.2	5127	589	1506	0.12	3.1	9.3	41670.11	0.0348	0.29960 (.12)	4.30539 (.13)	0.104226 (.04)	0.948	1689.3	1694.4	1700.7 ±0.8
X6b	5.7	3040	5	914	0.18	4.7	1.9	175458.89	0.0540	0.30177 (.16)	4.33746 (.17)	0.104247 (.04)	0.967	1700.1	1700.5	1701.1 ±0.8
CALC-SILICATE GNEISS (sample UG78-3)																
S1 (1)	4.6	352	70	113	0.20	5.1	42.0	697.23	0.0598	0.29759 (.18)	4.24929 (.21)	0.103561 (.11)	0.869	1679.3	1683.6	1688.9 ±1.9
S2 (1)	5.6	331	127	110	0.39	9.7	48.6	678.53	0.1182	0.29265 (.17)	4.17470 (.22)	0.103462 (.13)	0.800	1654.7	1669.1	1687.1 ±2.5
S3 (1)	11.0	469	201	152	0.44	10.6	59.7	1520.10	0.1305	0.29604 (.11)	4.22737 (.14)	0.103565 (.08)	0.829	1671.7	1679.4	1689.0 ±1.4
S5 (1)	3.2	202	98	66	0.50	11.8	8.6	1410.11	0.1478	0.29667 (.40)	4.23486 (.41)	0.103528 (.09)	0.974	1674.8	1680.8	1688.3 ±1.7
S6 (1)	1.3	340	121	107	0.37	9.0	7.7	1078.64	0.1088	0.29462 (.59)	4.20146 (.60)	0.103427 (.08)	0.991	1664.6	1674.3	1686.5 ±1.5
S8 (1)	1.5	286	131	92	0.47	11.2	7.0	1173.30	0.1386	0.29648 (.65)	4.22913 (.66)	0.103455 (.09)	0.991	1673.8	1679.7	1687.0 ±1.6
S17 (52)	6.9	340	115	113	0.35	8.6	69.4	594.01	0.1038	0.29303 (.14)	4.16779 (.16)	0.103157 (.06)	0.922	1656.6	1667.7	1681.7 ±1.1
S18 (18)	8.9	443	175	146	0.40	9.7	74.6	939.57	0.1192	0.29707 (.16)	4.23311 (.17)	0.103347 (.07)	0.912	1676.8	1680.5	1685.1 ±1.3
S21 (73)	3.2	629	156	192	0.25	6.8	53.1	634.69	0.0800	0.27649 (.19)	3.92130 (.21)	0.102861 (.09)	0.905	1573.7	1618.1	1676.4 ±1.7
S22 (41)	2.8	374	93	121	0.25	6.4	31.6	597.32	0.0754	0.29348 (.26)	4.16608 (.29)	0.102954 (.11)	0.921	1658.9	1667.4	1678.1 ±2.1

Table 1 — continued

Fractions	Estimated Wgt (µg)	Composition U (ppm)	Th (ppm)	Pb (ppm)	Th/U	Mol% ^{208}Pb	Com Pb (pg)	Isotopic Ratios $^{208}Pb/^{204}Pb$	$^{206}Pb/^{204}Pb$	$^{208}Pb/^{232}Th$	$^{207}Pb/^{235}U$	$^{206}Pb/^{238}Pb$	corr. coef.	Dates (Ma) $^{208}Pb/^{232}Th$	$^{207}Pb/^{235}U$	$^{207}Pb/^{206}Pb$
(1)	(2)	(3)	(3)	(3)	(3)			(4)	(5)	(6)	(6)	(6)				(7)
S24 (37)	11.6	94	23	32	0.25	6.3	42.5	467.08	0.0739	0.29840 (.28)	4.25267 (.29)	0.103360 (.08)	0.959	1683.4	1684.3	1685.3 ±1.5
S26 (1)	7.3	144	46	48	0.33	8.2	35.8	519.02	0.0988	0.29137 (.29)	4.16410 (.31)	0.103652 (.11)	0.938	1648.4	1667.0	1690.5 ±2.0
S27 (1)	8.4	115	48	38	0.43	10.3	26.9	638.26	0.1273	0.29393 (.42)	4.19945 (.45)	0.103621 (.14)	0.952	1661.1	1673.9	1689.9 ±2.5
S28 (1)	8.0	163	51	56	0.32	7.9	55.5	425.07	0.0952	0.29659 (.24)	4.23713 (.25)	0.103613 (.08)	0.946	1674.4	1681.2	1689.8 ±1.5

(1) fractions analyzed include the type of mineral, M=monazite, X=xenotime, S=sphene followed by analysis number. fraction numbers followed by a single lower case letter are fragments sliced from individual crystals. fraction descriptions include the following abbreviations: aa = air abraded; idio = idioblastic; xeno = xenoblastic. the number of crystals in sphene fractions are listed in parentheses after the fraction number

(2) sample weights were estimated using measured grain dimensions (± 5µm), an ellipsoidal geometry, and nominal densities of 5.0 g/cc for monazite, 5.2 g/cc for xenotime, and 3.5 for sphene. weights are known to within 20% based on comparisons of estimated and measured weights for all three minerals

(3) expressed as ppm U and Th and ppm radiogenic Pb. Th concentration and Th/U ratio calculated from the radiogenic ^{208}Pb and $^{208}Pb/^{206}Pb$ ratios, respectively, assuming concordance between the Th-Pb and U-Pb systems.

(4) measured ratio corrected for fractionation: Pb fractionation correction is 0.12% ± 0.04% per atomic mass unit (amu) for multicollector analyses and 0.15% ± 0.04% per amu for single collector analysis based on repeated analyses of NBS 981

(5) radiogenic Pb

(6) Pb/U isotopic ratios corrected for fractionation, spike, blank, and initial common Pb: U blank = 1 pg ± 50%; Pb blanks ranged from 5.2 to 1.1 pg during the course of this study and the data were reduced using a Pb blank of 3.5 pg ± 50% — for analyses with less than 3.5 pg total common Pb the total common Pb was assumed to be blank and the uncertainty was reduced to 10%; initial common Pb was calculated using the two-stage model of Stacey and Kramers (1975) using the interpreted age of the sample. Numbers in parentheses are the % error reported at the 2 sigma confidence interval.

(7) uncertainty in the Pb-Pb date in My at the 2 sigma confidence interval

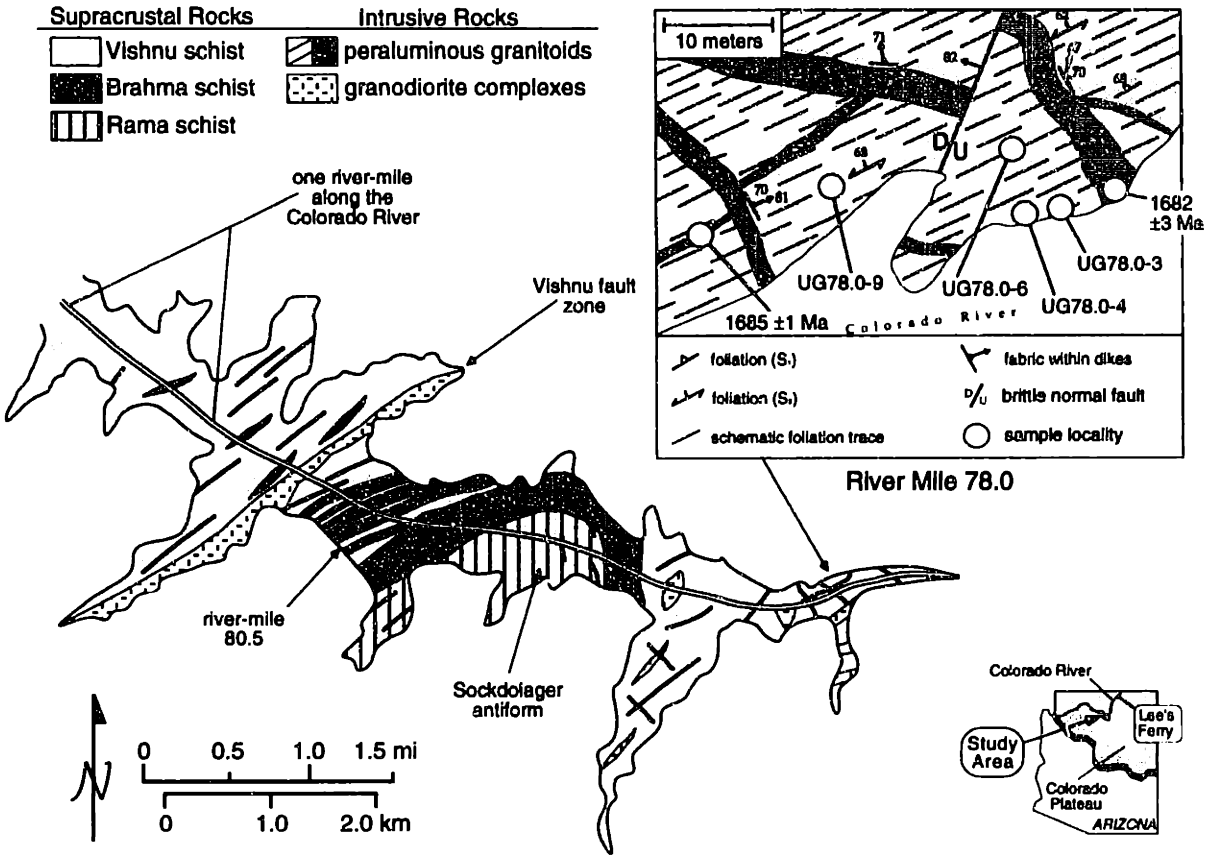
Supracrustal Rocks
Vishnu schist
Brahma schist
Rama schist
Intrusive Rocks
peraluminous granitoids
granodiorite complexes
one river-mile along the Colorado River
Vishnu fault zone
river-mile 80.5
Sockdolager antiform
0 0.5 1.0 1.5 mi
0 1.0 2.0 km
10 meters
1682 ±3 Ma
UG78.0-3
UG78.0-9
UG78.0-6
UG78.0-4
1685 ±1 Ma
Colorado River
foliation (S1)
foliation (S2)
schematic foliation trace
fabric within dikes
brittle normal fault
sample locality
River Mile 78.0
Colorado River
Lee's Ferry
Study Area
Colorado Plateau
ARIZONA

Figure 1

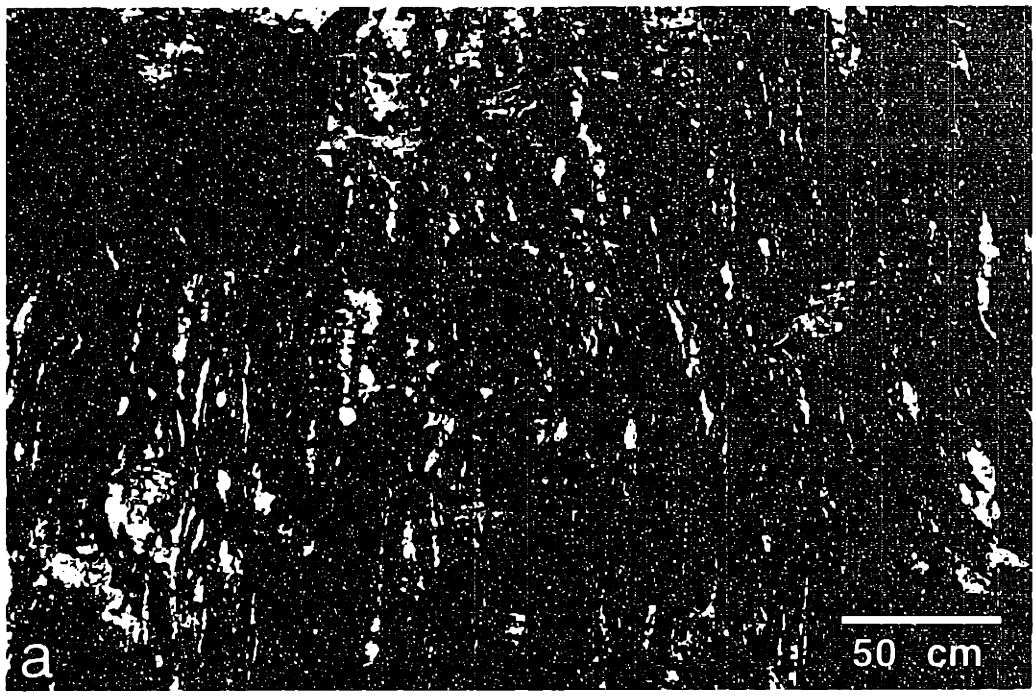

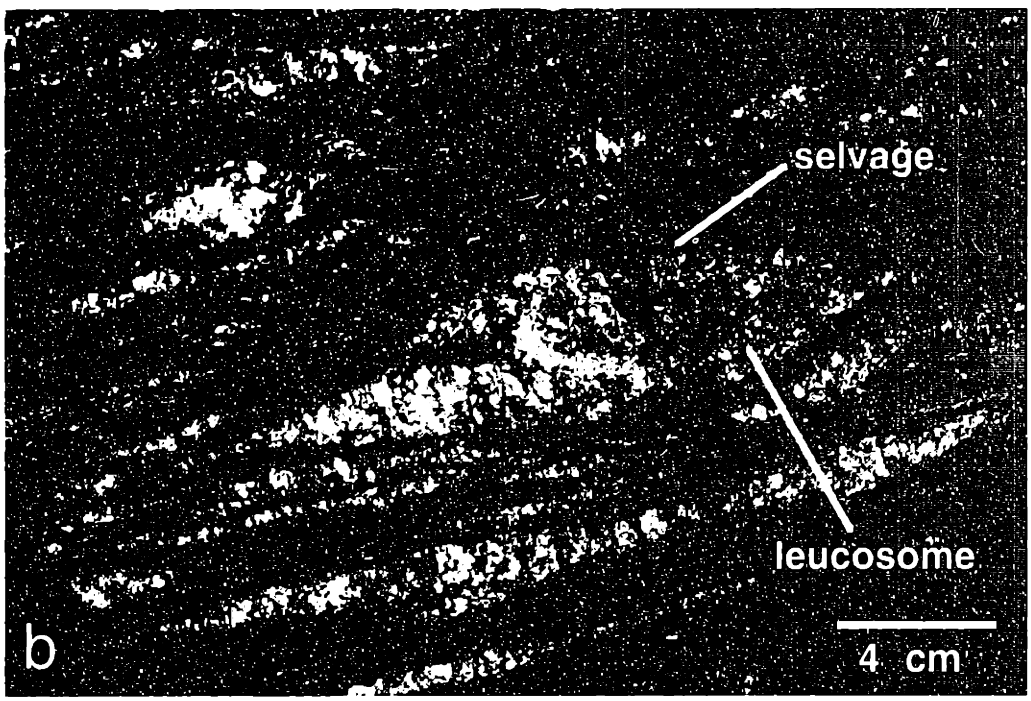

Figure 2

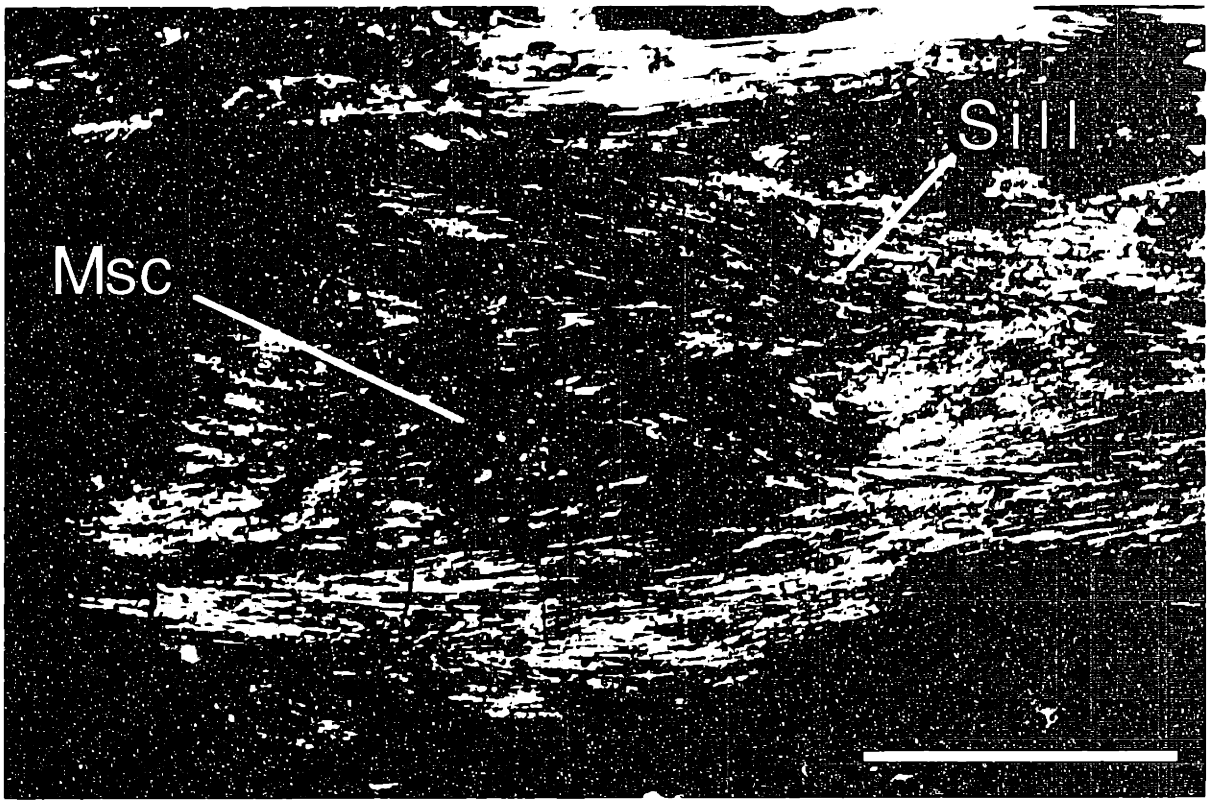

Figure 3

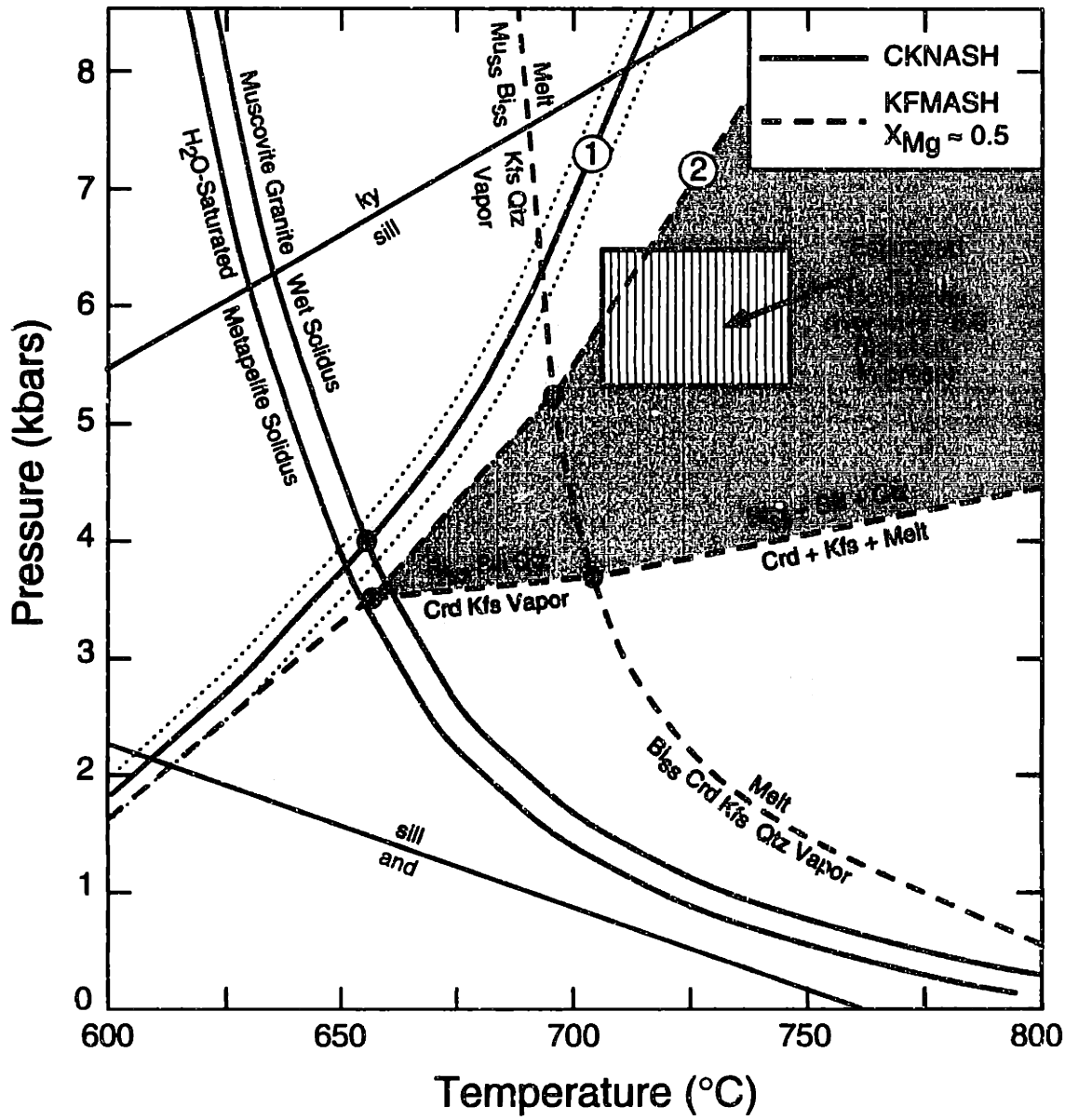
CKNASH
KFMASH
$X_{Mg} \approx 0.5$
Pressure (kbars)
Temperature (°C)
0
1
2
3
4
5
6
7
8
600
650
700
750
800
H_2O-Saturated
Muscovite Granite
Metapelite Solidus
Wet Solidus
Muss Bi$_{ss}$
Melt
Kfs Qtz
Vapor
ky
sill
and
Crd Kfs Vapor
Crd + Kfs + Melt
Bi$_{ss}$ Crd Kfs Qtz Vapor
Melt
①
②

Figure 4

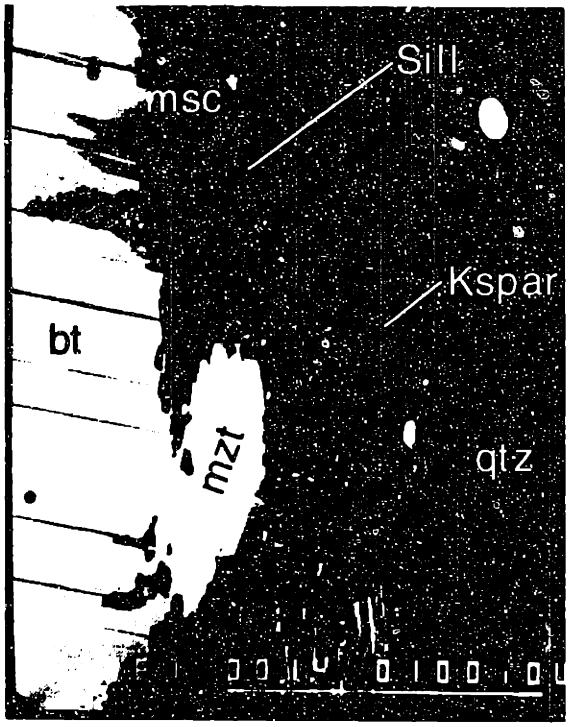

a

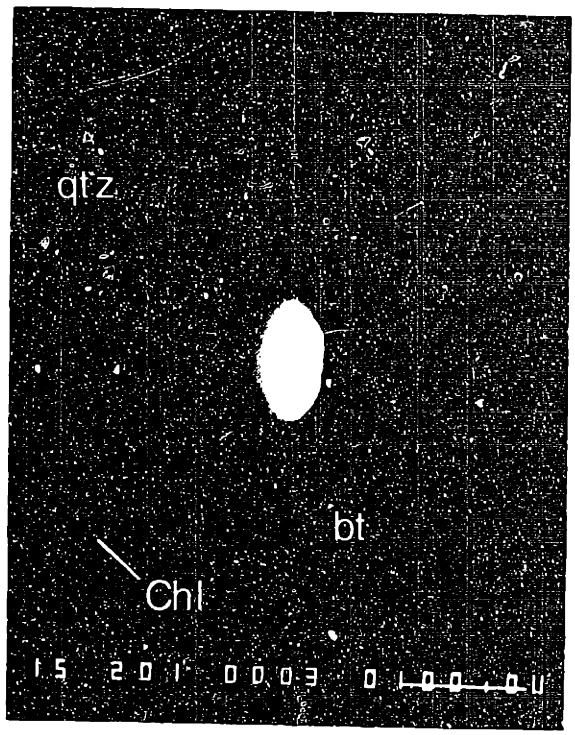

b

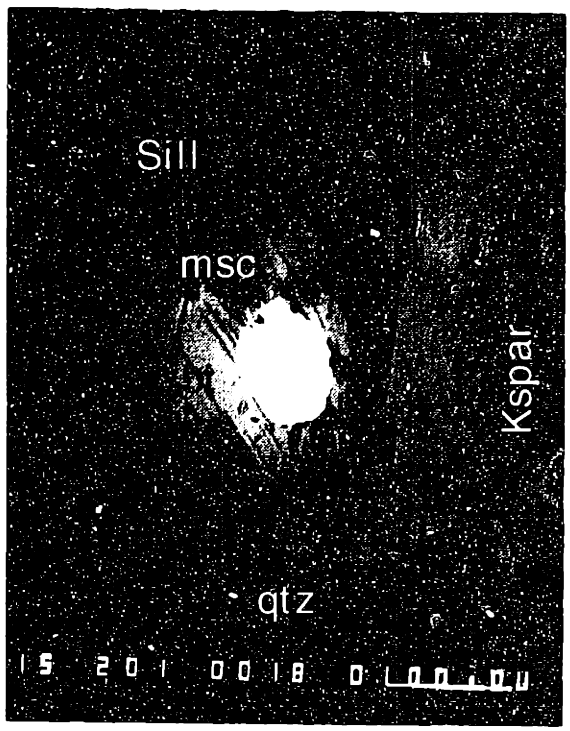

c

Figure 5

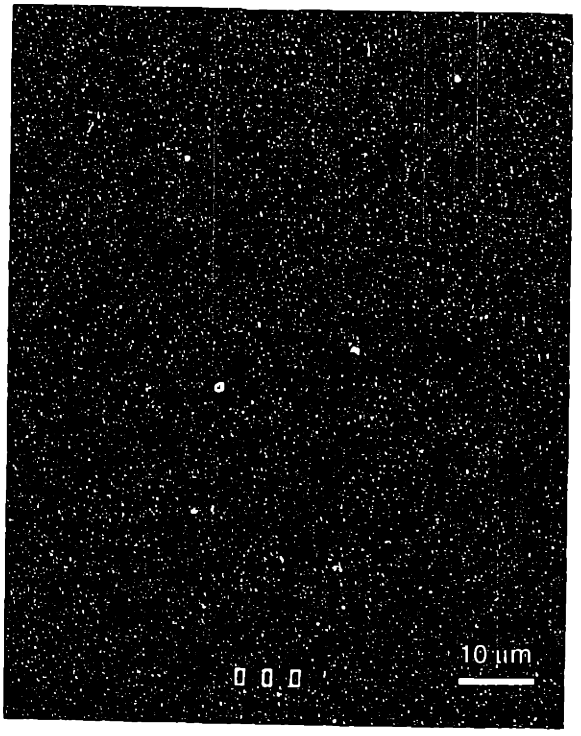

d

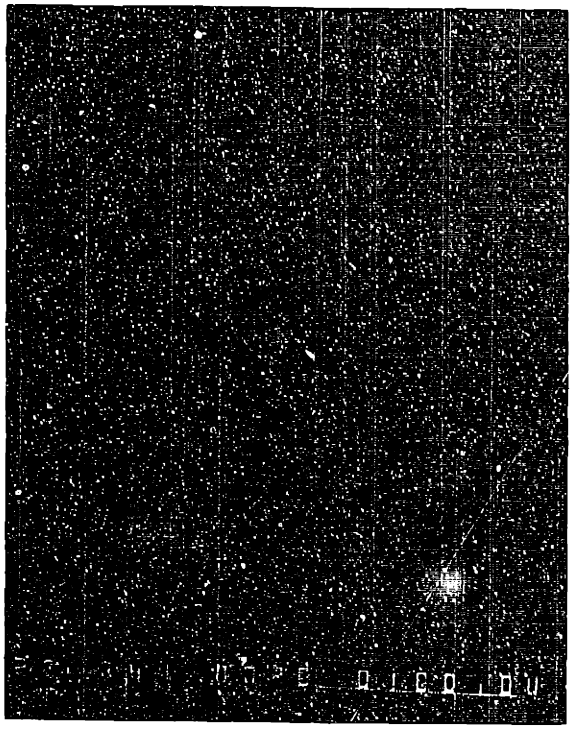

e

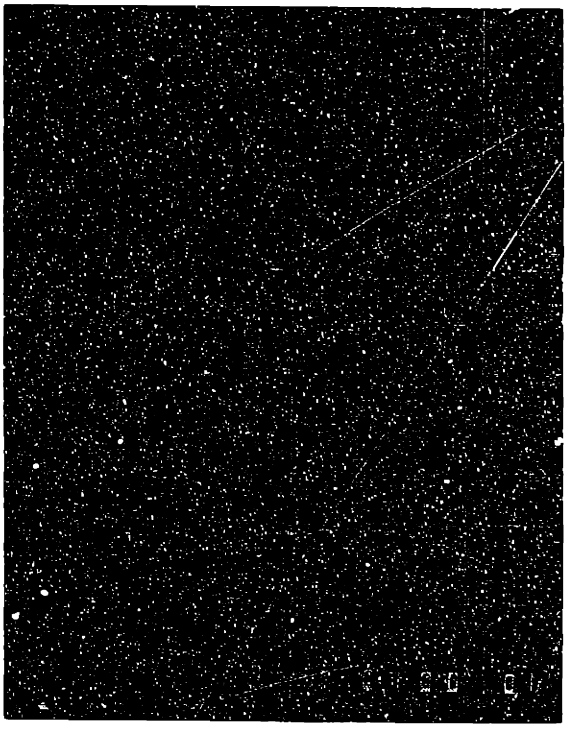

f

Figure 5

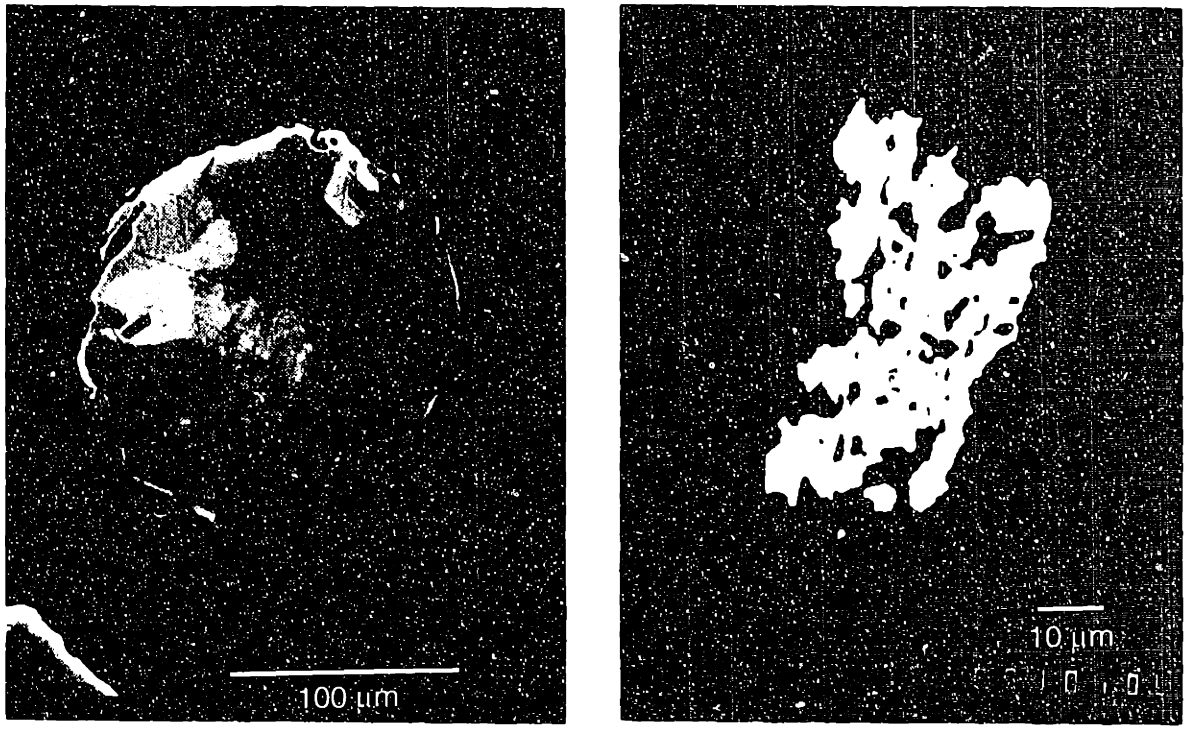

g h

Figure 5

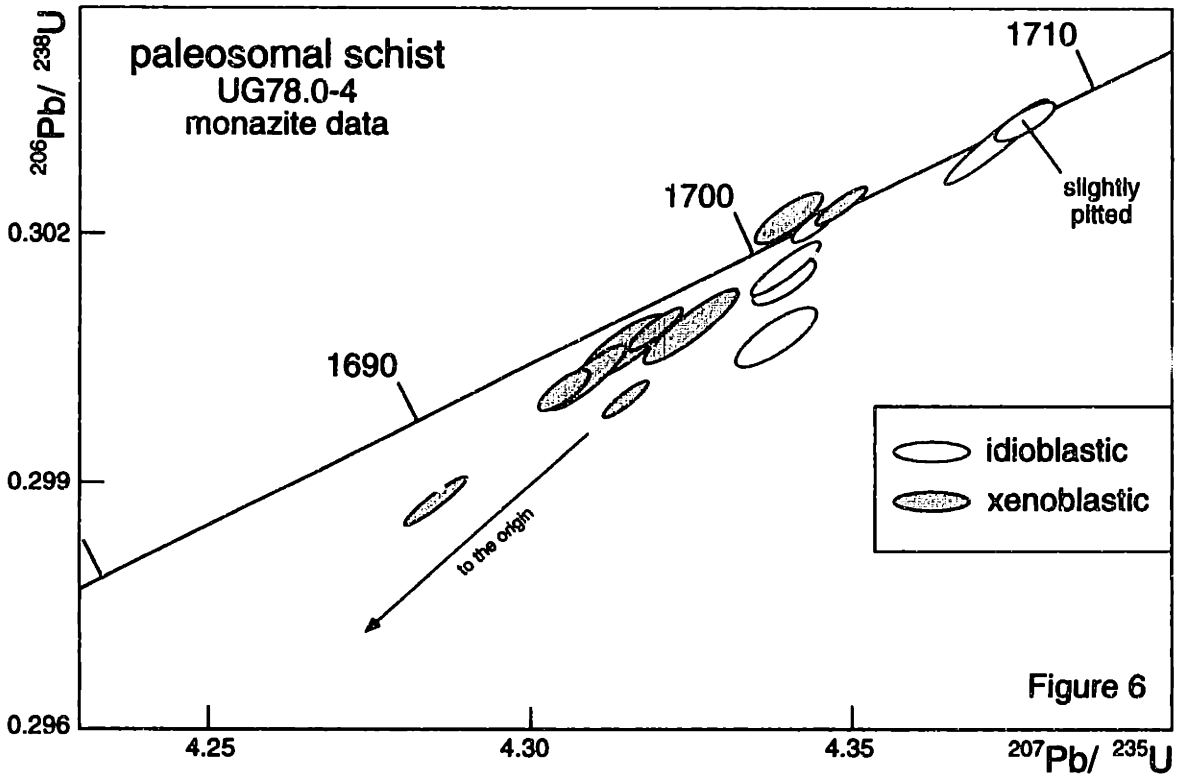

Figure 6

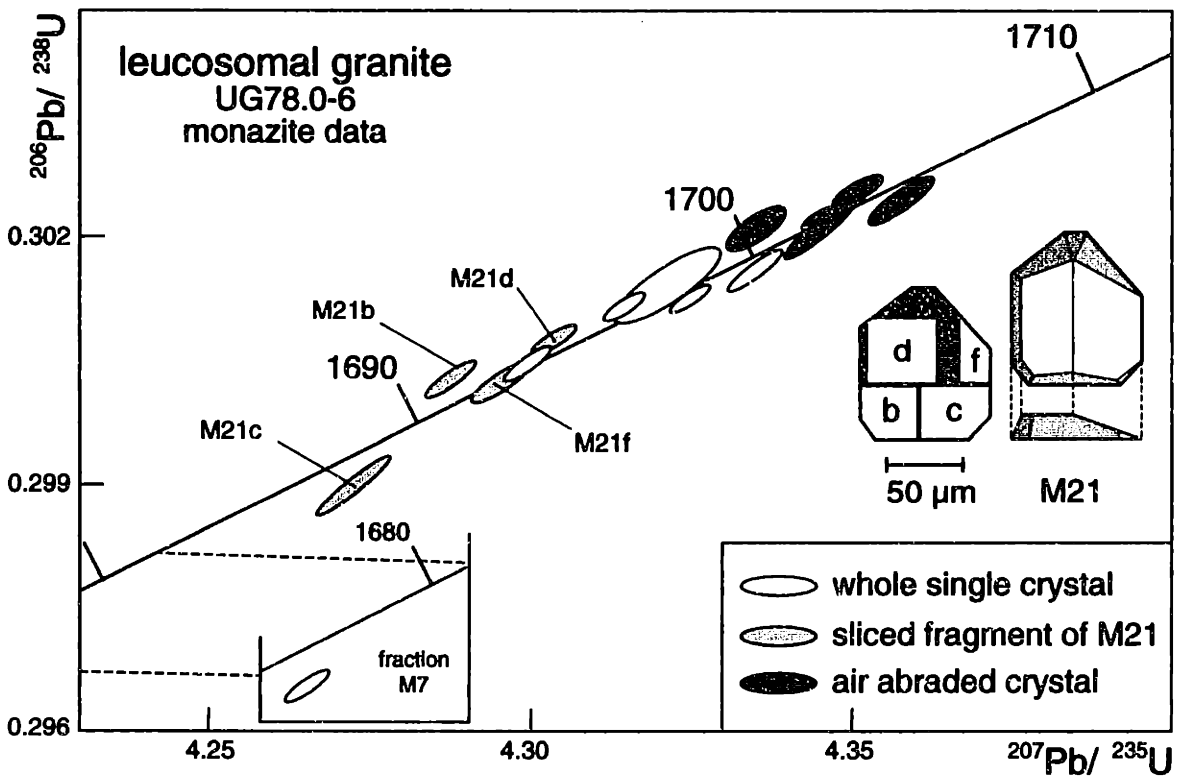

Figure 7

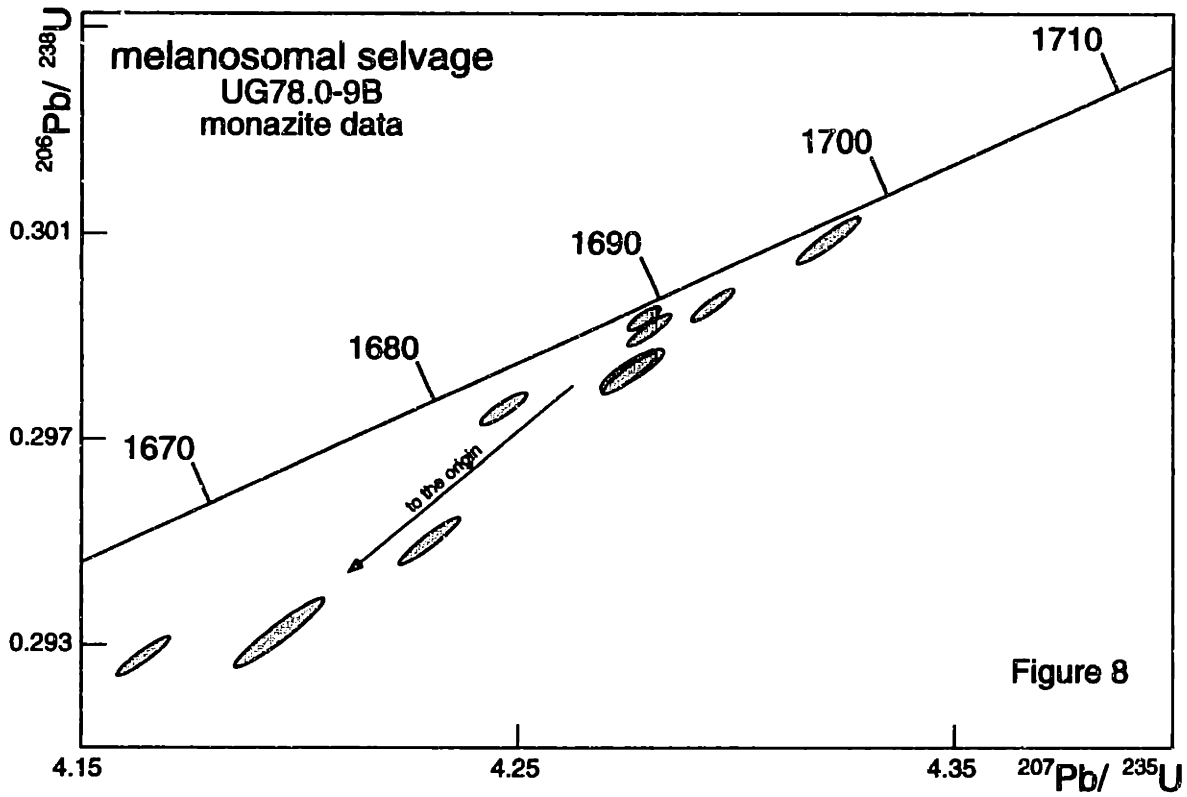

Figure 8

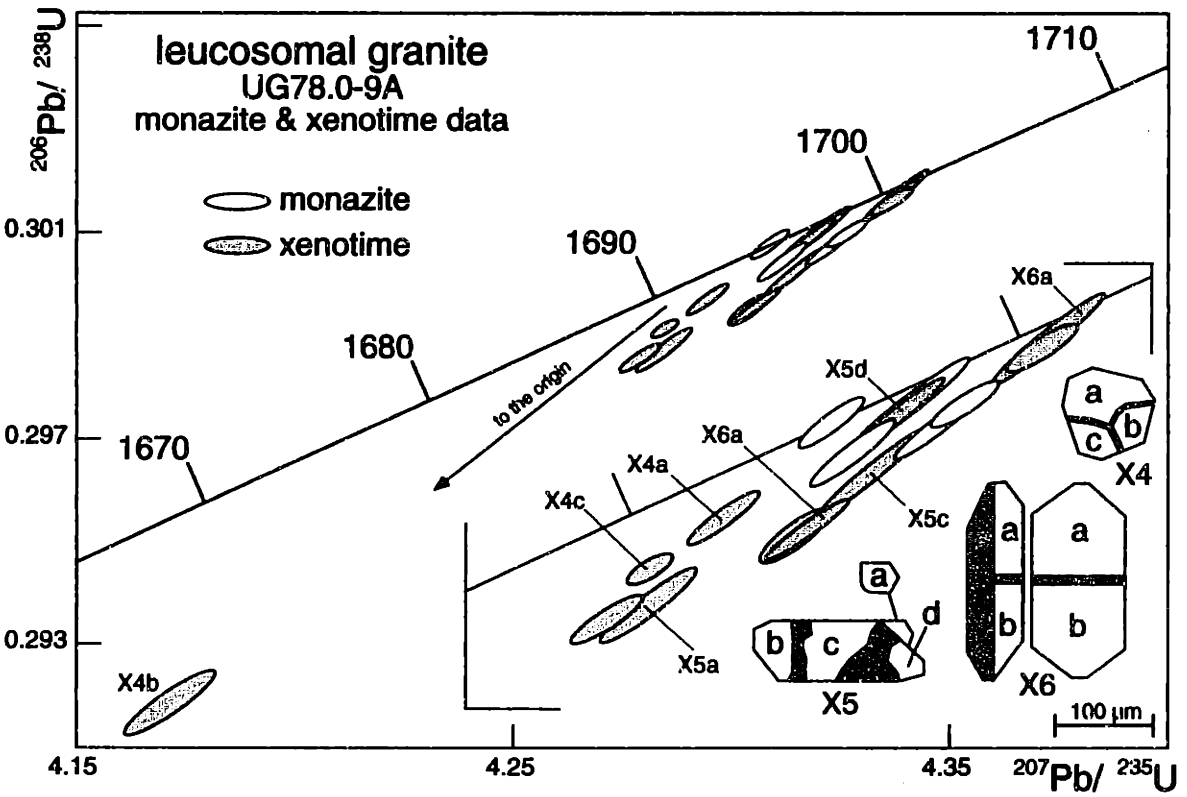

Figure 9

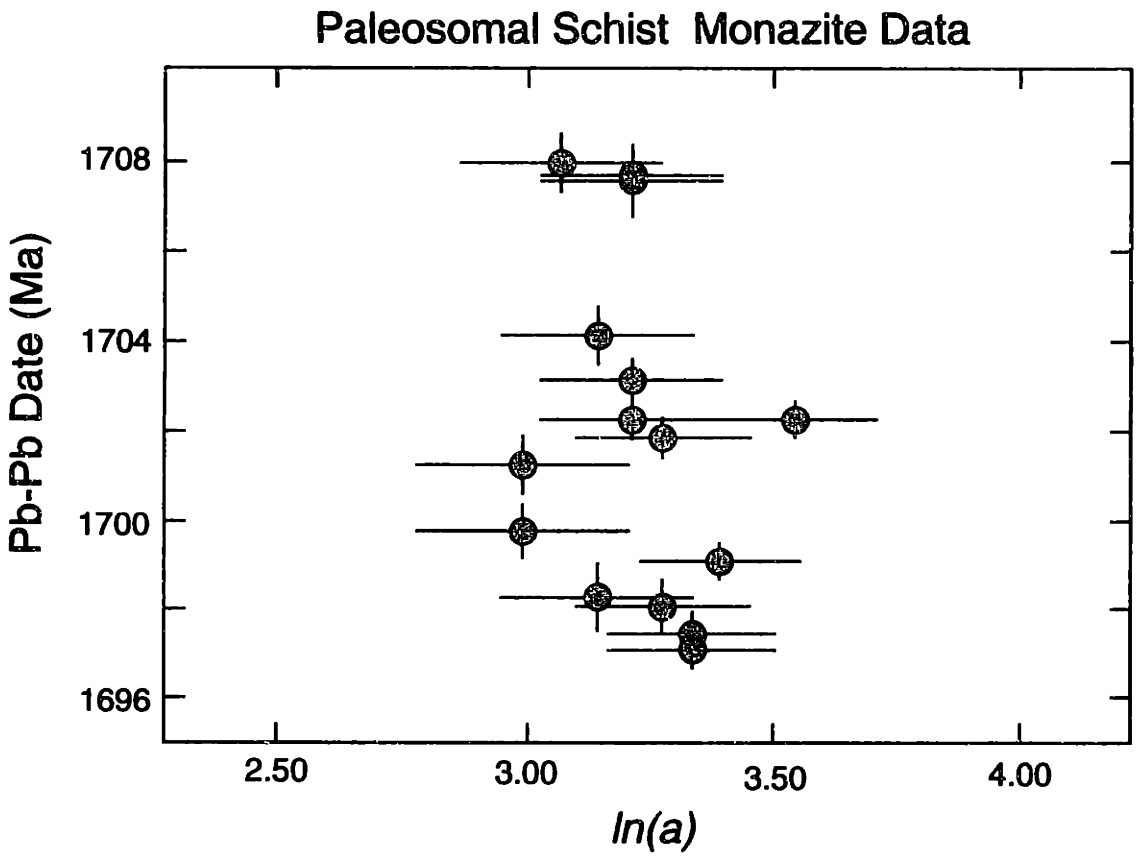
Paleosomal Schist Monazite Data
Pb-Pb Date (Ma)
1708
1704
1700
1696
2.50
3.00
3.50
4.00
ln(a)

Figure 10

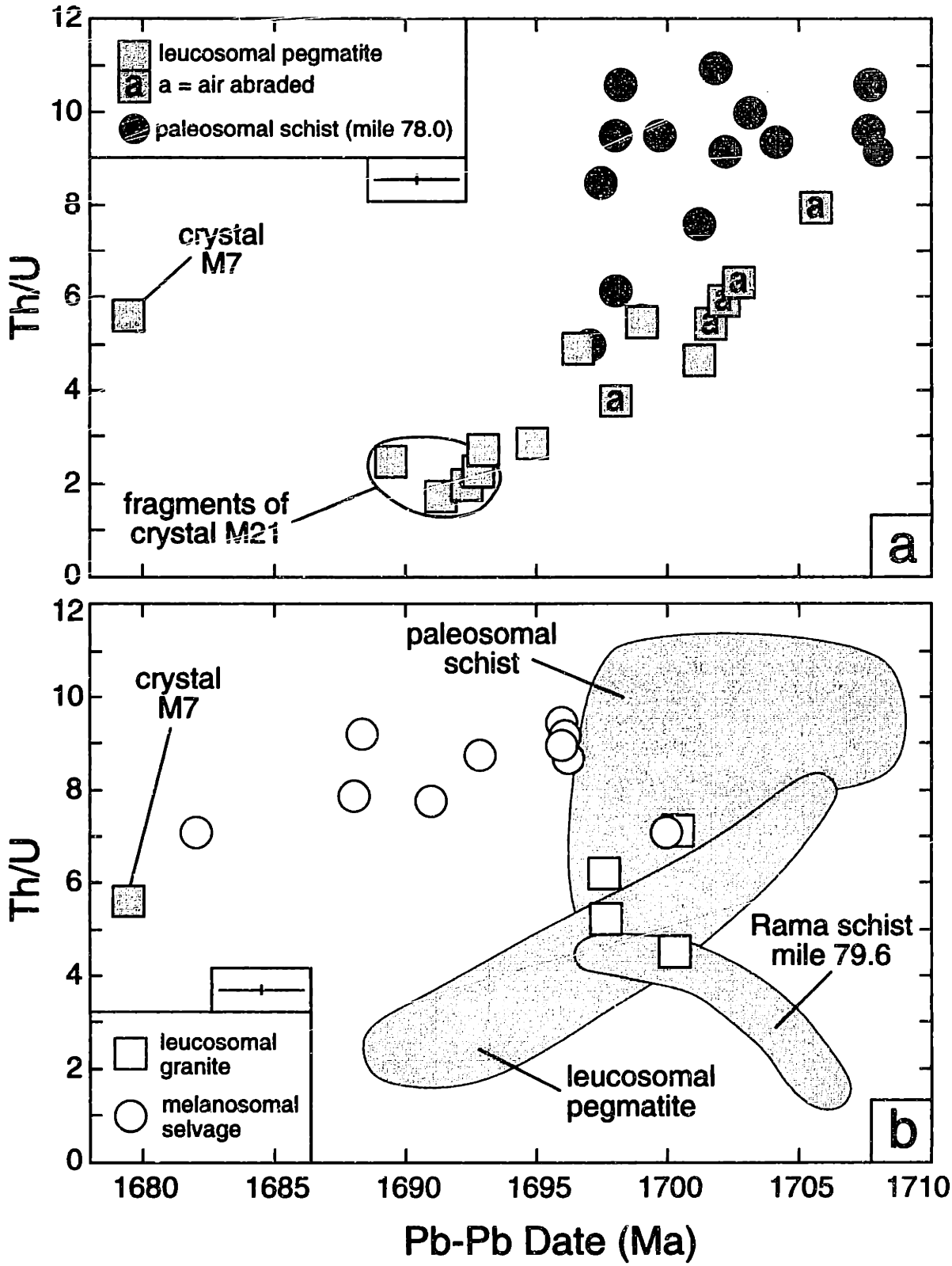
leucosomal pegmatite
a = air abraded
paleosomal schist (mile 78.0)
crystal M7
fragments of crystal M21
a
Th/U
paleosomal schist
crystal M7
Rama schist mile 79.6
leucosomal pegmatite
leucosomal granite
melanosomal selvage
b
Pb-Pb Date (Ma)

Figure 11

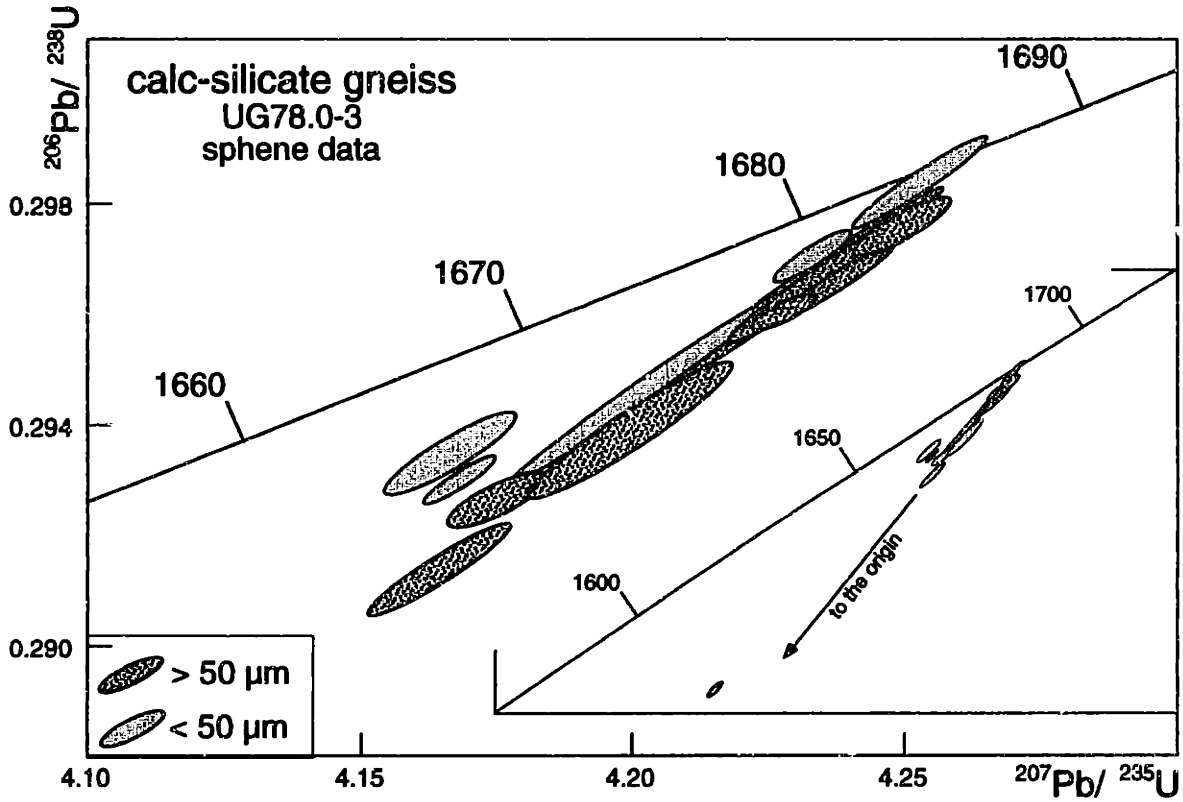
calc-silicate gneiss
UG78.0-3
sphene data
$^{206}Pb/^{238}U$
0.298
0.294
0.290
1690
1680
1670
1660
1700
1650
1600
to the origin
> 50 µm
< 50 µm
4.10
4.15
4.20
4.25
$^{207}Pb/^{235}U$

Figure 12

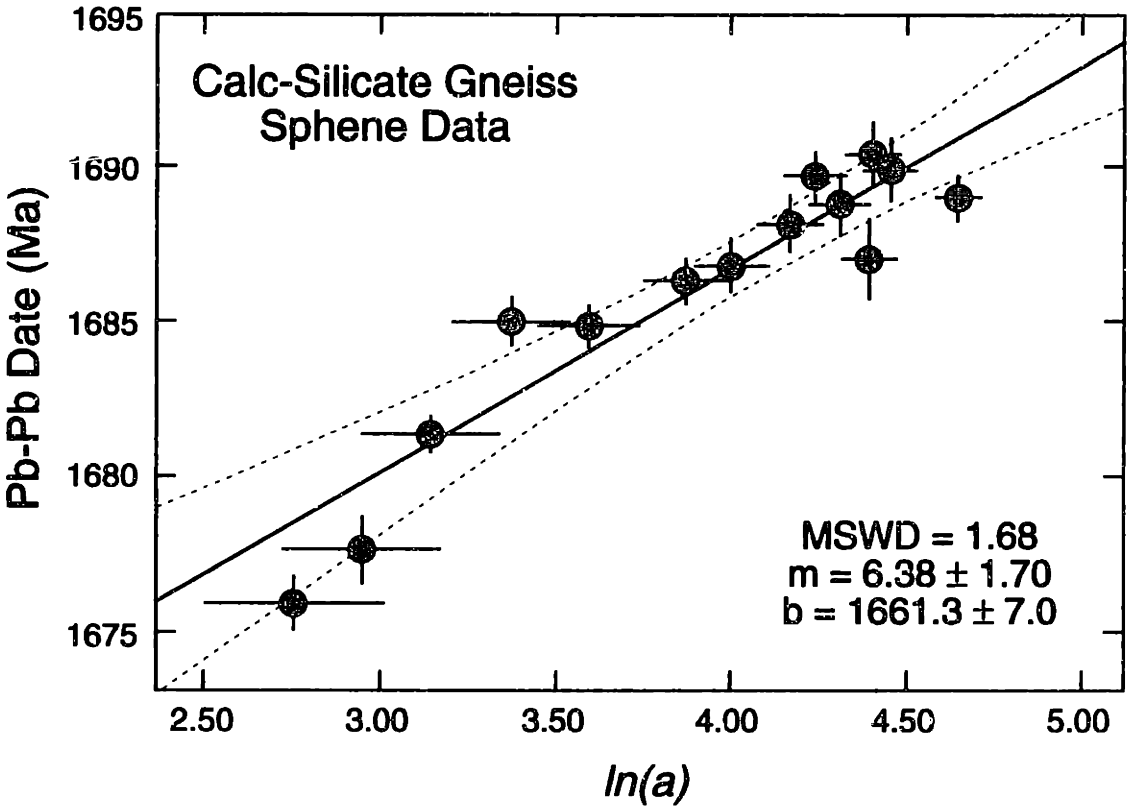
Calc-Silicate Gneiss
Sphene Data
MSWD = 1.68
m = 6.38 ± 1.70
b = 1661.3 ± 7.0
Pb-Pb Date (Ma)
ln(a)
1695
1690
1685
1680
1675
2.50
3.00
3.50
4.00
4.50
5.00

Figure 13

Mean Radius (μm)
Pb-Pb Date (Ma)
Closure Temperature (°C)
Mean Radius (μm)
Temperature (°C)
Time (Ma)

Figure 14

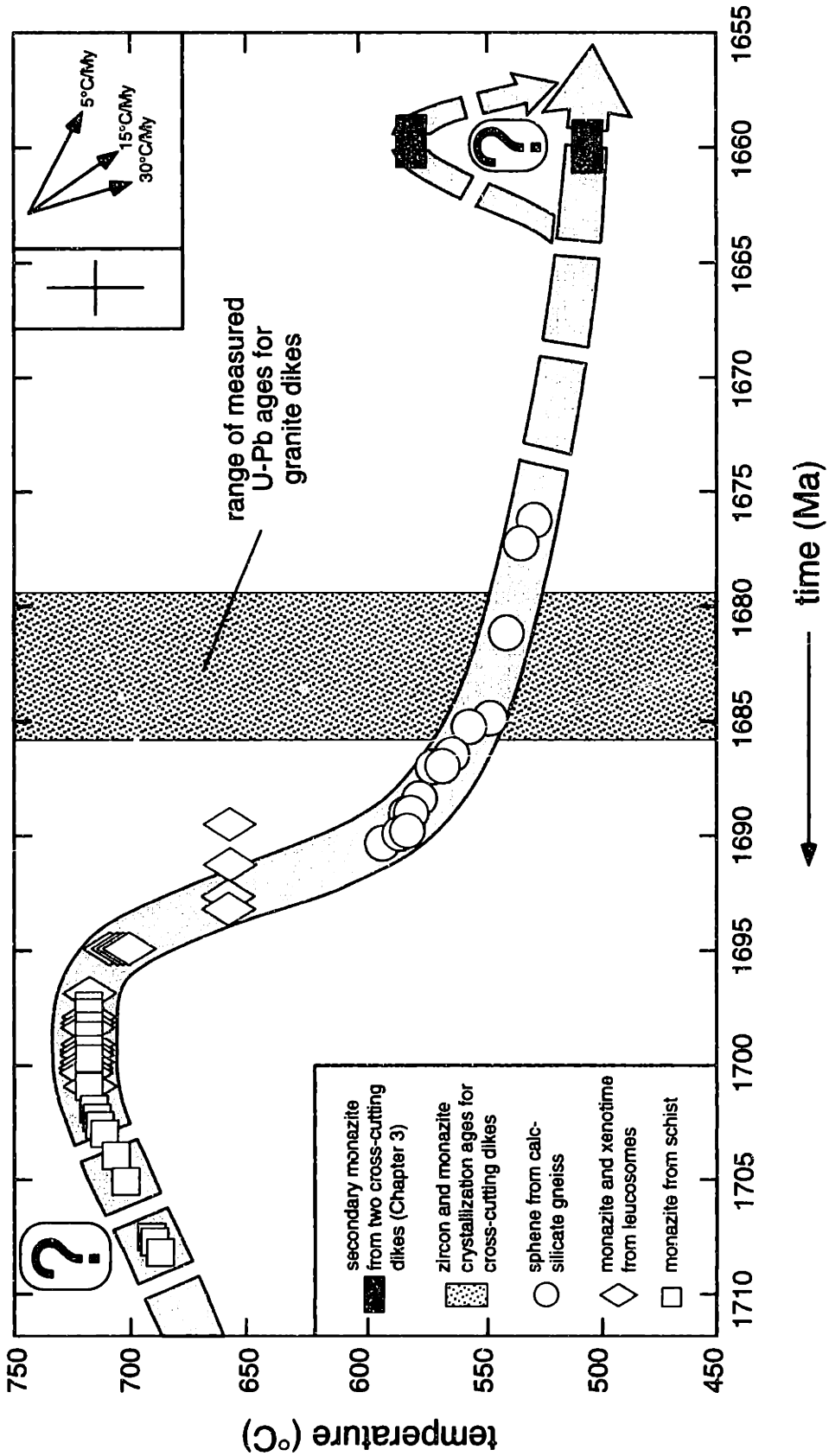
temperature (°C)
750
700
650
600
550
500
450
1710
1705
1700
1695
1690
1685
1680
1675
1670
1665
1660
1655
time (Ma)
range of measured U-Pb ages for granite dikes
5°C/My
15°C/My
30°C/My
?
?
secondary monazite from two cross-cutting dikes (Chapter 3)
zircon and monazite crystallization ages for cross-cutting dikes
sphene from calc-silicate gneiss
monazite and xenotime from leucosomes
monazite from schist

Figure 15

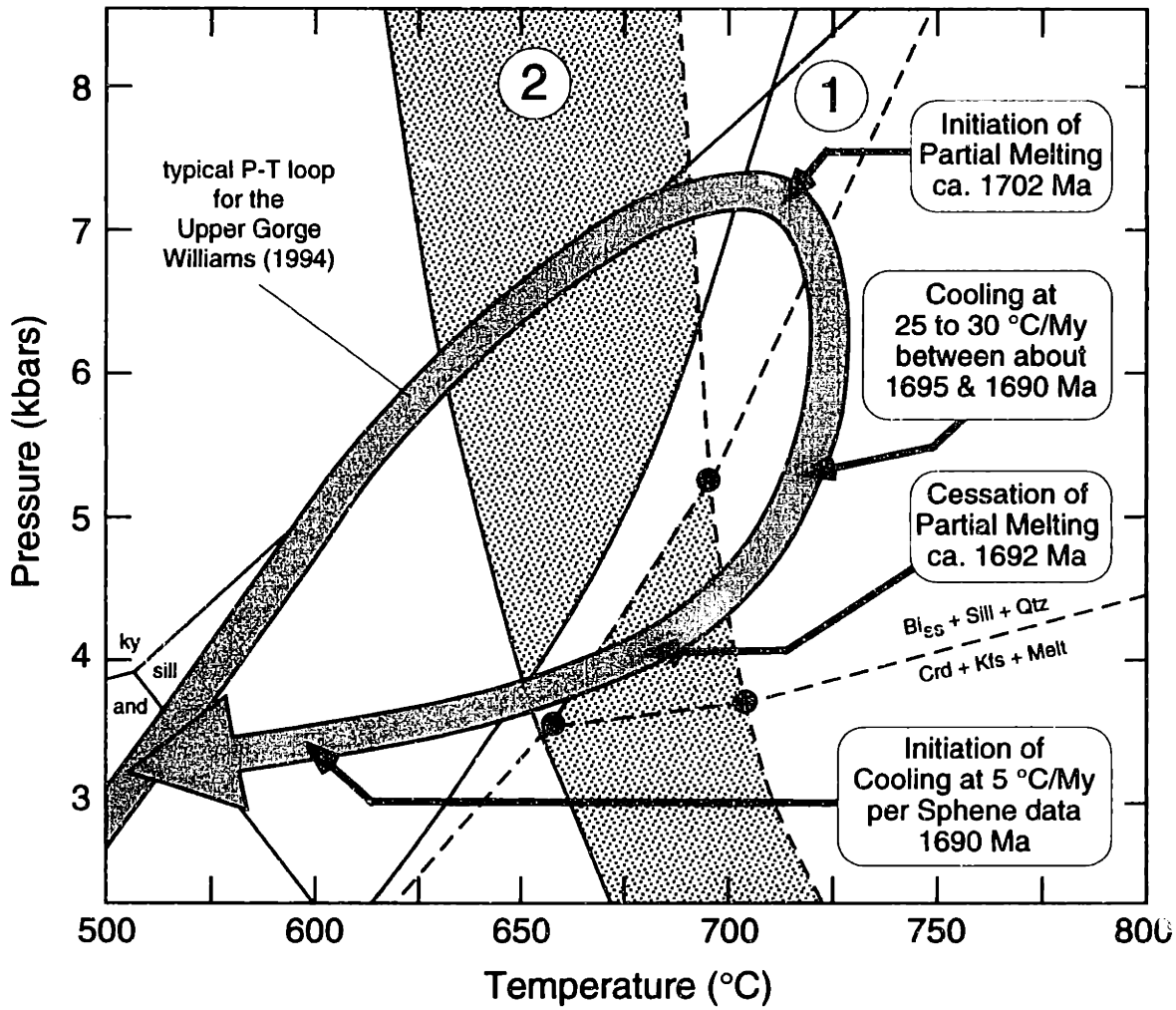
2
1
typical P-T loop
for the
Upper Gorge
Williams (1994)
Initiation of
Partial Melting
ca. 1702 Ma
Cooling at
25 to 30 °C/My
between about
1695 & 1690 Ma
Cessation of
Partial Melting
ca. 1692 Ma
Bi$_{ss}$ + Sill + Qtz
Crd + Kfs + Melt
Initiation of
Cooling at 5 °C/My
per Sphene data
1690 Ma
ky
sill
and
Pressure (kbars)
8
7
6
5
4
3
500
600
650
700
750
800
Temperature (°C)

Figure 16

CHAPTER 5

U-PB GEOCHRONOLOGICAL CONSTRAINTS ON THE SIGNIFICANCE OF THE BLOCK ARCHITECTURE OF THE UPPER GRANITE GORGE, GRAND CANYON, ARIZONA: CONTRASTING GEOLOGIC AND THERMAL HISTORIES ACROSS SHEAR ZONES IN PALEOPROTEROZOIC MIDDLE CRUST

INTRODUCTION

One of the outstanding questions concerning the Paleoproterozoic tectonothermal evolution of the southwestern United States concerns the significance of major shear zones. In central Arizona, steeply-dipping shear zones bound crustal blocks characterized by contrasting pre-orogenic geologic histories and post-orogenic thermal histories (Karlstrom et al., 1987; Karlstrom and Bowring, 1988; Bowring and Karlstrom, 1990; Chamberlain and Bowring, 1990). These observations have been interpreted to indicate that the shear zones are lithosphere-scale discontinuities, developed during orogenic assembly and accretion, that accommodated independent vertical displacement of the crustal blocks about 200 m.y. after accretion (Bowring and Karlstrom, 1990). If the block architecture and differential unroofing histories observed in central Arizona are characteristic of the orogenic system, then a similar block architecture should be present in other areas of the orogen.

The Upper Granite Gorge of the Grand Canyon is an ideal area for evaluating the block architecture. First, the Upper Gorge transect lies along strike from central Arizona (Fig. 1) and, unlike much of the central Arizona transect, offers complete exposures. Second, the transect is segmented by five shear zones that define six crustal blocks that

exhibit variable structural styles and preserve different metamorphic grades (Ilg et al., 1996b). Finally, the rocks in the transect contain appropriate minerals for U-Pb geochronology and thermochronology, essential tools for evaluating the significance of the block architecture.

In this chapter, a geochronologic and thermochronologic framework is developed to compare the tectonic and thermal histories of the six crustal blocks in the Upper Gorge. The geochronologic and thermochronologic framework includes data from Chapters 2, 3 and 4 as well as data from nine additional samples described herein. The significance of U-Pb dates from zircon, monazite, xenotime and sphene are evaluated using field, petrographic and textural observations. Published diffusion parameters are used to evaluate whether monazite and sphene dates reflect cooling through their respective closure temperatures. The interpreted dates are then compiled as a function of location within the Upper Gorge transect to construct and compare the thermal histories of the crustal blocks in the Upper Gorge. This approach reveals that one of the six crustal blocks has a distinct post-orogenic history, a result that underscores potential problems with correlating fabrics, structures and absolute timing relationships across the transect and raises important questions about the assembly and post-assembly history in this part of the orogen.

THE BLOCK ARCHITECTURE OF THE UPPER GRANITE GORGE

Five major shear zones divide the Upper Granite Gorge into six crustal blocks (Fig. 2; Ilg et al., 1996a,b). The blocks preserve contrasting metamorphic mineral facies. In general, the structural style and relative volume of peraluminous granite change as a function of metamorphic grade (Table 1). High-grade blocks, such as the Mineral Canyon block, are generally characterized by :1) upper amphibolite to lower granulite facies mineral assemblages; 2) strong, localized overprinting of group-one structures (S_1

foliation and F_1 folds) by group-two structures (S_2 foliation and F_2 folds); and 3) relatively high volumes of peraluminous granite intrusions. In contrast, low-grade blocks, such as the Topaz Canyon block, exhibit: 1) upper greenschist to lower amphibolite facies mineral assemblages; 2) well-preserved group-one structures that are only locally overprinted by group-two structures; and 3) a relatively low volume of peraluminous granite intrusions. Despite the wide range of peak temperatures (500 °C to 725 °C) estimated for the Upper Gorge, estimated peak pressures are relatively constant (≈ 6 kbars) across the transect (Ilg et al., 1996b). However, the timing and duration of metamorphism and magmatism within each of these blocks is unknown. Geochronologic and thermochronologic data provide a temporal framework from which to compare and contrast the timing of deformation, metamorphism, and magmatism as well as the rate of post-peak metamorphic cooling across the crustal blocks.

ANALYTICAL TECHNIQUES

Zircon, monazite, xenotime and sphene were separated by standard crushing, heavy liquid and magnetic techniques. Individual crystals were measured, photographed and washed in acetone and warm H_2O (monazite and xenotime) or acetone and 30% HNO_3 (zircon and sphene) prior to dissolution. Samples were dissolved in 300 µl teflon nanocapsules containing 11 - 12 N HCl (monazite and xenotime) or 50% HF + 14N HNO_3 (zircon and sphene) and a mixed ^{205}Pb-^{233}U-^{235}U tracer solution. Lead and uranium were separated from monazite, xenotime and zircon using HCl-based ion-exchange chromatography modified after Krogh (1973). Sphene ion-exchange chromatography used HBr chemistry for separation of Pb and HCl chemistry for separation of U. The samples were analyzed using conventional thermal ionization mass spectrometry on a VG Sector 54 mass spectrometer at the Massachusetts Institute of

Technology. Lead was analyzed either: 1) in static mode, using Faraday detectors for all isotopes except ^{204}Pb, which was measured simultaneously with the Daly detector in ion counting mode; or 2) by peak-jumping using a Daly detector in ion counting mode. Uranium was analyzed as a metal in static mode using Faraday collectors. Statistical analysis of the data uses the algorithms of Ludwig (1989). Additional analytical details are presented in Table 2.

To investigate potential intracrystalline variations in the U-Pb systematics of xenotime from the migmatite in Ninety-One Mile Creek (sample UG91.1-7A in Table 2), we sliced two crystals into fragments, carefully recording the original spatial relationships, and analyzed the fragments separately. These analyses are identified in Table 2 by a lower case letter at the end of the fraction name and are shown along with drawings of the crystals in figure 7. Our slicing technique produces fragments as small as 20 x 10 x 10 μm (≈ 100 ng total sample weight)— similar to the dimensions of the pit produced by an ion probe analysis (e.g., DeWolf et al., 1993; Harrison, et al., 1995) — with analytical uncertainties of better than 0.34% for the U-Pb dates and 0.13% for the Pb-Pb date (Table 2).

THERMOCHRONOLOGICAL APPROACH

The development of a meaningful geochronologic framework in a metamorphic terrain requires careful evaluation of the U-Pb results from each mineral dated (e.g., Chapters 3 and 4). Perhaps the most fundamental question is whether the calculated dates from *whole crystals* represent the time of crystallization, the time of cooling through a specific closure temperature, or a hybrid date representing physical mixtures of mineral domains preserving either contrasting age information (e.g., inheritance) or varying degrees of U-Pb disequilibrium(e.g., discordance). Recognition of cooling dates is particularly important because minerals that preserve cooling dates define segments of

the thermal history. To test for cooling dates we employ Wright diagrams (Wright et al., 1991), which portray the relationship between the grain size and the measured mineral date (see Chapter 4).

An important aspect of using Wright diagrams involves choosing appropriate values for the effective diffusion dimension (a) and the diffusion geometry (A)(Dodson, 1973; 1976; Wright et al., 1991). Several studies have shown that the effective diffusion dimension is equivalent to grain size for two of the minerals used in this study: monazite (Suzuki et al., 1994) and sphene (Mezger et al., 1991; Cherniak, 1993). Therefore, all of the crystals analyzed in this study were measured along three orthogonal directions prior to dissolution. Because previous workers used a spherical diffusion geometry (A=55) for monazite and sphene, the effective diffusion dimension reported in this chapter is the average of the three measured radii.

Throughout this chapter, the diffusion parameters of Cherniak (1993) are used to calculate closure temperatures and cooling rates for sphene analyses. The Cherniak (1993) diffusion data were recently called into question by Zhang and Schärer (1996) They argued that preservation of inheritance in sphene from a 35 Ma syenite requires closure temperatures that are about 50 °C higher than those predicted by Cherniak's diffusion data. However, to calculate the closure temperatures of their crystals, Zhang and Schärer (1996) use the long dimension (diameter) of their crystals as the effective diffusion dimension even though they employ a cylindrical diffusion geometry (A=27). According to Dodson (1973), the appropriate effective diffusion dimension for a cylindrical diffusion geometry is the radius of the cylinder, not the long dimension of the cylinder. This approach overestimates the closure temperature of these crystals and may account for much of the difference between Zhang and Schärer's calculated closure temperatures and those predicted by the Cherniak (1993) diffusion data. In addition, the results of Scott and St.-Onge (1995) suggest that closure temperatures calculated

from the Cherniak (1993) diffusion data are comparable to thermobarometrically determined temperatures for equilibria that produce metamorphic sphene. Therefore, throughout this paper we use the diffusion data of Cherniak (1993) to calculate closure temperatures. Future diffusion studies may reveal that the absolute temperatures calculated herein are systematically low, but the validity of the approach employed and the relative differences observed between mineral dates across the transect will remain valid.

U-PB GEOCHRONOLOGY

In this section, the U-Pb geochronologic data from each of the six crustal blocks in the Upper Gorge are described (in order from east to west) and interpreted (see Fig. 2 for sample locations). The descriptions include summaries of both the results presented in Chapters two through four and results presented here for the first time (see Table 2). Each subsection closes with a summary of the geochronologic constraints on the inferred thermal history of the block. The block names used in this paper are informal: they are used strictly for the purpose of brevity and are not meant as formal names.

Mineral Canyon Block

The thermal history of the Mineral Canyon block, which is described in some detail in Chapter four, is summarized in figure 3. Peak metamorphic conditions were 720 °C and 6 kbars (Williams, personal communication, 1995) at 1700 Ma. During the metamorphic peak (1702 - 1695 Ma), group-one structures were transposed and overprinted by group-two structures (Ilg et al., 1996b). The rocks were unroofed to about 3.5 kbars between 1700 and 1690 Ma and they cooled at an integrated rate of 15-30°C to about 600 °C. Cooling ages from metamorphic sphene crystals of varying sizes indicate a decrease in the rate of cooling at about 1690 Ma to approximately 4 °C/m.y. integrated

over the interval 1690 to 1676 Ma. Between 1685 and 1680 Ma, during post-peak cooling, large volumes of peraluminous granite dikes intruded the block and the development of group-two structures waned. Monazites from two of the granite dikes preserve evidence for secondary monazite growth at about 1659 Ma (Chapter three), but it is unclear whether this secondary growth represents a short-lived 'thermal spike' or a fluid-flow 'event' at ambient temperatures.

Clear Creek Block

The Vishnu shear zone separates lower granulite facies Vishnu schist in the Mineral Canyon block from middle amphibolite facies Vishnu schist in the Clear Creek block. The change in metamorphic grade is accompanied by a marked decrease in the relative volume of peraluminous granite intrusions. Metamorphic grade increases from east to west within the block from middle amphibolite facies at mile 82 to upper amphibolite facies at mile 86 (Ilg et al., 1996b). The increase in metamorphic grade is accompanied by an increase in the relative volume of peraluminous granite and pegmatite intrusions from less than 5% at mile 82 to about 50% at mile 87. A small peraluminous granite stock that intrudes the 1740 Ma Zoroaster granite yielded a crystallization age of 1698 ± 1 Ma and contains what we interpreted as inherited monazite (perhaps metamorphic monazite) with concordant dates at 1702 Ma (sample UG85.2-4 in Chapter 2). The age of this granite indicates that: 1) partial melting and melt accumulation occurred at about 1.70 Ga; and 2) both the development of S_1 fabric in the Zoroaster granite and the folding of that fabric into a kilometer-scale F_2 antiform predated 1698 Ma. A second peraluminous intrusion yielded whole crystals of monazite with Pb-Pb dates between 1677 and 1690 Ma from which a crystallization age could not be interpreted with confidence (sample UG85.6-2 in Chapter 3).

A sample of coarse-grained amphibolite (sample UG84.3-3) collected east of the Zoroaster pluton produced intact crystals of metamorphic sphene. Most crystals were clear, light-brown xenoblastic grains with minor cracks. Four single-crystal analyses and one multi-grain analysis yielded concordant to slightly discordant U-Pb dates with Pb-Pb dates ranging from 1695 to 1700 Ma (Table 1; Fig. 4). The data show a statistically significant correlation between grain size and Pb-Pb date, indicating that the crystals preserve cooling ages (Fig. 4). The slope and intercept of the best-fit line yields an integrated cooling rate of 5-10 °C/m.y. over the interval 1695 to 1700 Ma. Using the diffusion parameters of Cherniak (1993) and a cooling rate of about 7 °C/m.y., the calculated closure temperature for the largest crystals (S1, S3, S4) is 600 -615 °C, which is consistent with estimated peak temperatures from mile 84 (600-650 °C; Williams, personal communication, 1995).

U-Pb data from two samples provide broad but important constraints on the timing of metamorphism, deformation, magmatism and cooling in the Clear Creek block. The age of the peraluminous granite stock at mile 85.4, which contains inherited metamorphic monazite, indicates that at some depth the crust was melting at about 1700 Ma. The sphene data from the amphibolite at mile 84.3 indicate that the temperature at 1700 Ma was about 600 - 620 °C at the currently exposed crustal level. Group-two fabric formation initiated prior to 1698 Ma, probably synchronous with peak conditions (Ilg et al., 1996b), as axial planar cleavage to F_2 folds. Following the peak of metamorphism, the rocks cooled at an integrated rate of 5-10 °C/m.y. over the interval 1700 to 1695 Ma. Assuming that the crystallization age of the deformed pegmatite at mile 85.6 is 1691 Ma or younger, group-two structures continued to develop after 1695 Ma, although the lower bound of S_2 formation in this area is unconstrained.

Trinity Creek Block

The Bright Angel shear zone separates upper amphibolite facies Vishnu schist of the Clear Creek block on the east from upper amphibolite to lower granulite facies Brahma and Rama schist of the Trinity Creek block on the west (Fig. 2). The boundary is also marked by a dramatic decrease in the relative volume of peraluminous granite/pegmatite intrusions from about 50% at mile 87 to less than 20% at mile 89 (e.g., Ilg et al. 1996a). The eastern half of the block is characterized by Brahma and Rama schist intruded by sheet-like plutons of granodiorite, whereas the western half is dominated by Vishnu schist. Metamorphic grade is variable across the block: mineral assemblages are consistent with upper amphibolite to lower granulite facies (Table 2; Ilg et al., 1996b). Aside from moderate volumes (<20%) of dikes at mile 89.0, near the Horn pluton at mile 90.6, and in 94-mile Creek and a large pegmatite intrusion at mile 93.0, the Trinity Creek block exposes a relatively small volume of peraluminous granite/pegmatite. Nowhere in the Trinity Creek block does the relative volume of peraluminous dikes approach that of the western parts of the Mineral Canyon and Clear Creek blocks, despite comparable peak temperatures (Ilg et al., 1996a).

U-Pb data from several samples reported in Chapter two constrain the timing of deformation in the Trinity Creek block. The 1713 Ma Horn Creek pluton (sample UG90.6-2) contains both S_1 and S_2, thereby bracketing the formation of these fabrics to a time interval after 1713 Ma. Furthermore, the 1662 Ma Phantom Creek pluton, a large intrusion of peraluminous granite exposed immediately west of the Bright Angel shear zone, contains shear bands that offset co-magmatic pegmatitic segregation veins within the pluton. Correlation of these structures with group-one and group-two structures in the mechanically distinct country rocks may be problematic. It is unclear whether the shear bands are the product of: 1) a discrete deformational event that produced an S_3

fabric (Ilg et al., 1996b); 2) late deformation associated with group-two structures (Ilg et al., 1996b); or 3) localized deformation associated with emplacement of the pluton.

U-Pb data from samples reported in Chapter two also provide evidence for the timing of metamorphism. The Phantom Creek pluton, a two-mica peraluminous granite, provides evidence for partial melting in the Trinity Creek block at about 1665 Ma. Evidence for ca. 1660 Ma metamorphism is also provided by a ca. 1740 Ma calc-alkaline metavolcanic rock interlayered with amphibolite of the Brahma schist at mile 90.4 (sample UG90.4-1 in Chapter two). This rock contains a texturally complex population of zircons including epitaxial overgrowths on both partially resorbed crystals and euhedral crystals. Zircons from this rock yielded a wide range of Pb-Pb dates (1735 to 1658 Ma), but the least discordant analysis, has a Pb-Pb date of about 1665 Ma. The simplest interpretation is that zircon grew as a metamorphic mineral at about 1665 Ma. Together these two samples preserve evidence for metamorphism significantly younger than 1700 Ma.

U-Pb results from four additional samples constrain the timing of deformation, metamorphism and magmatism within the Trinity Creek block (Fig. 2). The results include: sphene dates from a sample of granodiorite from the Pipe Creek pluton in the eastern part of the block (UG89.6-1); sphene dates from the 1713 Ma Horn Creek pluton (sample UG90.6-2 from Chapter 2); monazite and xenotime dates for a coupled schist/granite pair from a migmatite exposed in Ninety-One Mile Creek (UG91.1-7A,B); and monazite and xenotime dates from a biotite - muscovite quartzofeldspathic gneiss collected near the western margin of the block (sample UG95.7-1 from Chapter 2).

The Pipe Creek pluton is a small sheet of foliated granodiorite that intrudes Brahma schist (Fig 2). Zircons from this sample are anhedral grains containing dusty inclusions, turbid domains and numerous cracks. Four extensively air-abraded (Krogh, 1982) crystals yielded discordant (1.3 to 30%) U-Pb dates with Pb-Pb dates ranging from 1689

to 1740. Because the data do not define a statistically significant discordia, the crystallization age of the rock remains in question.

Regardless of whether the crystallization age of the Pipe Creek pluton is 1710 or 1740 Ma, sphene dates from this rock are more than 100 m.y. younger. The sample yielded few whole sphene crystals; most grains were light brown fragments, many of which had two crystal faces. Seven fractions clustered near concordia (0 to 1.7% discordant) between 1572 and 1604 Ma (Fig. 5). The two oldest fractions are whole-crystal analyses of dark brown sphene that yielded Pb-Pb dates of 1604 and 1589 Ma. The remaining five fractions consisted of light brown fragments from the outer edges of larger crystals (as indicated by the preserved crystal faces). The Pb-Pb dates of these analyses (1572 and 1584 Ma) correlate with the average size of the fragments: fractions S3 (1583 Ma), S4 (1584 Ma) and S5 (1581 Ma) are roughly the same size ($\approx$ 55 μm) and have identical Pb-Pb dates. This observation suggests that the outer parts of the crystals are younger than the core regions, but there is no evidence for two generations of growth. For example, dark brown sphenes are significantly more radiogenic ($^{206}Pb/^{204}Pb > 1300$) than the light brown fragments ($250 < {}^{206}Pb/^{204}Pb < 381$), but there is no textural evidence that these crystals represent different generations of growth. Both types occur as euhedral, diamond- or wedge-shaped crystals intergrown with plagioclase, biotite and hornblende, and the light-brown sphene does not overgrow dark brown sphene. Moreover, dark fragments yielded dates that overlap with dates from light-colored fragments. Given that the pluton was emplaced before 1700 Ma, the data are consistent with either: 1) protracted dynamic recrystallization at temperatures below the closure temperature, or 2) protracted cooling (at $\leq$ 1 °C/m.y., assuming complete resetting at 1660 Ma) from temperatures above the closure temperature of the largest crystal.

The second sample from the Trinity Creek block is the Horn Creek pluton, which yielded a U-Pb zircon age of 1713 ± 2 Ma. The sample produced abundant sphene, but most of the grains were fragments of larger crystals. Both whole crystals and crystal fragments range in color from dark chestnut-brown to light-brown; large euhedral crystals tend to be dark-colored and fragments from the edges of large grains tend to be light-colored. Several grains, for example fraction S23, appear to be composite crystals composed of dark-colored cores partially over grown by light-colored rims - similar relationships were described by Getty and Gromet (1992). In addition, small euhedral sphene crystals occur in association with resorbed ilmenite crystals, whereas large euhedral sphenes are intergrown with biotite, hornblende, allanite and epidote.

U-Pb analyses of sphene from the Horn Creek pluton yielded complex U-Pb systematics. Ten fractions were analyzed: five whole-crystal analyses, including four single-grain analyses, and five multi-grain analyses of fragments chosen on the basis of size and color. The ten fractions are nearly concordant (0.08 to 1.3% discordant) and have Pb-Pb dates between 1596 and 1638 Ma (Fig. 6). The data do not define a statistically significant discordia and although the whole crystal analyses are older than the fragment analyses, the Pb-Pb dates from the whole grains do not correlate with grain size (Fig. 6). For example, one of the largest crystals (fraction S22) yielded one of the youngest Pb-Pb dates (1604 Ma; Fig. 6). In addition, fraction S23 which appeared to have core-overgrowth textures under the optical microscope, yielded the oldest Pb-Pb date instead of an intermediate date as might be expected.

Despite these complexities, several first order conclusions can be drawn. First, there is textural evidence for at least two generations of sphene growth. Second, the sphenes preserve dates that are more than 70 m.y. younger than the crystallization age of the pluton. Third, whole-crystal analyses tend to be older than analyses of fragments broken from crystal-edges. Finally, whole crystal analyses do not appear to preserve cooling

ages. There are several ways to interpret these results, but the simplest interpretation is that magmatic sphene was reset at some time prior to 1640 Ma, either by dynamic recrystallization or high-temperature Pb loss, and a second generation of sphene grew at some time after 1596 Ma. Thermal resetting of the largest (magmatic) sphene crystal (87 μm) would require heating at 650 °C for 1 m.y. (Cherniak, 1993), which, based on evidence for high-temperature metamorphism at about 1660 Ma, is geologically reasonable in this part of the Trinity Creek block.

The third sample from Trinity Creek block provides some constraints on the timing of metamorphism. A sample of migmatite containing paleosomal schist and several leucosomal pegmatite pods (samples UG91.1-7A, B) was collected in Ninety-One Mile Creek. The paleosome (sample 7B) is a biotite-muscovite schist that contains sparse needles of fibrolitic sillimanite at the margins of biotite crystals. The leucosomal granite pods represent less than 5% of the outcrop volume and occur as centimeter-scale, deformed stringers and pods generally lacking selvages.

Paleosome and leucosome were crushed separately prior to mineral separation; both samples yielded abundant monazite (clear, yellow to pale yellow, faceted to pitted, equant) and xenotime (pale yellow to colorless, faceted to subrounded, platy to equant). Idioblastic crystals from the schist and euhedral crystals from the leucosomal granite were analyzed in an attempt to reduce potential complexities of partially resorbed crystals (see Chapter 4).

Five monazite crystals and one xenotime crystal from the biotite schist yielded nearly concordant (-0.12 to +0.9% discordant) U-Pb dates with Pb-Pb dates between 1631 (fraction B-M6) and 1646 Ma (fraction B-X1; Fig. 7). The Pb-Pb dates of the monazites do not correlate with either grain size (Fig. 7) or grain shape.

Two monazite crystals and three xenotime crystals from the leucosomal granite pod are variably discordant and have Pb-Pb dates between 1642 and 1653 Ma (Fig. 7). In

addition, two large xenotime crystals were sliced into fragments: crystal X7, a 270 μm-long stubby prism that was sliced into six fragments representing all of the crystal volume; and crystal X8, a 200 μm-long platy crystal that was sliced into three fragments. Fragments from X7 form a discordant array (0.1 to 1.3% discordant) that yields an upper intercept age of 1662.2 ± 0.9 Ma (MSWD = 0.27; lower intercept = 18 ± 273 Ma). Fragments from X8 are variably discordant and have Pb-Pb dates of 1646.3 ± 1.5, 1648.1 ± 1.3, and 1649.7 ± 1.2 Ma and do not define a statistically significant discordia.

The sliced fragments from crystals X7 and X8 demonstrate limited intra-grain age variation (relative to the data set as a whole), indicating that the age dispersion in this sample is not caused by physical mixtures of crystal domains with contrasting ages. Instead, the monazites and xenotimes from this rock preserve either crystallization ages or cooling ages. Since the xenotimes do not exhibit a correlation between grain size and Pb-Pb date, one of two conclusions can be drawn: 1) the effective diffusion dimension of xenotime is smaller than the grain size; or 2) these grains preserve crystallization ages. The effective diffusion dimension of xenotime (with respect to Pb) is not known, but since the xenotime lattice is isostructural with that of zircon, the diffusion kinetics of these minerals are probably comparable. Therefore, I suggest that monazite and xenotime from the leucosomal granite preserve crystallization ages.

If the leucosomal granite pods represent *in situ* melts, then the monazite and xenotime dates directly date peak metamorphic conditions. However, several observations argue against *in situ* melting: 1) the lack of prominent selvages; 2) the paucity of sillimanite in the schist; and 3) the discrepancy in mineral dates between from the granite and the adjacent schist. The simplest interpretation is that the leucosomes represent melt that was injected into the schist and disrupted by deformation. Regardless of the origin of the leucosome, the mineral dates from the migmatite in Ninety-One Mile Creek indicate that metamorphic mineral growth, and perhaps deformation,

occurred between (or perhaps over the interval) 1645 and 1663 Ma in the central Trinity Creek block.

The fourth sample from the Trinity Creek block is a micaceous quartzofeldspathic gneiss (a meta-arkosic sandstone) from river-mile 95.7 (sample UG95.7-1). Detrital zircons from this sample yielded Pb-Pb dates between 2430 and 3269 Ma (chapter one), but metamorphic monazite an xenotime (idioblastic, yellow to pale yellow grains) yielded concordant U-Pb dates between 1559 and 1583 Ma. These dates are significantly younger than monazite and xenotime dates from the migmatite at mile 91. Three interpretations of these data are possible: 1) they represent the timing of cooling; 2) they represent the time of primary crystallization; or 3) the dates represent physical mixtures of crystal domains with contrasting U-Pb isotopic systematics. There is not enough data to evaluate rigorously whether these minerals preserve cooling ages (Fig 8). The young mineral dates cannot, however, be explained by intra-grain mixtures of a 1660 Ma age domain and an age domain younger than 1560 Ma because such mixtures would not plot along concordia (there is sufficient curvature in concordia to create normally discordant analyses). Thus monazite and xenotime grains from this rock preserve either cooling ages or crystallization ages. If these data preserve crystallization ages, it is not clear whether such growth reflects a metamorphic 'event' or simply precipitation from crustal fluids at ambient temperatures (below the closure temperatures of these crystals). A much more detailed petrologic and geochronologic study is required to test these interpretations.

In summary, the data from the Trinity Creek block document a complex deformational and thermal history that spans at least 100 m.y., between 1665 and 1560 Ma (Fig. 9). Deformation clearly post-dated 1662 Ma, but the relationship between this deformational 'event' and S_1/S_2 fabrics preserved in pre-1700 Ma rocks is unclear. The thermal history is constrained by U-Pb data from several samples. Sphene dates from granodiorite plutons are at least 80 m.y. younger than the emplacement ages. Two

samples preserve U-Pb monazite evidence for high-grade metamorphism and peraluminous magmatism at about 1665 Ma, and one sample appears to contain ca. 1665 Ma metamorphic zircons. In addition, one sample contains monazite and xenotime that may have grown below their closure temperatures over the interval 1585 to 1560 Ma.

The relationship between monazite and xenotime dates at mile 91.1 and mile 95.7 is difficult to explain. One explanation is that metamorphism occurred throughout the Trinity Creek block over this time interval. If so then the range of sphene dates in the Pipe Creek and Horn Creek plutons could be explained by neoblastic sphene or partial resetting of ca. 1662 Ma sphene during this 'metamorphic event' (Fig. 9). Another possible explanation is that monazite and xenotime growth at mile 95.7 is related to movement on the Ninety-Six Mile shear zone prior to juxtaposition with the adjacent Topaz Canyon block. Such an interpretation would provide further evidence for movement on the block-bounding shear zones long after arc accretion (e.g., Chamberlain and Bowring, 1990; Bowring and Karlstrom, 1990; Hodges and Bowring, 1995). Finally, the pattern of mineral dates could reflect differential unroofing rates across the block, so that the exposures today preserve an oblique crustal section. A simple test of this hypothesis would be to date monazite/xenotime and sphene in the Vishnu schist from several localities between miles 92 and 95.

Topaz Canyon Block

The Topaz Canyon block is bounded on the east by the Ninety-Six Mile shear zone and on the west by the Crystal Creek shear zone. It has the lowest-grade metamorphic mineral assemblages in the Upper Gorge. The geology is characterized by upper greenschist to lower amphibolite facies Vishnu schist (500 °C, 6 kbars; Ilg et al., 1996b) intruded by two intermediate-composition plutons. Zircons from both plutons are completely metamict and were not analyzed for U-Pb geochronology. However, a

sample of the Ninety-Six Mile pluton (UG96.2-1) produced abundant chestnut-brown sphene. Four sphene fractions were analyzed, including a whole single crystal fraction, two single fragment analyses, and one multi-fragment analysis. The analyses yielded variably discordant U-Pb dates with identical Pb-Pb dates: the upper intercept age is 1714.1 ± 0.9 Ma (MSWD = 0.10; lower intercept = -26 ± 156 Ma) and the weighted mean of the Pb-Pb dates is 1714.2 ± 0.8 Ma (MSWD = 0.51). Given the relatively low peak temperatures, the large size of the single crystal (average radius = 142 μm), and the lack of age variation in the sample, the upper intercept age of 1714 ± 1 Ma is accepted as the crystallization age for the pluton.

This result has several important implications. First, because strain is partitioned around the margin of the pluton, some component of the total finite strain in the surrounding Vishnu schist accumulated after 1714 Ma. Second, the pluton cooled rapidly, because grains with diffusion radii between 83 and 190 μm yielded the same age. Rapid cooling is consistent with a large thermal gradient between the country rocks and the pluton during emplacement. Third, the temperature did not approach the closure temperature of the smallest sphene crystal (about 585 °C) after 1714 Ma. Finally, if monazite and xenotime growth east of the Ninety-Six Mile shear zone at mile 95.7, just 0.4 miles upstream from the pluton, was controlled by movement on the shear zone, as suggested above, then either: 1) fluid-flow and deformation associated with the shear zone were partitioned into the Trinity Creek block; or 2) the Topaz Canyon block was not juxtaposed with the Trinity Creek block at 1560 Ma irrespective of the motion on the shear zone.

Tuna Creek Block

The Tuna Creek block is bounded on the east by the Crystal Creek shear zone and on the west by the Bass shear zone. The geology is dominated by two mafic- to

intermediate-composition plutonic complexes and an impressive intrusive complex of peraluminous granite/pegmatites dikes and plutons that comprises 50 to 100 % of the outcrop volume between miles 99.0 and 103.0. Vishnu schist containing upper amphibolite facies mineral assemblages records a complex thermal and baric history (Ilg et al., 1996b). The intermediate plutonic complexes are the 1717 Ma Ruby pluton (sample AZ-398 from Chapter two) and the ca. 1710 to 1740 Ma Tuna Creek complex (sample UG99.2-1 from Chapter two). A granodiorite intrusion from the Tuna Creek pluton yielded abundant chestnut-brown sphene including both whole crystals and crystal fragments.

Three multi-crystal analyses (Fig. 10) yielded Pb-Pb dates ranging from 1699 (concordant) to 1712 Ma (1.3% discordant). The two youngest fractions were whole-crystals with average radii of approximately 75 μm. The relatively small size of these grains requires that the temperature did not approach their closure temperature (approximately 590 °C at cooling rate of 8 °C/m.y.; and about 575 °C at cooling rate of 3 °C/m.y.). This result is consistent with the lowest temperatures estimated by thermobarometry for the area (600 - 700 °C; Ilg et al., 1996b).

Walthenberg Canyon Block

The Walthenberg Canyon block exposes the 1840 Ma Elves Chasm pluton which crops out in the western part of the Upper Granite Gorge between miles 113 and 119. A sample from a folded peraluminous granite dike collected two miles east of the Elves Chasm pluton yielded a crystallization age of 1697 Ma (sample UG111.8-1 from Chapter 2). This age indicates that: 1) partial melting at deeper levels in the crust occurred at about 1697 Ma; 2) S_1 fabric in this area formed prior to 1697 Ma; and 3) axial planar S_2 fabric formed after 1697 Ma. Perhaps the most intriguing question about this block is

whether any record of the pre-1750 Ma thermal history is preserved. Sphene data from two samples address this question.

The first sample is a medium-grained amphibolite collected in the supracrustal sequence at the eastern margin of the Elves Chasm pluton (sample 112.9-3). The sample contained abundant, water-clear, colorless sphene, but most crystals contain inclusions of fine-grained hornblende. One analysis of 24 whole-crystals containing few hornblende inclusions was concordant at 1691 Ma, but the errors on the U-Pb dates are large (20 m.y.) because the sample was overspiked for the small U load (210 picograms). Nonetheless, the analysis is sufficiently radiogenic to yield a reliable Pb-Pb date. Because the crystals had a radius of only 51 μm, the temperature had to be relatively low (575 °C at a cooling rate of 8 °C/m.y. or 560 °C at a cooling rate of 3 °C/m.y.) by 1691 Ma. Furthermore, the rocks were not heated above this temperature after 1690 Ma.

The second sample is a granodiorite collected from the Elves Chasm pluton at mile 117.1 (AZ-399). The rock yielded abundant water-clear, colorless to pale-brown sphene crystals and fragments. Six fractions, including one single-crystal fraction (S1) and five crystal-fragment analyses, produced near-concordant U-Pb dates with Pb-Pb dates ranging from 1657 ± 2 to 1674 ± 5 Ma. Because only one whole crystal analysis is available for this sample, we cannot demonstrate whether these grains preserve cooling ages or crystallization ages. However, the data clearly indicate that sphene from the western Walthenberg Canyon block do not preserve geochronologic evidence of the pre-1750 Ma thermal history.

DISCUSSION

U-Pb geochronologic data from the Upper Granite Gorge reveal a thermal and deformational history for the Trinity Creek block that is distinct with respect to the Mineral Canyon, Clear Creek and Walthenberg Canyon blocks (Fig. 13). The differences

are highlighted by comparing mineral ages from the various blocks. For example, metamorphic monazites in the Mineral Canyon block preserve formation ages between 1710 Ma and 1695 Ma, whereas metamorphic monazites and xenotimes from the Trinity Creek block preserve formation ages in two time intervals, one between 1630 and 1665 Ma and the other between 1550 and 1590 Ma. The only potential similarity between monazite dates from these two blocks is the evidence for secondary monazite growth at about 1659 Ma in the Mineral Canyon block, however, the thermal significance of this 'event' is unclear. Sphene dates show similar differences: cooling ages from metamorphic sphene in the Mineral Canyon and Clear Creek blocks are more than 50 m.y. years older than sphenes from > 1710 Ma magmatic rocks in the Trinity Creek block. These results demonstrate that the Trinity Creek block experienced a fundamentally different thermal history than other blocks in the Upper Gorge.

The contrasting thermal history of the Trinity Creek block raises questions about our understanding of crustal evolution in the Upper Gorge. On the one hand, several observations suggest that the crustal blocks represent a relatively coherent pre-orogenic arc complex that was segmented by shear zones during accretion. These include: 1) the similarity of the supracrustal lithotectonic units across the transect; 2) the nearly horizontal enveloping surface (Ilg et al., 1996b); 3) the consistent relationship between group-one and group-two structures in each of the blocks; and 4) estimated peak pressures of 6 kbars across the transect (Ilg et al., 1996b). On the other hand, the evidence for post-Yavapai metamorphism raises the possibility that the Trinity Creek block is allochthonous.

From a regional perspective, deformation and magmatism at 1660 Ma is not unusual. Large areas of the orogen, including the Mazatzal orogenic belt to the southeast and the Mojave province to the west (Fig. 14), underwent continental margin magmatism during this time (Conway and Silver, 1989; Wooden and Miller, 1990). The unusual

aspect of the 1660 Ma 'event' in Upper Gorge transect is that only one block appears to have been affected to any significant degree.

Several explanations for this problem are possible. As suggested above, the Trinity Creek block could be allochthonous with respect to the other crustal blocks. The question then becomes; was the displacement largely horizontal or largely vertical? There is no geological evidence for strike-slip motion and no obvious provenance for these rocks. Furthermore, an hypothesis involving strike-slip displacement is untestable because potential piercing points have not been recognized in the region. Vertical displacement along the steeply-dipping block-bounding shear zones is a more attractive alternative. The contrasting metamorphic grades, structural styles, and relative volumes of peraluminous granitoids between the crustal blocks may indicate that each block represents a slightly different crustal level. The contrasting thermochronologic histories demonstrate that different blocks were unroofed at different rates and at different times. The Mineral Canyon, Clear Creek, and Walthenberg Canyon blocks appear to have cooled rapidly (>5-10 °C/m.y.) to about 500 °C following ca. 1.70 Ga and were not significantly affected by subsequent thermal pulses. This relatively rapid cooling may correspond to the decompression (from 6 to 3 kbar) segment of the P-T loop (Williams, 1994), suggesting that these crustal blocks probably resided at conditions of about 500 °C and 3 kbars by 1660 Ma. The Trinity Creek block, on the other hand, may have remained at temperatures higher than 500 °C and pressures of about 6 kbar until after 1560 Ma, prior to unroofing and juxtaposition with the adjacent blocks. Deformation and magmatism could represent response to heat influx and far-field stresses associated with plate margin magmatism occurring over this time interval to the south and west. This model is consistent with: 1) the contrasting metamorphic and cooling history of the Trinity Creek block; 2) the lack of a contact aureole in the adjacent Topaz Canyon block; 3) the regional evidence for 1.66 to 1.60 Ga magmatism (Conway and Silver, 1989;

Wooden and Miller, 1990); and 4) evidence for thermal resetting of magmatic sphene in the Horn Creek pluton prior to neoblastic sphene growth. . A similar scenario was proposed for deformation associated with ca. 1.4 Ga plutons in the southwestern United States (Nyman et al., 1994; Kirby et al., 1995).

A simple test of this model involves further thermochronology. Specifically, a detailed thermochronologic study of the low-temperature thermal history may provide insight into the relative timing of cooling (and exhumation) in each of the crustal blocks. A study of this type would concentrate on geochronometers such as apatite and rutile in the U-Pb system and muscovite and biotite in the $^{40}Ar/^{39}Ar$ system. The resulting thermal histories should reveal the time interval over which the cooling history of the Trinity Creek block was distinct and when the cooling histories of the blocks converged.

The results presented in this Chapter also have general implications for the study of metamorphic terrains worldwide. The contrasting thermal history of the Trinity Creek block implies that methods for reconstructing the tectonothermal evolution of the Upper Gorge should be revised. In Chapter 2, a tectonic and thermal evolution for the Upper Gorge was constructed using timing constraints from throughout the transect (see Fig. 14 in Chapter 2). This approach assumed that the relative timing of fabric development, metamorphism and peraluminous granite magmatism was similar throughout the transect. Because the results presented herein indicate that this assumption is not necessarily valid, the approach developed in Chapter 4 — obtaining timing relationships from relatively small, representative areas within each block — may be a more prudent method of developing chronologies in segmented metamorphic terrains. Such an approach not only permits more meaningful regional comparisons, but also offers the best opportunity to recognize spatial distribution of deformation, magmatism and metamorphism through time. Therefore, the findings of this study underscore the need

for sampling and analytical strategies designed to improve our understanding of tectonic and thermal processes in the middle crust.

CONCLUSIONS

U-Pb geochronologic data from the shear-zone-bounded crustal blocks in the Upper Granite Gorge indicate that three blocks preserve evidence for ca. 1700 Ma deformation and metamorphism associated with the Yavapai orogeny. Two of these blocks apparently cooled at moderate rates (<30 °C/m.y.) following the peak of metamorphism and thereafter remained at temperature below about 575 °C. In contrast, ca. 1.70 Ga deformation and metamorphism was overprinted by deformation and upper amphibolite to lower granulite facies metamorphism occurred at about 1660 Ma in the Trinity Creek block. There is also evidence for metamorphism between 1560 and 1590 Ma in close proximity to the Ninety-Six Mile shear zone at the west margin of the block. These findings are best explained by long-term residence of the Trinity Creek block at 6 kbars following ca. 1.70 Ga metamorphism.

REFERENCES

Bowring SA, Karlstrom KE (1990) Growth, stabilization and reactivation of Proterozoic lithosphere in the southwestern United States. Geology 18:1203-1206

Chamberlain KR, Bowring SA (1990) Proterozoic geochronologic and isotopic boundary in northwestern Arizona. Journ of Geol 98:399-416

Cherniak DJ (1993) Lead diffusion in sphene and preliminary results on the effects of radiation damage on Pb transport. Chem Geol 110:177-194

DeWolf CP, Belshaw N, O'Nions RK (1993) A metamorphic history from micron-scale $^{207}Pb/^{206}Pb$ chronometry of Archean monazite. Earth Planet Sci Lett 120:207-220

Dodson, MH (1973) Closure temperature in cooling geochronological and petrological systems. Contrib Mineral Petrol 40:259-274

Dodson, MH (1976) Kinetic processes and thermal history of slowly cooling solids. Nature 259:551-553

Getty SR, Gromet LP (1992) Geochronological constraints on ductile deformation, crustal extension, and doming about a basement-cover boundary, New England Appalachians. Am J Sci 292:359-397

Harrison TM, McKeegan KD, LeFort P (1995) Detection of inherited monazite in the Manaslu leucogranite by $^{208}Pb/^{232}Th$ ion microprobe dating: crystallization age and tectonic implications. Earth Planet Sci Lett 133:271-282.

Hodges KV, Bowring SA (1995) $^{40}Ar/^{39}Ar$ thermochronology of isotopically zoned micas: Insights from the southwestern USA Proterozoic orogen. Geoch Cosmochim Acta 59:3205-3220.

Ilg BE, Karlstrom KE, Williams ML, Hawkins DP (1996a) Precambrian crystalline rocks In: Huntoon PW (ed) Geologic Map of the Eastern Part of the Grand Canyon National Park, Arizona (geologic map). Grand Canyon Association, Grand Canyon, Arizona

Ilg BE, Karlstrom KE, Hawkins DP, Williams ML (1996b) Tectonic evolution of Paleoproterozoic rocks in the Grand Canyon: Insights into middle crustal processes. Geol Soc Am Bull (in press)

Karlstrom KE, Bowring SA (1988) Early Proterozoic assembly of tectonostratigraphic terranes in southwestern North America: Journl Geol 96:561-576

Karlstrom, K.E., and Daniel, C.G., 1993, Restoration of Laramide right-lateral strike-lip in northern New Mexico by using Proterozoic piercing points: Tectonic implications from the Proterozoic to the Cenozoic: Geology, v. 21, p. 1139-1142.

Karlstrom KE, Bowring SA, Conway C (1987) Tectonic significance of an Early Proterozoic two-province boundary in central Arizona: Geol Socy Am 99:529-538

Krogh TE (1973) A low-contamination method for hydrothermal decomposition of zircon and extraction of U and Pb for isotopic age determination. Geochim Cosmochim Acta 37:485-494

Krogh TE (1982) Improved accuracy of U-Pb ages by the creation of more concordant systems using an air abrasion technique. Geochim Cosmochim Acta 46:637-649

Ludwig KR, (1989) Pb.Dat: A computer program for processing raw Pb-U-Th isotope data. US Geol Surv Open-File Rep 88-557

Kirby E, Karlstrom KE, Andronicus CL, Dallmeyer RD (1995) Tectonic setting of the Sandia pluton: an orogenic 1.4 Ga granite in New Mexico. Tectonics

Mezger K, Rawnsley CM, Bohlen SR, Hanson GN (1991) U-Pb garnet, sphene, monazite and rutile ages: Implications for the duration of high-grade metamorphism and cooling histories, Adirondack Mtns. J Geol 99:415-428

Nyman MW, Karlstrom KE, Kirby E, Graubard CM (1994) Mesoproterozoic contractional orogeny in western North America: evidence from ca. 1.4 Ga plutons. Geology 22:901-904

Scott DL, St-Onge MR (1995) Constraints on Pb closure temperature in sphene based on rocks from the Ungava orogen, Canada: implications for U-Pb geochronology and P-T-t path determinations. Geology 23:1123-1126

Suzuki K, Adachi M, Kajizuka I (1994) Electron microprobe observations of Pb diffusion in metamorphosed detrital monazites. Earth Planet Sci Lett 128:391-405

Wooden JL, Miller DM (1990) Chronologic and isotopic framework for Early Proterozoic crustal evolution in the eastern Mojave Desert region, SE California. Journ Geophys Res 95:20,133-20146

Wright N, Layer PW, York D (1991) New insights into thermal history from single grain $^{40}Ar/^{39}Ar$ analysis of biotite. Earth Planet Sci Lett 104:70-79

Zhang L-S, Schärer U (1996) Inherited Pb components in magmatic sphene and their consequence for the interpretation of U-Pb ages. Earth Planet Sci Lett 138:57-65

FIGURE CAPTIONS

Figure 1 Distribution of Paleoproterozoic rocks (dark shading) in Arizona, California and Nevada. The 500 km long transect in the Transition Zone on the southern margin of the Colorado Plateau (light shading) is cut by a series of north- to northeast-striking shear zones that project as subsurface lineaments (heavy dashed lines) beneath the Colorado Plateau. The shear zones define eight tectonostratigraphic blocks with contrasting pre-assembly histories (Karlstrom and Bowring, 1988). Note that the Upper Granite Gorge of the Grand Canyon occurs along strike from the central Arizona transect. Modified after Karlstrom and Bowring (1988).

Figure 2 Simplified geologic map of Paleoproterozoic rocks in the Upper Granite Gorge between river-miles 77 and 119 showing the block architecture and the location of samples analyzed in this study. Five major shear zones are shown as clusters of broken lines projected outside the outcrop area. Abbreviations for the shear zones are: 96-MSZ = Ninety-Six Mile shear zone; BASZ = Bright Angel shear zone; BSZ = Bass shear zone; CRSZ = Crystal Creek shear zone; VFZ = Vishnu shear and fault zone. Plutons mentioned in the text are identified as follows: ECP = Elves Chasm pluton; HP = Horn Creek pluton; NP = Ninety-Six Mile pluton; PhP = Phantom Creek pluton; PP = Pipe Creek pluton; RP = Ruby pluton; TCP = Tuna Creek pluton; ZP = Zoroaster pluton. Modified after Ilg et al. (1996a,b).

Figure 3 Summary of geochronologic results from the Mineral Canyon block portrayed as a sample location versus rock age or mineral date (increasing from top to bottom). The data define peak metamorphism between 1702 and 1695 Ma and perhaps retrograde metamorphism at 1660 Ma. Summarized from Chapter four of this thesis.

Figure 4a,b **a** Concordia diagram for U-Pb sphene data from an amphibolite in the Clear Creek block. These data do not yield a statistically significant weighted mean of the Pb-Pb dates. **b** Wright diagram for sphene crystals analyzed for this sample. The data define a statistically significant correlation between grains radius and age indicating the sphenes preserve cooling ages. The parameters derived from this plot yield a cooling rate of 15-10 °C/m.y. over the interval 1700 to 1695 Ma.

Figure 5 Concordia diagram for the Pipe Creek pluton. Note that the although the zircon data do not define the crystallization age, they suggest a crystallization for the pluton that is more than 100 m.y. older than sphene dates from the same rock. Inset shows sphene data in detail.

Figure 6a,b **a** Concordia diagram for the Horn Creek pluton. Zircon data from chapter two define a crystallization age of 1713 Ma, whereas sphene dates from the same rock are 70 to 110 m.y. younger. Inset shows sphene data in detail. **b** Wright diagram for whole-crystals of sphene. the data do not exhibit a correlation between grain radius and Pb-Pb date.

Figure 7a,b,c Concordia diagram (**a**) and Wright diagrams (**b,c**) for samples of migmatite from Ninety-One Mile Canyon. **a** Inset shows location of fragments sliced from crystals X7 and X8. Note that both crystals exhibit little to no intra-grain age dispersion. Monazites from the paleosomal schist (**b**) and xenotimes from the

leucosomal granite (c) do not exhibit a correlation between grain radius and Pb-Pb date indicating that these minerals do not preserve cooling ages.

Figure 8a,b **a** Concordia diagram for monazite and xenotime data from the quartzofeldspathic schist at mile 95.7. The data are significantly younger than monazite and xenotime from mile 91.1 (see fig 7). **b** Wright diagram showing monazite crystals from this rock do not preserve cooling ages.

Figure 9 Summary of geochronologic results from the Trinity Creek block portrayed as a sample location versus rock age or mineral date (increasing from top to bottom). The data are consistent with metamorphism at about 1660 Ma and perhaps over the interval 1585 to 1555 Ma. These results contrast with the history of the Mineral canyon block (see Fig. 3).

Figure 10 Concordia diagram for sphene data from the Ninety-Six Mile pluton. Because the data were obtained from sphene crystals of different sizes, 1714 Ma is a reasonable crystallization age for the pluton.

Figure 11 Concordia diagram for sphene data from the Tuna Creek pluton. Zircon data for this sample suggest a crystallization age of 1.71 - 1.75 Ga (see Fig 7 in Chapter two).

Figure 12 Concordia diagram for sphene data for an amphibolite from the eastern margin of the 1840 Ma Elves Chasm pluton and from the pluton itself. These data preserve no evidence of the pre-1.75 Ga thermal history.

Figure 13 Summary diagram of the thermochronological results from the Upper Granite Gorge. The data are portrayed by river mile versus age or mineral date. Note that the Trinity Creek block has a distinct thermal history.

Figure 14 Distribution of Paleoproterozoic rocks along the southwestern margin of the Colorado Plateau. Diagonally hachured boxes outline areas that expose 1.66 to 1.60 Ga granitoid plutons. These rocks have been interpreted to represent continental margin magmatism over this time interval. Modified after Karlstrom and Bowring (1994) and Karlstrom and Daniel (1993) with data from Conway and Silver (1989) and Wooden and Miller (1990).

Table 1. Generalized descriptions of the crustal blocks in the Upper Granite Gorge (modified after Ilg et al., 1996b)

Crustal Block	Metamorphic Facies Estimated Peak Conditions	Structural Elements	Relative Volume of Peraluminous Granite	Thermochronology (this study)
Mineral Canyon (mile 77.4 - 81.0)	upper amph to lower granulite (600-725°C, 6 kbars)	km-scale F_2 S_2 / S_1	moderate to high	720°C at 1700 Ma 15-30°C/My 1700-1690 Ma 4 °C/My 1690-1676 Ma
Clear Creek (mile 81.0 - 88.0)	lower amph to upper amph (600-650°C, 6 kbars)	km-scale F_2 S_2 / S_1	low to very high	615 to 600°C at 1700 Ma 5-10°C/My 1700-1695 Ma
Trinity Creek (mile 88.0 - 96.0)	upper amph to lower granulite (600-725°C, 6 kbars)	S_2 / S_1 S_1 locally	moderate to very low	> 650°C 1710 to 1640Ma mzt/xtm growth 1663 to 1630 Ma mzt/xtm growth 1560 to 1583 Ma
Topaz Canyon (mile 96.0 - 98.0)	upper greenschist to lower amph (600-725°C, 6 kbars)	S_1 F_1 local S_2	very low to absent	T did not exceed 600°C after 1714 Ma
Tuna Creek (mile 98.0 - 108.0)	upper amph (variable 600-700°C)	S_1 F_1 local S_2	extremely high to moderate	T did not exceed 600°C after 1710 Ma
Walthenberg Canyon (mile 77.4 - 81.0)	upper amph (variable 600-700°C)	S_1 F_1 local S_2	low to high	T did not exceed 600°C after 1690 Ma

Table 2 U-Pb analytical results for monazite, sphene, xenotime and zircon from the Grand Canyon

Sample Fractions (1)	Estimated Wgt (µg) (2)	Composition U (ppm) (3)	Th (ppm) (3)	Pb (ppm) (3)	Th U (3)	Mol% ^{208}Pb	Com Pb (pg)	Isotopic Ratios $^{206}Pb/^{204}Pb$ (4)	$^{208}Pb/^{206}Pb$ (5)	$^{206}Pb/^{238}U$ (6)	$^{207}Pb/^{235}U$ (6)	$^{207}Pb/^{206}Pb$ (6)	corr. coef.	Dates (Ma) $^{206}Pb/^{238}U$	$^{207}Pb/^{235}U$	$^{207}Pb/^{206}Pb$ (7)
COARSE-GRAINED AMPHIBOLITE (sample UG84.3-3)																
S1 (1) wg	28.9	15	5	6	0.32	8.0	51.4	167.38	0.0955	0.29996 (.53)	4.30566 (.63)	0.10411 (.31)	0.870	1691.1	1694.4	1698.6 ±5.8
S3 (1) wg	30.9	19	3	7	0.17	4.3	58.3	192.75	0.0496	0.29732 (.42)	4.27172 (.48)	0.10420 (.21)	0.898	1678.0	1687.9	1700.3 ±3.9
S4 (1) wg	10.2	33	11	12	0.33	8.2	26.7	239.24	0.0983	0.29727 (.72)	4.26822 (.74)	0.10413 (.14)	0.983	1677.8	1687.3	1699.1 ±2.5
S9 (17) wg	56.0	27	9	11	0.33	8.0	152.8	189.69	0.0957	0.29979 (.20)	4.29487 (.25)	0.10391 (.15)	0.816	1690.2	1692.4	1695.0 ±2.7
S10 (1) wg	56.7	37	8	14	0.21	5.4	153.4	255.98	0.0627	0.30010 (.16)	4.29850 (.21)	0.10389 (.13)	0.777	1691.8	1693.1	1694.7 ±2.5
PIPE CREEK PLUTON (sample UG89.6-1)																
Z1 aa	2.2	586	83	176	0.15	3.9	26.2	855.24	0.0450	0.28745 (.23)	4.14467 (.24)	0.10457 (.08)	0.939	1628.8	1663.2	1706.8 ±1.5
Z3 aa	1.6	714	231	230	0.33	8.1	8.8	2418.99	0.0980	0.30580 (.21)	4.48884 (.22)	0.10646 (.06)	0.967	1720.0	1728.9	1739.7 ±1.0
Z6 aa	6.6	99	15	28	0.15	4.3	5.3	2167.36	0.0495	0.27759 (.32)	4.03823 (.32)	0.10551 (.06)	0.982	1579.2	1641.9	1723.2 ±1.1
Z7 aa	4.1	171	25	39	0.15	5.5	19.0	470.82	0.0637	0.20791 (.38)	2.96535 (.44)	0.10344 (.22)	0.863	1217.7	1398.8	1686.8 ±4.1
S1 (1) wg	14.7	120	54	37	0.47	11.2	18.6	1619.58	0.1381	0.28147 (.21)	3.83944 (.22)	0.09893 (.08)	0.936	1598.8	1601.1	1604.1 ±1.5
S2 (2) wg	15.4	65	12	18	0.19	4.8	12.2	1394.76	0.0555	0.27491 (.33)	3.71980 (.34)	0.09813 (.09)	0.963	1565.7	1575.6	1589.0 ±1.7
S3 (5) fr	29.2	33	9	10	0.28	7.0	42.7	380.96	0.0824	0.27598 (.30)	3.72312 (.35)	0.09784 (.16)	0.884	1571.1	1576.4	1583.4 ±3.1
S4 (4) fr	38.4	14	9	5	0.67	15.3	23.9	380.59	0.1990	0.27745 (.54)	3.74469 (.56)	0.09789 (.14)	0.967	1578.5	1581.0	1584.3 ±2.7
S5 (5) fr	28.0	20	5	6	0.25	6.5	31.9	297.23	0.0761	0.27269 (.63)	3.67454 (.67)	0.09773 (.22)	0.943	1554.5	1565.9	1581.3 ±4.2
S7 (31) fr	98.4	11	5	4	0.46	11.2	75.3	249.52	0.1383	0.27436 (.32)	3.68284 (.39)	0.09736 (.21)	0.846	1562.9	1567.7	1574.1 ±3.9
S8 (28) fr	71.7	19	8	7	0.45	10.8	87.9	264.91	0.1328	0.27611 (.23)	3.70191 (.27)	0.09724 (.12)	0.892	1571.7	1571.8	1571.8 ±2.3
HORN CREEK PLUTON (sample UG90.6-2)																
S15 (9) fr	136.6	168	35	50	0.21	5.4	272.5	1429.15	0.0622	0.28481 (.14)	3.91582 (.15)	0.09972 (.05)	0.948	1615.5	1617.0	1618.8 ±0.9
S16 (7) fr	170.0	42	17	14	0.41	10.0	290.2	416.06	0.1225	0.27951 (.19)	3.79601 (.23)	0.09850 (.12)	0.853	1588.9	1591.9	1595.9 ±2.3
S17 (9) fr	111.4	62	21	20	0.35	8.5	170.4	698.00	0.1024	0.28383 (.10)	3.88966 (.12)	0.09939 (.07)	0.840	1610.6	1611.5	1612.7 ±1.3
S18 (35) wg	18.3	403	98	122	0.25	6.3	92.0	1373.52	0.0734	0.28731 (.14)	3.98013 (.15)	0.10047 (.05)	0.940	1628.1	1630.2	1632.8 ±1.0
S19 (115) fr	34.5	567	121	166	0.22	5.6	177.2	1855.78	0.0650	0.28333 (.13)	3.89686 (.14)	0.09975 (.05)	0.938	1608.1	1613.0	1619.5 ±0.9
S20 (119) fr	64.3	102	31	32	0.31	7.7	193.6	577.10	0.0915	0.28217 (.15)	3.85183 (.17)	0.09900 (.08)	0.891	1602.3	1603.7	1605.4 ±1.4
S21 (1) wg	13.0	545	68	156	0.13	3.3	43.4	2804.66	0.0376	0.28757 (.10)	3.97908 (.11)	0.10035 (.05)	0.913	1629.4	1629.9	1630.7 ±0.8
S22 (1) wg	11.0	164	40	51	0.25	6.3	58.9	521.00	0.0739	0.27885 (.18)	3.80259 (.20)	0.09890 (.09)	0.903	1585.6	1593.3	1603.5 ±1.6
S23 (1) wg	9.5	544	124	160	0.23	5.9	33.7	2627.53	0.0692	0.28663 (.16)	3.98232 (.18)	0.10076 (.07)	0.926	1624.7	1630.6	1638.2 ±1.2
S24 (1) wg	7.2	229	41	69	0.18	4.7	36.5	778.09	0.0544	0.28493 (.20)	3.92976 (.22)	0.10003 (.07)	0.942	1616.2	1619.8	1624.6 ±1.4
MIGMATITIC BIOTITE-SILLIMANITE SCHIST (samples UG91.1-7A = leucosome and UG91.1-7B = paleosome/melanosome)																
B-M1	7.7	8622	28322	4506	3.37	47.3	31.5	36041.62	0.9891	0.28946 (.21)	4.01913 (.21)	0.10070 (.04)	0.981	1638.8	1638.1	1637.1 ±0.8
B-M4	1.3	4330	36618	3968	8.67	70.0	19.3	5004.15	2.5645	0.28814 (.10)	4.00935 (.12)	0.100919 (.07)	0.817	1632.2	1636.1	1641.1 ±1.3
B-M5	1.5	2577	32424	3171	12.91	77.6	15.5	4315.03	3.8088	0.28876 (.13)	4.01930 (.15)	0.100950 (.08)	0.847	1635.4	1638.1	1641.7 ±1.5
B-M6	0.6	2882	32489	3246	11.60	75.6	7.8	3912.77	3.4109	0.28787 (.15)	3.98406 (.18)	0.100375 (.09)	0.860	1630.9	1631.0	1631.1 ±1.7
B-M7	0.2	3863	61430	5726	16.31	81.4	5.4	2580.74	4.8165	0.28882 (.25)	4.02275 (.27)	0.101018 (.08)	0.950	1635.6	1638.8	1642.9 ±1.6
B-X2	6.2	3576	560	1018	0.16	4.1	7.8	50195.87	0.0476	0.28812 (.09)	4.01883 (.10)	0.10117 (.05)	0.878	1632.1	1638.0	1645.6 ±0.9
A-M1	2.1	6877	47331	5478	7.06	65.3	7.2	35454.21	2.0738	0.29006 (.10)	4.03730 (.11)	0.100950 (.05)	0.905	1641.8	1641.7	1641.6 ±0.9
A-M3	2.1	5214	53194	5475	10.47	73.6	9.1	21183.13	3.0631	0.29125 (.11)	4.05565 (.12)	0.100993 (.05)	0.911	1647.8	1645.4	1642.4 ±0.9

Table 2 — continued

Sample Fractions (1)	Estimated Wgt (μg) (2)	Composition U (ppm) (3)	Th (ppm) (3)	Pb (ppm) (3)	Th U (3)	Mol% ^{208}Pb	Com Pb (pg)	Isotopic Ratios $^{206}Pb/^{204}Pb$ (4)	$^{208}Pb/^{206}Pb$ (5)	$^{206}Pb/^{238}U$ (6)	$^{207}Pb/^{235}U$ (6)	$^{207}Pb/^{206}Pb$ (6)	corr. coef.	Dates (Ma) $^{206}Pb/^{238}U$	$^{207}Pb/^{235}U$	$^{207}Pb/^{206}Pb$ (7)
A-X1	7.7	5400	1464	1601	0.28	6.9	7.6	97572.52	0.0820	0.29111 (.13)	4.07631 (.14)	0.101558 (.06)	0.907	1647.1	1649.6	1652.8 ±1.1
A-X2	3.4	3520	1072	1050	0.31	7.7	4.7	46287.70	0.0922	0.29048 (.07)	4.06690 (.09)	0.101540 (.05)	0.835	1644.0	1647.7	1652.5 ±0.9
A-X6	4.8	2086	1094	661	0.54	12.6	9.6	18333.49	0.1590	0.29150 (.11)	4.09367 (.12)	0.101854 (.05)	0.902	1649.0	1653.0	1658.2 ±1.0
A-X7a	1.4	3204	2390	1074	0.77	17.0	3.4	24605.25	0.2250	0.29352 (.08)	4.13048 (.10)	0.102062 (.06)	0.771	1659.1	1660.4	1662.0 ±1.2
A-X7b	0.8	2482	1825	856	0.75	16.8	25.3	1380.14	0.2224	0.29290 (.13)	4.12342 (.21)	0.102101 (.14)	0.714	1656.0	1659.0	1662.7 ±2.7
A-X7c	5.0	1209	966	411	0.82	17.9	3.1	36425.25	0.2408	0.29388 (.10)	4.13650 (.12)	0.102084 (.06)	0.845	1660.9	1661.5	1662.4 ±1.2
A-X7d	4.3	1879	1467	635	0.80	17.6	5.4	27135.15	0.2357	0.29338 (.20)	4.12873 (.23)	0.102066 (.13)	0.834	1658.4	1660.0	1662.0 ±2.4
A-X7e	1.3	2088	1917	729	0.94	20.2	10.0	4787.93	0.2791	0.29142 (.15)	4.10222 (.17)	0.102095 (.07)	0.902	1648.6	1654.7	1662.6 ±1.4
A-X7f	1.7	2298	1794	773	0.80	17.8	9.3	7388.32	0.2382	0.29008 (.32)	4.08095 (.34)	0.102032 (.12)	0.931	1641.9	1650.5	1661.4 ±2.3
A-X8a	1.8	2436	1091	737	0.46	11.2	4.6	17159.77	0.1389	0.28337 (.15)	3.96134 (.17)	0.101388 (.07)	0.919	1608.3	1626.3	1649.7 ±1.2
A-X8b	2.3	1343	545	411	0.42	10.0	5.2	10844.70	0.1226	0.29022 (.13)	4.05357 (.15)	0.101301 (.07)	0.877	1642.6	1645.0	1648.1 ±1.3
A-X8c	2.8	2066	804	614	0.40	9.9	6.1	16563.54	0.1208	0.28233 (.18)	3.93972 (.20)	0.10121 (.08)	0.905	1603.1	1621.9	1646.3 ±1.5
BIOTITE-MUSCOVITE QUARTZOFELDSPATHIC SCHIST (sample UG95.7-1)																
M1	1.1	7463	76351	7498	10.50	73.8	15.0	8856.17	3.0961	0.27647 (.14)	3.71151 (.15)	0.09736 (.07)	0.907	1575.6	1573.9	1574.2 ±1.2
M2	82.0	56	530	53	9.68	72.2	5.0	16114.74	2.8578	0.27773 (.10)	3.74511 (.11)	0.09780 (.05)	0.877	1579.9	1581.1	1582.6 ±1.0
M3	1.0	4729	51912	5066	11.26	75.2	67.6	1158.41	3.3211	0.27658 (.14)	3.71327 (.16)	0.09737 (.09)	0.848	1574.1	1574.2	1574.4 ±1.6
M4	0.3	4832	58986	5639	12.52	77.1	40.3	682.76	3.6896	0.27627 (.15)	3.70257 (.19)	0.09720 (.11)	0.817	1572.6	1571.9	1571.1 ±2.1
M5	0.3	5742	59659	5828	10.66	74.1	5.1	6645.37	3.1383	0.27667 (.24)	3.71050 (.27)	0.09727 (.12)	0.901	1574.6	1573.6	1572.4 ±2.2
X2	0.4	6664	62115	6231	9.56	72.0	22.2	1875.54	2.8223	0.27358 (.10)	3.64325 (.12)	0.09659 (.06)	0.862	1558.9	1559.0	1559.2 ±1.1
X6	10.0	406	3692	373	9.33	71.5	2.6	27632.61	2.7574	0.27561 (.11)	3.69430 (.13)	0.09721 (.06)	0.875	1569.2	1570.1	1571.4 ±1.2
NINETY-SIX-MILE PLUTON (sample UG96.2-1)																
S2 (1) wg	37.3	148	194	64	1.35	26.3	231.2	440.58	0.3948	0.30413 (.17)	4.40260 (.19)	0.10499 (.07)	0.922	1711.8	1712.8	1714.1 ±1.3
S7 (1) fr	10.2	168	218	69	1.33	26.1	43.6	719.65	0.3908	0.30298 (.18)	4.38706 (.21)	0.10502 (.12)	0.836	1706.0	1709.9	1714.6 ±2.2
S10 (1) fr	8.0	121	135	50	1.15	23.4	36.0	498.84	0.3367	0.30311 (.29)	4.38765 (.30)	0.10499 (.08)	0.967	1706.7	1710.0	1714.0 ±1.4
S12 (6) fr	14.4	343	392	157	1.17	24.4	434.1	211.14	0.3560	0.29432 (.15)	4.26155 (.21)	0.10502 (.13)	0.756	1663.1	1686.0	1714.6 ±2.5
TUNA CREEK PLUTON (sample UG99.2-1)																
S2 (8) wg	101.0	59	14	22	0.24	6.0	434.1	255.25	0.0701	0.30036 (.13)	4.32589 (.24)	0.10446 (.19)	0.655	1693.1	1698.3	1704.8 ±3.4
S3 (11) wg,fr	116.2	59	14	22	0.25	6.2	456.4	279.32	0.0728	0.30163 (.13)	4.33055 (.22)	0.10413 (.17)	0.624	1699.4	1699.2	1699.0 ±3.2
S4 (11) wg,fr	136.4	119	47	47	0.40	9.8	1214.7	250.49	0.1197	0.30006 (.09)	4.33813 (.13)	0.10485 (.08)	0.744	1691.6	1700.6	1711.8 ±1.5
MEDIUM-GRAINED AMPHIBOLITE (sample UG112.9-3)																
S1 (24) wg	47.5	4	1	2	0.16	4.1	17.9	226.76	0.0468	0.29839 (1.17)	4.26448 (1.20)	0.10365 (.19)	0.988	1683.3	1686.5	1690.5 ±3.5
ELVES CHASM PLUTON (sample AZ-399; river-mile 117.1)																
S1 (1) fr	50.7	15	1	5	0.03	0.5	25.3	549.73	0.0100	0.29407 (.34)	4.14960 (.37)	0.10234 (.13)	0.939	1661.9	1664.1	1667.0 ±2.4
S6 (17) fr	31.7	15	1	5	0.05	0.7	23.2	362.59	0.0154	0.29277 (.56)	4.12072 (.60)	0.10208 (.19)	0.950	1655.4	1658.4	1662.3 ±3.5
S7 (15) fr	28.0	12	1	4	0.05	0.6	14.3	435.76	0.0142	0.28712 (.79)	4.03068 (.81)	0.10181 (.12)	0.988	1627.1	1640.4	1657.4 ±2.3
S8 (20) fr	61.6	21	2	8	0.10	2.0	127.6	188.50	0.0288	0.29571 (.28)	4.18754 (.39)	0.10271 (.25)	0.768	1670.0	1671.6	1673.6 ±4.6
S9 (27) fr	59.6	14	1	4	0.07	0.9	46.3	314.95	0.0200	0.29093 (.36)	4.08633 (.39)	0.10187 (.14)	0.932	1646.2	1651.6	1658.4 ±2.7
S10 (80) fr	50.5	33	2	10	0.06	1.9	66.6	444.40	0.0172	0.29311 (.20)	4.12705 (.22)	0.10212 (.10)	0.904	1657.0	1659.7	1663.0 ±1.8

(1) fractions analyzed include the type of mineral, M=monazite, S=sphene, X=xenotime, Z=zircon followed by analysis number. fraction numbers followed by a single lower case letter are analyses of fragments sliced from individual crystals. fraction descriptions for sphene analyses include the number of sphene crystals in parentheses and the type of grains analyzed: fr=fragments (most of which include at least one crystal face); wg=whole grains.
(2) sample weights were estimated using measured grain dimensions (± 5μm), an ellipsoidal geometry, and nominal densities of 5.0 g/cc for monazite, 3.5 for sphene, 5.2 g/cc for xenotime, and4.5 g/cc zircon . weights are known to within 20% based on comparisons of estimated and measured weights for all four minerals. sphene fractions for sample UG99.2-1 were weighed prior to dissolution.
(3) expressed as ppm U and Th and ppm radiogenic Pb. Th concentration and Th/U ratio calculated from the radiogenic ^{208}Pb and $^{208}Pb/^{206}Pb$ ratios, respectively, assuming concordance between the Th-Pb and U-Pb systems.
(4) measured ratio corrected for fractionation: Pb fractionation correction is 0.12% ± 0.04% per atomic mass unit (amu) for multicollector analyses and 0.15% ± 0.04% per amu for single collector analysis based on repeated analyses of NBS 981
(5) radiogenic Pb
(6) Pb/U isotopic ratios corrected for fractionation, spike, blank, and initial common Pb: U blank = 1 pg ± 50%; Pb blanks ranged from 5.2 to 1.1 pg during the course of this study. The monazite and xenotime data were reduced using a Pb blank of 3.5 pg ± 50% — for analyses with less than 3.5 pg total common Pb the total common Pb was assumed to be blank and the uncertainty was reduced to 10%; the Pb blank for sphene analyses was 5pg ± 50%. initial common Pb was calculated using the two-stage model of Stacey and Kramers (1975) using the interpreted age of the sample. Numbers in parentheses are the % error reported at the 2 sigma confidence interval.
(7) uncertainty in the Pb-Pb date in My at the 2 sigma confidence interval

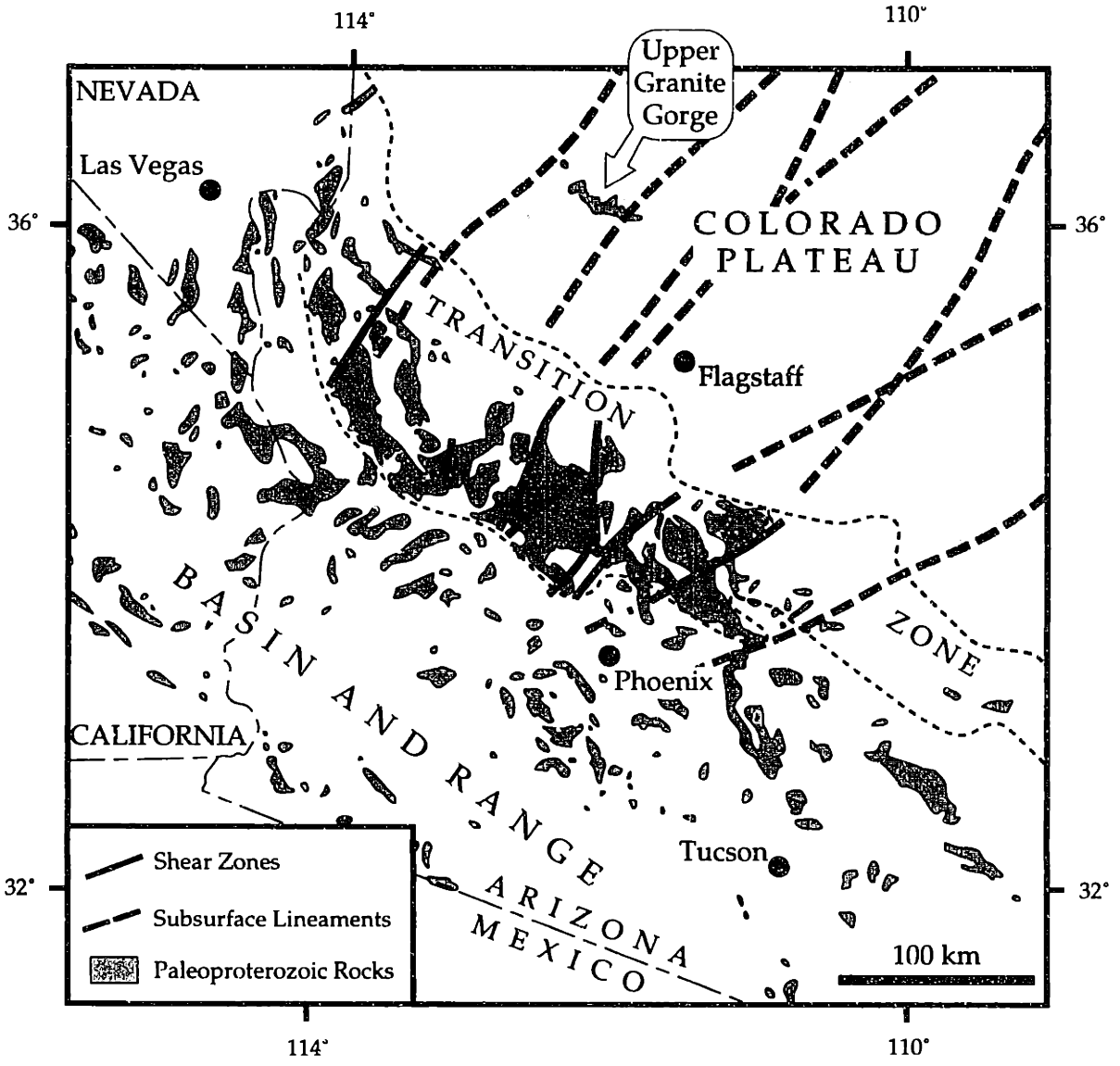
114°
110°
Upper
Granite
Gorge
NEVADA
Las Vegas
36°
COLORADO
PLATEAU
TRANSITION
Flagstaff
ZONE
BASIN AND RANGE
Phoenix
CALIFORNIA
Tucson
ARIZONA
MEXICO
32°
Shear Zones
Subsurface Lineaments
Paleoproterozoic Rocks
100 km

Figure 1

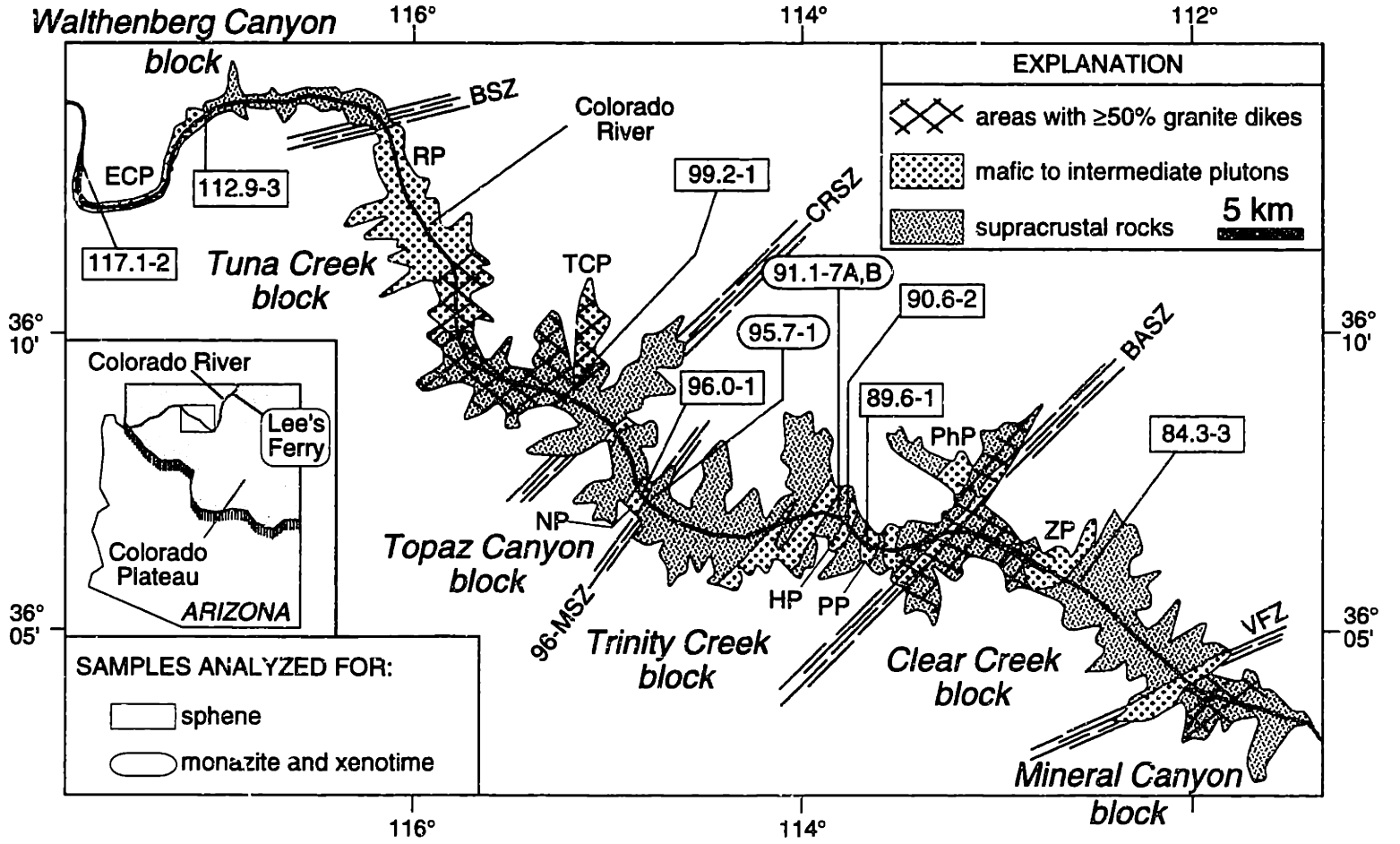
Walthenberg Canyon block
116°
114°
112°
EXPLANATION
areas with ≥50% granite dikes
mafic to intermediate plutons
supracrustal rocks
5 km
BSZ
Colorado River
RP
ECP
112.9-3
99.2-1
CRSZ
117.1-2
Tuna Creek block
TCP
91.1-7A,B
90.6-2
36° 10'
95.7-1
BASZ
Colorado River
96.0-1
89.6-1
Lee's Ferry
PhP
84.3-3
NP
ZP
Topaz Canyon block
Colorado Plateau
ARIZONA
HP
PP
96-MSZ
Trinity Creek block
Clear Creek block
VFZ
36° 05'
SAMPLES ANALYZED FOR:
sphene
monazite and xenotime
Mineral Canyon block
116°
114°

Figure 2

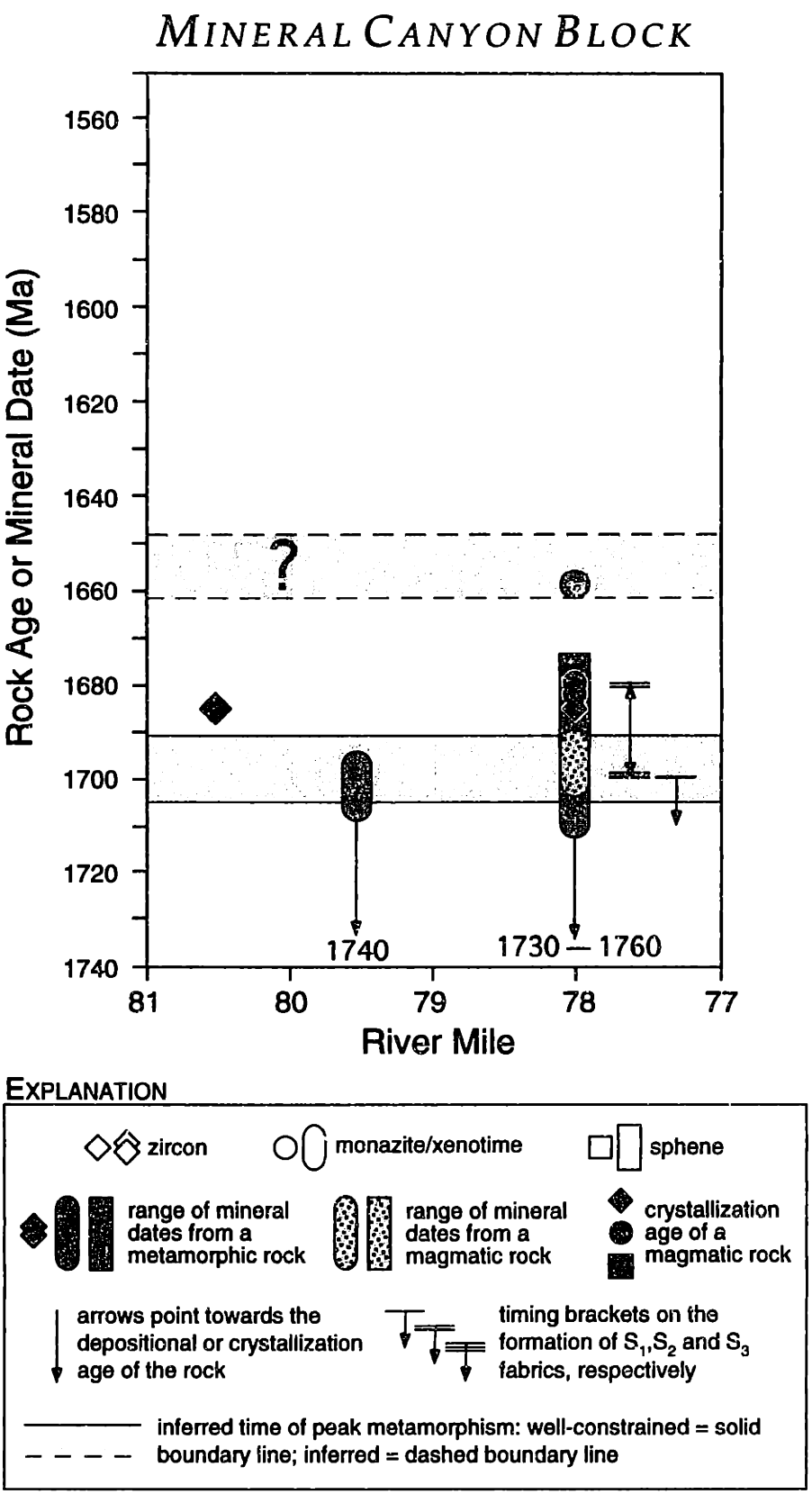
MINERAL CANYON BLOCK
Rock Age or Mineral Date (Ma)
1560
1580
1600
1620
1640
1660
1680
1700
1720
1740
?
1740
1730 — 1760
81
80
79
78
77
River Mile
EXPLANATION
zircon
monazite/xenotime
sphene
range of mineral dates from a metamorphic rock
range of mineral dates from a magmatic rock
crystallization age of a magmatic rock
arrows point towards the depositional or crystallization age of the rock
timing brackets on the formation of S_1,S_2 and S_3 fabrics, respectively
inferred time of peak metamorphism: well-constrained = solid
boundary line; inferred = dashed boundary line

Figure 3

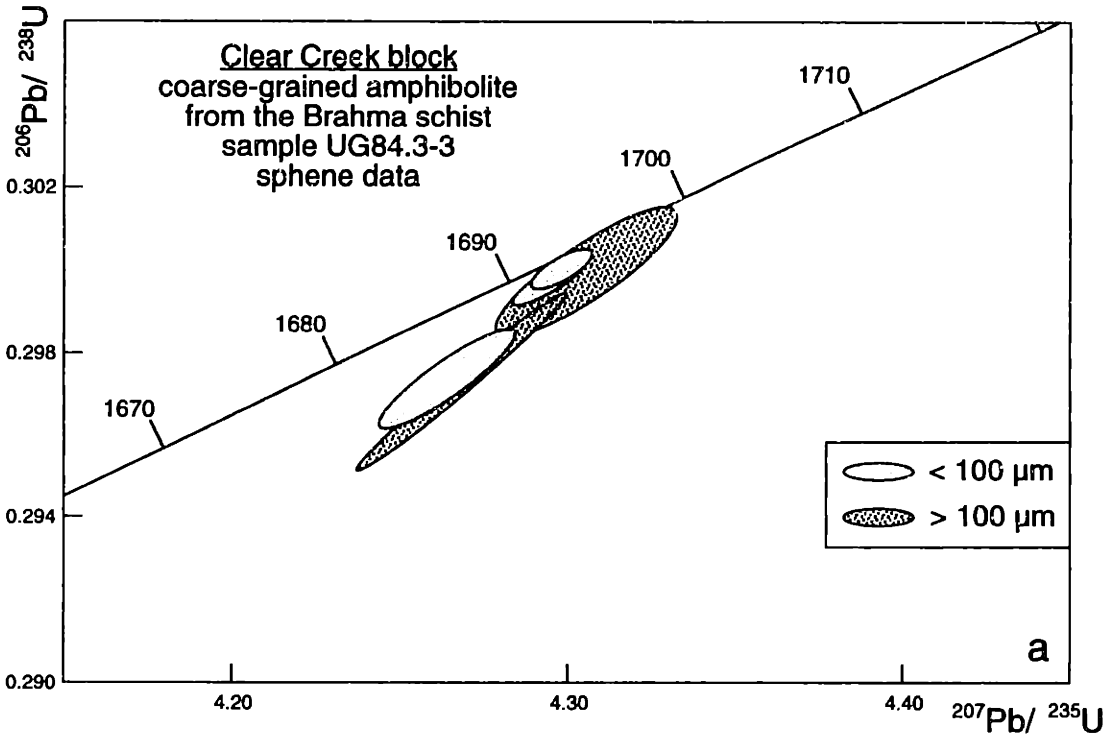
Clear Creek block
coarse-grained amphibolite
from the Brahma schist
sample UG84.3-3
sphene data
1710
1700
1690
1680
1670
0.302
0.298
0.294
0.290
4.20
4.30
4.40
$^{206}Pb/^{238}U$
$^{207}Pb/^{235}U$
< 100 µm
> 100 µm
a

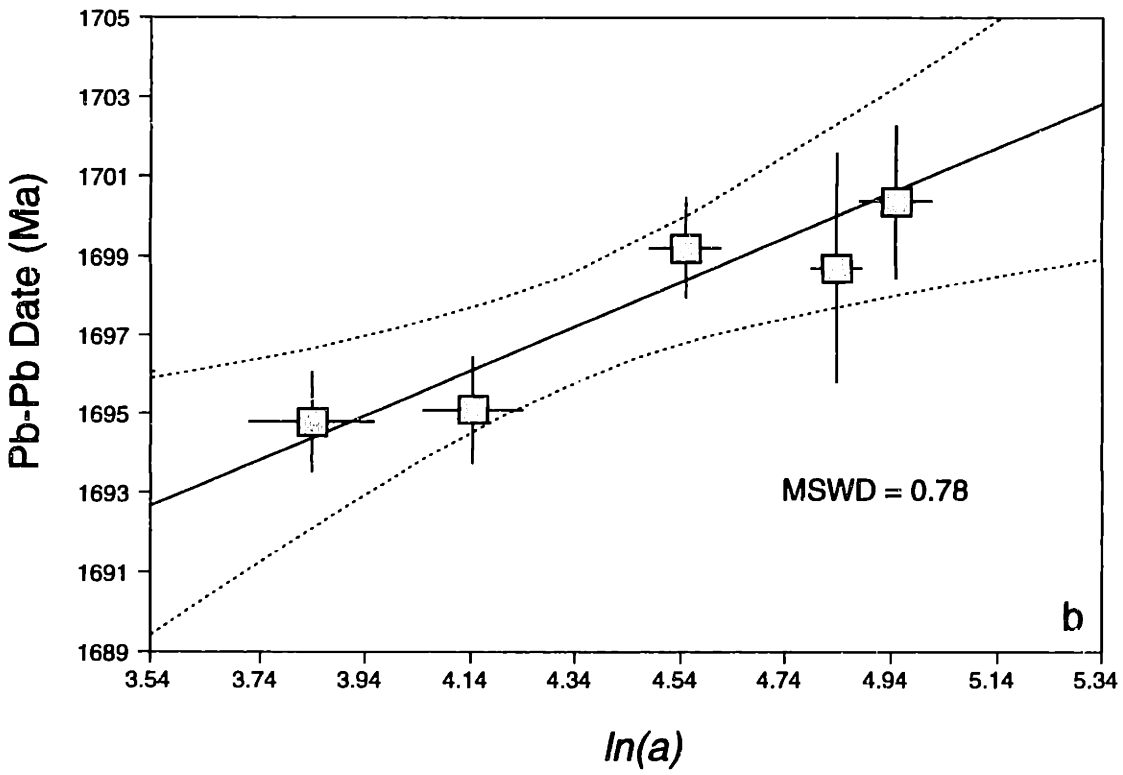
1705
1703
1701
1699
1697
1695
1693
1691
1689
Pb-Pb Date (Ma)
3.54
3.74
3.94
4.14
4.34
4.54
4.74
4.94
5.14
5.34
ln(a)
MSWD = 0.78
b

Figure 4

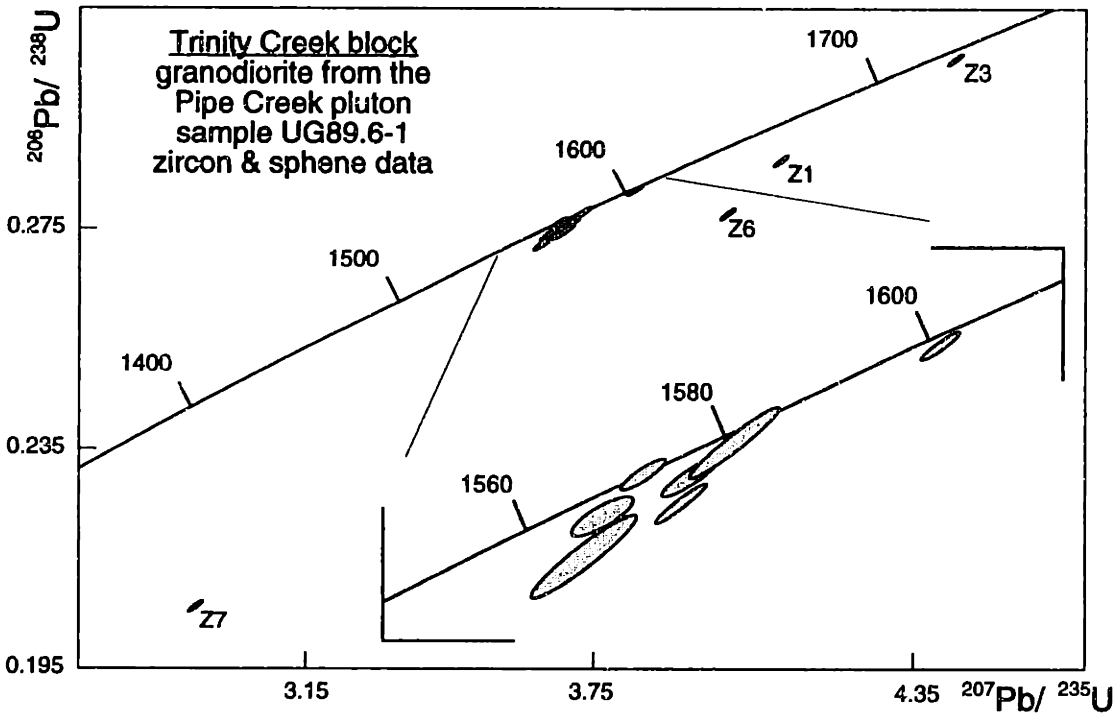
Trinity Creek block
granodiorite from the
Pipe Creek pluton
sample UG89.6-1
zircon & sphene data
206Pb/ 238U
207Pb/ 235U
0.275
0.235
0.195
3.15
3.75
4.35
1700
1600
1500
1400
1600
1580
1560
Z1
Z3
Z6
Z7

Figure 5

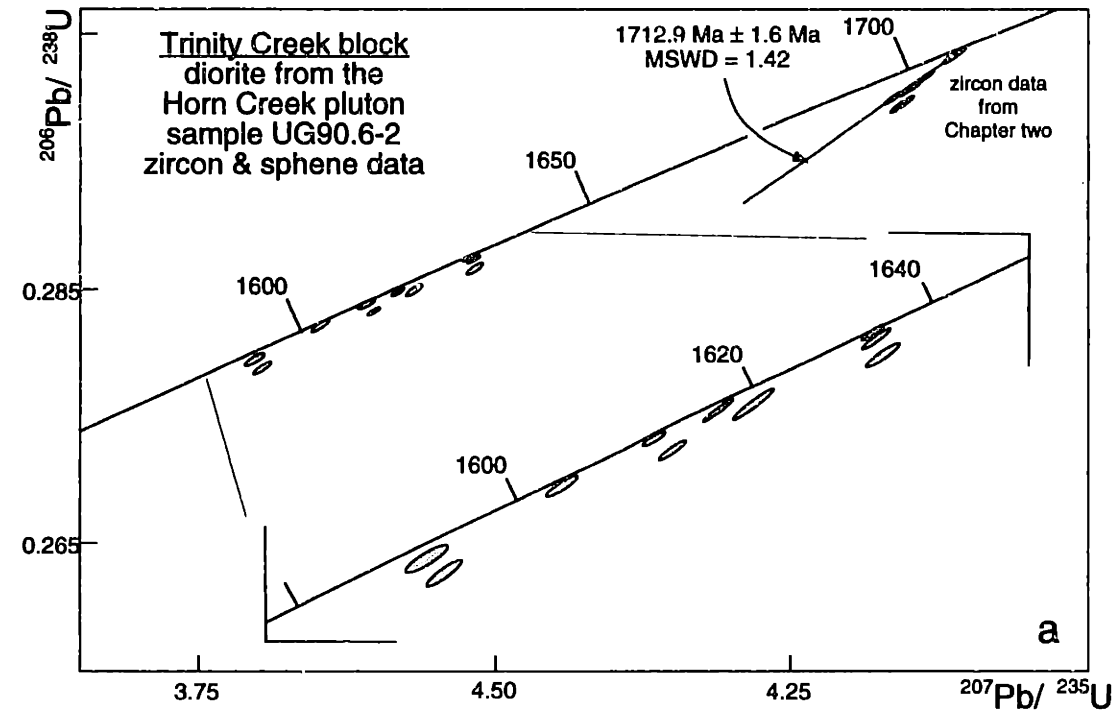
Trinity Creek block
diorite from the
Horn Creek pluton
sample UG90.6-2
zircon & sphene data
1712.9 Ma ± 1.6 Ma
MSWD = 1.42
1700
zircon data
from
Chapter two
1650
1600
1640
1620
1600
0.285
0.265
3.75
4.50
4.25
$^{206}Pb/^{238}U$
$^{207}Pb/^{235}U$
a

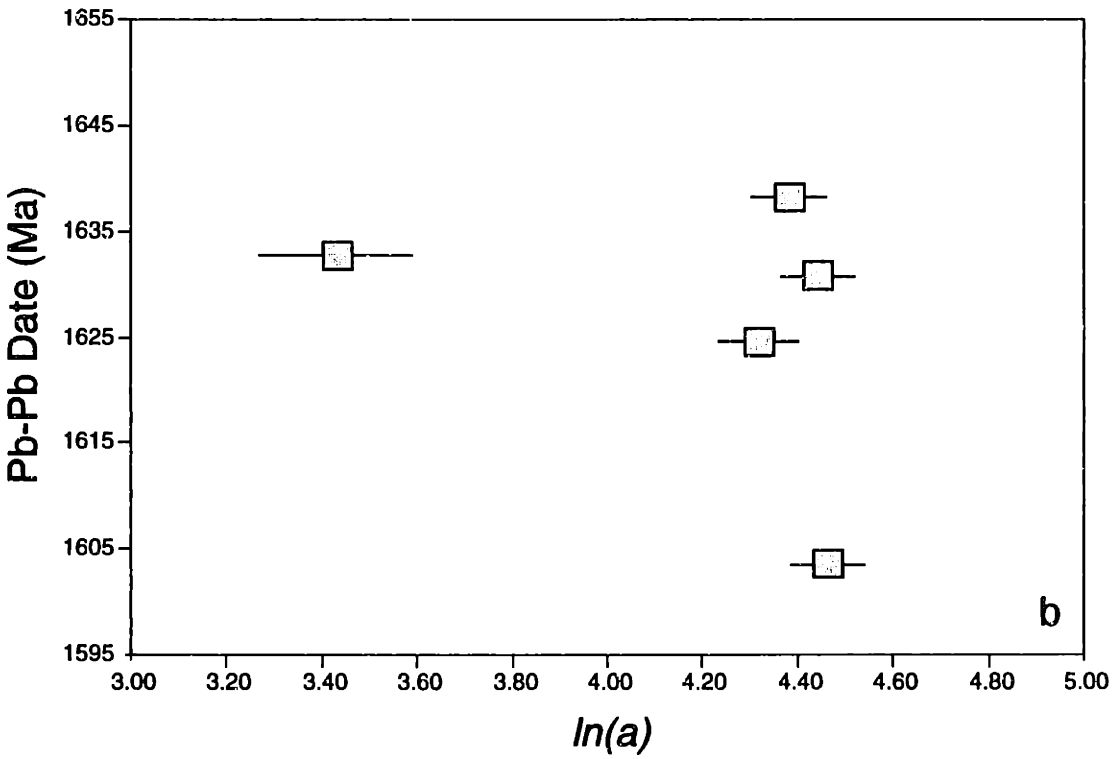
1655
1645
1635
1625
1615
1605
1595
Pb-Pb Date (Ma)
3.00
3.20
3.40
3.60
3.80
4.00
4.20
4.40
4.60
4.80
5.00
ln(a)
b

Figure 6

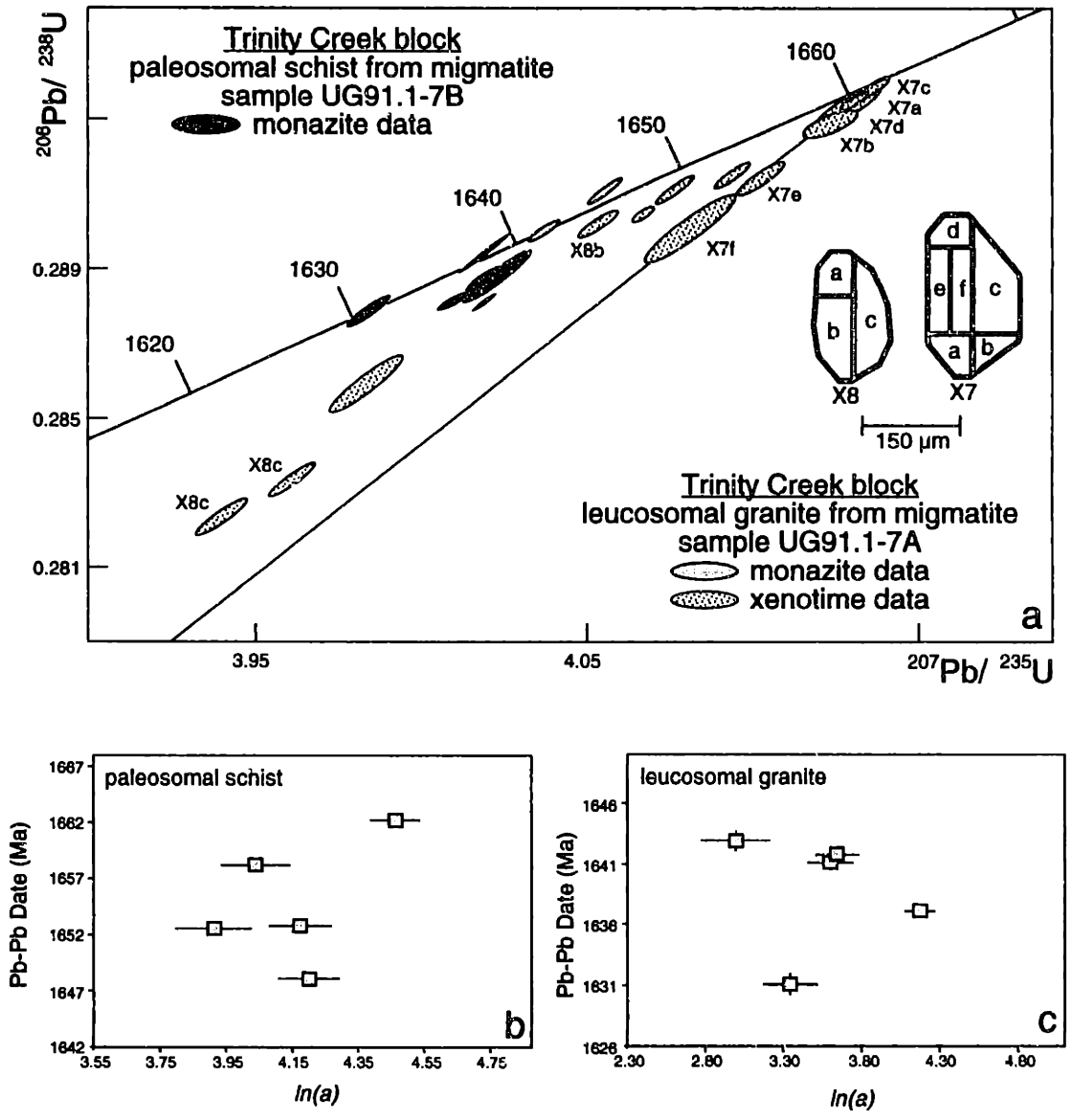
Trinity Creek block
paleosomal schist from migmatite
sample UG91.1-7B
monazite data
1660
1650
1640
1630
1620
X7c
X7a
X7d
X7b
X7e
X7f
X8b
X8c
X8c
0.289
0.285
0.281
3.95
4.05
$^{206}Pb/^{238}U$
$^{207}Pb/^{235}U$
a
b
c
d
e
f
X8
X7
150 µm
Trinity Creek block
leucosomal granite from migmatite
sample UG91.1-7A
monazite data
xenotime data
paleosomal schist
leucosomal granite
Pb-Pb Date (Ma)
ln(a)
b
c

Figure 7

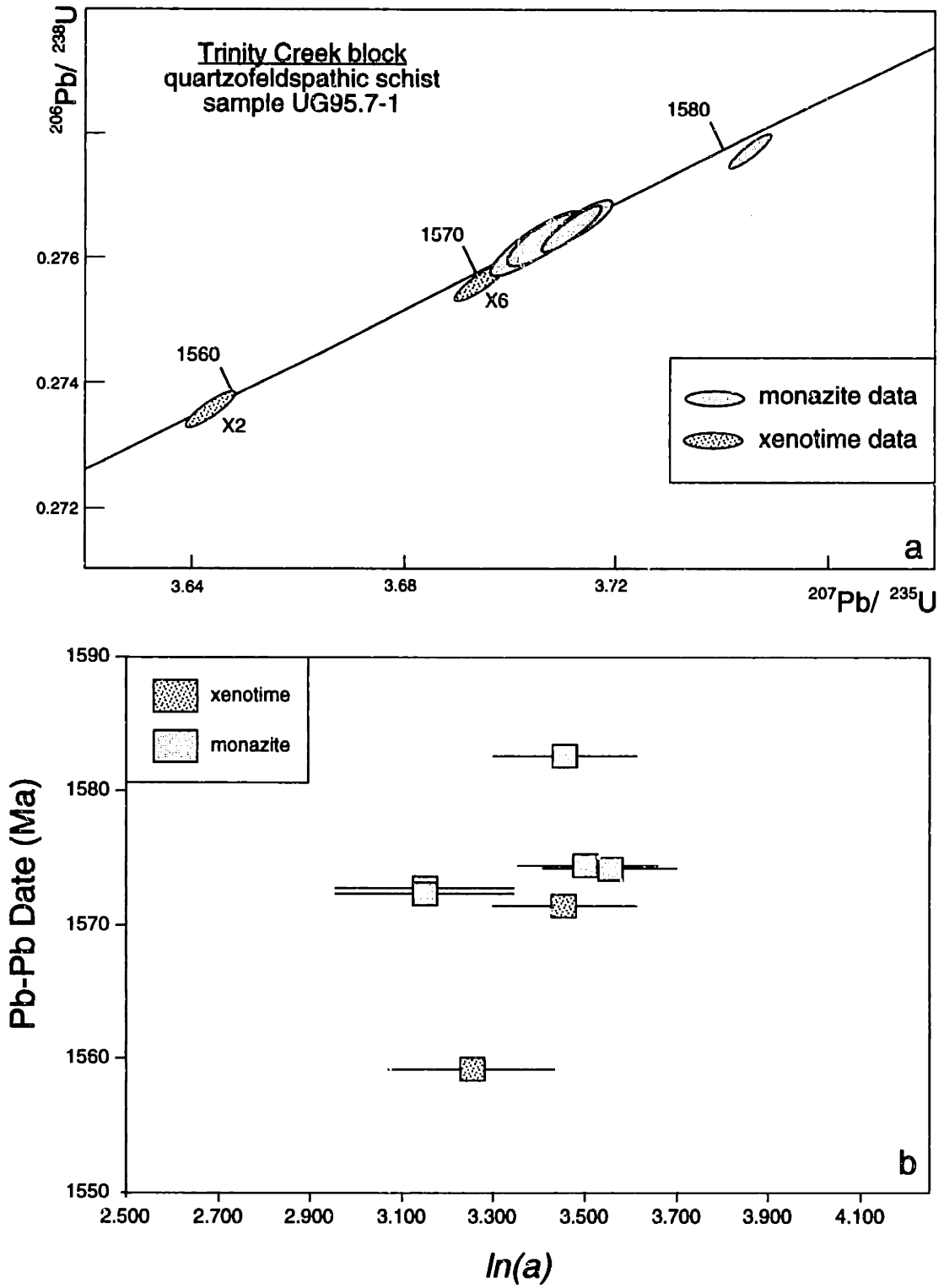
Trinity Creek block
quartzofeldspathic schist
sample UG95.7-1
1580
1570
X6
1560
X2
0.276
0.274
0.272
monazite data
xenotime data
a
3.64
3.68
3.72
207Pb/ 235U
206Pb/ 238U
1590
1580
1570
1560
1550
xenotime
monazite
Pb-Pb Date (Ma)
b
2.500
2.700
2.900
3.100
3.300
3.500
3.700
3.900
4.100
ln(a)

Figure 8

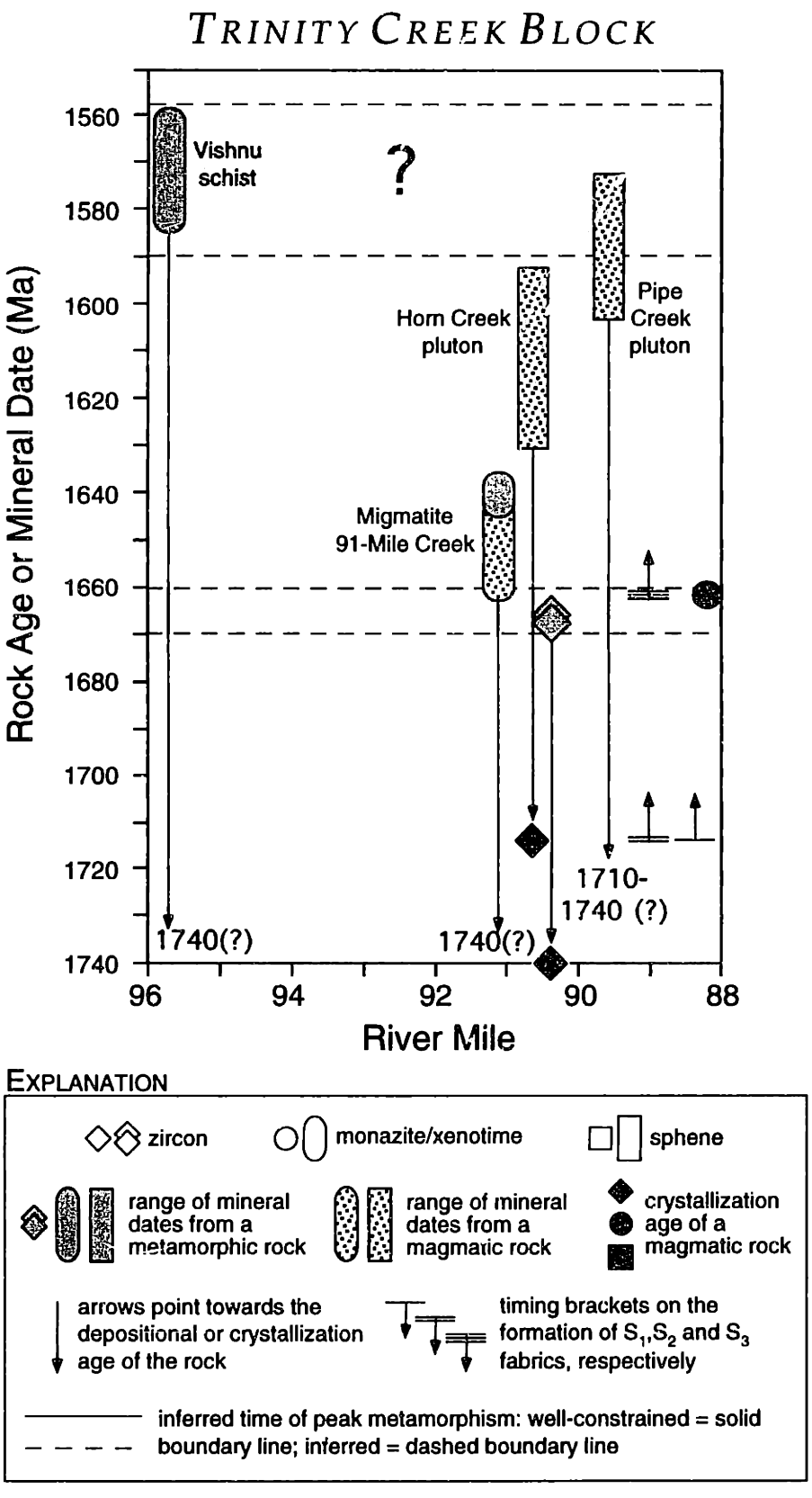
TRINITY CREEK BLOCK
Rock Age or Mineral Date (Ma)
1560
1580
1600
1620
1640
1660
1680
1700
1720
1740
96
94
92
90
88
River Mile
Vishnu schist
?
Horn Creek pluton
Pipe Creek pluton
Migmatite 91-Mile Creek
1740(?)
1740(?)
1710-1740 (?)
EXPLANATION
zircon
monazite/xenotime
sphene
range of mineral dates from a metamorphic rock
range of mineral dates from a magmatic rock
crystallization age of a magmatic rock
arrows point towards the depositional or crystallization age of the rock
timing brackets on the formation of S1,S2 and S3 fabrics, respectively
inferred time of peak metamorphism: well-constrained = solid boundary line; inferred = dashed boundary line

Figure 9

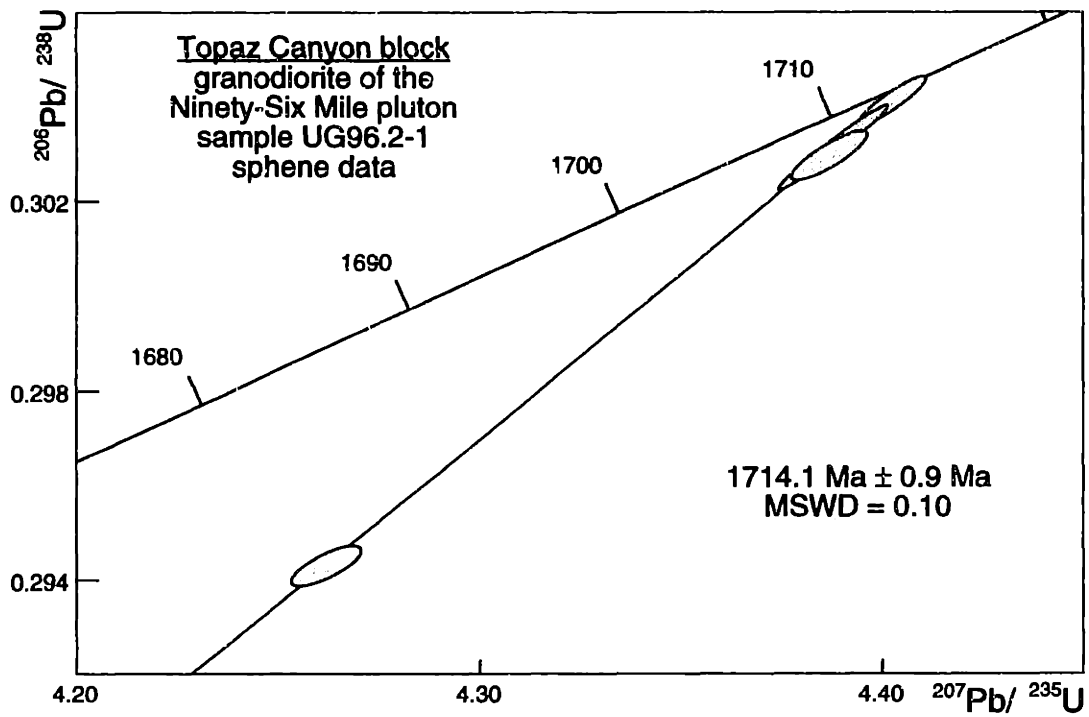
Topaz Canyon block
granodiorite of the
Ninety-Six Mile pluton
sample UG96.2-1
sphene data
1710
1700
1690
1680
0.302
0.298
0.294
1714.1 Ma ± 0.9 Ma
MSWD = 0.10
4.20
4.30
4.40
206Pb/ 238U
207Pb/ 235U

Figure 10

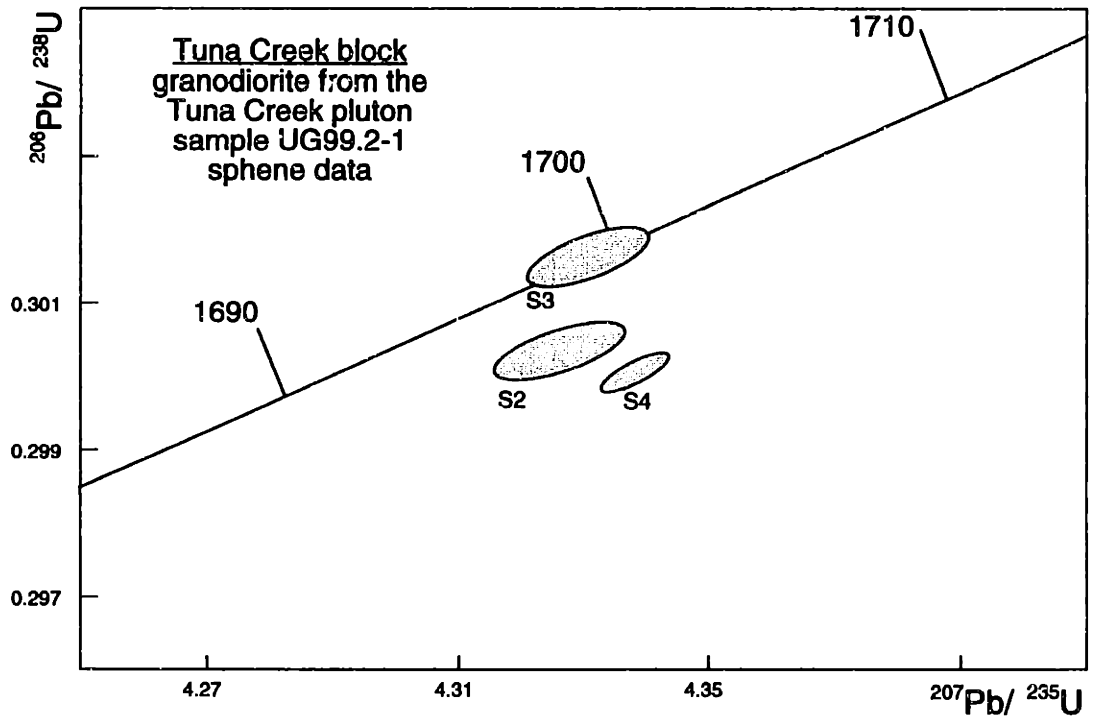
Tuna Creek block
granodiorite from the
Tuna Creek pluton
sample UG99.2-1
sphene data
1710
1700
1690
S3
S2
S4
0.301
0.299
0.297
4.27
4.31
4.35
206Pb/ 238U
207Pb/ 235U

Figure 11

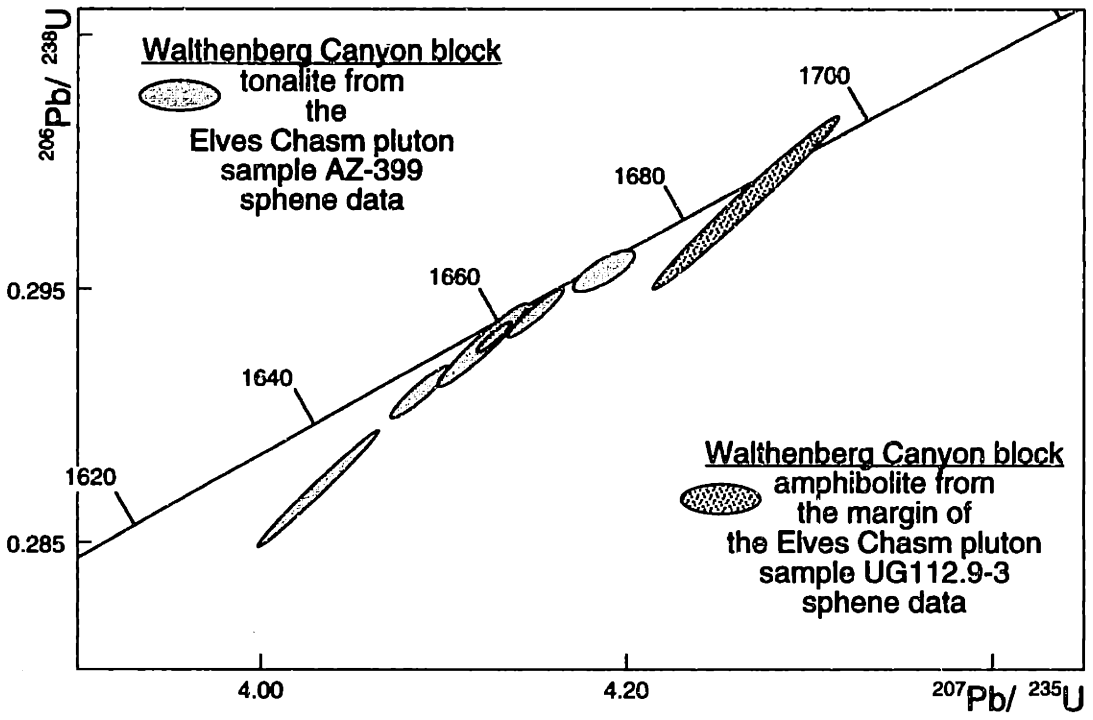
Walthenberg Canyon block
tonalite from
the
Elves Chasm pluton
sample AZ-399
sphene data
1700
1680
1660
1640
1620
0.295
0.285
Walthenberg Canyon block
amphibolite from
the margin of
the Elves Chasm pluton
sample UG112.9-3
sphene data
4.00
4.20
$^{206}Pb/^{238}U$
$^{207}Pb/^{235}U$

Figure 12

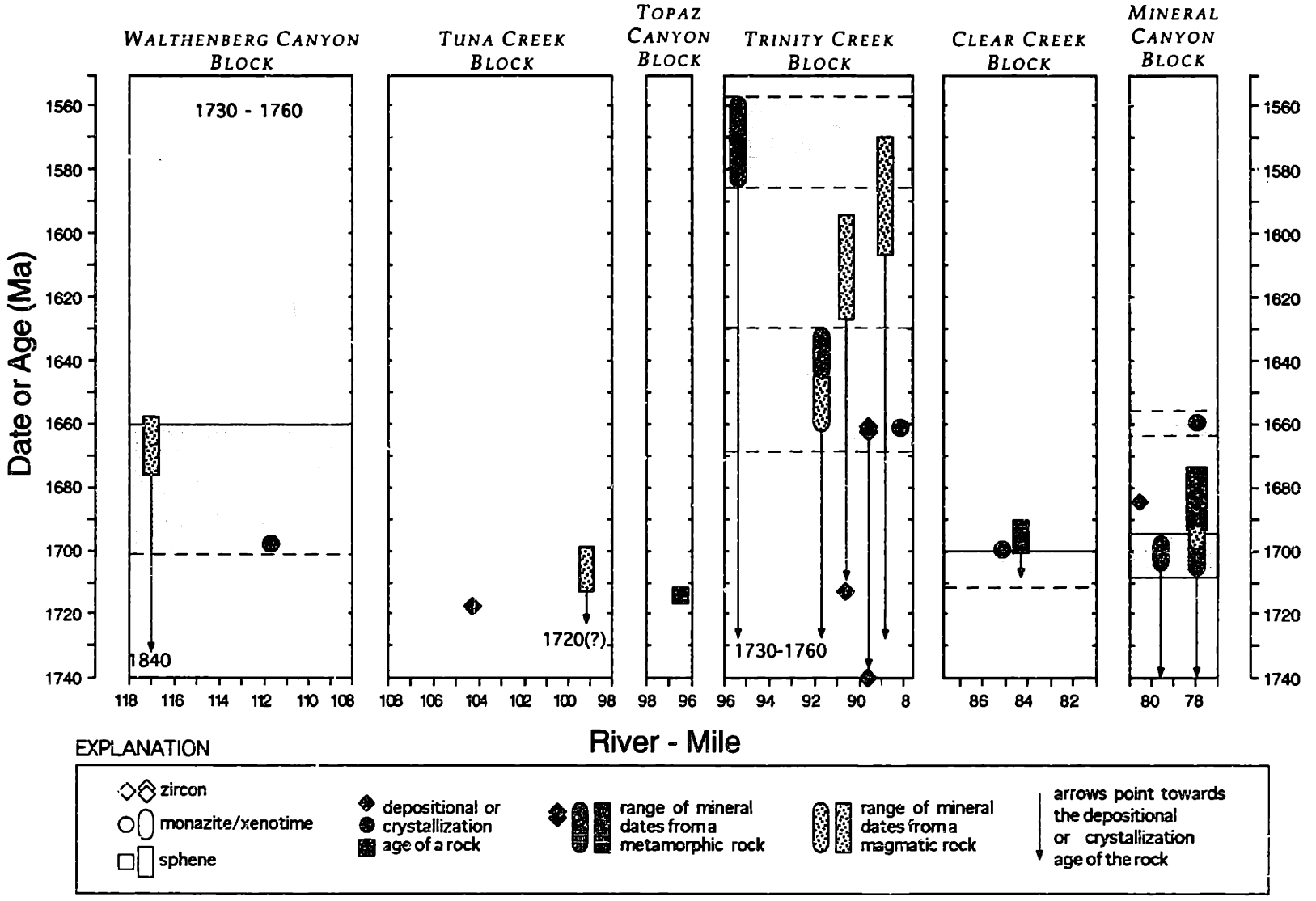
WALTHENBERG CANYON BLOCK
TUNA CREEK BLOCK
TOPAZ CANYON BLOCK
TRINITY CREEK BLOCK
CLEAR CREEK BLOCK
MINERAL CANYON BLOCK
1730 - 1760
1840
1720(?)
1730-1760
Date or Age (Ma)
River - Mile
EXPLANATION
zircon
monazite/xenotime
sphene
depositional or crystallization age of a rock
range of mineral dates from a metamorphic rock
range of mineral dates from a magmatic rock
arrows point towards the depositional or crystallization age of the rock

Figure 13

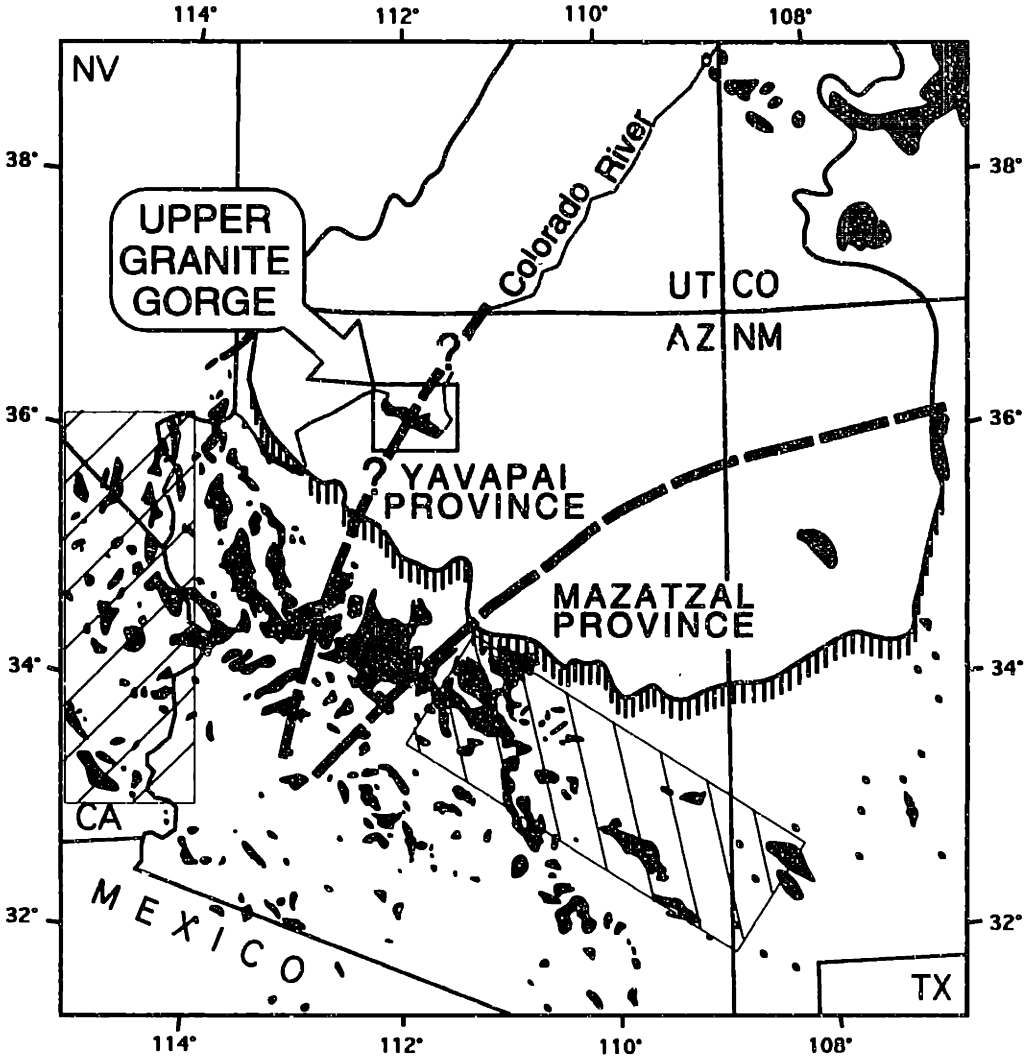
114°
112°
110°
108°
NV
38°
UPPER
GRANITE
GORGE
Colorado River
UT CO
AZ NM
36°
? YAVAPAI
PROVINCE
MAZATZAL
PROVINCE
34°
CA
32°
MEXICO
TX

Figure 14